UNIVERSITÀ DI PARMA

UNIVERSITÀ DEGLI STUDI DI PARMA

Dipartimento di Scienze Chimiche, della Vita e della Sostenibilità Ambientale (SCVSA)

Dottorato di ricerca in Scienze della Terra

Ciclo XXXIV

Potentials and limitations of new-generation multisource resistivity-meter: numerical modeling and applications

Coordinatore:
Chiar.mo prof. Marco Roveri

Tutor:
Chiar.mo prof. Roberto Francese
Co-tutor:
Dott. Federico Fischanger

Candidato:

Federico Bocchia

Anni Accademici 2018/2019-2020/2021

CONTENTS

1. INTRODUCTION

Resistivity method is nowadays a very common and established tool for subsurface investigation, and it is probably within the most widespread geophysical techniques. The reduction of the costs of high-precision electronics along with the method effectiveness boosted its application to a variety of study-cases. Applications span from traditional engineering and geology, to archaeology and hydrology, from the study of glacial dynamics to soil-plant issues. This great success was achieved during the 80-90's (***Binley and Slater, 2020***), since the advent of the so-called Electrical Resistivity Tomography (ERT), and increased constantly. Looking at the last 30 years, and making a parallelism with respect to the world of information technology, the major efforts was devoted to the "software" component of the method. The "software" component is an ensemble of procedures and environments that enable data visualization, processing and inversion. Again, this aspect was influenced by the rapid evolution of personal computers. On the other hand, the "hardware" aspects were partially overshadowed. For "hardware" here is not intended only the physical components employed in the field, but also how resistivity data are collected. In the afore mentioned period, in fact, no big changes were implemented, except for multi-channel acquisition procedures and new arrays optimized for specific tasks.

Finally in the last decade, new ideas have been brought and partially shared with the scientific community, and they are mainly focused on two aspects:

1) the improvement of the signal-to-noise ratio;

2) the reduction and/or simplification of logistics, especially for what concerns the deployment of heavy cables on the ground.

Regarding point 2) manufacturers realized modular systems, in which groups of electrodes are managed by autonomous units deployed along survey lines, i.e. the so called Distributed Acquisition Systems (***Kingman et al., 2007; Legault et al., 2008; Eaton et al., 2010; Lee et al., 2015***). Point 1) was faced introducing high-power transmitters, particularly indicated for deep surveys. This solution is still valid, even though other approaches are possible. A new-concept multisource (MS) system appeared in the market in 2013. This system overcomes the problem of the low signal-to-noise ratio in depth via multiple current injections using several simultaneous current dipoles. MS (***LaBreacque et al., 2013a***) represents a major breakthrough in ERT imaging, generating a lot of interest for deep surveying (*Deep ERT*, or *DERT*). Even if the system is already on the market from almost a decade, very few publications concerning its use and the associated potentialities are available (***LaBreacque et al., 2013a ; LaBreacque et al., 2013b***).

The aim of this research is to analyze potentials and limitations in the application of this new system filling a knowledge gap. The MS was tested in a variety of subsurface scenarios (changing target shapes, changing target-background resistivity contrasts, changing topography, etc) in order to understand the MS response to specific problems and assess the most effective deployment schemes.

Problems and simulation scenarios were associated to hydrogeological hazard. Italy, with its hilly mountainous (74%, according to ***Trigilia & Iadanza, 2008***) and highly urbanized/populated territory, is particularly vulnerable to extreme rainfall events often associated to catastrophic effects. According

to ***Herrera et al.., 2018***, almost 66% of the 900.000 landslides reported in Europe are in Italy. Floods and landslides cost about 1 billion dollars per-year since the end of World War II (***Trigilia et al., 2018***).

The development of specific geophysical techniques to image the subsurface is a first step to cope with the hydrogeological risks. The MS could represent a valid tool of analysis but, since its novelty, the final goal of this work is to define some "rules of thumb" in order to utilize the system in specific scenarios, and finally to interpret its results. A continuous comparison respect to traditional ERT survey results is part of this process.

The general workflow of this thesis started with the review of the scientific literature concerning the resistivity method.

The main features of the MS and the modelling/inversion algorithm were then discussed.

A first generation of numerical simulations was generated for the MS system over simple subsurface scenarios. The results of this simulation gave a first benchmark of the system response and resolving power, and they were compared respect to the results obtained by traditional arrays over the same structures.

The resolving power of the MS was then compared respect to traditional dipole-dipole in two simulated scenarios, specifically related to hydrogeological hazard. The selected scenarios were a river embankment and a landslide with a deep-buried sliding surface.

Simulation results were transposed into two real study cases, namely the levees of the Brenta river (where filtration phenomena during floods are present) and the Vajont landslide sliding surface.

The results obtained from simulations and real study cases were finally analyzed and discussed in order to comprehend the MS main potentialities and drawbacks. Some important future developments have been proposed too.

2. THE RESISTIVITY METHOD

The resistivity method is the measure of the ground attitude to conduce artificial electrical currents. This attitude could be used for several purposes but, at the end, it is strictly correlated to the geology of the subsurface or to the property of the investigated medium. These concepts are well known and pretty much accepted but they result from outstanding advancements in the knowledge of both artificial electrical circuitry theory and physics of earth materials. The employment of the resistivity method means applying circuitry theory (which involves the use of artificial currents) to media, generally characterized by poor-conducting attitude. Many authors demonstrated (***Ward, 1990; Loke et al., 2013; Binley and Slater, 2020***) how this approach works pretty well.

$$ERT = Electrical\ Properties\ of\ Rocks\ \&\ Minerals + Circuitry\ Theory$$

2.1 HISTORY OF THE METHOD

The 18th century could be reasonably considered the date of birth of a new way of looking at the earth interior. Right in this century a small group of scientists was making some sensational observations, leading to an innovative method of investigating the subsurface. The first study dates back to 1720 and shows the results collected by Stephen Gray and Granville Wheeler, about rock conductivity. A few years later (1746) William Watson discovered that the ground was a good electrical conductor (***Van Nostrand and Cook, 1966***).

A significant step-forward in the knowledge of electrical behavior of earth is due to Robert W. Fox who, in 1830, created a new method of investigation. Fox was a brilliant scientist of the Regency period. His studies in different branches of earth physics (e.g. magnetism or geothermal) earned him the posthumous appellation of "grandfather of geophysicists" (***Kunetz, 1966***). In the field of geoelectricity, he discovered the phenomenon of *spontaneous/self potential* (SP) by studying Cornwall's copper mines. Natural electrical currents of variable intensity were produced in case high concentration of sulfides. Despite his rudimental instrumentation (a compass needle enclosed in a turned wire as galvanometer; copper plates as electrodes), he was able to measure electric currents flowing between different points. Nevertheless, he was also the first scientist to propose a classification of minerals (or, at least, a part of those) based on their electrical behavior (conductor, poor conductor or non conductor), as well as to outline the presence of telluric currents (***Van Nostrand and Cook, 1966***).

These first observations have been further developed more than a half-century later (1882). Carl Barus, an American physicist of the United States Geological Survey (USGS), published the results obtained applying Fox's SP theory to the mining districts of Comstock Lode and Eureka, Nevada (USA). Results of his SP survey are comparable, in terms of technical approach, to nowadays measurements. For the first time in history, he designed non-polarizing electrodes as a combination of a metal strip and a zinc sulfate solution, in order to avoid electrode noise issues (moisture conditions, interchanging of position). The field technique employed by Barus during his survey was quite similar to the early 1900s SP mapping techniques. One electrode was kept in a fixed position

while a second electrode was moved in the area to be surveyed. Finally, he highlighted the relationship between resistance and moisture content of rocks (***Van Nostrand and Cook, 1966***).

The "new school" of USGS further expanded Barus's work between this period and the beginning of WWI (1914), especially with the efforts of Roger C. Wells. After a series of laboratory experiments concerning electrochemical processes of rocks, he was able of both recognizing the main causes of SP anomalies nearby ore bodies and specifying the direction in which the current flowed in their surroundings (***Van Nostrand and Cook, 1966***).

All these precursors, except for the low efficiency of their instruments, had one important thing in common: they actually measured electricity produced by nature itself and this current is variable in time and space (***Kunetz, 1966***).

The recognized "father of electrical soundings" is, without any doubt, the Alsatian engineer Conrad Schlumberger who "initiated the idea of introducing electric currents into the earth" (***Kunetz, 1966***). It is the same approach used today in electrical surveying. Firstly, he introduced the use of alternating currents (AC) and applied this concept to a point source, in order to map equipotential lines at various distances. He switched from AC to direct current (DC) to cope with the induced polarization effects: in this way he was able to draw potential profiles using two current electrodes. In summer 1912 Schlumberger designed and tested the method successfully in Normandie. He kept working in the area for mining applications since WWI begun. Schlumberger was aware about the presence of spontaneous natural potentials in his measurements and he proposed a first direct method to remove this noise. Thanks to this knowledge, he was able to discover important ore deposits in Serbia. Schlumberger thought this method in a sense of comparison between what he was actually measuring on the field (with its complex and heterogeneous nature) and what would exist if the same artificial current was applied to an homogeneous body; today, we call this latter concept "apparent resistivity" (***Kunetz, 1966***).

At the same time, on the other side of the Atlantic, Frank Wenner, a physicist at the U.S. Bureau of Standards, defined independently almost the same concept of "apparent resistivity" studying the properties of an inline configuration of electrodes designed by himself (1915). Today, we call this configuration Wenner configuration. This is not the only contribution that Wenner gave to geoelectricity (definition of the "theorem of reciprocity" in 1912), but the invention that he was able to patent was actually the first "modern" device capable of measuring the resistivity of the ground (in North America), after those of Fred Brown (1883) and Alfred Williams (1902, together with Leo Daft). Wenner derived the use of alternating non-commuted currents to avoid polarization effects. On the other hand, he definitively improved the instrumental capability both in injection (50-150 V between current electrodes, use of an ammeter to read current intensities, etc) and reception (use of a galvanometer, a phase shifter and a potentiometer to measure differential potentials) (***Van Nostrand and Cook, 1966***).

The "Schlumberger method", after WWI, was finally introduced in the two traditional domains of geophysical prospecting: mineral and oil deposits; geological framework. After the first successful ore deposits explorations (during the 20's) in Normandie (iron), Bray (iron), Alsace (potash) and southwestern France (lignite), the method was then applied to dam construction and water exploration in Africa. In oil exploration, the first important discovery made by Schlumberger was the correct detection and mapping of the Aricesti dome (Rumanìa) in 1923 (***Orellana, 1982***). A few years later,

the method was successfully applied also in North America for the study of zinc (USA) and sulfide (Canada) deposits (***Kunetz, 1966***).

Nevertheless, Schlumberger understood the importance of defining solid theoretical basis to its method: in this effort, together with his brother Marcel, with the Rumanian mathematician Sabba Stefanescu and with the French physicist Raymond Maillet, he tried to define the dynamics and problems (from a physical-mathematical point of view) of the propagation of direct currents in heterogeneous and stratified media. The main results of these studies are included in ***Stefanescu, 1932*** and ***Maillet and Doll, 1932***. Overseas, the standard electrode array was the Wenner but data interpretation lacked of rigorous physical and mathematical basis and it was carried out intuitively, completely ignoring (probably because of industrial coverage) Schlumberger advances.

Russia immediately understood the importance of Schlumberger's method and tried to implement it as a standard exploration technique. The country was immense and the location of minerals and hydrocarbons were almost unknown. The Russian government was fascinated by the methods developed in Sweden starting from the introduction in the country of the Daft-Williams method in 1906 (***Van Nostrand and Cook, 1966***). The mining engineers Hans Lundberg and Harry Nathorst, in fact, had invented a new system (1918) in which an alternating current of audio frequency (50-10000 cycles/second) was injected in the survey area by the mean of two parallel lines of electrodes. In this way, it was possible to map the equipotential lines beneath the ground surface. Nevertheless, a couple of years later (1921) another mining engineer, Karl Sundberg, put the basis of the Electromagnetic Method (EM), mingling together the electromagnetic galvanic method and the induction method. However, starting from 1928, the Russian government contracted Schlumberger's company in order to test his method for petroleum exploration (***Orellana, 1982***). The first results recorded in northern Caucasus (Grozny area) were remarkable and from this moment ahead the Russian school started an impressive development. Schlumberger's technique became the most important tool for petroleum exploration in the Soviet Union and led Russian scientists to further develop the method:

- between 1938-1939, L.M. Alpin ideated and tested the dipole survey method (independently from Geneslay);
- in 1945, Yarishev realized the first deep survey in the Grozny area;
- in 1947, A.P. Kraev, A.S. Semenov and A.G. Tharkov reached the incredible depth of 10 Km;
- since 1939, I.M. Blokh applied the dipole method to electrical logs, obtaining the first important results;
- I.V. Nazarenko ideated the first ERT marine survey (***Orellana, 1982***).

Another important introduction operated by Schlumberger and its company in Russia was the so-called "telluric method", ideated in the 30's in order to account for the effects of strange natural electrical currents (named telluric currents) that often interfere with the real electrical potential values measured in the field, especially in deep surveys. Starting from the second half of the 40's, the Compagnie General de Geophysique (CGG) started to use this latter method all around the world, but again was in Russia, since 1954, that was extensively adopted. Following the statement of ***Orellana (1982)***, 24 different teams prospected a total surface of almost 120.000 Km^2 per-year (as to1959).

Substantially, the methods defined between 1920-1940 remained unaltered until the 80's of the last century. Three techniques were actually the milestones of resistivity method:

1) electrical profiling, with the 4 electrodes at fixed distance moved along the survey line;

2) mise-à-la-masse method, with a single current source fixed in a conductor and a series of potential electrodes moved a part in order to measure the potential difference (and produce potential maps);

3) vertical electrical soundings (VES), i.e. the center of the survey line was kept fixed and the distance between the electrode was progressively incremented.

All these methods have their advantages, but they are also affected by a severe limitation: the subsurface electrical image is uni-dimensional (1D). Moreover, large scale exploration using the 4-electrodes approach was a gigantic effort in terms of logistics. The 80's were a crucial period for the development of the method. Cheaper electronics along with the exponential growth of information technology gave access to solutions simply unthinkable a few years before. In 1985 D.H Griffiths and J. Turnbull (University of Birmingham, UK) revolutionized the technique with the introduction of the first multi-electrode array by combining a microprocessor and a switching unit with a standard resistivity-meter (***Griffiths and Turnbull, 1985***). The new system was connected to 20 electrodes by a multicore cable resulted in the possibility of fast multiple acquisitions giving rise of the 2D acquisition method.

This great innovation was correlated to another major scientific breakthrough the use of numeric techniques to invert the field measurements to a true resistivity model. The previous standard was the use of a series of pre-calculated models of 1D sub-horizontal strata to determine resistivity and thickness of electrical stratification in the subsurface (chapter 2).

The growing power of computation enabled the utilization of inverse problem theory to solve this task, giving access to a more sophisticated reconstruction capability. The first proposed algorithms were defined by the linear filter method during the 70's (***Ghosh, 1971; Koefoed, 1979***), or again the damped least-squares method of **Inman, 1975**. A further development in this sense came out during the 90's with the creation of fast and stable automatic data inversion techniques (***deGroot-Hedlin and Constable, 1990; Li and Oldenburg, 1992; Loke and Barker, 1995***) that run on microcomputers. Hence, modern 2D georesistivity was actually born and this approach is currently in use.

The technological challenge was the construction of a system capable of handling an elevate number of electrodes and also to progressively reduce the amount of time needed for collecting the data. Since the 2000's, a series of "multi-channel" resistivity meters (with multiple potential dipoles "recording" the potential difference with a single transmitting dipole) were designed and tested, with 100 channels per-injection of some experimental systems (***Stummer et al., 2002***). Nevertheless, new configurations were ideated in order to better suite this kind of acquisition (***Dahlin and Zhou, 2006***).

Recent improvements in ERT have extended their use in much more complicated scenarios, especially in dimensional terms:

- 3D-ERT imaging consist of survey lines deployed in the form of a grid, with injection and reception that, at a certain point, will happen between different alignments instead of just along a single line. This reconstruction is possible in a 3D-native inversion environment, especially for large datasets. Despite the first 3D surveys were realized using a pole-pole configuration (***Park and Van, 1991***), today the most commonly employed configurations for 2D imaging (dipole-dipole, pole-dipole) are easily used in the third dimension (e.g. ***Papadopoulos et al., 2010; Chambers et al., 2013; Van Hoorde, 2017; Tejero-Andrade et al., 2018***);

- 4D-ERT imaging is a repetition of the measurements with a time shift between each survey (eg. ***Chambers et al., 2014; Supper et al., 2014; Kuras et al., 2016; Schmidt-Hattenberger et al., 2016; Wilkinson et al., 2015***) . Actually, there are no big issues about this kind of measurements, except for the automatization of the process, which of course requires the construction of an independent control unit. Diverse techniques of joint inversion have been proposed during the last years, however, very often, the differences between different sections are evaluated from distinct inversions.

The late improvements regard various aspects of resistivity measurements and they can be summarized as follows:

- increasing current intensity;
- reducing the use of heavy cables;
- continuous measuring of the potential differences during but also before and after a survey;
- remote controlling of the survey line.

2.2 ELECTRICAL PROPERTIES OF ROCKS

The resistivity tomography clearly depends on a natural property. This property is an attitude expressing the capacity of rocks to hamper electrical current flows; this "*hinder-effect*" is intimately correlated to lithological-mineralogical aspects. This attitude is defined as *specific electrical resistivity*. Many different controlling factors combined together result in very diverse resistivity ranges. The controlling factors are:

1. porosity;

2. efficient porosity (connection of pores);

3. percentage and nature of fluids;

4. clay percentage;

5. metallic percentage.

The most important process preventing rocks to be perfect insulators is known as *electrolytic conduction*: it is due essentially to the number of ions present in a solution and to their velocity??? mobility. The most common solution present underground is water with mineral ions, i.e. molecules with an excess or defect of electrons. The nature of these ions is the result of the lithology of an area. This process, globally, corresponds to an actual transport of material, expressed by more or less strong chemical transformations.

The majority of rock forming minerals are usually characterized by a very strong attitude to resist current flow, while in porous and water-bearing rocks this attitude is rather weak. Geological process can definitively act on resistivity both as a amplifier (metamorphism, carbonate precipitation, induration, silification) or as a buffer (again metamorphism, weathering, shearing and faulting, dissolution, salt water intrusion, clay alteration).

Two major subdivisions of rocks could be considered:

1. dense or anhydrous rocks;

2. hydrated rocks.

Dense or anhydrous rocks are not so common in the shallow crust, and their resistivity is mostly controlled by the matrix (i.e. lithology), and by other parameters, like the presence of flaws. These rocks show essentially a very high resistivity and a reverse proportionality between resistivity and both temperature-pressure.

Hydrated rocks can be further divided in two smaller groups, depending on the way they conduce the current. A rock is defined "clean" in case of conduction occurring throughout the pore-water (electrolytic conductivity). Differently the rock belongs to the "world of clays". G.E. Archie, back in 1942, analyzed the resistivity of a rock (ρ_r) developing a mathematical relation (1). Archie correlated this overall resistivity (ρ_r) to the resistivity of the fluid (ρ_w) present in the rock pores and he also defined a formation factor F expressing the relative percentage of filled pores.

$$\rho_r = F p_w = a\phi^{-m} S^{-n} p_w \qquad (1)$$

In this equation φ is the porosity of the rock and S is the degree of saturation; a, m and n are constants (with $0.5<a<2.5$, $1.3<m<2.5$ and $n\approx2$). Further versions of this equation have been lately developed, but their validity is restricted to specific rock/soil conditions (e.g., ***Schön et al., 2015***).

Starting from the same porosity (and, of course, lithology), the discrepancy between this and what the hydrogeologists define as "*efficient porosity*" (i.e. the interconnection between pores) determines that reducing the percentage of water inside the micro-cavities increases the effective resistivity of the rock, being occupied by a larger volume of air, gases or oil (generally extremely or highly resistive). Saturation could be also expressed in terms of ratio, also defined Archie's Resistivity Index (IR), between the resistivity of partial (R_t) and saturated rocks (R_0):

$$IR = \frac{R_t}{R_0} \qquad (2)$$

Various models have been proposed for non-shaly rocks to separate matrix and fluid resistivity. Layer models define rocks as a succession of layers of different resistivity, whose thicknesses are function of their volume fraction. Inclusion models consider rocks with a low percentage of voids. Changing the shape of inclusions i.e. modifying their geometrical properties results in varying the equations used to estimate resistivity. The spatial arrangement of inclusions (oriented or random) is also taken into account in these models. A few "capillary models" have been also proposed for the same rocks, assuming an electrical current flow in the direction of the capillary (***Spangenberg, 2001; Schön et al., 2015; Müller-Huber et al., 2015***).

Shales have a complex behavior because clay minerals, in contact with an electrolytic solution, give rise to a supplementary conductivity. Intensity of this secondary component is mainly related to the typology, volume and distribution of rock clay minerals. This latter aspect is the one considered to derive models to compute resistivity. For example, a laminated shaly sand distribution could be modeled as a parallel conductor according to Poupon (1954) equation (***Schön, 2015***):

$$\frac{1}{R_t} = C_t = (1 - V_{sh}) \cdot C_{sd} + V_{sh} \cdot C_{sh} \qquad (3)$$

where:

V_{sh}: laminar shale content;

R_{sh}: shale resistivity;

C_{sh}: shale conductivity;

R_{sd}: sand resistivity;

C_{sd}: sand conductivity;

R_t: measured rock resistivity;

C_t: measured rock conductivity.

Considering a shale rock with a fraction of shales partially mixed with the pore fluid, the conductivity of this fraction increases the overall fluid value. The Waxman-Smits (1968) equation model this "dispersed shaly sand", assuming the cationic exchange at the "clay mineral-water" interface:

$$\frac{1}{R_0} = C_o = \frac{1}{F^*} \cdot (C_w + B \cdot Q_v) \qquad (4)$$

Where:

C_0: conductivity of the shaly sand ($C_0=R_0^{-1}$), if water saturated;
B: equivalent conductivity of sodium clay-exchange cations [$S \cdot cm^2 \cdot mEq^{-1}$];
F^*: formation factor of the shaly sand;
C_w: conductivity of the formation water ($C_w=R_w^{-1}$);
Q_v: shalyness factor (cation exchange capacity per unit volume expressed in $mEq \cdot cm^{-3}$).

$$Q_v = CEC \cdot \frac{1-\phi}{\phi} \cdot \rho_{mineral}$$

where $\rho_{mineral}$ is the density of the mineral component [in $g \cdot cm^{-3}$];
φ is the porosity;
CEC is the cation exchange capacity [$mEq \cdot g^{-1}$].

2.3 CIRCUITRY THEORY APPLIED TO SUBSURFACE GEOLOGY

Attitude or measured property has been defined qualitatively, without providing any theoretical background to quantify current flow in different media (i.e. carbonates, granites, clays, etc).

A medium according to basic knowledge of circuitry theory could be modeled as an ensemble of resistance (R – resistance to movement of charge), capacitance (C – capacity to store charge) and inductance (L - ability to generate current from moving charges caused by varying magnetic fields). Resistivity surveys use direct current also to avoid the complexities caused by effects of subsurface capacitance and inductance. In practice there are two major limitations in the use of direct current: polarization of the ground around the electrodes; presence of natural (telluric) currents and spontaneous potentials. These phenomena cause potential gradients that could be mitigated using alternating low-frequency (0.03-3 Hz) currents (***Ward et al., 1990***).

The subsurface resembles an additional resistance *R* (measured in Ohms, Ω) in a generic circuitry with a single generator (**Fig.1a**). The generator can be thought as a device that is able to modify electrical neutrality of a material by concentrating and rarefying electrons: these domains are called negative and positive pole respectively. This unbalanced charge is called potential difference ΔV (measured in volts, V).

The first and the second Ohm's law can be then applied to this system:

$$R = \frac{\Delta V}{I} \qquad (5)$$

$$R = \rho \cdot \frac{l}{A} \qquad (6)$$

The resistance R of the circuit is directly proportional to ΔV and inversely proportional to the current intensity I (measured in Amperes, A). Resistance R is actually the combination of a geometry parameter (l/A, length to section surface) and an intrinsic parameter (resistivity ρ, expressed in Ω·m).

The method could be applied to devise resistivity of rock samples in laboratory or directly o outcrops in the field. The procedure is pretty the same, but the techniques developed for field measurements are more complicated compared to laboratory testing, especially for the spatial variability of physical properties in the subsurface.

Laboratory measurements use two couple of dipoles (**Fig. 1b**): a first dipole (usually referred as AB) is connected with a generator and an ammeter (to measure I). The second dipole (MN) is connected to a voltmeter (to measure ΔV). The rock samples are cylinders of length l and section $A=\pi \cdot r^2$ (r is the radius). Both ends are submerged in an electrolytic solution for a better galvanic coupling. The specific rock resistivity (***Schön, 2015***) is then a modified arrangement of (6):

$$\rho_r = \frac{A}{l} \cdot \frac{\Delta V_{MN}}{I_{AB}} \qquad (7)$$

Some values of rock resistivity of are reported in **Table 1**. A high value of resistivity for natural materials is of the order of thousands Ω·m, while a low value ranges between few Ω·m and several tens of 100 Ω·m. In general rock stiffness is directly proportional to its overall resistivity. Unfortunately there is no straight correlation between lithology/texture and resistivity due to the large number of variable affecting resistivity. For example resistivity in a block of unaltered limestone could be as high as 3 KΩ·m. Resistivity in the same block in presence of fractures and in dry conditions could rise to 4-5 KΩ·m while in saturated conditions could drop down to 1 KΩ·m or less. At the same time, a very compressed block of clay, measuring some tens of Ω·m in a standard physic state, would not be so "physically different" respect to the limestone block, even though geologically speaking the two materials cannot be compared. In this sense, probably the best way to measure resistivity is to know precisely the geology of the site we are studying.

Field measurements are somewhat similar although the system is organized in two components (***Carrara et al., 1992***):

- Injecting component (dipole AB): it has the function of ensuring a good input current intensity I for the receiving dipole MN and it is comprised of:

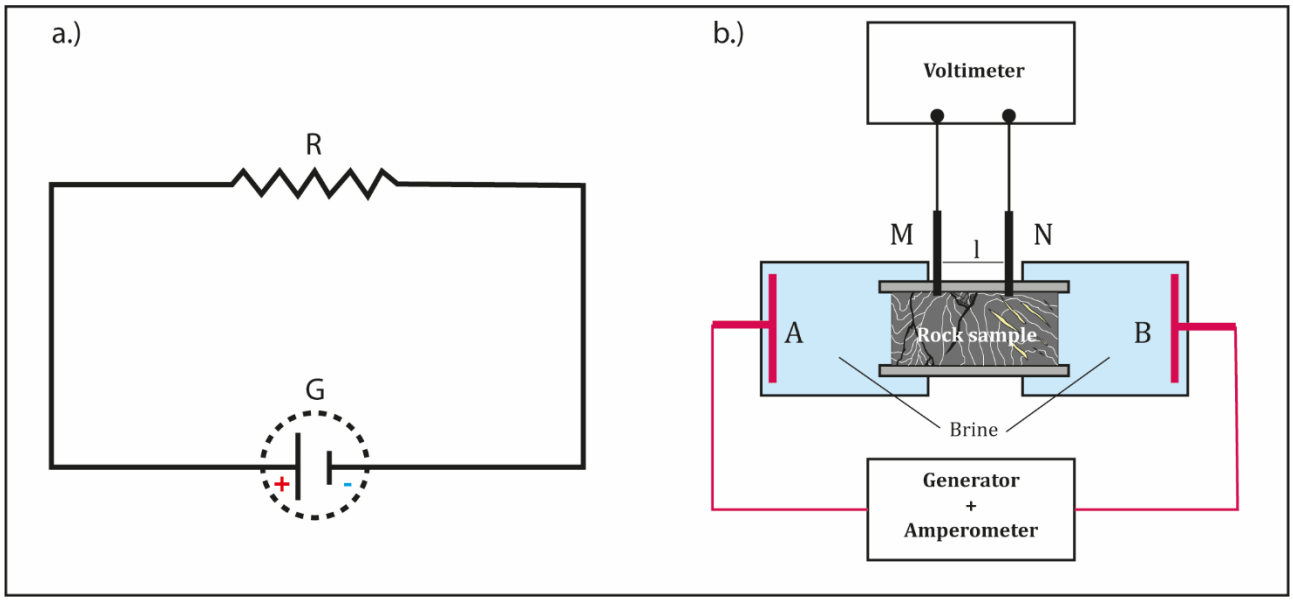

*Figure 1: a) elementary circuit with a generator (G) and a resistance (R); b) laboratory equipment for resistivity measurement of a rock sample: AB and MN are the current and potential dipole respectively (modified from **Schön, 2015**).*

- a 12 V car battery is generally an adequate current generator for shallow imaging (several tens of meters) while power generators should be employed in case of deep targets;
- an ammeter measures, in a parallel circuit, the intensity of the injected current. The accepted error is about 1%. Since the current is periodically inverted (to avoid polarization effects) the input signal is a Rademacher function;
- cables: they are characterized by a high flexibility and insulation (>3 KV) and a low ohmic resistance (<9 Ohm/Km). The diameter and the associated weight depend on the injected current (*I*) intensity.
- stainless steel or copper electrodes: they are metal stakes of almost 1 m of length and 10-30 mm of diameter. Electrodes allows ground coupling.

*Table 1: Laboratory resistivity values for minerals, rocks, water and sediments (from **Schön, 2015** and **Telford, 1991**).*

Mineral	ρ (Ω·m)	Rock	ρ (Ω·m)-range	Water/Fluid	ρ (Ω·m)-range
Quartz	$2.0x10^{14}$	Granite	$4.5x10^{3}$-$1.3x10^{6}$	Rainwater	300-2000
Amphibole	$4.8x10^{10}$	Diorite	$1.9x10^{3}$-$2.8x10^{4}$	Groundwater	5.0-300
Microcline	$1.8x10^{11}$	Gabbro	10^{3}-10^{6}	Seawater	0.18-0.22
Orthoclase	$1.4x10^{12}$	Basalt	10-$1.3x10^{7}$	Mineral/health water	0.5-1.0
Albite	$4.8x10^{8}$	Lavas	10^{2}-$5x10^{4}$	Tertiary sediments	0.7-3.5
Anorthite	$7.7x10^{9}$	Tuffs	$2x10^{3}$-10^{5}	Mesozoic sediments	0.31-47
Muscovite	$2.2x10^{12}$	Sandstones	1-$6.4x10^{8}$	Paleozoic sediments	0.29-7.1
Biotite	$8.3x10^{10}$	Conglomerates	$2x10^{3}$-10^{4}	Chloride waters from oilfields	0.049-0.95
Chlorite	$1.6x10^{9}$	Marble	10^{2}-$2.5x10^{8}$	Sulphate waters from oilfileds	0.43-5.0

Kaolinite	$3.2x10^7$	Clays & Marls	1-100	Bicarbonate water from oilfields	0.24-10
Dolomite	$4.3x10^{13}$	Dolomite	$3.5x10^2$-$5x10^3$		
Anhydrite	$1.0x10^9$	Limestones	50-10^7		
Gypsum	$1.05x10^{11}$	Schists	20-10^4		
Hematite	$1.0x10^2$	Hornfels	$8x10^3$-$6x10^7$		
Magnetite	$1.0x10^{-4}$				
Pyrite/Galena	$1.0x10^{-3}$				
Graphite	$1.4x10^{-5}$				

The current flowing in this component is:

$$I = \frac{V}{R_c} \quad (8)$$

Rc is the resistance of the input circuit and it is given by:

$$R_c = R_{cc} + R_g + R_{eg} \quad (9)$$

where R_{cc} is the cable resistance, R_g the ground resistance and finally R_{eg} the electrode-ground resistance.

- Receiving component: it has the function of measuring the potential difference induced by the injection of current in AB. It is comprised of:
  - a voltmeter: it measures the potential difference between electrodes M and N;
  - a suppressor: it is the deputy of cutting disturbances of both natural and artificial origin;
  - cables: same as injecting component;
  - electrodes: same as injecting component. Nonpolarizing electrodes (composed of a ceramic bottle with a porous bottom containing a solution of CuSO4 and a copper bar) are also utilized.

Potential difference (ΔV) measurements, as mentioned above, could be affected by severe levels of noise especially when the transmitting dipole is very large. Industrial, telluric or secondary coupling currents are always flowing in the ground and this presence can have a relevant impact on the survey. Furthermore the equipment itself generates disturbances. The transmitting and the receiving units have their own circuitry resistances. The measured potential $\Delta V'$ is a function of the real potential ΔV and of the resistance of electrodes M (R_m) and N (R_n):

$$\Delta V' = \frac{R_c}{R_i + R_m + R_n} \cdot \Delta V \quad (10)$$

With an absolute error value ε given by:

$$\varepsilon = \Delta V - \Delta V' = \frac{R_m + R_n}{R_i + R_n + R_m} \cdot \Delta \mathrm{V} \quad (11)$$

2.2.1 CURRENT FLOW AND ACQUISITION TECHNIQUE

In the most favorable scenario, we can assume a homogeneous subsurface characterized by a single resistivity value. Considering a generic quadrupole ABMN (**Fig.2**) current flows from A to B. Consequently, current I is distributed on a hemispherical surface of area $2\pi r^2$ (r is the radius of a generic sphere). Current density J and electric field E are defined as:

$$J = \frac{I}{2\pi r^2} \qquad (12)$$

$$E = -\frac{\delta V}{\delta r} \qquad (13)$$

Current density $J = E/\rho$ then:

$$\frac{\delta V}{\delta r} = -\frac{I}{2\pi r^2}\rho \qquad (14)$$

Applying this definition to the tripole AMN:

$$\Delta V_{MN}^{A} = \int_{M}^{N} \delta V = \frac{I\rho}{2\pi}\int_{r1}^{r2}\frac{1}{r^2}\delta r = \frac{I\rho}{2\pi}\left(\frac{1}{r_1} - \frac{1}{r_2}\right) \qquad (15)$$

The same derivation can be done for tripole BMN ($\Delta V_{MN}^{B} = \frac{I\rho}{2\pi}(\frac{1}{r_3} - \frac{1}{r_4})$). The resulting potential difference between electrodes M and N is the algebraic sum of the two terms:

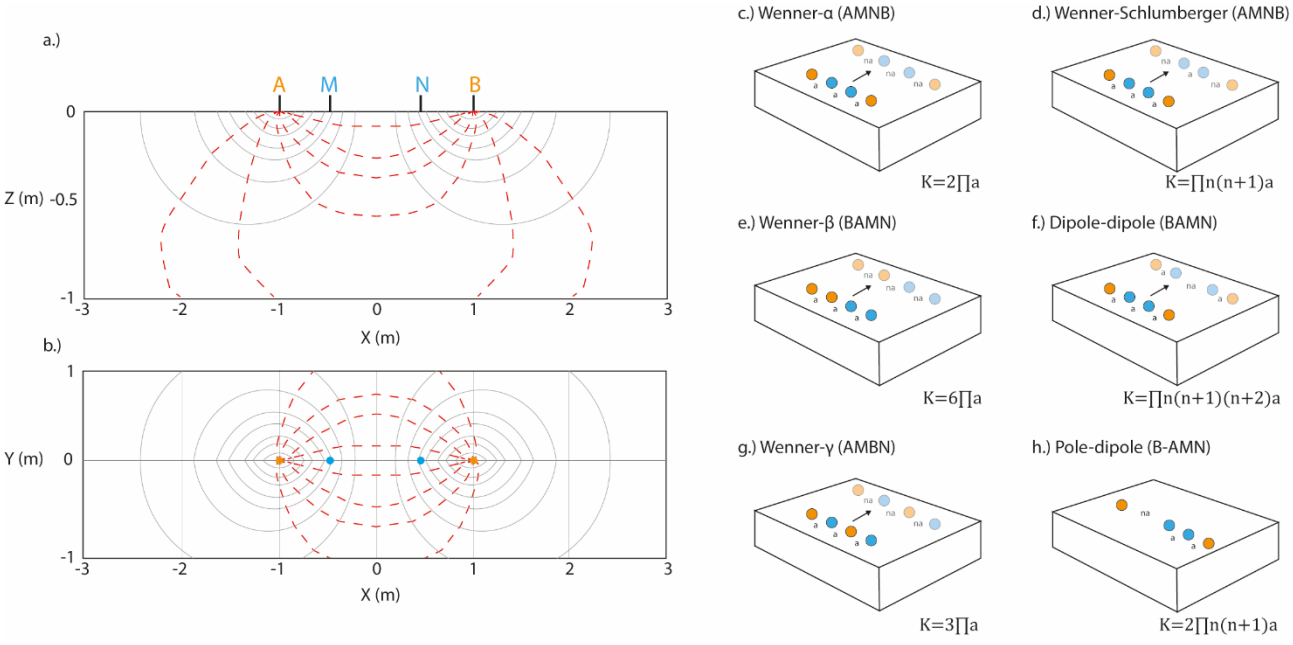

Figure 2: section (a) and plain (b) view of current lines (red) and equipotential surfaces (grey) for a generic AMNB quadrupole. c-h: electrode arrangement for traditional arrays (current dipole in orange; potential dipole in blue).

$$\Delta V = \Delta V_{MN}^{A} + \Delta V_{MN}^{B} = \frac{I\rho}{2\pi}\left(\frac{1}{r_1} - \frac{1}{r_2} - \frac{1}{r_3} + \frac{1}{r_4}\right) \qquad (16)$$

The resistivity measured with a generic AMNB quadrupole is:

$$\rho = \frac{\Delta V}{I} 2\pi \frac{1}{(\frac{1}{r_1} - \frac{1}{r_2} - \frac{1}{r_3} + \frac{1}{r_4})} = \left(\frac{\Delta V}{I}\right) K \quad (17)$$

The coefficient K is also known as "*geometrical factor"* and it depends upon the geometry of the quadrupole. Different quadripolar configurations result from changing the positions of A, B, M and N. Among the most used array there are:

- Wenner-α: the arrangement of electrodes is AMNB, with an equal spacing "a" between the electrodes. The geometrical factor is the minimal possible for a quadrupole ($K=2\pi a$). This array delivers the maximum signal-to-noise ratio (resulting from the low value of *K*). Slightly different versions are BAMN known as the Wenner-β ($K=6\pi a$) and AMBN known as Wenner-γ ($K=3\pi a$);
- Wenner-Schlumberger: the arrangement of electrodes is again AMNB, but while MN is kept equal to "a", AM and NB are equal to "na" ($K=\pi n[n+1]a$);
- Pole-dipole: a current electrode (A) is kept at "infinite" distance from B, M and N. Possible arrangements are ABMN, AMNB and AMBN ($K=2\pi n[n+])a$);
- Dipole-dipole: the arrangement of electrodes is ABMN, with a fixed distance "a" between BM and AB=MN=na ($K=\pi na[n+1][n+2]$).

Various other arrangements are possible laying down electrodes inline and cross-line (e.g., equatorial dipole-dipole).

Longer lines generally result in larger depth of penetration. The aperture of the current dipole AB and its distance with respect to the potential dipole MN control the vertical extent of the artificial electrical field E in the subsurface. The "rule of thumb" suggests a depth of investigation ranging from 0.16 to 0.20 times the line length. A quantitative relationship between array type and depth of investigation is given by the "sensitivity function" (***Edwards, 1977***). The sensitivity function expresses how a change in resistivity in an infinitesimal subsurface volume (dx, dy, dz located at x, y, z) affects the potential at the surface. This function, assuming a 2-electrode (pole-pole) array with the current electrode at the origin (0, 0, 0) and the potential electrode at a distance "a" (a, 0, 0) and with a current intensity of 1A, could be expressed (Loke and Barker, 1995) as:

$$F_{3D}(x,y,z) = \frac{1}{4\pi^2} \cdot \frac{x(x-a) + y^2 + z^2}{[x^2+y^2+z^2]^{1.5}[(x-a)^2+y^2+z^2]^{1.5}} \quad (18)$$

This equation is valid for a homogeneous subsurface. The sensitivity function is expressed by an absolute value, whose magnitude indicates the degree of confidence of the quadrupole in resolving subtle resistivity changes. The function has been computed for the basic arrays (**Fig.3**) considering a homogeneous background resistivity ρ of 10 Ω·m.

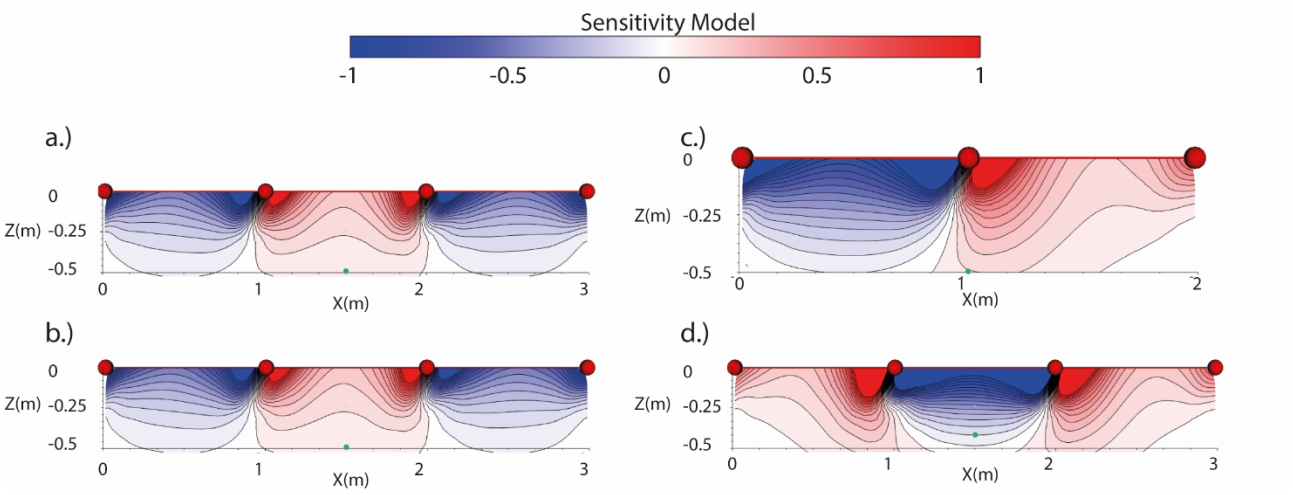

Figure 3: sensitivity functions for some basic arrays; a) Wenner-α; b) Wenner-Schlumberger; c) Pole-dipole (the remote/infinite pole is located at x=-10m); d) dipole-dipole.

The "depth of investigation characteristic" (DIC), sensu ***Roy and Apparao, 1971,*** could be obtained integrating (16) along the x-y axis. It is often indicated as the 1D solution of the sensitivity function (19):

$$F_{1D} = \frac{2}{\pi} \cdot \frac{z}{(a^2 + 4z^2)^{1.5}} \qquad (19)$$

DOI of each array could be obtained plotting equation (19). The "median depth of investigation" suggested by ***Edwards (1977)*** is a robust guess of DOI. The "achievable" depth corresponds to half of the area bounded by the DIC curve (**Fig. 4**).

Horizontally, the medium point of a quadrupole is used to place its corresponding datapoint.

The quadrupole approach has been used since the beginning of ERT method (Carpenter and Habberjam, 1956). In particular, two basic techniques have been widely:

1) Vertical Electrical Soundings (VES): a AMNB quadrupole is laid down on the ground and a first measurement is taken. The AB dipole is then progressively opened taking measurements step by step while the MN dipole is kept fixed. Once the measured potential (ΔV) drops below noise level the MN dipole is enlarged with respect to the AMNB center. AB dipole is then further opened repeating few stations to match the resistivity curves with different MN spacing. VES are particularly useful for imaging 1D resistivity distribution;

2) Horizontal Electrical Profiling (HEP or EP): a fixed quadrupole is shifted along the survey line using single or multiple AB apertures. This approach is useful to map lateral resistivity variations at various depths.

a.)

	z/a	z/L	K
Wenner-α	0.519	0.173	6.2832
Wenner -β	0.416	0.139	18.850
Wenner-γ	0.594	0.198	9.4248
Wenner-Schlumberger			
n=1	0.519	0.173	6.2832
n=2	0.925	0.186	18.850
n=3	1.318	0.189	37.699
n=4	1.706	0.190	62.832
n=5	2.093	0.190	94.248
Pole-dipole			
n=1	0.519	0.296	12.566
n=2	0.925	0.308	37.699
n=3	1.318	0.330	75.398
n=4	1.706	0.341	125.66
n=5	2.093	0.349	188.50
Dipole-dipole			
n=1	0.416	0.139	18.850
n=2	0.697	0.174	75.398
n=3	0.962	0.192	188.50
n=4	1.220	0.203	376.99
n=5	1.476	0.211	659.73

b.)

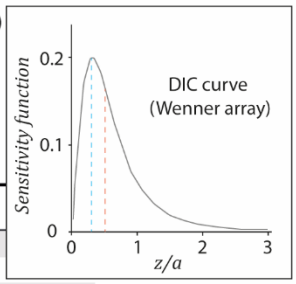

*Figure 4:a) relationships between DOI (z) and electrode spacing (a) or line length (l), with respect to the geometrical factor (K) of each configuration (**Edwards, 1977**); b) example of 1D sensitivity function plot.*

The introduction, in the late 80's, of multicore cables (resulting in 16, 24, 48, 96 or more electrodes) along with the application of a microprocessor-relèe (switch) system enabled to address multiple quadrupoles leading to modern resistivity-meters. A programmed sequence of $A_iB_jM_kN_l$ measurements is loaded and executed, combining VES and HEP, resulting in a full 2D automated survey (***Griffiths and Turnbull, 1985***).

Modern resistivity-meter are comprised of:

1) a command console, that could host all the components (battery, ammeter, voltmeter, microprocessor, switching unit) and execute the acquisition sequence measuring I and ΔV for each current injection;

2) a cable-electrode ensemble to transmit currents and carry.

This setup enables to automatically take from few hundreds to several thousands of measurements unraveling a solid quantitative approach for electrical imaging of the subsurface. An example of such a survey, using 24-electrodes and Wenner-α array, is shown in **Fig.5**.

2.2.2 INVERSION FROM APPARENT TO TRUE RESISTIVITY

Measured resistivity (ρ) is actually the result of a constrained simplification. The j-measured current (I_j) and voltage (ΔV_j) along with the geometrical factor (K_j) return a j-value of resistivity value at a certain depth (z_j) depending on the specific DOI of the quadrupole. This value is defined *apparent resistivity* (***Hallof, 1957***). The concept of *apparent resistivity* was already expressed by both Conrad

Schlumberger and Frank Wenner at the beginning of 20th century. Hundreds or thousands of apparent resistivity values are nowadays collected by automatic resistivity-meters along survey lines. The plot of this ensemble of data-points is called "pseudo-section". The pseudo- prefix indicates that z is not a true z but it just indicates the level of a specific data-point. The more the AB is opened, the more the pseudo-z increases. At this stage of representation no geological interpretations could be done.

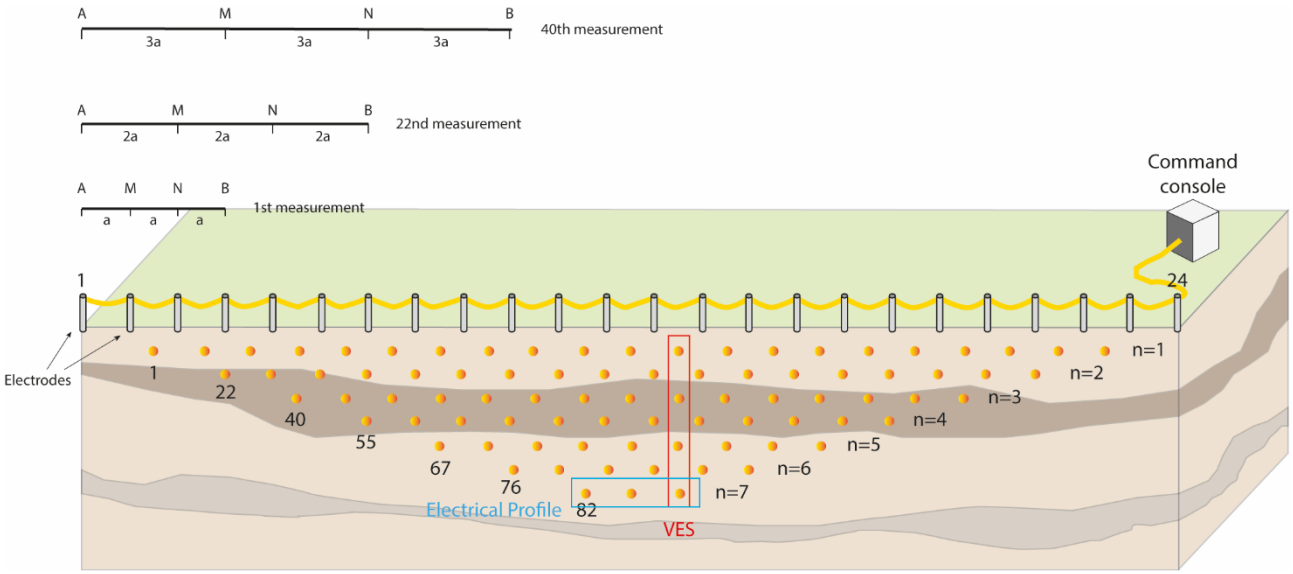

Figure 5: example of a survey lined comprised of 24 inline electrodes. Data-points are collected using a Wenner-α configuration; n represents the order of dipole (aperture). The orange circles represent the data-points in a pseudo-section representation (modified from ***Loke et al., 2013****). Basic VES and a EP datasets are also represented.*

The concept of "apparent resistivity" (ρ_a), to a certain extent, could be a correct assumption for shallow survey, but it is absolutely misleading for deeper measurement. Some additional steps are required to turn the "apparent resistivity" pseudo-section onto a "real resistivity" image of the investigated medium.

This process, in case of 1D surveys (VES and EP), could be assimilated to overlapping the field curves (plotted as AB/2 versus ρ_a) to a set of pre-computed curves and find the best match (***Mooney and Wetzel, 1956; C.G.G., 1963; Orellana & Mooney, 1966; E.A.E.G., State Public Works Service, 1969; Mundry & Homilius, 1979***).

The process, in modern 2D measurements, is based on a forward-inverse approach and it takes advantage of electronic calculators (personal computers, workstations, mainframes, etc). Inverse theory (***Rosenfeld and Kak, 1981; Scales, 2001; Tarantola, 2005; Guzzi, 2012***) is actually the cascade combination of two processes going in opposite directions:

1) forward problem: it is the calculation of potential differences resulting from a executing a designed acquisition sequence on a specific electrode array (with its peculiar spacing) on a known resistivity distribution (initial subsurface model). According to Ohm's laws, the corresponding apparent resistivity can be calculated. Mathematically speaking this is a "good-posed" problem, in the sense that for a specific cause exists at least one solution, and this solution is unique. The solution of the forward problem is the solution of a differential second-order equation known as *Poisson equation*:

$$-\nabla \cdot [\sigma(x,y,z) \cdot \nabla V(x,y,z)] = I\delta(x_s)\delta(y_s)\delta(z_s) \qquad (20)$$

where:

- Σ is the electrical conductivity;
- V is the potential difference;
- I is the current intensity;
- ∇ is the Laplace operator;
- δ is the Dirac's delta function;
- x, y, z are the Cartesian data-point coordinates;
- x_s, y_s, z_s are the point-source coordinates.

The Poisson's equation is generally solved numerically to simplify calculation. Solution types will be discussed in the following chapters. The majority of these solutions requires a-priori discretization of the medium. A survey in the field is somewhat a forward-problem-solving procedure except for the fact that the resistivity distribution in the medium is unknown. Forward-problem-solving is currently used also to simulate the response to a specific array of a known resistivity distribution. It is the forward modeling, and various authors (e.g. ***Dahlin and Zhou, 2004; Martorana et al., 2009***) have already demonstrated the effectiveness of this approach in improving survey design and assisting data processing and interpretation.

2) inverse problem: this process is the opposite of forward modeling. A known ensemble of measured potentials are turned into a resistivity distribution within the medium. It is a classical "ill-posed" problem, i.e. a specific potential distribution (the measured ΔV dataset) could be obtained by several different resistivity models.

The solution of the ambiguity takes advantage of computer's calculus power. The initial resistivity model is iteratively modified to obtain a set of calculated potentials that better approximate the measured values. Unfortunately the problem still remains undetermined (requiring the generation of an unrealistic number of models to be tested) nevertheless a set of constraints is introduced to reduce the number of possible models.

2.2.3 COST-EFFECTIVENESS OF ERT SURVEYS

Cost-effectiveness of a geophysical survey should be properly taken into account although it is not generally within the target of a scientific experiment nor of theoretical developments.

Cost-effectiveness of ERT imaging depends on two factors:

1) Line geometry (number and spacing of electrical probes), site morphology (escarpments, topography gradients, infrastructures, etc) and surface conditions (outcrops, soft soils, mud, water bodies, etc);

2) Survey crew as regards to skills, experience and number of operators.

Considering an ideal case with in the following conditions:

- Flat topography;
- No infrastructures;
- Soft soil;
- Crew comprised of 2 operators.

The acquisition of a 48-electrode line, with 1 m electrode, could be accomplished in 45-60 minutes of fieldwork. The daily production of 5-6 ERT lines is then a realistic objective. Increasing the electrode spacing to 5 m (in similar flat conditions) affects just marginally survey time.

Survey design and planning is also crucial to speed up field operations.

3. THE MULTI-SOURCE SYSTEM

The Multi-Source system (MS) was firstly introduced in 2013 (***LaBreacque et al., 2013a; LaBreacque et al., 2013b***) and since its appearance very few papers have been published on this topic. The MS was developed to overcome a major and acknowledged limitation of the traditional systems: the low signal-to-noise-ratio at large transmitter-receiver aperture. MS enables the simultaneous injection of currents with several transmitting dipoles, meanwhile the potential is measured at a single dipole. MS has been already utilized for mineral exploration with little or no applications in other fields.

3.1 GENERAL FEATURES

The MS is a distributed resistivity-meter, with a slight difference with respect to standard DAS (Distributed Acquisition Systems; see ***Kingman et al., 2007; Legault et al., 2008; Eaton et al., 2010; Lee et al., 2015***). The distributed parts of the system are both transmitters and receivers. In order to do that, the system makes use of stand-alone units that incorporate both the injection and the measuring components. These units are called *transceivers* (transmitter-receiver), and they form the elementary component of the MS (**Fig.6a**). Every single unit manages three different electrodes. Unit and electrodes are connected via a standard (1.5 mm^2) monopolar cable. Three distinct electrodes result in three different dipole combinations: 1-2, 2-3 and 1-3. Each dipole could be addressed as a transmitter (TX) or as a receiver (RX). Two dipoles are short, namely 1-2 and 2-3, while the third dipole, namely 1-3, is longer. Every unit is independent and it has its own power supply provided by a 12V NiMH battery capable of 240 Watt-hours.

Except for the connection between the electrodes and their corresponding unit, no cables or other physical connections are present among different units. For this reason the MS can be considered *wireless*. Units are operated via a *command console* hosted on a laptop. Moreover, every unit is equipped with an internal GPS for both timing and positioning. Timing is crucial and it should be extremely precise in order to run the acquisition scheme, meanwhile positioning is not as crucial and describes the unit layout. The communication bridge between the command console and the boxes is provided by a powerful ISM radio (868-900 MHz) based on small antennas present on each unit and on the console itself (**Fig.6b**). The radio coverage is few kilometers depending on topography and vegetation. Except for transporting the stainless steel electrodes, the major diffuclty in deploying this kind of instrumentation on rough terrains is represented by the need of moving the battery.

Anyway, the most important and innovative feature of MS is definitively its possibility of using multiple simultaneous transmitting dipoles per-measure. The general idea behind this technology is a new strategy for the improvement of the S/N ratio. Other systems use generator-supplied power while MS uses multiple units to transmit in parallel (***LaBrecque et al., 2013b***). In this scenario, the standard 12V batteries (or similar) are still usable. Evidently, this was mainly intended for *DERT* surveys. The transmitters are multiple and simultaneous meanwhile the recording dipole per measure is single.

MS offers several advantages with respect to more conventional *DERT* systems: mob/demob costs are lower; no need of a power generator; no need of gasoline; no generator-related noise; minimal safety concerns. MS delivers a maximum power of 350 W, resulting in a maximum differential

potential of 300 V hence of a maximum current intensity of 2.5 A; moreover, the deployable units in a single survey are as high as 255, and no major limitations are known about the possible number of simultaneous transmitters.

MS, considering the features of both transmitters and receivers, represents the first true wireless resistivity-meter. Due to its peculiar design MS collect data only in dipole-dipole configuration.

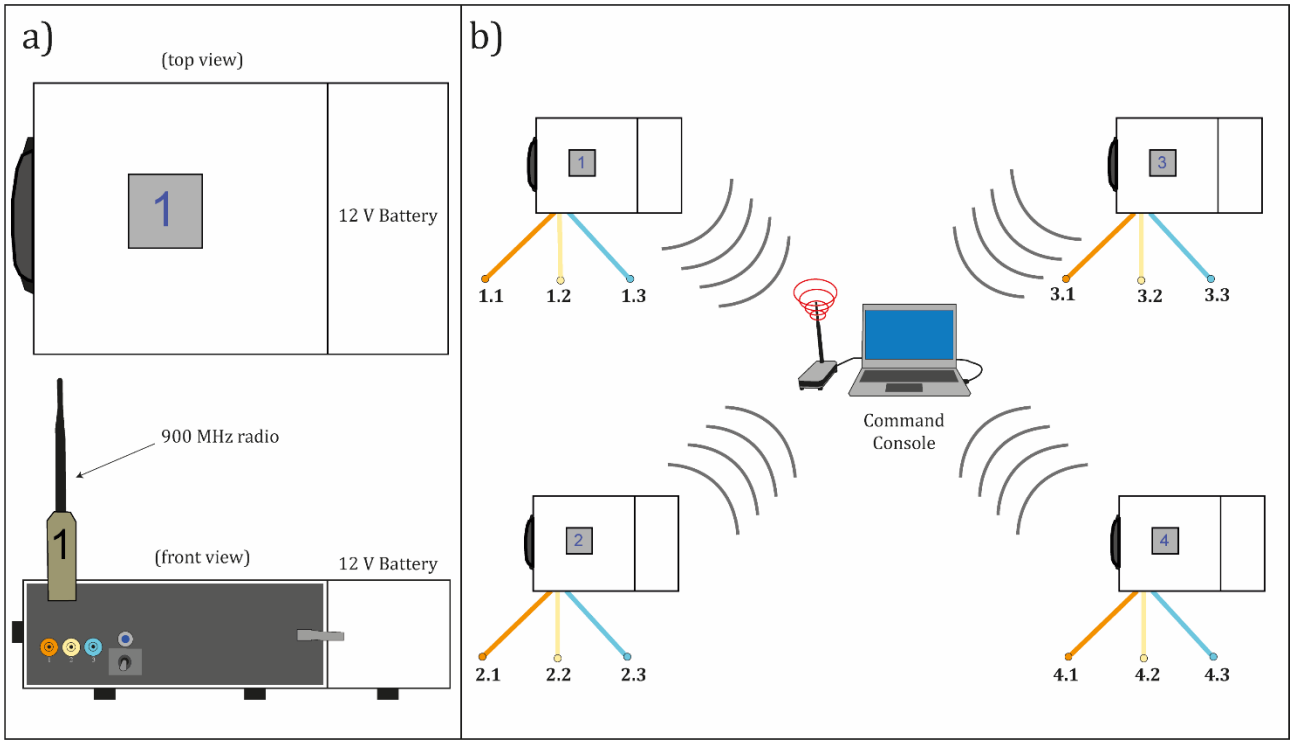

Figure 6: a) Scheme of a MS transceiver; b) four transceivers radio-linked to the command console.

3.2 THE DIPOLE-DIPOLE ARRAY: APPLICATIONS TO DERT AND MS VERSION

The transmitting electrodes in a dipole-dipole array are external with respect to the receiving electrodes. DD measures the earth resistivity at growing depth either by increasing the distance between the centers of the current and the voltage dipoles at constant spacing or by enlarging the spacing. The DD array was experimented after the Wenner and the Schlumberger arrays and it was introduced in order to overcome the problems encountered in deep VES surveys. Long cables, current losses and induction effects on the MN circuitry were among the major problems. All these issues were almost canceled by the use of the dipole-dipole array, in the sense that short cables were required to accomplish survey objectives (***Orellana, 1982***). Russian scientist discovered these advantages at first and they used DD arrays massively in industrial operations (***Alpin, 1950***). Other advantages of this kind of geometry were soon discovered (***Orellana, 1982***):

- the possibility of bilateral measurements, with the deployment of two different MN dipoles symmetrically with respect to AB;
- the great horizontal sensitivity to resistivity changes in the subsurface (***Keller, 1975***);

- the possibility of duplicate measurements (switching the injection and the receiving dipole) for quality control.

On the other hand, enlarging the AB-MN distance implied also the necessity of employing current generators in order to inject high intensity current and obtain an adequate S/N ratio at the target depth of exploration. Moreover, the DD array is very sensitive to topography, even though this last issue today could be easily solved. The DD array, over the last 60 years, has driven DERT applications in industrial and research projects. Some examples are discussed in ***Anderson and Keller (1966), Keller et al. (1975), Monteiro Santos et al. (1997), Storz et al. (2000), Tamburiello et al. (2008) and Rizzo et al. (2019)***.

For these reasons, the MS system is designed to operate only as a dipole-dipole array

In MS mode, the TX units cannot operate both as TX and RX units thus limiting the number of the possible combinations. This is obvious, because the coexistence of a same electrode in the transmitting and in the receiving circuitry needs to be avoided. Furthermore the multiple simultaneous transmitters need to be selected from different units: for example, in case of double injections the two transmitters should belong to two different MS units. This constraint reduces the maximum opening of the transmitting dipoles to a value of *2a*. The same constraint applies also to the receiving dipole. No specific limitations are known for the order factor n.

A simple example, considering 5 inline units, could clarify the MS-DD operating scheme (**Fig.7**). Five units result in 15 different electrodes *a*-spaced. In single-transmitter mode (1TX) the sequence is somewhat similar to a standard DD resulting in 100 measurements. E1 and E2 of unit #1 operate as transmitter while all the possible couples of the remaining units, with the same aperture, act as receivers. The last potential is measured using the couple E2-E3 of unit #5. With m representing the number of electrodes, a total of (m+1)/2 measurements are acquired in this first order of measure (m/2 if the number of electrodes is even).

The transmitter is then switched to E2 and E3 of unit #1 and the scheme is repeated from the beginning. The dipole aperture is then enlarged (from *a* to *2a*) and now E1 and E3 of unit #1 operate as transmitter and repeats the acquisition for all the possible couples, corresponding to (m+1)/4 in number (m/4 when the number of electrodes is even). Unit #2 is then selected to inject current in the subsurface using electrodes E1 and E2 (aperture *a*), and so on.

The result of such acquisition scheme is a clusterized distribution of apparent resistivity data, as shown in **Figure 7**. In this kind of acquisition scheme, the actual number of measurements acquired is doubled, because the system is designed to acquire also reciprocal measurements. The possibility of reciprocal (duplicated) removals is left to the user: Reciprocals generally increase the computation time during inversion, as well as in the acquisition operations; on the other hand, their values carry very useful information concerning the noise present in a dataset.

In double-transmitter mode (2TX), the measuring scheme is somewhat similar just the number of transmitters in increased of one. The first two units (electrodes E1-E2) are used as transmitters, meanwhile the third unit host the first receiver (electrodes E1-E2). Maintaining the same TX positions, the RX is moved towards the end of the line from an electrode couple to the successive, with a final overall number of (m+1)/3 (or m/3 when the number of electrodes is even). The TX dipole couple is then shifted of one unit (couples 2-3) and the sequence is repeated; finally, the opening of the dipoles is doubled (as in the previous case) and the number of measurements equals (m+1)/6 (or

m/6). According to this scheme, there are no duplicated measurements and the pseudo-plot of the measurements is less dense than the 1TX mode.

The procedure is analogous also for the quadruple-transmitter mode (4TX).

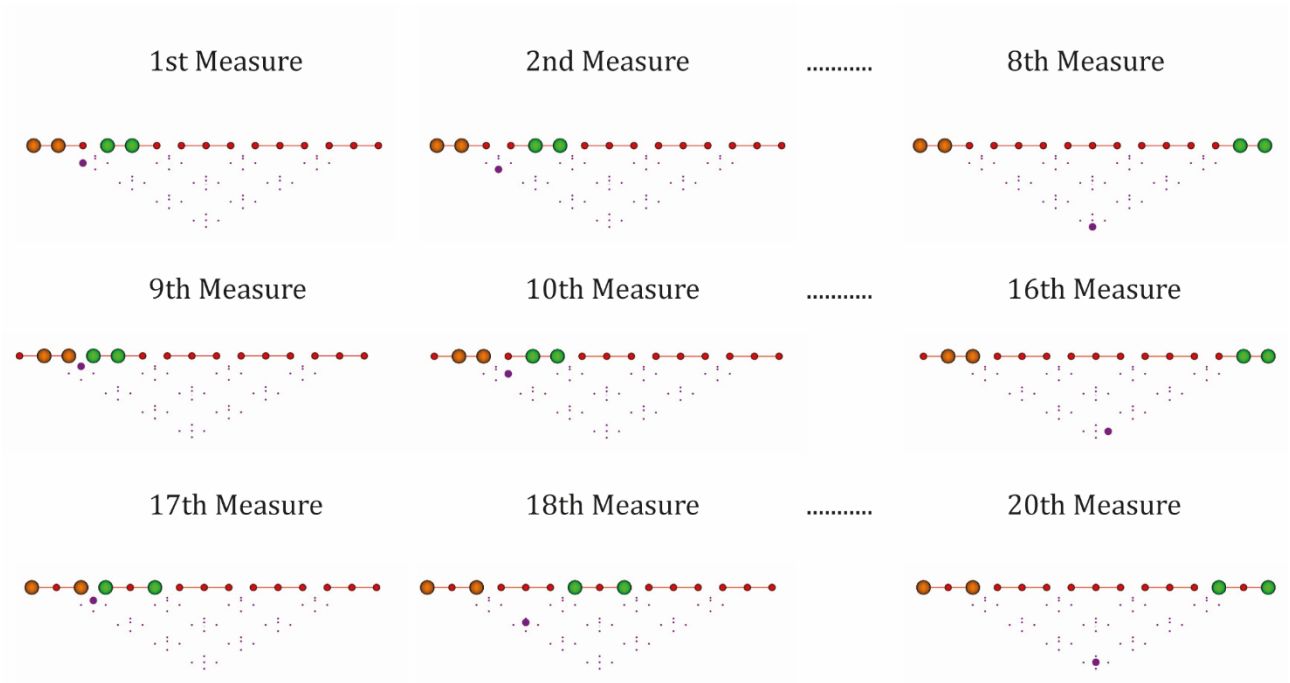

Figure 7: Sequence of measurements for the MS in 1TX mode. The scheme is repeated in multiple transmitter mode. The transmitting dipole is orange, while the receiving one is green.

Multiple transmissions means multiple measures per time, and each measure is characterized by a specific geometrical factor (K) influencing the corresponding voltage. Considering a generic quadrupole AMNB, K is calculated as follows:

$$K = 2\pi\left(\frac{1}{d1} - \frac{1}{d2} - \frac{1}{d3} + \frac{1}{d4}\right)^{-1} \qquad (20)$$

where d1 and d2 are respectively the distances AM and MB while d3 and d4 represents AN and BN. If the considered quadrupole is a dipole-dipole array, like the one in **Fig.8A**, the four distances take the form of:

$$d1 = (n+1)a$$

$$d2 = na$$

$$d3 = (n+2)a$$

$$d4 = (n+1)a$$

… it follows that:

$$K = 2\pi\left(\frac{1}{(n+1)a} - \frac{1}{na} - \frac{1}{(n+2)a} + \frac{1}{(n+1)a}\right)^{-1} \qquad (20.1)$$

… and finally:

$$K = 2\pi\left(\frac{-2}{na(n+1)(n+2)}\right)^{-1} = -\pi na(n+1)(n+2) \quad (20.2)$$

The apparent resistivity could be calculated as:

$$\rho_a = K \cdot \frac{\Delta V}{I} = -\pi na(n+1)(n+2) \cdot \frac{\Delta V}{I} \quad (21)$$

The formula, in case of multiple transmitters, is slightly different. Assuming, for example, the case of four simultaneous transmitters case (**Fig.8B**). The medium where the current flows is considered homogeneous (constant ρ). Since transmission is from four different simultaneous dipoles four different voltages are theoretically measured at any receiving dipole. According to the superimposition principle:

$$\Delta V = \Delta V_1 + \Delta V_2 + \Delta V_3 + \Delta V_4 \quad (22)$$

Indicating with V_1, V_2, V_3 and V_4 the voltage corresponding to the first, the second, the third and the fourth transmitting quadruople of the transmission. Resistivity for transmitter #1 is:

$$\rho = K_1 \cdot \frac{\Delta V_1}{I_1} \quad (23)$$

The voltage for transmitter #1 is:

$$\Delta V_1 = \frac{\rho \cdot I_1}{K_1} \quad (24)$$

The overall voltage is then:

$$\Delta V = \Delta V_1 + \Delta V_2 + \Delta V_3 + \Delta V_4 = \frac{\rho \cdot I_1}{K_1} + \frac{\rho \cdot I_2}{K_2} + \frac{\rho \cdot I_3}{K_3} + \frac{\rho \cdot I_4}{K_4} \quad (25)$$

… resulting in:

$$\Delta V = \rho\left(\frac{I_1}{K_1} + \frac{I_2}{K_2} + \frac{I_3}{K_3} + \frac{I_4}{K_4}\right) \quad (25.1)$$

The apparent resistivity for the four simultaneous transmissions in then calculated as:

$$\rho = \frac{\Delta V}{\left(\frac{I_1}{K_1} + \frac{I_2}{K_2} + \frac{I_3}{K_3} + \frac{I_4}{K_4}\right)} \quad (26)$$

The same approach is valid for a generic measure with N transmitter:

$$\rho = \Delta V \sum_{i=1}^{N} \frac{1}{\frac{I_i}{K_i}} \quad (27)$$

3.3 MS SIGNAL

The elementary waveform of a MS transmission is a square wave but, differently from the majority of traditional systems, a time shift of "0 current" is inserted, with a period of the same temporal length with respect to the injection. This shape of the signal was designed with the specific purpose of

recording the differential potenital not only in terms of immediate response respect to the injected current, but also in terms of late response (potential versus time) controlled by the electrical nature of the subsurface. In other words, the system is designed to acquire both, resistivity and spectral data.

The MS signal is entirely programmable. The default is a 3-stack square wave, with each stack comprised of 2 cycles. The final waveform is then comprised of 3 x 2 = 6 cycles. Spectral measurements are taken during the same acquisition cycle.

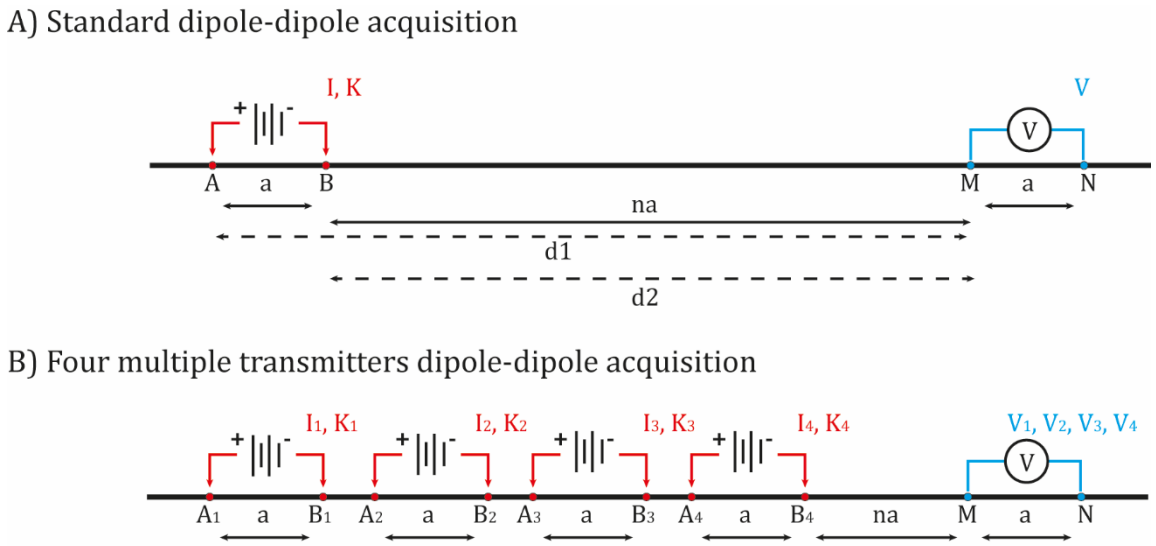

Figure 8: A) Traditional dipole-dipole array; B) 4TX MS dipole-dipole afrray. Dipole aperture is indicated with letter "a" while dipole order is indicated with letter "n".

The measurement in the MS system takes place in the following 4 steps (**Fig.9**):

1) the electrical current is injected for a period (Ttx) of 1/(4·BF), where BF indicates the Base Frequency (typically 1Hz, and so Ttx=250 ms);

2) the unit waits for a specific time interval (usually 0.010 s), namely the Resistivity Time Delay (TRDely), and then measures the voltage averaged on the Resistivity Measurement Time (TlnghtR, ~0.017 s);

3) the current is turned off for a period Ttx, meanwhile the TDIP decay waveform is measured in one or more time windows;

4) the polarity is then reversed and the measures are repeated closing the basic injection cycle.

3.4 FORWARD MODELING ON SINGLE/MULTIPLE MS RESPONSE

Forward modeling could be used as a preliminary aid in estimating the different subsurface response moving from single to multiple simultaneous current injections.

DOI and expected Vmn (**Fig. 10a-b**) could be estimated once defined background resistivity (Ω·m) and input current (A). The sensitivity versus depth curve could be also estimated (**Fig. 10c-d**).

A simple simulation using 5 inline units (with 1 m electrode spacing) could provide initial insight on MS signal intensity. Modeling parameters are a homogeneous background resistivity 100 Ω·m and a current intensity of 1000 mA.

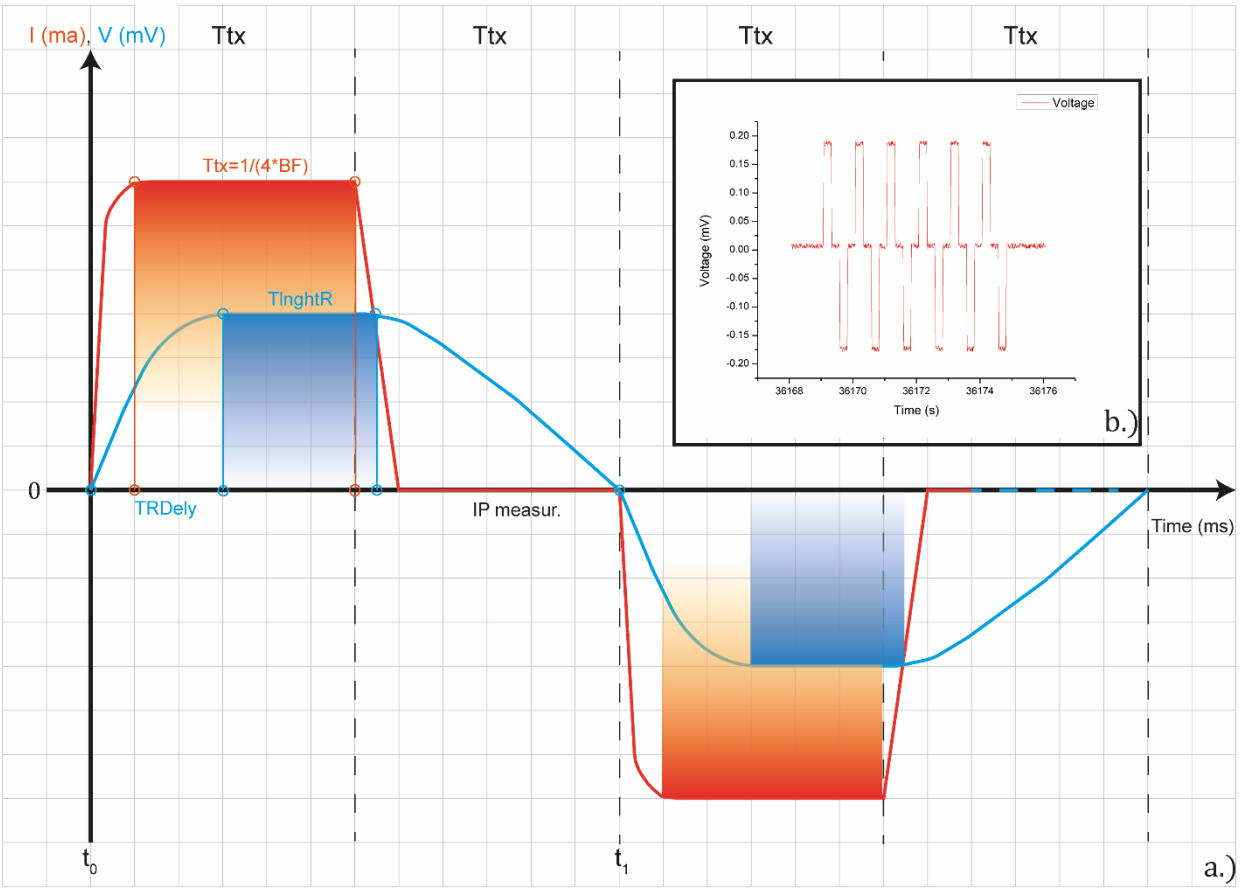

Figure 9: a) MS signal. Current intensity: orange line; Injection occurs in the time interval marked by the shadowed area. Voltage Drop (blue line); Voltage drop is measured in the time interval marked by the shadowed area. IP data are collected during the no-current time shift. b) Real MS signal (6 cycles) measured in the field.

In 1TX mode (**Fig.11a**), and considering dipole 1-2 of the first box as transmitter, it can be seen how the expected voltage decreases from a value of almost 1330.6 mV, measured at the closest TX-RX interval (two times the electrode spacing, **Fig.11-a1**), to a value of 14.6 mV measured respect electrodes 2-3 of box 5 (**Fig.11-a2**). Even though the sensitivity/DOI graph does not show great variances between the various receivers, the decay curve in the expected signals can be followed quite good looking at the potentials virtually recorded at each receiving dipole (**Fig.11-a3-right**).

Very similar considerations can be done looking at the injection between the first two boxes of the line, considered as transmitters in the 2TX mode (**Fig. 11b**), and dipole 1-2 and 2-3 of boxes 3 and 5 respectively (**Figg.11, b1-b2**). In this sense, the addition of one more transmitter seems not very helfpful in the closest case (1482.6 mV), meanwhile in the far receiver scenario its use should affect importantly the survey (46.8 mV), resulting in almost 3 times the expected signal in the single-transmitter case (**Fig.11-b3-right**).

Some easy preliminary tests like the ones just discussed could be a strategic procedure for any kind of survey.

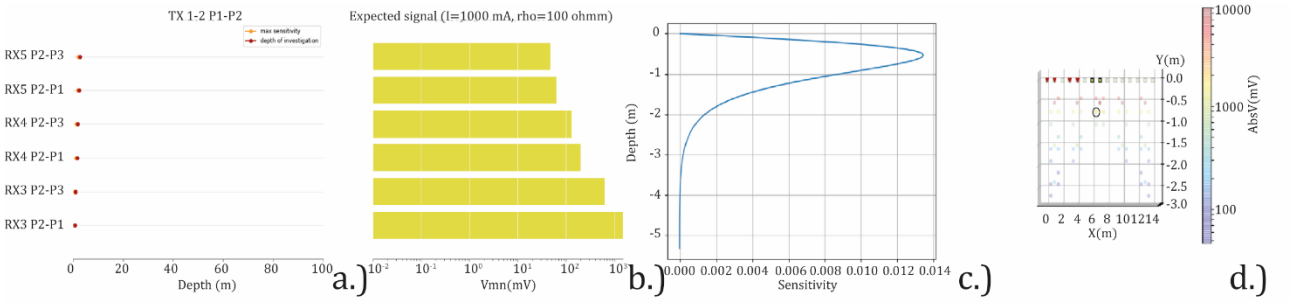

Figure 10: a) and b) depth of investigation/expected voltage chart: the example shows the results obtained with an inline MS project made using 5 different transceiver units (15 electrodes). The expected signal intensity to all the receiving units when a specific transmitter combination is active (b) can be monitored; also the expected maximum sensitivity and the relative depth of investigation are visible (al). c) and d): dataset visualization modules: in d), the various TX-RX combinations are plotted in a 3-D volume, and the expected voltages respect to their relative depth of acquisition can be visualized for each measure. The sensitivity plot can be seen as well (c).

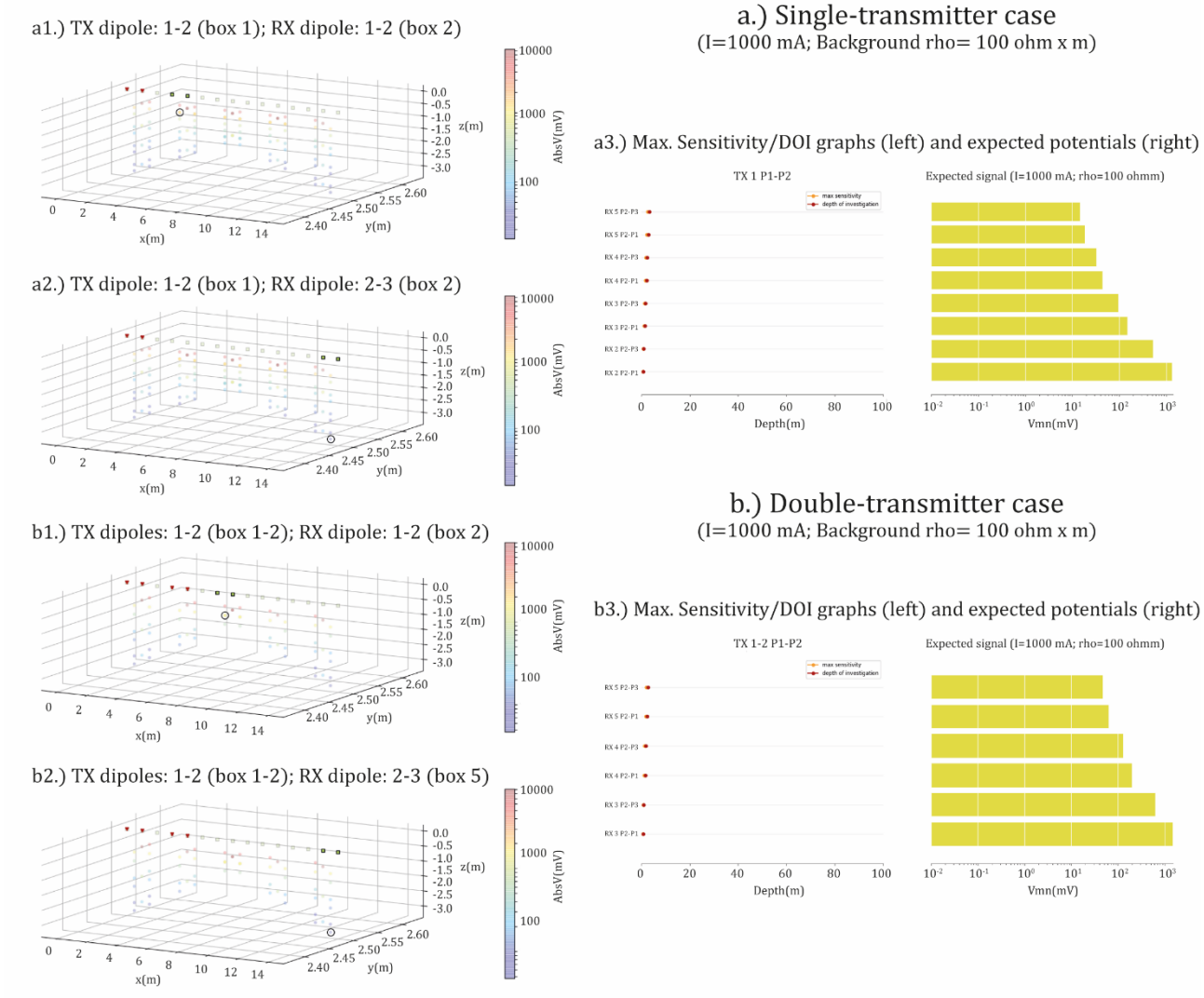

Figure 11: expected voltage analysis considering the simple case of an in-line single (a1, a2 and a3) and double (b1, b2 and b3) transmitter cases.

4. INVERSE THEORY

Forward and inverse modelling are based on a finite-element discretization algorithm for the forward-problem solving, and on an iterative, smoothness-constrained approach for the generation of the inverted model. The working environment (WE) is pretty much the same for a variety of commercial and academic codes and it is comprised of the following tasks (**Fig.12**):

1) sequence generation;

2) geometry input;

3) mesh generation;

4) forward-problem solver;

5) inverse-problem solver.

The xyz positions of the electrodes in local or global coordinates are required prior to process the data. Usually, the required accuracy is about 10% with respect to electrode spacing (resulting in 5% accuracy with respect to the mesh size). A simple geometry could be easily reproduced in the WE just by defining the number of cables, number of electrodes per-cable and electrode spacing. A specific array can be then used to create a synthetic dataset. The XY position of each data-point is generally calculated as the centroid of the quadrupole (mean of the two dipoles centroids), while the z positions are calculated according to the median depth of investigation derived from equation (17). A digital terrain model could be also added in case of rough topography. The lateral extent of the DTM depends on the maximum AB aperture. DTM is crucial to properly model electrical field distortion (***Fox et al., 1980, Viero et al., 2015***).

Mesh generation in science and engineering is the process of discretizing a medium in cells using basic shapes (polygons) or basic solids (polyhedrals). Meshes could be used to approximate sections (2D) or volumes (3D). Mesh could be also used to model surfaces (3D) using basic shapes (2D).

The mesh described and used for the purpose of this study is based on a finite element discretization algorithm and it creates a volume of aggregated tetrahedrons. In case of a planar topography and of regularly spaced electrodes, an adequate degree of resolution could be obtained using cells half the size of electrode spacing. Although this is not a geophysical rule-of-thumb as the cell size depends on several variables (e.g. the shape of object to be modeled, the presence of discontinuities, the number of the data-points and their position, etc) the value of 50% of the electrode spacing is pretty much accepted.

Media discretization for computational purposes is often organized in regions. The inner region is generally the objective of the simulation while the outer region is needed for numerical stability and to avoid boundary artifacts. Cells in the outer region are larger size and in many cases they also grow in size towards the model boundaries.

The inner region, also defined as the foreground region, spans the interval comprised between the first and the last electrode and it extends down to depth given by the maximum DOI value.

The foreground region represents the target area/volume for both the forward- and inverse-problem solution. The outer region, also defined as the background region, extends from the foreground region to +/- N times the cell size along the X and Y axes and -N times the cell size along the Z axis.

The default of the code used for simulations and for processing of the real data is to discretize the background region with cells sizing up to 8 times the foreground region cells.

The boundary conditions are essentially three:

i) Dirichlet condition: assuming a 2D half space and indicating the potential of a mesh node in X, Z position (along the outer boundary of the background region) as $\phi_{X,Z}$,its value is:

$$\phi_{X,Z} = 0 \qquad (28)$$

The potential is then null along the entire outer border of the background region (left, right, forward, backward and downward). The same constraint is also imposed at thesurface (medium-air contact) of both the foreground and the background regions.

ii) Neumann condition: considering a 2D environment, the flux of current towards the outer margins of the background region is null.

$$\partial\phi_{X,Z}/\partial\eta = 0 \qquad (29)$$

η=X for lateral frontiers;

η=Z for the bottom frontier.

iii) Mixed condition: a combination of Dirichlet and Neumann conditions.

The mixed condition is probably the most utilized boundary condition as it is suitable for the majority of the possible cases. In the "mixed condition approach" the Dirichelet condition is imposed to the background lateral (+/-X and +/-Y) boundaries and to the lower margin (-Z), while the Neumann condition is imposed at the air-ground/medium contact (+Z). The Neumann condition can be extended, with modifications, in some specific situations, for example when the survey line ends abruptly near a steep cliff.

The algorithm, while generating the mesh, considers also rough topography. Tetrahedrons are distorted both in size (scale factor) and shape (anisotropy factor) to properly model sudden surface jumps. The process could then lead to distorted cells but it has to be carefully evaluated on a case-by-case basis; a mesh characterized by regular cells is always preferable because it greatly reduces numerical instability.

Each cell is then initialized with a resistivity value. The logic behind the assignment of resistivity is slightly different in forward or inverse modeling. In the first case, we can assume an homogeneous underground model (all cells have the same resistivity value) or a model containing a background reference value and one or more anomalies. The anomaly has to be inserted with simple squared geometries as multiples of the elementary cell. Although this approach restricts the geometrical complexity of anomalies (respect, for example, to the approach of ***Rucker et al., 2006***) it is a very powerful tool to test specific quadrupolar arrays over defined targets during survey design. In the second case, all mesh elements are initialized with the same resistivity value and generally the value adopted corresponds to the median value of the measured apparent resistivity.

Mesh generation is crucial for the solution strategy (***Pridmore et al., 1981***) of both, forward and inverse problems. The forward-problem is solved by analytically determining Poisson's equation for the 3D ground domain (equation 18). The solution, than, is actually approximated in each individual mesh element by a single function V_k'(x,z) (with mesh element k=1,…n), which is non-null in its corresponding element, and null anywhere else. These approximation functions are expressed in terms of shape functions (depending on the actual shape of the mesh elements adopted) and of the potential values at the cell nodes, i.e. the real unknown of the system. Summarizing the process the algorithm solves a sytem of linear equations like:

$$S_m \cdot V = C_s \qquad (30)$$

where:

S_m is the stiffness matrix;

C_s is the current source vector;

V is the vector of the nodal potentials (unknown).

The stiffness matrix contains the terms expressing element geometry and element conductivity. The boundary conditions are imposed on the current source vector. The system expressed in the above equation is then solved iteratively. The software implements a SORCG iterative solver proposed for the first time by ***Spitzer et al., 1995*** and based on the Pre-conditioned Conjugate Gradient (PCG) method. This last approach is faster in finding the solution of the linear system with respect to the classical conjugate gradient method for both, 1) the selection of the descending directions iteratively selected to minimize the quadratic form of the solution and, 2) the conditioning of S_m, after the introduction of a preconditioning matrix.

The inversion algorithm follows an Occam's inversion strategy (sensu ***Constable et al., 1987***): the forward problem is iteratively solved until calculated apparent resistivity fits the observations. The constraints to this undetermined problem are that the appropriate model has to be the smoothest possible and fits the real data up to a a-priori χ-squared statistic of noise. In other words, the final objective of the inversion algorithm is to find the maximum value of α, i.e. the stabilization (or smoothness) parameter, for which minimizing the equation:

$$\phi(m) = \|W[d - h(m)]\|^2 + \alpha\|L(m - m_0)\|^2 \qquad (31)$$

resulting in:

$$\chi^2(m) = \chi^2{}_{a\ priori} \qquad (31.1)$$

where:

- χ^2(m)= $W[d - h(m)]$
- d is the vector of known data values (voltages or apparent resistivities);
- m_0 is the reference model;
- h(m) are the calculated measures for the m model (forward solution);
- W is the weight matrix, i.e. diagonal matrix of variance reciprocals;
- m is the vector of potentials (unknown parameter);
- L is the roughness (or smoothness) matrix, and it is given by:

$$L = x^T(w_x^T w_x)x + z^T(w_z^T w_z)z \qquad (32)$$

where x and z are the first-order difference operators in the X and Z directions and w_x and w_z are diagonal weighting matrices;

α is the most crucial parameter because it controls the weighting of the smoothness with respect to the data residual, relatively to the target function to minimize. Since the minimization process does not involve the so-called "misfit function" directly (first term of expression (30)), but its norm-2, the algorithm actually follows a least-square approach. The term $\alpha\|L(m-m_0)\|^2$ is also known as stabilizing functional Ω_p (***Tikhonov and Arsinen, 1977***) and enables the solution of the ill-posed inverse problem (sensu ***Hadamard, 1923***) by reducing the infinite number of possible solutions to only one, in which the final resistivity model is the one with the smallest structure (no sudden jumps in resistivity between adjacent cells of the model).

The adopted inversion algorithm is different compared to the approach proposed by Constable et al., 1987. The calculation of α and of the weights contained in the W matrix is more sophisticated (***Labrecque et al., 1996; Morelli and LaBrecque, 1996***). After starting each iteration with an approximation of *F(p)* by the first order term of a Taylor's expansion series *($h(m)=h(m_i)+A_i(m-m_i)$)*, a root finding algorithm (***Press et al., 1986***) is implemented to find the maximum value of α for which:

$$(d - A_{i-1}m_i)^T W^T W (d - A_{i-1}m_i) = \chi^2_{a\ priori} \quad (33)$$

where:

- m_i is the vector of estimated parameters at the i-th iteration:
  $$m_i = m_{i-1} + (A_{i-1}^T W A_{i-1} + \alpha R)^{-1} A_{i-1}^T W [d - F(m_{i-1})] + \alpha R m_{i-1} \quad (34)$$
- A_i is the sensitivity matrix estimated at the i-th iteration;
- A_{i-1} is the sensitivity matrix estimated at the (i-1)-th iteration.

The estimate of the weights in the W matrix is done at each iteration, only for those elements whose fit with respect to the reconstructed model is poor. This process involves a progressive weight reduction of the "bad terms" contained in the W matrix and it stops when no further effects are observed on the L1 norm of the misfit residual.

The most important parameters in the inverse solver are the model roughness and the percentage of noise. The roughness is controlled by three parameters: the initial factor assigned to the model, the multiplier for changing roughness factor and the roughness weights in the X, Y and Z directions (with a default anisotropy along the vertical axis).

The initial roughness factor, by default, is set on 10 and its value is a good compromise in terms of stabilization of equation (30). The second member of equation (30) is balanced between the two extremes of a completely rough or a completely smooth reconstruction. Similarly, the parameter multiplier makes model variations larger than one-order of magnitude from trial to trial impossible (set to 10). The parameter weights are actually the elements constituting the L matrix, and represent how the roughness has to be modified (multiplied) along the three Cartesian directions: by default, a greater importance is attributed to the vertical variations (assigning a multiplier of 0.1), favoring stratified model reconstructions (X and Y directions set to 1). Anyway, these last multipliers can be modified according to the desired reference model (i.e. isotropic models, lateral inhomogeneity, etc).

The noise assumed by default during inversion is considered on the V/I ratio, and it is further subdivided in two components. A first component, called "Percentage error term", is calculated directly on the dataset, considering a Gaussian distribution of noise. Usually, this is assumed

statistically equal or lower to 1%. A second component, called "Data Constant error term", is constant in value, and it is usually set to 0.0001 Ω. This value is chosen in order to take in consideration the presence of noise during the calculus of the misfit function, but at the same time without influencing real data values. A better estimate of this last parameter can be specifically obtained for each study case in case reciprocal measurements are available (for example, in the 1TX case of MS measurements). This second term is summed to the first term resulting in an overall noise term.

The default inversion parameters (for resistivity) are summarized in the following table (**Tab.2**).

Table 1: default values of inversion parameters.

Roughness (Ω)			Noise (Ω)	
Initial Roughness Factor		10	Percentage error term (%)	1
Multiplier for changing roughness factor		10	Data Constant error term (V/I)	0.0001
Constant Value for parameters weights	x	1		
	y	1		
	z	0.1		

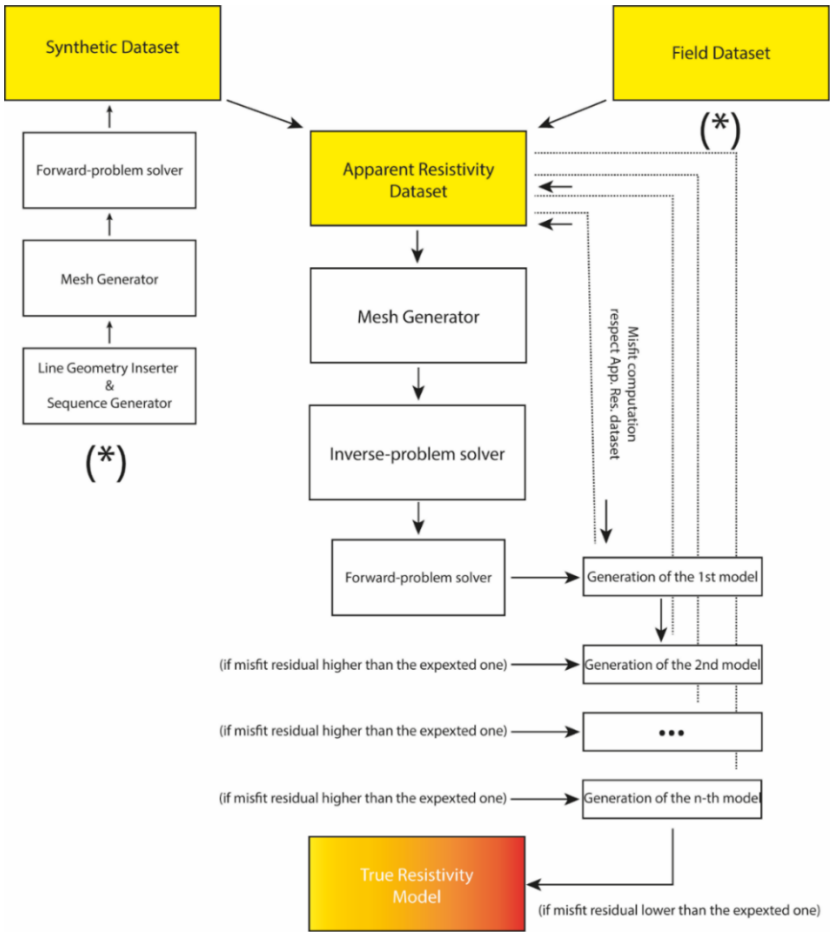

Figure 12: general workflow during the forward modelling or the inversion (from a synthetic or a field dataset) procedure.

5. PRELIMINARY TESTS

Numerical modeling was utilized as a primary aid in assessing the sensitivity and the associated resolving power of basic and MS arrays in a variety of geometry settings.

Since MS operates in dipole-dipole (DD) configuration, the overall target is the comparison of traditional DD and MS-DD devoting particular attention to the impact of multiple-transmitters on signal amplitude.

The Wenner-α (W) and the pole-dipole (PD) configurations have been also considered because of the high signal intensity and as representative cases of the sensitivity function. Topography was not considered in these initial simulations and the tested arrays are all comprised of 48 electrodes spaced of 1.0 m.

Since the early 90's several authors have been used numerical simulations. The focus was mostly on the selection of the more suitable configurations to resolve specific subsurface resistivity distributions and properly image the survey targets.

Dahlin and Zhou (2004) compared inversions obtained by 10 different electrode arrays (pole-pole, pole-dipole, half-Wenner, Wenner-α, Schlumberger, dipole-dipole, Wenner-β, gamma, gradient, midpoint-potential-referred) over 5 different geological models (involving the presence of dikes, dipping strata or buried objects). The authors recommend the use of the gradient, pole-dipole, dipole-dipole and Schlumberger arrays, with preferences depending on geology, targets, logistics, etc. ***Candansayar (2008)***, showed how the joint inversion of three- (pole-dipole) and four-electrode (Wenner-α, Schlumberger, dipole–dipole) arrays produces better results with respect to specific array inversions. ***Martorana et al., (2009)*** described the results obtained modeling four different resistivity scenarios (related to buried objects and salty-water intrusions) using 4 different electrode arrays (dipole-dipole, Wenner-α, Wenner-Schlumberger, linear grid). Inversions with different levels of Gaussian noise were compared. The authors concluded that in case of targets larger than the array resolution (defined as the cell dimensions) all the tested arrays generate reasonable images but, differently, the dipole-dipole array is the best selection choice to guess the true resistivity of the tested anomalies. ***Szalai et al., (2013)*** showed the results obtained using 6 different electrode arrays (Wenner-α, Wenner-β, pole-pole, pole-dipole, dipole-dipole, Stummer), over 8 resistivity models of growing geometrical complexity. The simulations were carried out with 0% and 5% of Gaussian noise. The authors concluded that, except for the strong influences of noise and model geometry on the inversions, the dipole-dipole and the Stummer arrays provide a more detailed reconstruction of the tested model. ***Carey et al., (2017)*** simulated resistivity changes in time-lapse measurements during rainfalls. In order to better understand the presence of processing artifacts in real case studies, the authors considered 4 different scenarios using the dipole-dipole configuration and 7 other arrays (extended dipole-dipole, dipole-dipole gradient, gradient, pole-dipole, Schlumberger, Wenner-α and modified pole-dipole) over a simple 2 strata model (saprolite + soil layer). They concluded that different arrays are best suited to image the vadose zone during water infiltration. The dipole-dipole array, as expected, is prone to processing artifacts, while Wenner-α and modified pole-dipole arrays are not as noisy but they exhibit poorer resolution.

As shown in ***Candansayar (2008)***, the joint inversion of three- and four-electrode arrays produces better results with respect to single array inversions. Anyway, the analysis of the resolving power of aggregated arrays is far from the logic of the present work, especially in the sense of a 1:1 comparison between traditional and MS DD.

Author's conclusions about the potentials of DD array are crucial for the present study. According to ***Dahlin and Zhou (2004)***, the DD is characterized by higher anomaly effects, but it is also more prone to noise if compared to other arrays. At the same time, the resolution of the DD (similarly to the pole-dipole) is higher, compared to other arrays, for the imaging of vertical and dipping structures, while it is lower at larger depths. For ***Martorana et al., (2009)***, the DD array resolves pretty well vertical structures nearby the surface while resolution is definitely poor in depth especially in comparison to other arrays with the same electrode layout. According to ***Szalai et al., (2013)***, the DD is probably the best array to guess subsurface resistivity distribution. Finally, according to ***Carey et al. (2017)***, the DD is more prone to artifacts in case of large resistivity contrasts between the target and the background values.

Numerical simulation, besides the differences in the selection of the parameters adopted for the creation of the automatic measuring sequence, was considered particular useful by several authors (***Martorana et al., 2009***; ***Carey et al., 2017***) as a kind of "forecasting tool" for some specific case studies.

In this sense, the models proposed in the next paragraphs are important for two main reasons: first, they further corroborate these first results in new subsurface scenarios; second, they bring new information about the resolving power the MS system, also in comparison to traditional arrays. Results should be evaluated carefully as they somewhat depend on the inversion algorithm.

5.1 REFERENCE MODELS

Simple reference models were considered to evaluate the effectiveness of the various arrays. All the models have a homogeneous background with a single anomaly of variable geometry and depth.

Three variables have been considered in the definition of the anomaly:

- lateral continuity (inline and crossline);
- vertical continuity (i.e. anomaly thickness);
- depth.

Three base models were created (**Fig.13**):

- (1) bottom interface: two-strata like;
- (2) top / bottom interfaces: three-strata-like;
- (3) top / bottom and lateral interfaces: prism-like.

The two-strata like model refers to a stratum (anomaly) with its specific resistivity inserted in a homogenous background. The top interface of the anomaly is the surface while the bottom interface is progressively moved down thus thickening the anomaly. Moreover, the anomaly has been designed as an infinite continuous body both inline (in the +/−X direction) and crossline (in the +/− Y direction). In the starting model the anomaly thickness is equal to the electrode spacing, (i.e. 1.0 m). The anomaly thickness was then increased of 1.0 m at a time up to a maximum of 6.0 m.

The three-strata-like model is similar to the previous case in terms of the lateral continuity of the stratum (anomaly). In this case the anomaly thickness was kept constant at 2.0 m (i.e. two times the electrode spacing). In the starting model the top of the anomaly is the surface. The anomaly was then moved down of 1.0 m at a time. The total number of shifts was set to six (maximum depth of the anomaly base equal to 7.0 m).

The prism-like model consists of a prismatic anomaly of 5 m (along the x axis) by 5 m (along the y axis), and with a thickness of 2.0 m, inserted in a homogeneous background. The starting model was set with the anomaly at surface. The anomaly was then moved down of 1.0 m at a time. The anomaly was positioned in the middle of the line below electrodes from 20 to 25.

Anomaly resistivity, in the first run, was set to 100 Ω·m while the background was set to 10 Ω·m, Background and stratum resistivity differ then by one order of magnitude. The complementary models were also generated.

Each one of the three models was discretized with the same mesh geometry (**Fig. 14**). The mesh was used in the forward and inverse processes. The cell size was set to half of the electrode spacing (i.e. 0.5 m) in the three directions (X, Y and Z), while the vertical extent was calculated as a fraction of the DOI. The mesh parameters are listed in **Tab.3**.

Table 3: mesh parameters adopted for forward and inverse modeling.

	X	Y	Z	TOTAL
Min.	43	86	-5.7	
Max.	63	114	1.9	
El. size	0.5	0.5	0.5	
Pads (Background region)	1 2 4 8 16 24 32 40 48 56 64	1 2 4 8 16 24 32 40 48 56 64	1 2 4 8 16 24 32 40 48 56 64	
Cells (Foreground region)	117	25	28	81900

5.2 TRADITIONAL ARRAYS

According to ***Szalai & Szarka (2008)*** more than hundred different electrode arrays are described in the literature (experimented or just defined theoretically) but less than ten are used in real applications. In this restricted group, three arrays were considered for the simulations:

- Wenner-alpha , W-α;
- dipole-dipole, DD;
- pole-dipole, PD.

The selection was guided also by the different sensitivity function of each array (see chapter 2). The W-α is definitively characterized by a strong vertical sensitivity, which makes it an optimal solution

when the desired target is layered horizontally (***Loke, 2020***).The DD array shows a stronger sensitivity to horizontal changes in resistivity, and so it is particularly recommended when lateral transitions of electrical properties are to be imaged (***Loke, 2020***). The PD array is a sort of imaging compromise between W-α and DD..

Simulation layout was a line of 48 electrodes for all the numerical simulations (**Fig.15**). Electrode spacing was set to 1.0 m.

Reference model 1.)

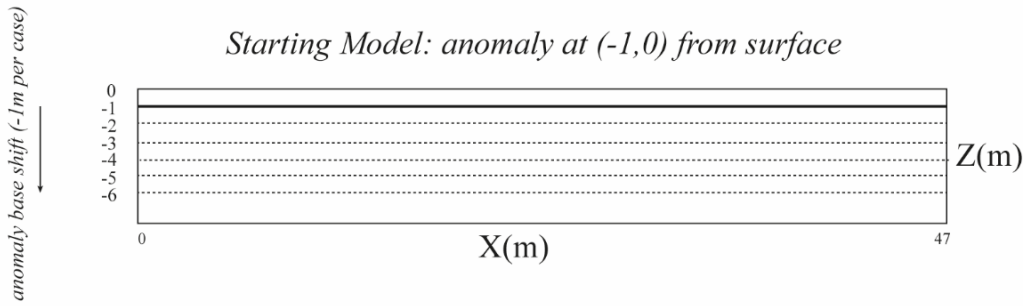

Reference model 2.)

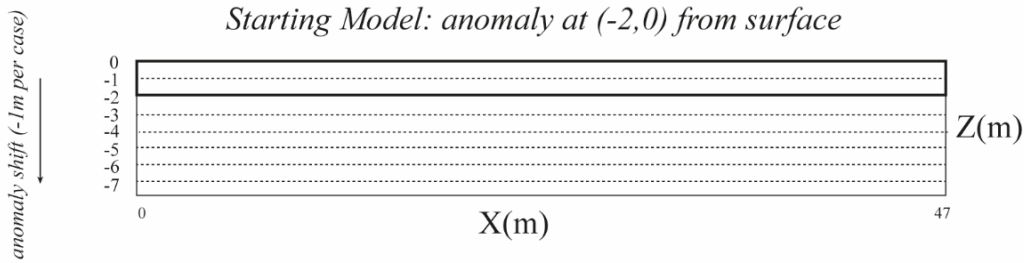

Reference model 3.)

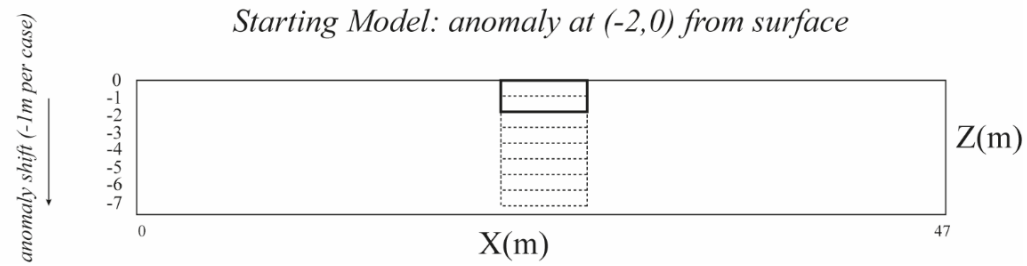

Figure 13: the reference models for forward and inverse modeling: 1) two-strata like model; 2) three-strata-like model; 3) prism-like model.

The W-α array dataset is comprised of 360 data-points (**Fig. 15**) obtained increasing the "a" factor from 1 to 15 and with a "n" factor equals to unity. The advantages of this array were clear since the advent of the lateral profiling/vertical soundings (***Van Nostrand and Cook, 1966***; ***Whiteley, 1973***), and with the introduction of electrical tomography its use has become massive. The geometry of the quadrupole enables to measure generally higher signal intensity compared to other arrays (***Loke, 2020***). The vertical resolution, combined with its sensitivity to lateral resistivity changes makes the W-α the most stable electrode array. The major limitation of this array is the limited number of data-

points (lower data density) compared to other arrays. W-α array parameters are summarized in **table 4**.

The DD array dataset is comprised of 945 data-points (**Fig. 15**). Data density is very high in the upper portion of the pseudo-plot and a progressive reduction of data density occurs in depth. The "a" and "n" parameters were selected in accordance with the indications of **Loke (2020)** thus limiting the "n" factor to the value of 6. Overcoming this limit could result in a too low S/N ratio. An "a" factor of 5 was employed. Usually, this is assumed as as a good compromise in terms of number of measurements/time of the survey in real exploration campaigns.

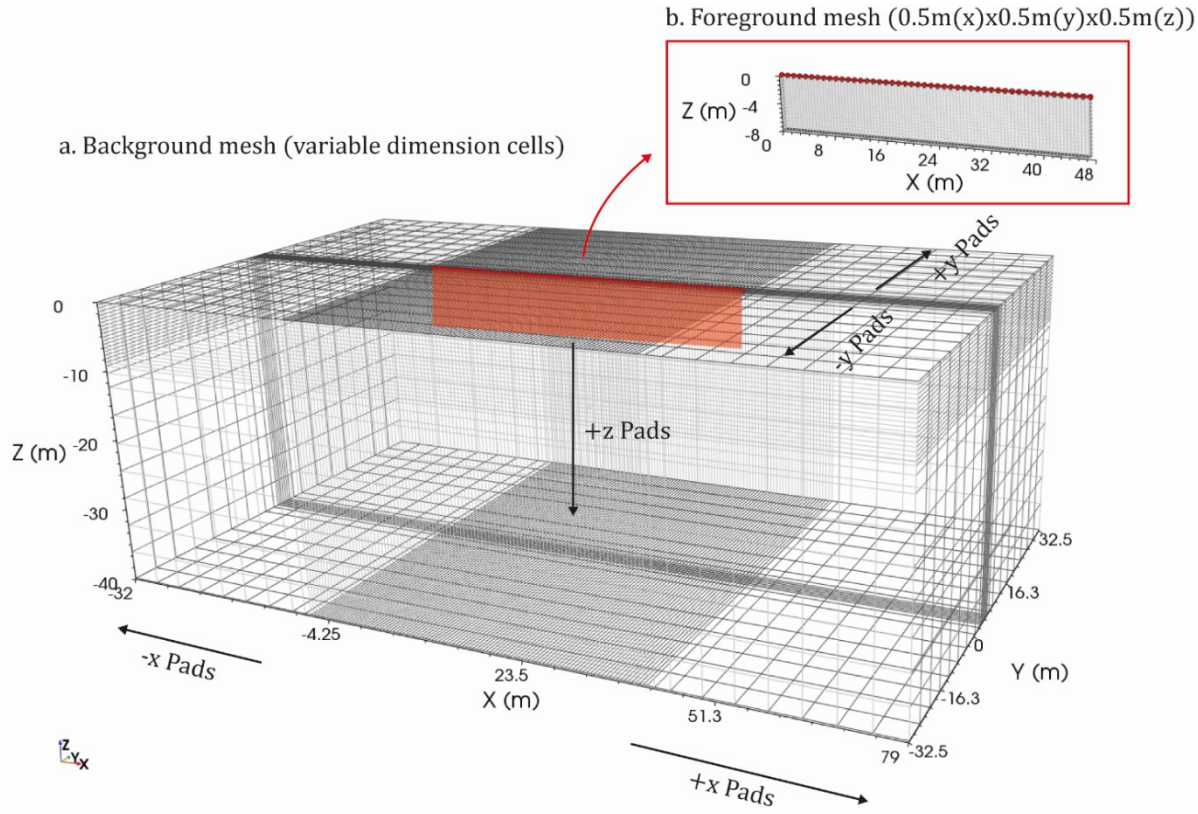

Figure 14: mesh utilized for the generation of the forward models. a) full mesh (foreground region and background region); b) foreground mesh.

The S/N ratio of the DD array because of its larger geometrical factor is lower compared to the W-α array. DD is known to be a noisy configuration. This array is preferable when the demand is for a high horizontal resolution. Moreover, since the injecting and measuring dipoles are always separated, this configuration also provides a lower electromagnetic coupling effect (***Orellana, 1982***). DD array parameters are summarized in **Table 4**.

The PD array dataset is comprised of 1035 data-points resulting in the maximum number of measurements delivered by traditional configurations. The PD offers a higher number of measurements just by the addition of one offline supplementary electrode (i.e. the remote pole). Moreover, the remote/infinite pole enables greater AB apertures resulting in a greater depth of investigation along with a high degree of resolution in the shallow and central portions of the

investigated medium. At the same time, this configuration is more affected by the presence of noise. The position of the remote/infinite pole has to be carefully evaluated on a case by case basis considering the expected resistivity distribution in the investigated medium. In the current simulation the remote pole was positioned along the negative x-axis at a distance of 47 m from electrode one (backward pole). A reverse configuration (forward pole) was not considered.

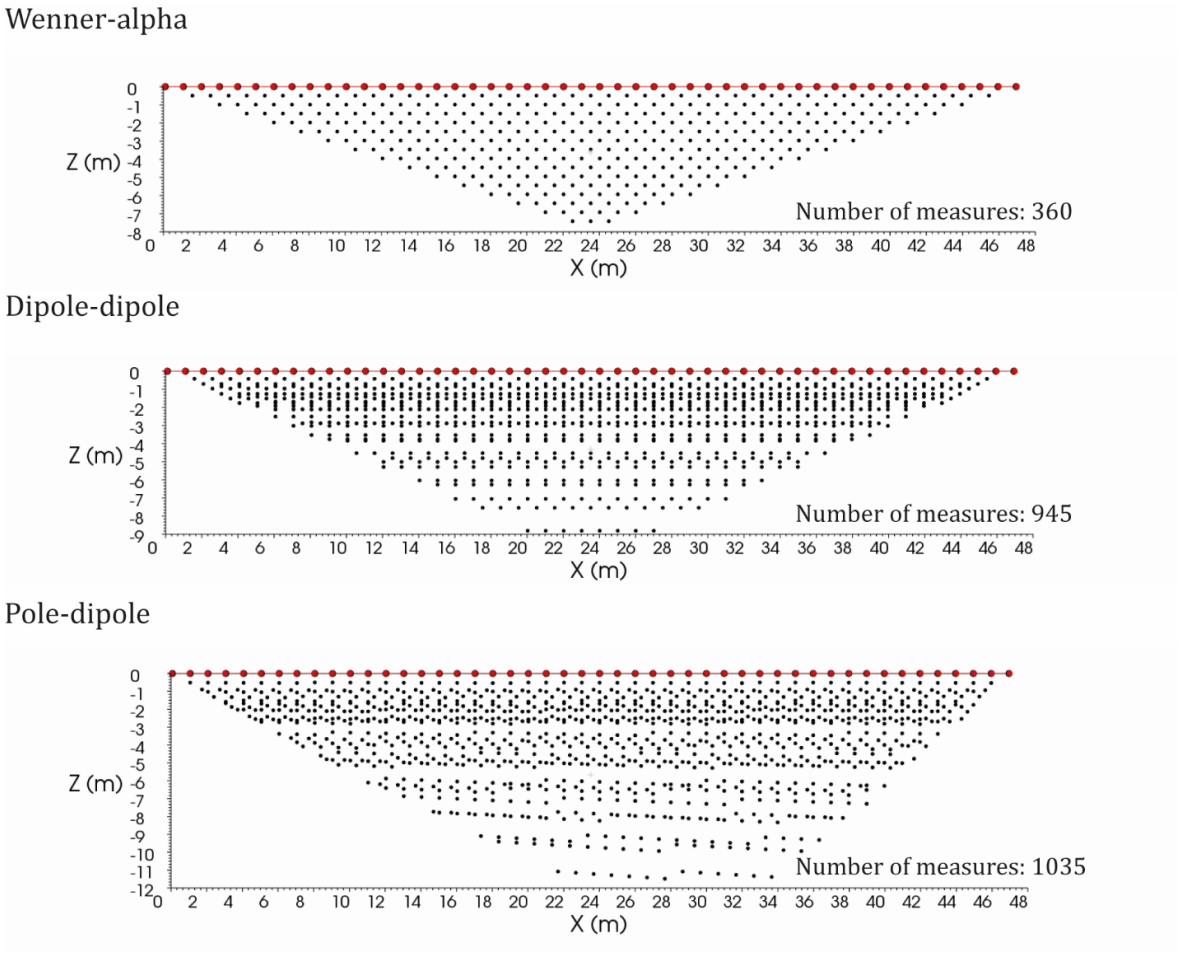

Figure 15: Pseudo-plot of the data-points for the three different arrays.

The distance is at least 20 times the electrode spacing (***Keller and Frischknecht*, 1966**) but it is not the ideal infinite distance that is suggested under a theoretical point of view. PD array parameters are summarized in **Table 4**.

Table 4: Parameters for the traditional arrays.

Array	"a" factor (m)	"n" factor	Data-points N	DOI (m)	|K| min-max (m)	Remote pole (m along x-axis)
Wenner-alpha	1:15	1	360	7.8	6.3 - 94.2	-
Dipole-dipole	1:5	1:6	945	8.9	18.9 - 5278	-
Pole-dipole	1:5	1:6	1035	11.5	12.6-1583	-47

5.3 MULTISOURCE ARRAYS

In the MS case the DD array is mandatory and the selection choices are just the number of the simultaneous transmitters. Moreover, the MS is designed to take measurements according to a specific and peculiar logic in the programmed sequence (as already discussed in chapter 3).

Three different MS DD arrays (**Fig. 16**) have been tested: single transmitter (1TX), double transmitter (2TX), quadruple transmitter (4TX). The idea was to assess the change of the S/N using multiple transmitters. The 1TX is a quasi-standard DD sequence, in which only one transmitter at a time injects the electric current into the ground. The major difference between the traditional DD and the MS-DD is the value of the 'n' factor. The system is natively multi-channel, as it uses as many channels as the number of receiving units for each single- or multiple- transmission. When one or more transmitting dipoles are injecting current, multiple recording dipoles are acquiring the potential difference. Since synchronization occurs via GPS timing this operation is almost instantaneous without the need of time-consuming internal switching operations. The quality of the electronics and the sophisticated approach in measuring the self potential allows the collection of dipole-dipole quadrupoles with very high value of the 'n' factor. The acknowledged upper value for the "n" factor generally ranges from 5 to 6. The MS has no such a limitation and good quality measurements could be collected with a value of the "n" larger than 22 as demonstrated by a series of recent experiments (Bocchia et al., 2021)

The n factor for the MS–DD 1TX array could be then expressed as:

$$n = (Nx3) - 3 \quad (35)$$

where:

- N is the number of MS units;
- a is the electrode spacing.

Considering a dipole opening of 2a, in 1TX mode, the maximum value of the "n" factor is lower. Combining measurements with dipole apertures of "a" and "2a" the resulting dataset is comprised of 1200 data-points (including reciprocal measurements). The acquisition of the reciprocals is not time-consuming and these data could crucial to evaluate noise conditions although there is no benefit in including these additional data-points in the inversion. The number of measurements to be considered for inversion is then 600. The pseudo-plot is rather peculiar as it shows a clear clusterization of data-points in the pseudo-plot (**Fig.16**). MS-DD 1TX array parameters are summarized in **Table 5**.

The double transmitter sequence (2TX) generate a conceptually new dataset. The logic of the programmed sequence is similar to the 1TX mode but with a major geometrical limitation. Different transmitting dipoles mandatory belong to different MS units. In other words a single unit cannot act as a multiple transmitter. The number of unique data-points for the 2TX array is 1050. For each measurement are recorded two currents, two geometric factors and one voltage resulting in a single value of apparent resistivity. DOI is reduced of a negligible percentage (~3%) switching from 1TX to 2TX mode. Data-points distribution in the pseudo-plot (**Figure 16**) is more or less regular with respect to 1TX case.

The quadruple transmitter sequence (4TX) is comprised of 780 data-points (**Figure 16**).

DOI lowers approximately 3% switching from 1TX to 2TX while the reduction is about 12% switching from 1TX to 4TX.

Results for a 4TX simultaneous injection are stored in four lines of the final data-point record. Current (*I*) and geometrical factor (*K*) are different in each of the four lines while the potential (ΔV) is a unique value resulting from the measurement taken at the RX dipole.

Table 5: Parameters for the MS-DD arrays.

Mode	"a" factor (m)	"n" factor	Data-points N	DOI (m)	|K| min-max (m)
1TX	1:2	1:45	600 (1200 with duplicates)	-11.6	11.8-305300
2TX	1:2	1:45	1050	-11.2	11.8-305300
4TX	1:2	1:45	780	-10.1	11.8-305300

5.4 NUMERICAL SIMULATION RESULTS

Inversion parameters are exactly the same for all the tested arrays to better compare results.

5.4.1. TRADITIONAL ARRAYS

5.4.1.1. TWO-STRATA LIKE MODEL

A conductive anomaly of 10 Ω·m in a background of 100 Ω·m (**Figure 17** and **Figure 18**) was simulated at first. The DD and the PD arrays are more accurate in defining the shape of the anomaly, while in the W-α two side lobes are clearly visible. The lobes are numerical artifacts caused by the inversion and they are typical of the Wenner array. The misfit of the inversion process is lower than 5% for the totality of the tested arrays and cases.

In cases I, II and III, the interfaces seem to be better resolved in DD and PD arrays with respect to the W-α array The interface in DD and PD inversion is almost planar and no lateral distortions are visible in the resistivity model. In DD data the image of the resistive background is pretty much focused in the center of the section.

The background resistivity (70-80 Ω·m in case I) is closer to its real value of 100 Ω·m in DD data while it is 50-60% off in PD data. The target resistivity in DD data fits better its real value while the W-α array results in the best fit of background resistivity. The misfit on the target anomaly ranges from 30% of case I to 50-60% of case III.

In cases from IV to VI the advantage the W-α array becomes evident and this array is effective in resolving the interface geometry. In cases IV and V the DD array emphasizes a focused anomaly

missing resolving power, while the PD array shows a clear asymmetry in the interface geometry showing an undefined image opposite to the remote pole position. In case VI the W-α array is the sole configuration capable of providing a meaningful image of the target anomaly despite a larger uncertainty in the anomaly position.

The misfit on the background resistivity for the W-α array is about 60% for case IV and grows to about 70-75% in case V. Misfit on background resistivity is large also for DD and PD arrays with values up to 75-80% in cases V-VI.

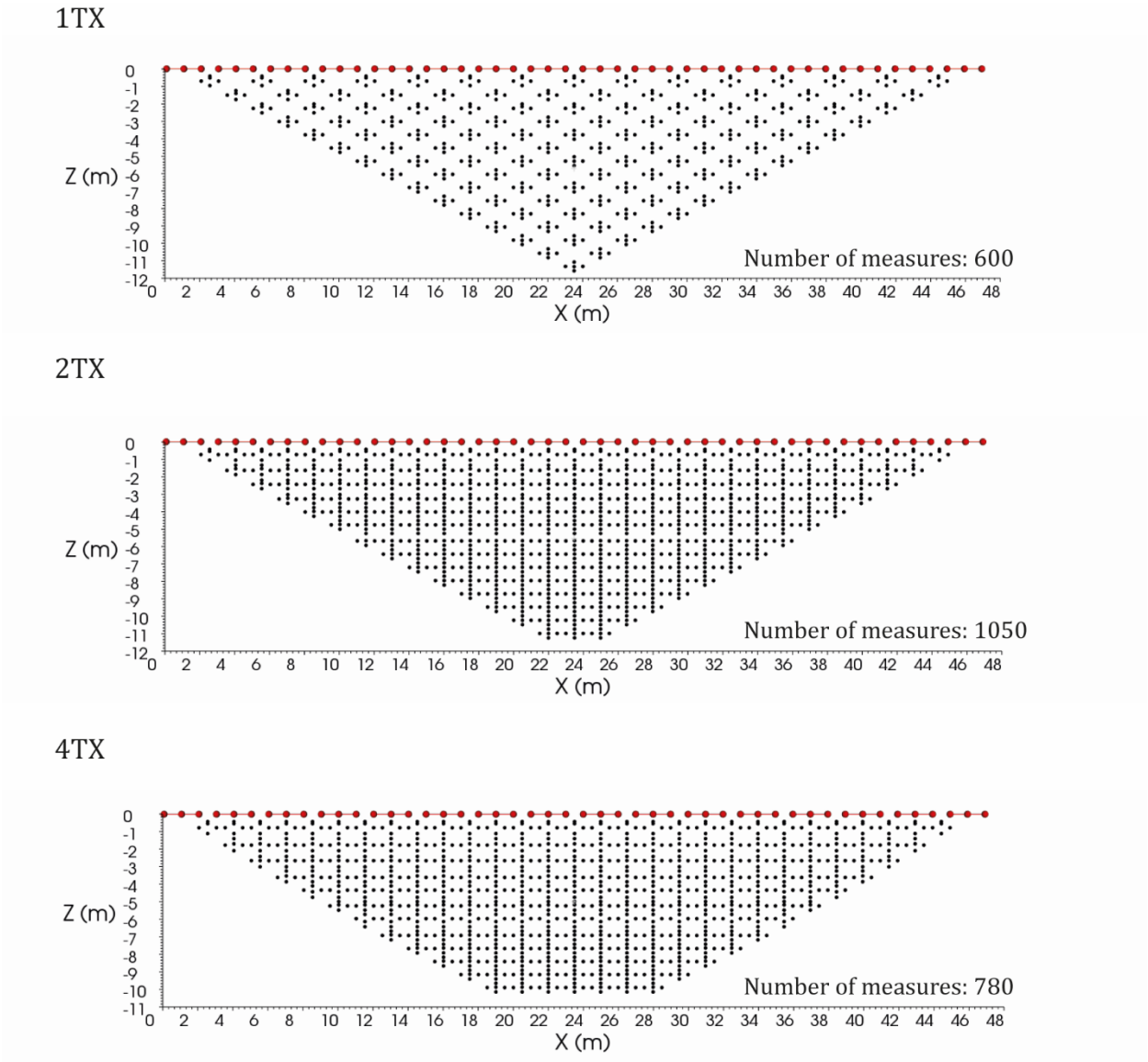

Figure 16: MS-DD array. Pseudo-plot of data-points for 1TX, 2TX and 4TX MS-DD arrays.

The resistive anomaly of 100 Ω·m in a conductive background of 10 Ω·m was the second simulated scenario (**Figure 19** and **Figure 20**). Also in this case, the DD and the PD arrays seem generally more accurate in resolving the target anomaly - background interface with respect to the W-α array. Side lobes, caused by numerical artifacts are visible in both W-α and DD array responses. The misfit of the inversion process in some cases is higher than 10%.

In cases I-III, the three different arrays seem equivalent in terms of target anomaly resolution with a slighter improvement of the PD array in case III.

In case I the misfit on the target anomaly is almost 30% for the W-α array while it is approximately 40% for the PD array. In cases I-III the misfit on the target anomaly is more or less similar for the three arrays with a maximum of about 25%.

In cases IV-VI, side lobes are particularly evident in the image of the resistive target of the W-α array but also of the DD array. Resistivity distribution varies significantly in the images obtained with the different arrays although the images are accurate. A weak asymmetry is visible in the PD array. In case VI the target anomaly - background interface is barely deformed in the PD array.

In cases IV-VI, the misfit on the target anomaly is particularly high and larger than 50% in the W-α array while it is very low in the PD array. PD array is particularly effective in matching the target resistivity in case VI with a misfit lower than 10%. In this depth range the DD array misfit is particularly large on both the target anomaly and the background resistivity.

5.4.1.2. THREE-STRATA-LIKE MODEL

A conductive anomaly of 10 Ω·m in a background of 100 Ω·m (**Figure 21** and **Figure 22**) was simulated at first also for this model. All the selected arrays seem to be quite effective for the resolution of this model. The side lobes in the W-α inversions are barely visible. The misfit of the inversion process is lower than 6% for the totality of the tested arrays and cases.

The W-α imaging capability, in case I, is rather poor compared to the DD and the PD arrays. The presence of the side lobes results in the exaggeration of the layer thickness of about 1 m.

In case I the misfit between inverted and target resistivity is about 50% (below 5 Ω·m) while the misfit on the background resistivity is approximately 40%.

In cases II-III, the response of the three arrays is almost identical. The lateral continuity of the interfaces, along with the thickness of the target layer, are properly imaged.

The misfit in cases II-III is moderately low and it is about 20% (2-3 Ω·m) for the target layer while it is larger than 50% for the background resistivity. All the three arrays fail in imaging the resistive background below the conductive target anomaly. The misfit for the background resistivity above the conductive target is less than 10% in the DD array and in the W-α array (case II) while it is larger than 25% for the other arrays.

In cases IV-VI the target anomaly progressively disappears from the inverted models so much that just one interface is still visible in the image. This is particularly evident in the W-α array since depth case IV while DD and PD responses still show a clear lenticular body although its length is off by 50% and on the side resistivity approximates the background reference value.

In cases IV-VI the misfit on the target anomaly, of 10 Ω·m, is significantly large for all the tested arrays. The W-α array returns values ranging from 30 Ω·m to 50 Ω·m. The lower misfit is returned by the DD array in case V with a returned value of 25 Ω·m.

The resistive anomaly of 100 Ω·m in a conductive background of 10 Ω·m was the second simulated scenario (**Figure 23** and **Figure 24**) also for this model. The target anomaly is resolved just in the first depth cases while it is completely lost in depth. Side lobes, caused by numerical artifacts are

visible the W-α array. The misfit of the inversion process is lower than 7% for all the arrays and all the depth cases.

In the depth case I the target anomaly is properly imaged by all the tested arrays as for lateral continuity and thickness. W-α and PD arrays return a better approximation of the layer thickness.

The maximum misfit for the target anomaly is about 25% while all the arrays return the proper value for the background resistivity.

In case II, the imaging of the upper boundary of the target anomaly is quite accurate for all the tested arrays. The lateral continuity is also properly imaged while the thickness is overestimated. The lower boundary of the target anomaly is not resolved in the PD array and also in the W-α array it is poorly imaged mostly because of the side lobes.

The misfit for the target anomaly in case II is very high and more then 50 %.

In cases III-IV all the tested arrays image the target anomaly although its bottom boundary is poorly resolved. The W-α array performs barely better than the other arrays despite overestimating the target anomaly thickness.

The misfit for the target anomaly in cases III-IV is pretty high and greater than 70 % for all the tested arrays.

In cases V-VI the imaging is definitely poor and the misfit for the target anomaly is higher than 80-85 % for all the tested arrays.

5.4.1.3. PRISM LIKE MODEL

A conductive anomaly of 10 Ω·m in a background of 100 Ω·m (**Figure 25** and **Figure 26**) was again simulated at first also for this model. All the selected arrays seem to be quite effective for the resolution of this model when the target anomaly is shallow. The misfit of the inversion process is generally low for the totality of the tested arrays with an average value of 1.6%.

In cases I-II the target anomaly is clearly resolved in both thickness and lateral extension. The PD array returns slight excess in thickness, in case I, while the DD array provides a better image in depth case II.

The misfit, in cases I-II, is less than 10% for the target anomaly while it is of about 20-25% for the background resistivity.

In case III the target anomaly is still clearly resolved by the tested array although in the W-a array the anomaly appears upshifted.

The misfit in case III is pretty high for the target anomaly (around 50%) while it is less than 5% for the background resistivity below the anomaly. The misfit for the background resistivity above the anomaly is greater than 50%.

In depth cases IV-V the DD array is the only capable of resolving the target anomaly with a misfit of about 50-60%.

For what concerns depth case VI, the anomaly seems almost undistinguishable with respect to the background.

A resistive anomaly of 100 Ω·m in a background of 10 Ω·m (**Figure 27** and **Figure 28**) was the second model to be analyzed. All the selected arrays performed quite poorly in resolving the target anomaly and fitting its resistivity. The misfit of the inversion process is generally low for the totality of the tested arrays with an average value of 1.4%.

The target anomaly is clearly resolved in the uppermost depth case by the three arrays with respect to vertical and lateral extension. The thickness in the W-α response is slightly underestimated. The misfit is also particularly low for the DD (~10%) and for the PD (<10%) arrays. The misfit on the background resistivity, as expected, is negligible.

In case II the target anomaly is still detected but it is barely visible. The misfit on the target anomaly is very large with a minimum of about 75% for the W-α array.

Since depth case III, the target anomaly is barely visible and the misfit gets larger and larger.

5.4.2. MULTI-SOURCE ARRAYS

5.4.2.1 TWO-STRATA LIKE MODEL

A conductive anomaly of 10 Ω·m in a background of 100 Ω·m (**Figure 29** and **Figure 30**) was simulated at first for the MS-DD array. The response of the 1TX, 2TX and 4TX arrays is more or less similar. The average misfit of the inversion process is about 8.5 % with lower values for the 4TX case (limited number of data-points).

In cases I-II the response of the three arrays is almost identical. The target anomaly is resolved in both lateral extension and thickness. The misfit for the target resistivity is lower than 5% while it grows up to 40% for the background resistivity. In depth case II the misfit for the background resistivity is slightly lower.

In case III the target anomaly is resolved in terms of thickness but it appears to be partly focused in the middle of the section. The misfit for the target resistivity is lower than 5% while there is no fit at all for the background resistivity.

Depth case IV is similar to case III. The target anomaly appears to be partly focused in the middle of the section and the fit to its real resistivity value is high.

Since depth case V the target anomaly is no more visible.

A resistive anomaly of 100 Ω·m in a conductive background of 10 Ω·m (**Figure 31** and **Figure 32**) was the second simulation with MS-DD array on this model. The response of the 1TX, 2TX and 4TX arrays is more or less similar. The very near surface response appears to be quite anomalous for all the tested arrayas. The average misfit of the inversion process is about 16.7 % with lower values for the 4TX case (probably because of the limited number of data-points).

In depth case I the target anomaly is clearly resolved although its thickness is partly overestimated (20-25%). The lateral continuity is also degraded but mostly in the 4TX mode. The misfit for the target anomaly is high with a minimum of about 50% in 4TX mode. The background resistivity is perfectly fit in all of the three arrays.

In case II the target anomaly is resolved and the lateral continuity is defined for almost the entire section. The misfit for the target anomaly is negligible in the 1TX and 2TX modes while it is about 5% in the 4TX mode. The background resistivity is perfectly fit in all of the three arrays.

Target anomaly, in cases III-IV, is resolved and, its lateral continuity is defined for almost the entire section. The target resistivity is overestimated and it grows up as shifting from 1TX to 4TX mode. The maximum misfit is approximately 35% for case III and more than 50% for case IV. The background resistivity is reasonably fit for all of the three arrays in case III only.

Target anomaly in cases V-VI is still detected although poorly imaged. The misfit gets higher compared to previous cases for both target anomaly and background.

5.4.2.2. THREE-STRATA-LIKE MODEL

A conductive anomaly of 10 Ω·m in a background of 100 Ω·m (**Figure 33** and **Figure 34**) was simulated at first for the three-strata like model with the MS-DD array. The response of the tested modes is slightly different. The average misfit of the inversion process is particularly low (1.8 %).

The target anomaly, in cases I-II, is clearly resolved; the layer image is sharp with laterally continuous boundaries. The fit on the target anomaly is better for the 2TX and 4TX mode arrays exhibiting values as high as 90-95 % while the fit on the background resistivity is rather poor (about 40%).

From case III, a "*focus effect*" starts to alter the anomaly lateral continuity (<25%). Nevertheless, the resistivity distribution is pretty accurate, with a 20% exaggeration of the background portion above the anomaly and a <5 Ω·m misfit for the anomaly.

Since case III the target anomaly, although resolved, appears focused in the central portion of the inverted section. Two side lobes are visible in the 1TX array response. The misfit for the target anomaly gets higher in particular for the 4TX array while is somewhat comparable in the 1TX and 2TX responses (about 50%).

Target anomaly, in depth cases V-VI, is partly resolved as just the top interface is imaged in the inverted sections. The 2TX and 4TX arrays perform better in spite of some side artifacts probably due to the low data-point coverage. The misfit is very high for both the target anomaly and the background resistivity.

A resistive anomaly of 100 Ω·m in a conductive background of 10 Ω·m (**Figure 35** and **Figure 36**) was then simulated for the three-strata like model with the MS-DD array. The response of the tested modes is slightly different in this case also. The average misfit of the inversion process is particularly low (1.9 %).

The anomaly is well distinguishable in case I, both in terms of resistivity (from 50-55 Ω·m to 100-105 Ω·m) and thickness. The addition of multiple transmitters results in a progressive focusing of the anomaly, with a loss of 30 % of its horizontal extension going from 1TX to 4TX. The background below the anomaly is accurately recovered.

Target anomaly, in case I, is clearly resolved in terms of layer thickness and lateral extension. The misfit for the same anomaly is less than 5% with a minimum for the 2TX mode array. The background resistivity is perfectly fit by the three arrays. Switching from single to multiple transmitters results in a progressive focusing of the target anomaly in the central part of the section.

In case II the target anomaly is clearly imaged but for the thickness that is overestimated. The response of the 1TX array shows evident side lobes. Misfit for the target anomaly is particularly high and higher than 50%. The fit on the background resistivity is also very low.

In case III, both the top and bottom interfaces of the target anomaly are somewhat resolved. The misfit is very high (about 75%). The response of the three arrays is similar.

In case IV the target anomaly appears to be barely visible in the conductive background. The misfit is particularly high.

In cases V-VI the target anomaly is no longer distinguishable from the conductive background.

5.4.2.3. PRISM LIKE MODEL

A prismatic anomaly of 10 Ω·m in a background of 100 Ω·m (**Figure 37** and **Figure 38**) was simulated at first for the prism like model with the MS-DD array. The response of the tested modes is more or less similar. Near surface cells are noisy in cases I-III. The average misfit of the inversion process is particularly low (1.5 %).

Target anomaly, in cases I-II, is clearly resolved. The misfit is very low and less than 5% for case II in the various array responses. Inversion fit reasonable also the background resistivity (with a better performance of 2TX and 4TX). Marginal differences, in case II, are visible among the three inversions.

Target anomaly, in case III, is imaged although not entirely resolved. The target anomaly, in 1TX mode, maps at shallower depth compared to reality. The misfit is particularly high and larger than 100%.

This anomaly trend involves also case IV (resistivity of 50-75 Ω·m) and worsen at depth case V (70-80 Ω·m), while at depth case VI the anomaly is not clearly discriminable from the background. No big differences concerning the use of simultaneous multiple transmitters are evidenced.

The target anomaly image degrades moving from case IV to case VI. In this depth interval there is no fit at all. The target anomalies are better focused in the 2TX mode responses.

A prismatic anomaly of 100 Ω·m in a conductive background of 10 Ω·m (**Figure 39** and **Figure 40**) was also simulated for the prism like model with the MS-DD array. The response of the tested modes is more or less similar with a better performance of the 2TX array at larger depth. The average misfit of the inversion process is particularly low (1.4 %).

Target anomaly, in case I, is clearly resolved. The misfit for the target anomaly is strictly dependent on the array. It is less than 5% for the 4TX array, it grows up to 30% for the 2TX array and finally it further grows up to 70% for the 1TX array. The fit for the background anomaly is very high.

In depth case II the target anomaly is detected but it is not completely resolved. The misfit is significant as it is as high as 75%.

The target anomaly, in cases III-IV, is barely visible in the inverted sections with a misfit higher than 90%.

In cases V-VI the target anomaly is no longer detectable.

5.5 DISCUSSION

The quick analysis of resistivity inversions, obtained via traditional arrays, confirms the results of other authors. It also gives a first insight on the inversion algorithm with respect to the expected misfit and finally it represents an important benchmark for the MS datasets. Numerical simulations are noise free the results have been then obtained in ideal conditions.

5.5.1 TRADITIONAL ARRAYS

Traditional arrays performed differently on the three reference models.

In the "two-strata like" and "three-strata like" models DD and PD arrays better resolved the lateral continuity of the anomaly in cases from I to IV. The anomaly-background interface appears to be sharp and marked by a sudden jump in the resistivity values. DD and PD arrays in cases from V to VI are not as effective and results are even worse in case of a conductive layer located just below the electrodes The W-α array, as expected, seems to be more reliable in reconstructing the vertical changes in resistivity (especially in the central portion of the section) although the overall geometry of the interface is poorly resolved exhibiting a typical curved anomaly in the resistivity image.

The resolving power of the arrays for the "prism like" model, is remarkable but mostly for the conductive target anomaly. The resistive background aids in outlining the borders of the finite object. The DD array returns the best image of the target anomaly in both shallow and deep cases. In near surface cases the DD array outlines the geometry of the anomaly and reasonably fits its resistivity. Depth case VI seems to fall outside resolving capability for all the tested arrays. Results are satisfying when the target anomaly is a near surface resistor while a deep resistor could be hardly imaged.

The following conclusions could be then drawn for traditional arrays:

1) DD and PD arrays are generally able to better resolve the reference models selected. DD array is preferable especially in case of resistive layers located near the surface;

2) DD array is not affected by the typical asymmetry of the PD array. The position of the remote pole partly distorts the inverted resistivity image.

5.5.2 MULTI-SOURCE ARRAYS

MS-DD array results are of prominent interest for this study.

In the "two-strata like" models the 2TX array is more effective in terms of imaging the target anomaly and fitting its resistivity. This is more evident in case of a conductive target anomaly while , meanwhile in the complementary case also the 1TX array is a valid proposal, even if the deep background recovery seems more complicated.

An interesting feature in this first example is the relationship between the number of adopted transmitters and the anomaly lateral (X direction) reduction with depth.

In the "three-strata-like" models, the 2TX and 4TX arrays are the most effective in imaging the geometry of the target anomaly for cases I-IV. Resolution capability was poor for all the tested arrays for cases V-VI.

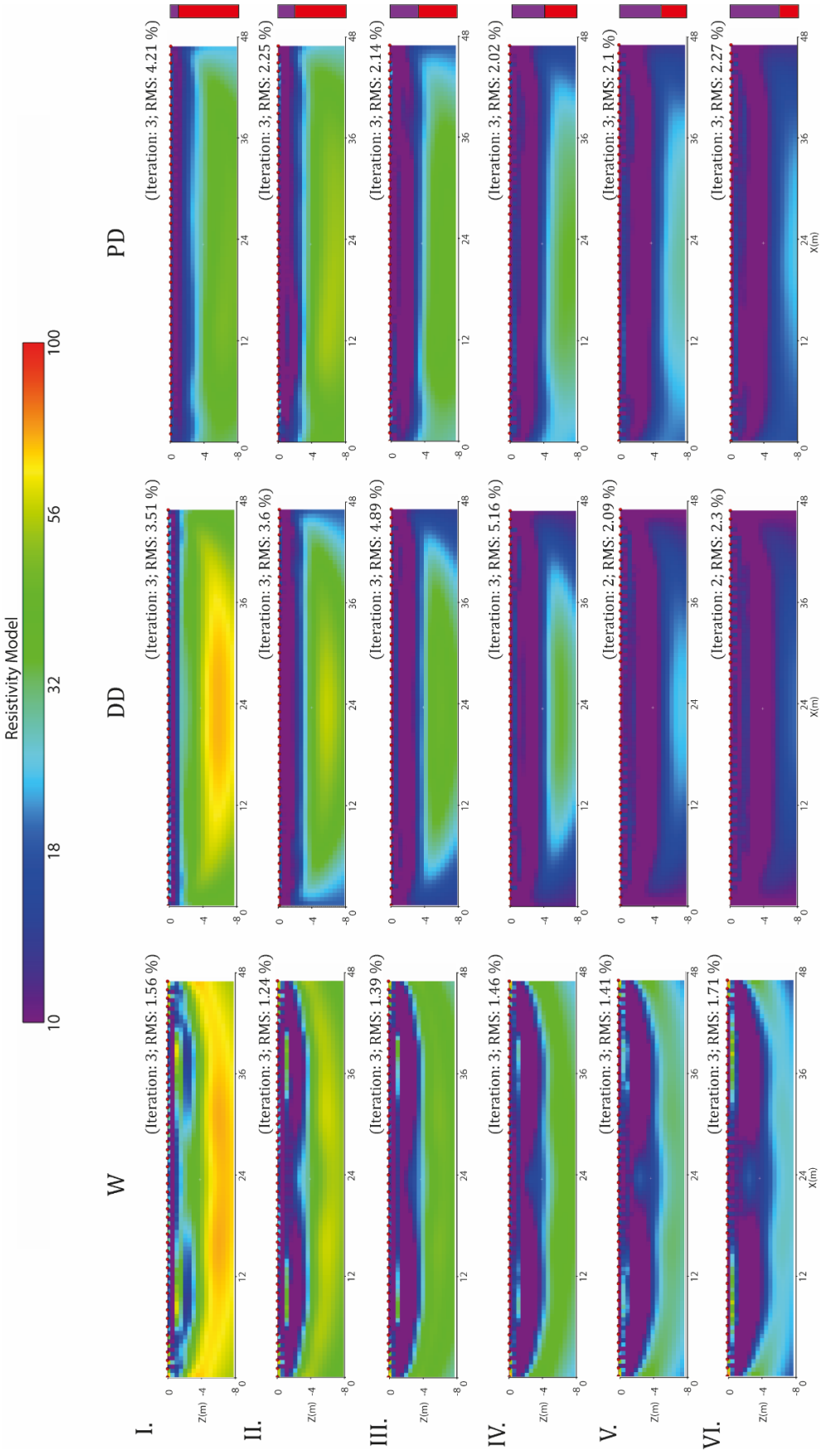

Figure 17: two-strata like model: conductive target anomaly (10 Ω·m, purple) in resistive background (100 Ω·m, red) for depth cases I-VI. Inversion results: W: Wenner-alpha array; DD: dipole-dipole array; PD: pole-dipole array. Reference model on the right.

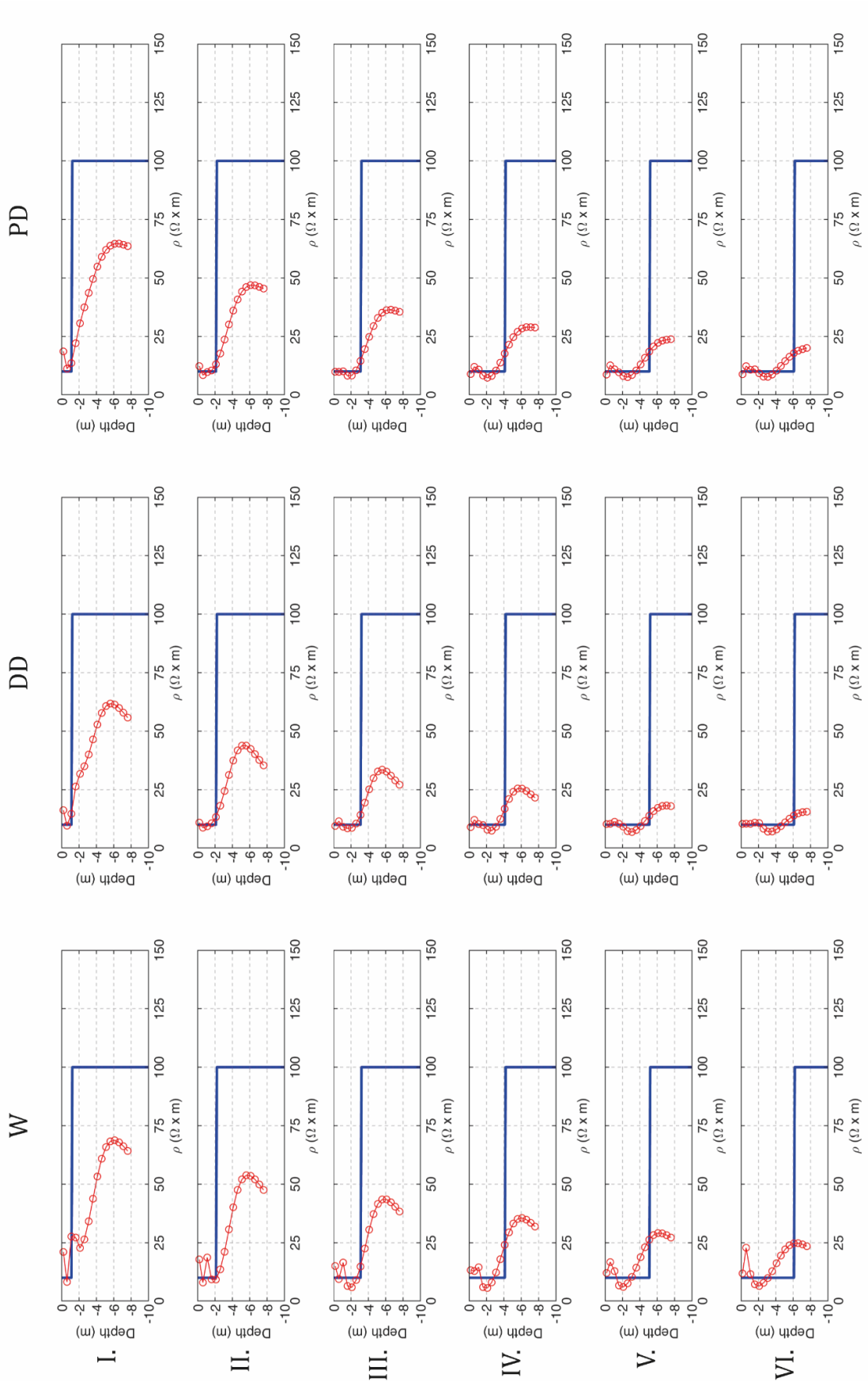

Figure 18: two-strata like model. Resistivity profile averaged from the inverted section (marked red line) superimposed to the reference model (blue line).

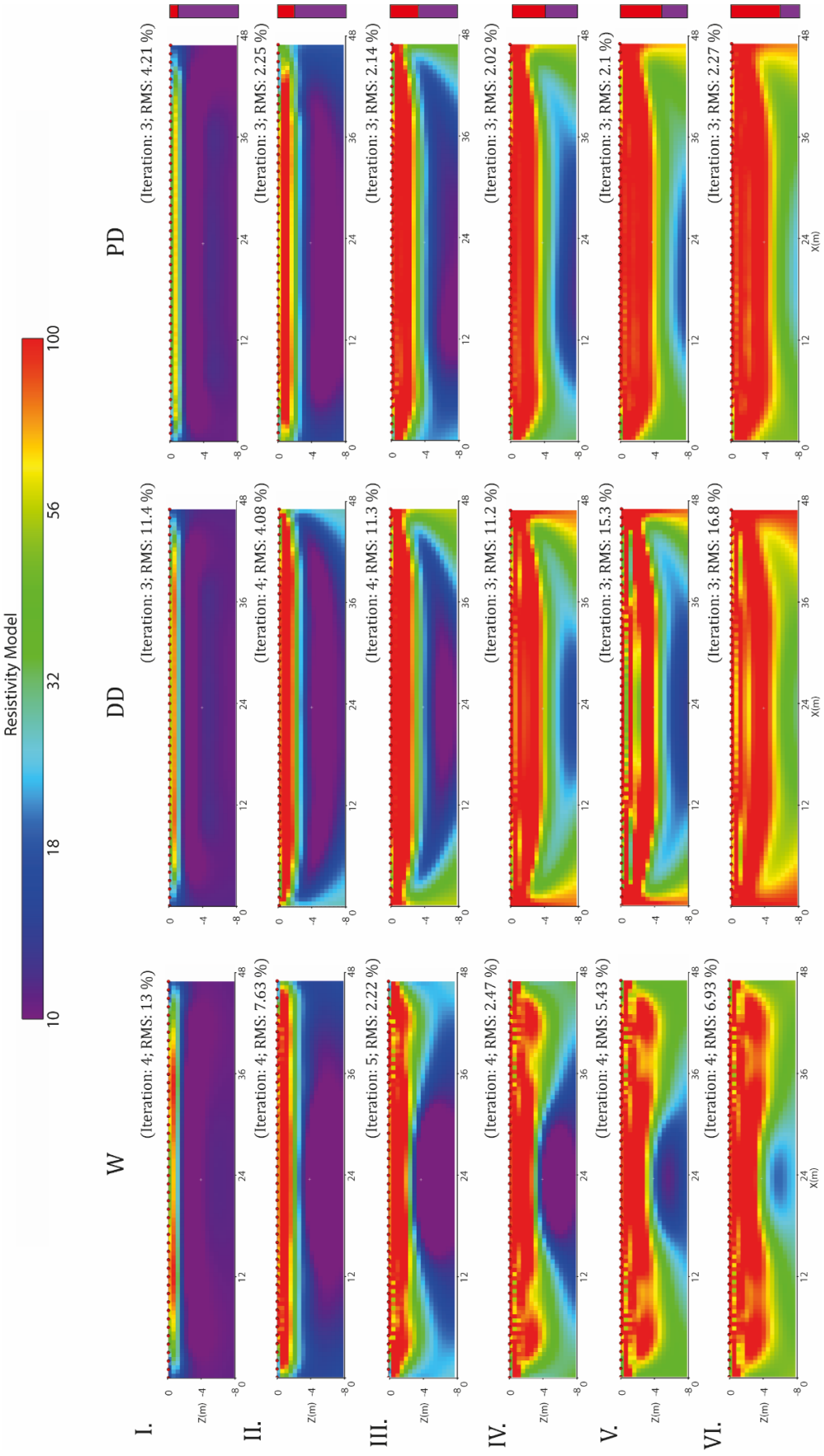

Figure 19: two-strata like model: resistive (100 Ω·m, red) anomaly in conductive (10 Ω·m, purple) background for depth cases I-VI. Inversion results: W: Wenner-alpha; DD: dipole-dipole; PD: pole-dipole.

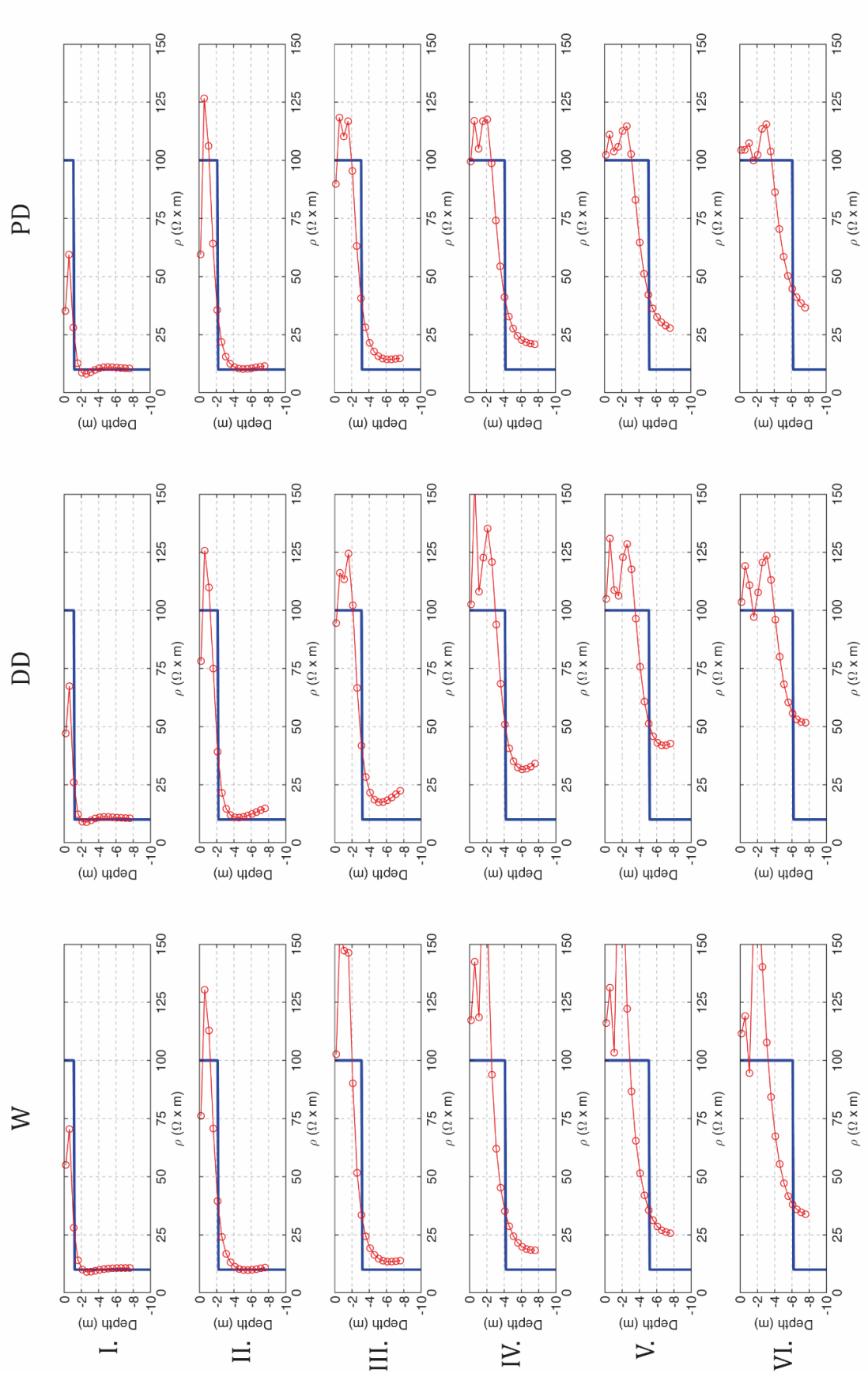

Figure 20: two-strata like model. Resistivity profile averaged from the inverted section (marked red line) superimposed to the reference model (blue line).

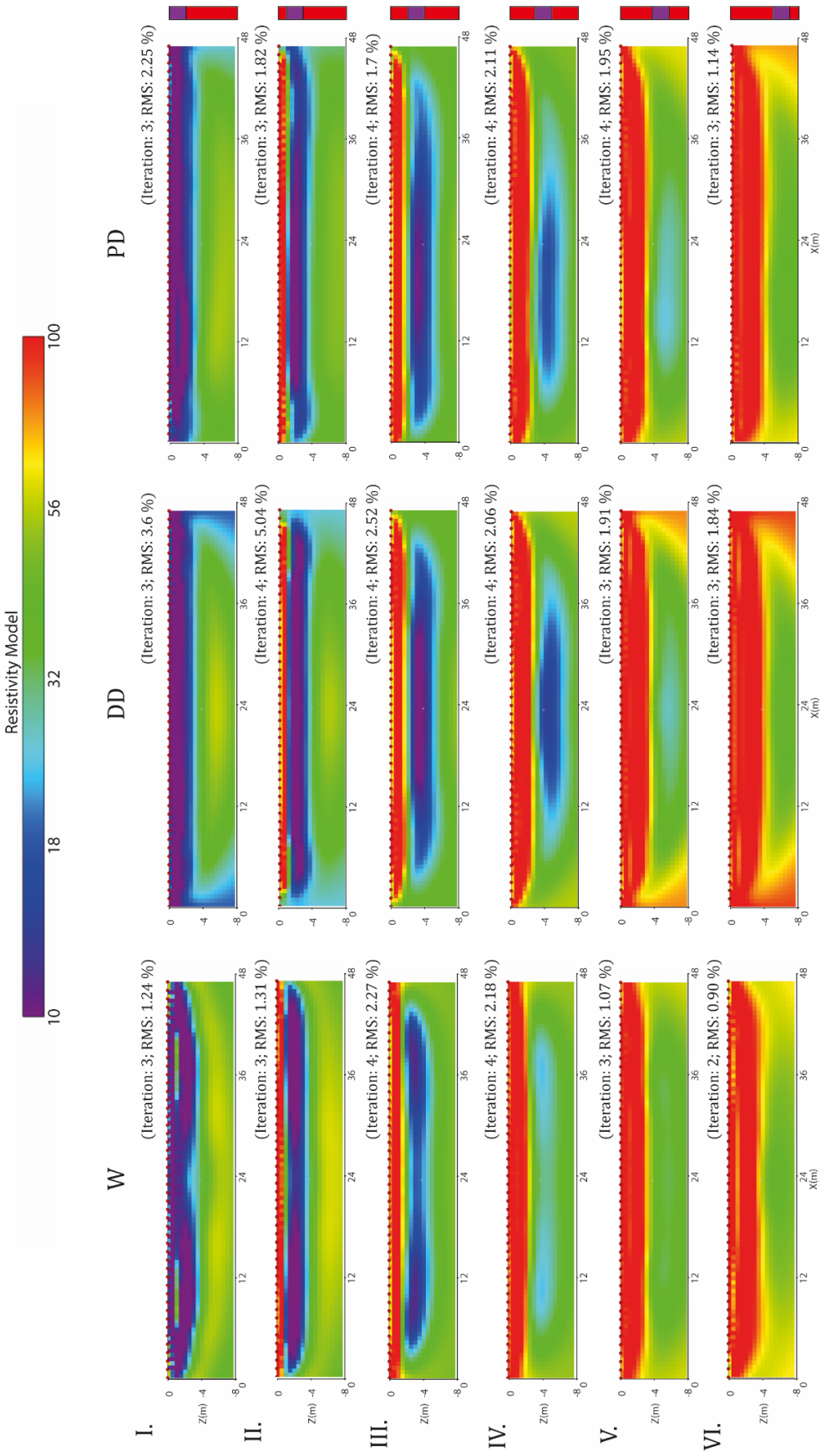

Figure 21: three-strata like model: conductive (10 Ω·m, purple) anomaly in resistive (100 Ω·m, red) background for depth cases I-VI. Inversion results: W: Wenner-alpha; DD: dipole-dipole; PD: pole-dipole.

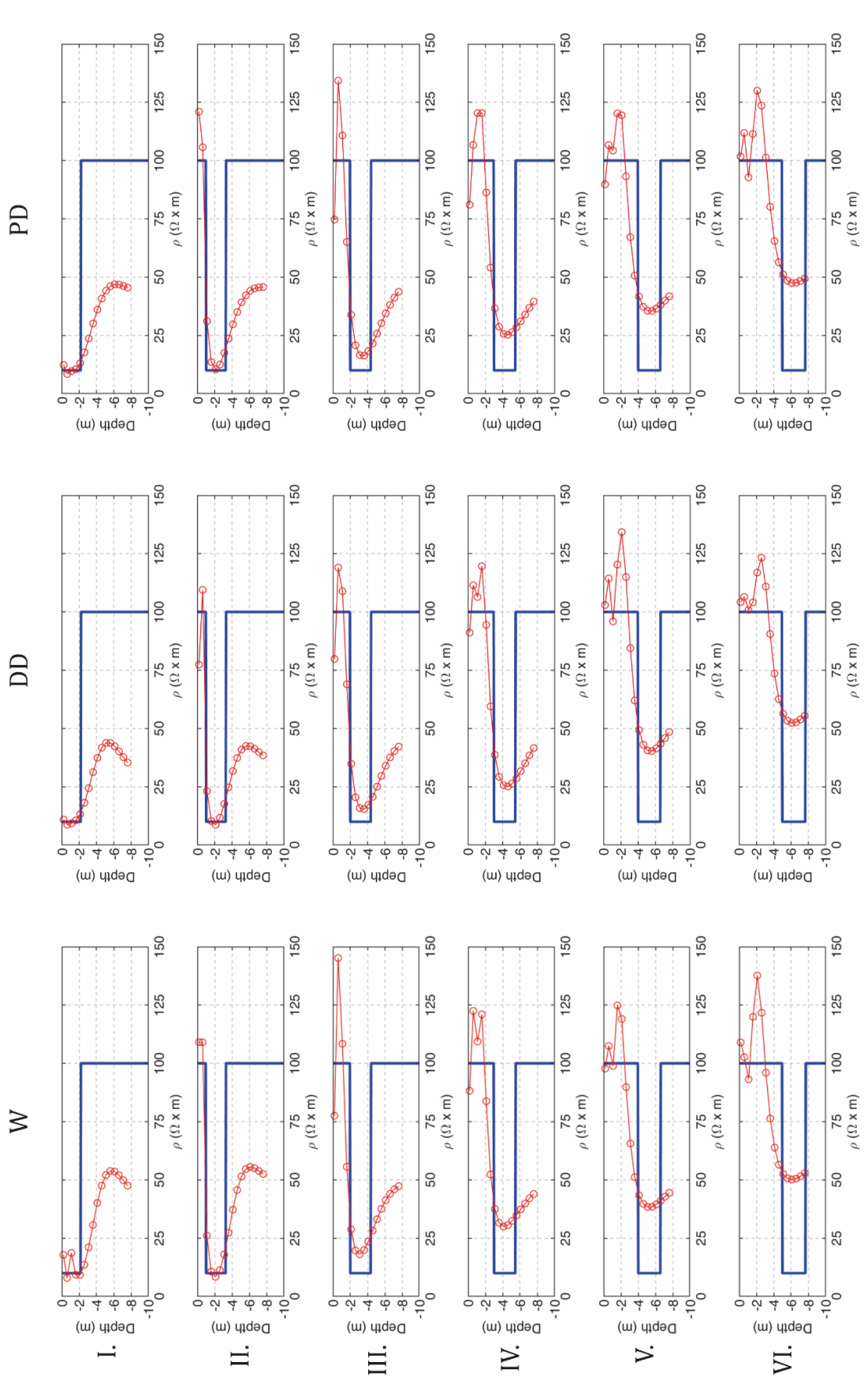

Figure 22: three-strata like model Resistivity profile averaged from the inverted section (marked red line) superimposed to the reference model (blue line).

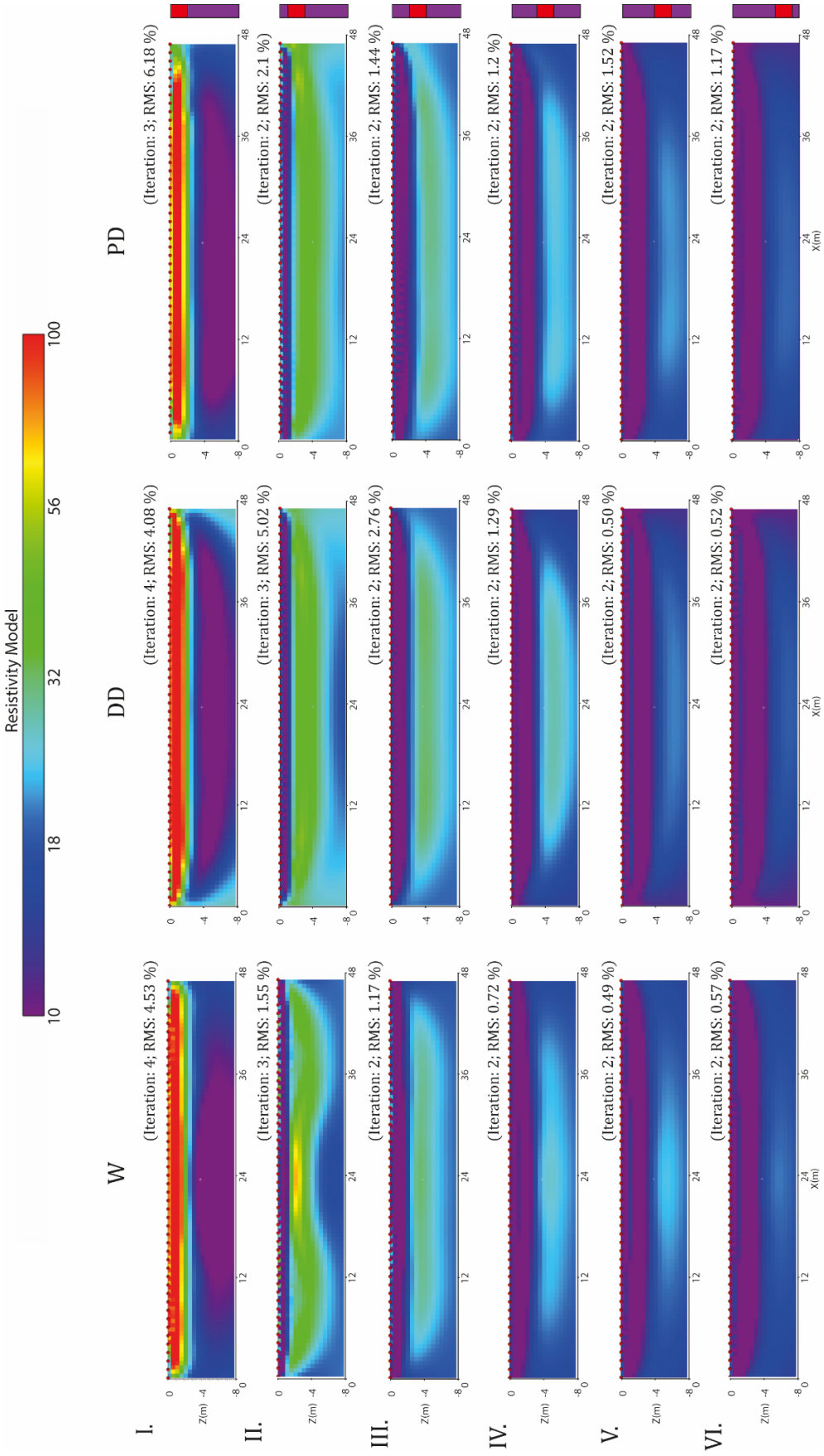

Figure 23: three-strata like model: resistive (100 Ω·m, red) anomaly in conductive (10 Ω·m, purple) background for depth cases I-VI. Inversion results: W: Wenner-alpha; DD: dipole-dipole; PD: pole-dipole.

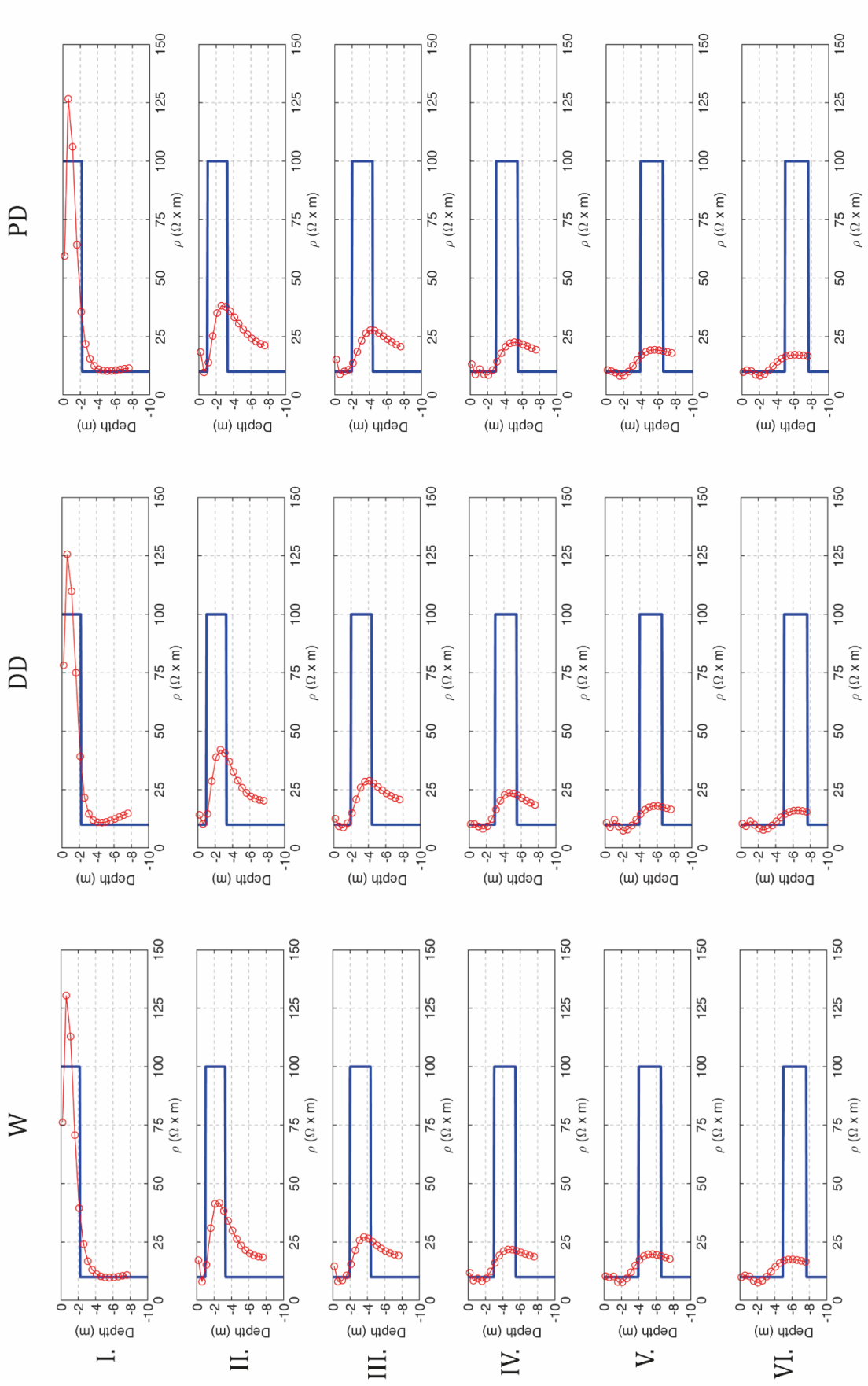

Figure 24: two-strata like model. Resistivity profile averaged from the inverted section (marked red line) superimposed to the reference model (blue line).

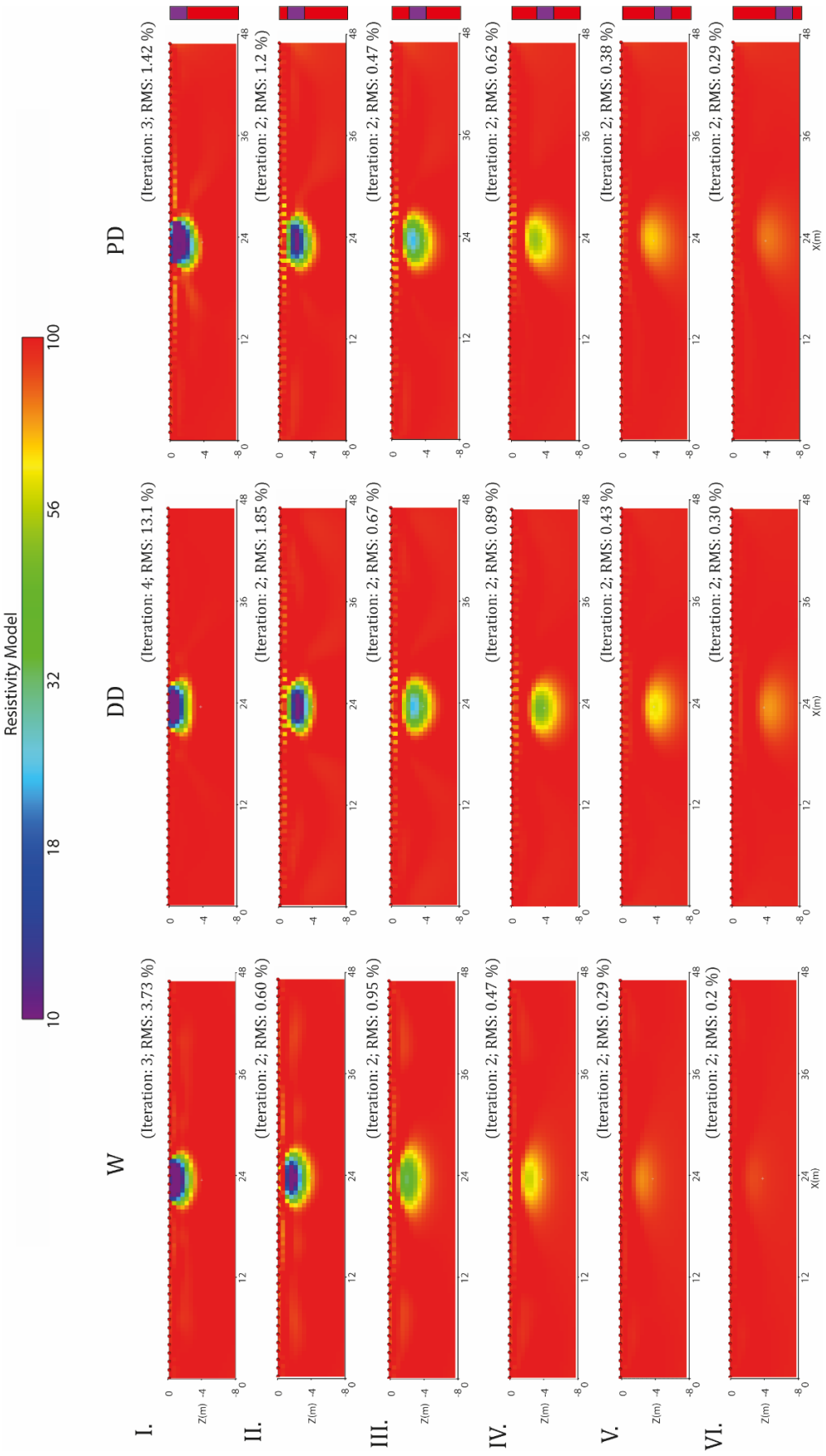

Figure 25: prism like model: conductive (10 Ω·m, purple) anomaly in resistive (100 Ω·m, red) background for depth cases I-VI. Inversion results: W: Wenner-alpha; DD: dipole-dipole; PD: pole-dipole.

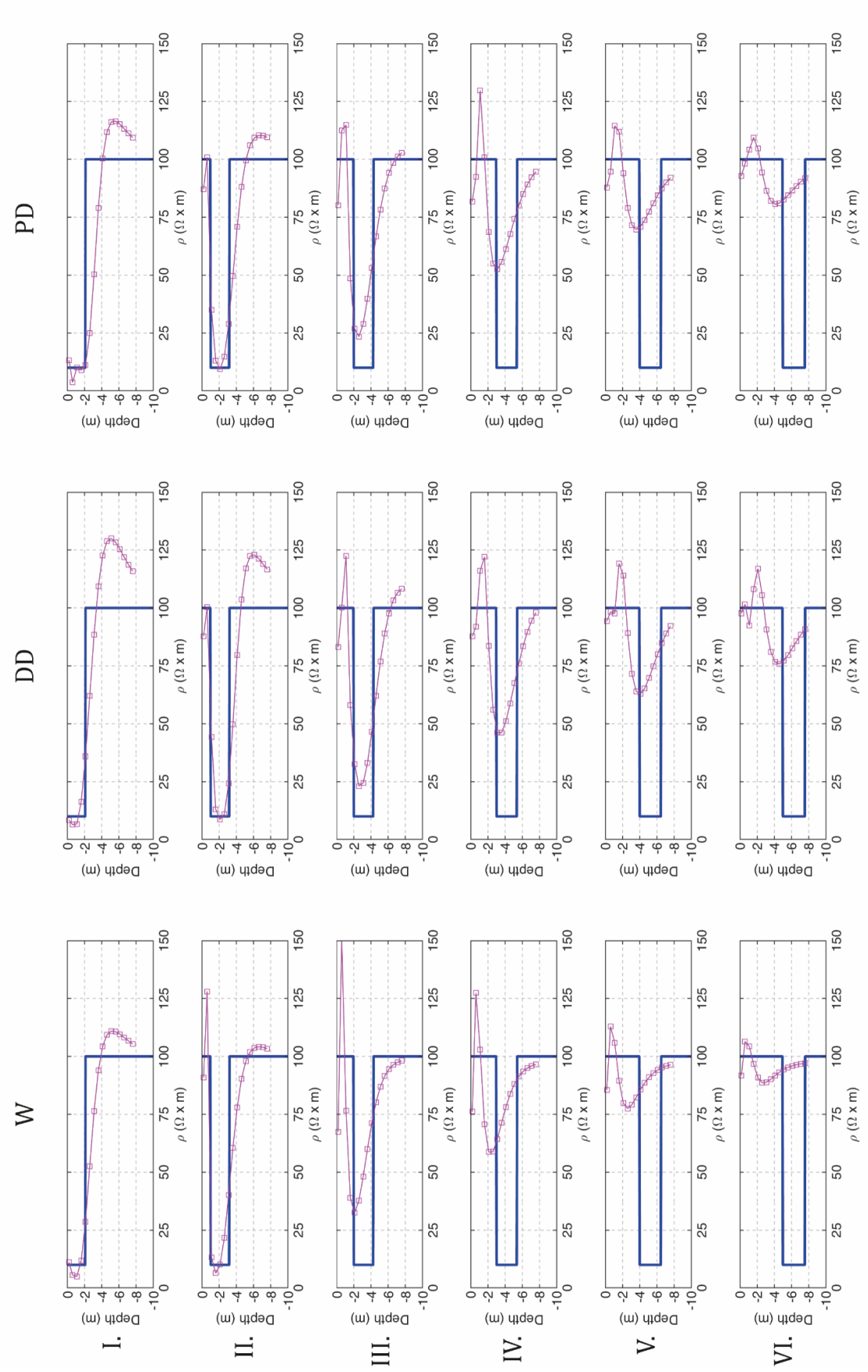

Figure 26: prism like model. Half-line resistivity profile (marked purple line) superimposed to the reference model (blue line).

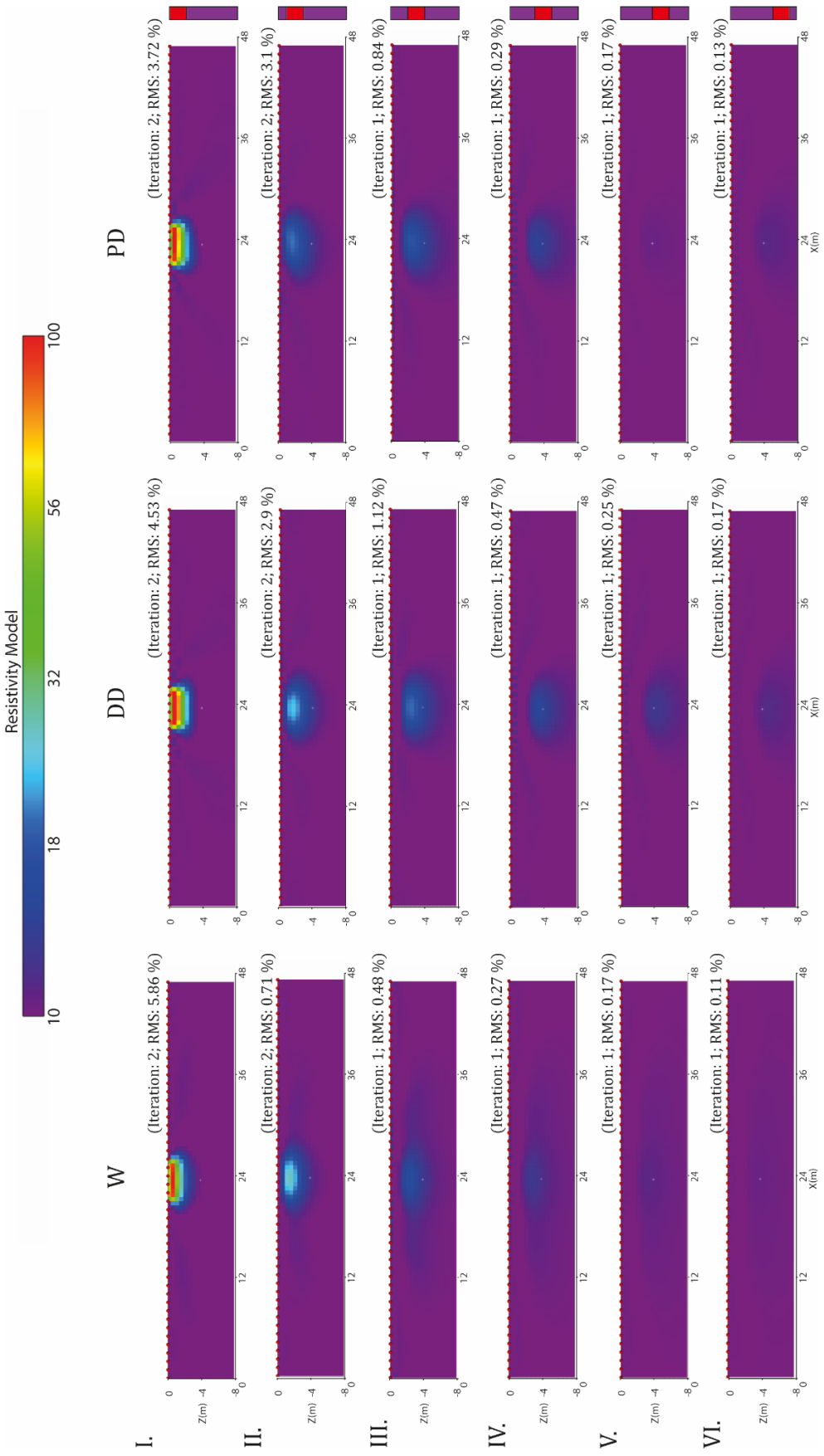

Figure 27: prism like model: resistive (100 Ω·m, red) anomaly in conductive (10 Ω·m, purple) background for depth cases I-VI. Inversion results: W: Wenner-alpha; DD: dipole-dipole; PD: pole-dipole.

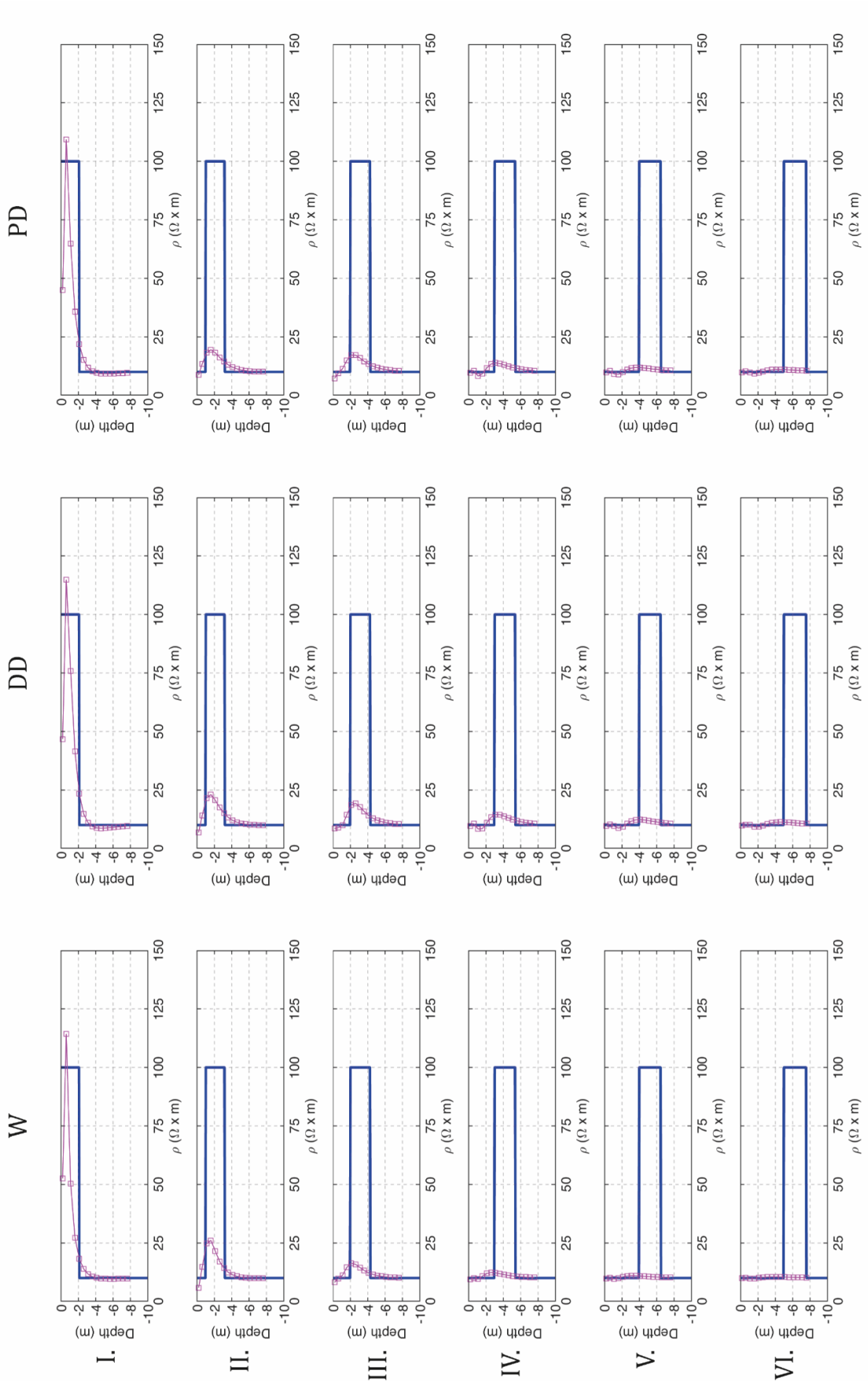

Figure 28: prism like model. Half-line resistivity profile (marked purple line) superimposed to the reference model (blue line).

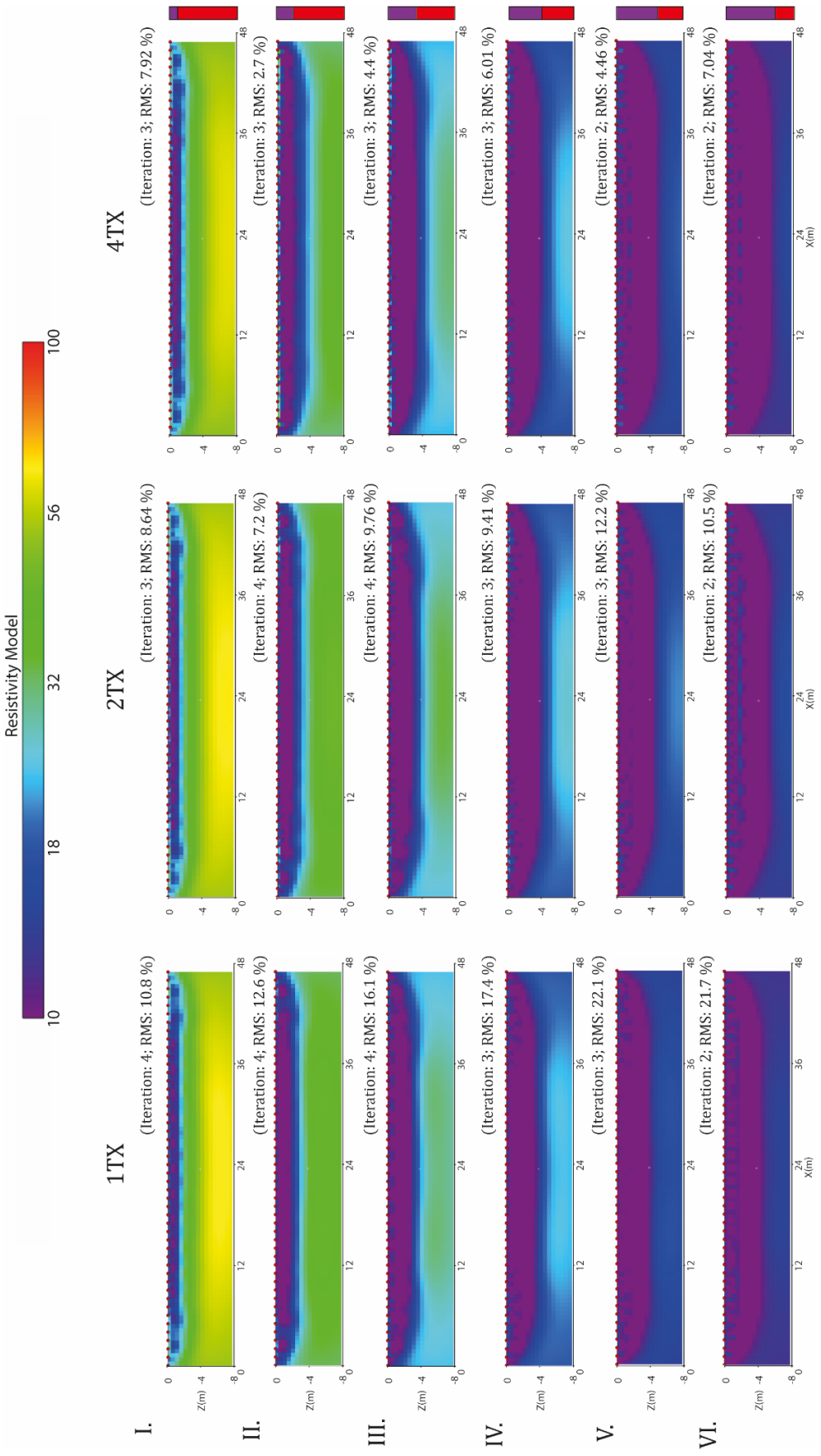

Figure 29: two-strata like model: conductive (10 Ω·m, purple) anomaly in resistive (100 Ω·m, red) background for depth cases I-VI. Inversion results: 1TX: MS single transmitter; 2TX: MS double-transmitter; 4TX: MS quadruple-transmitter.

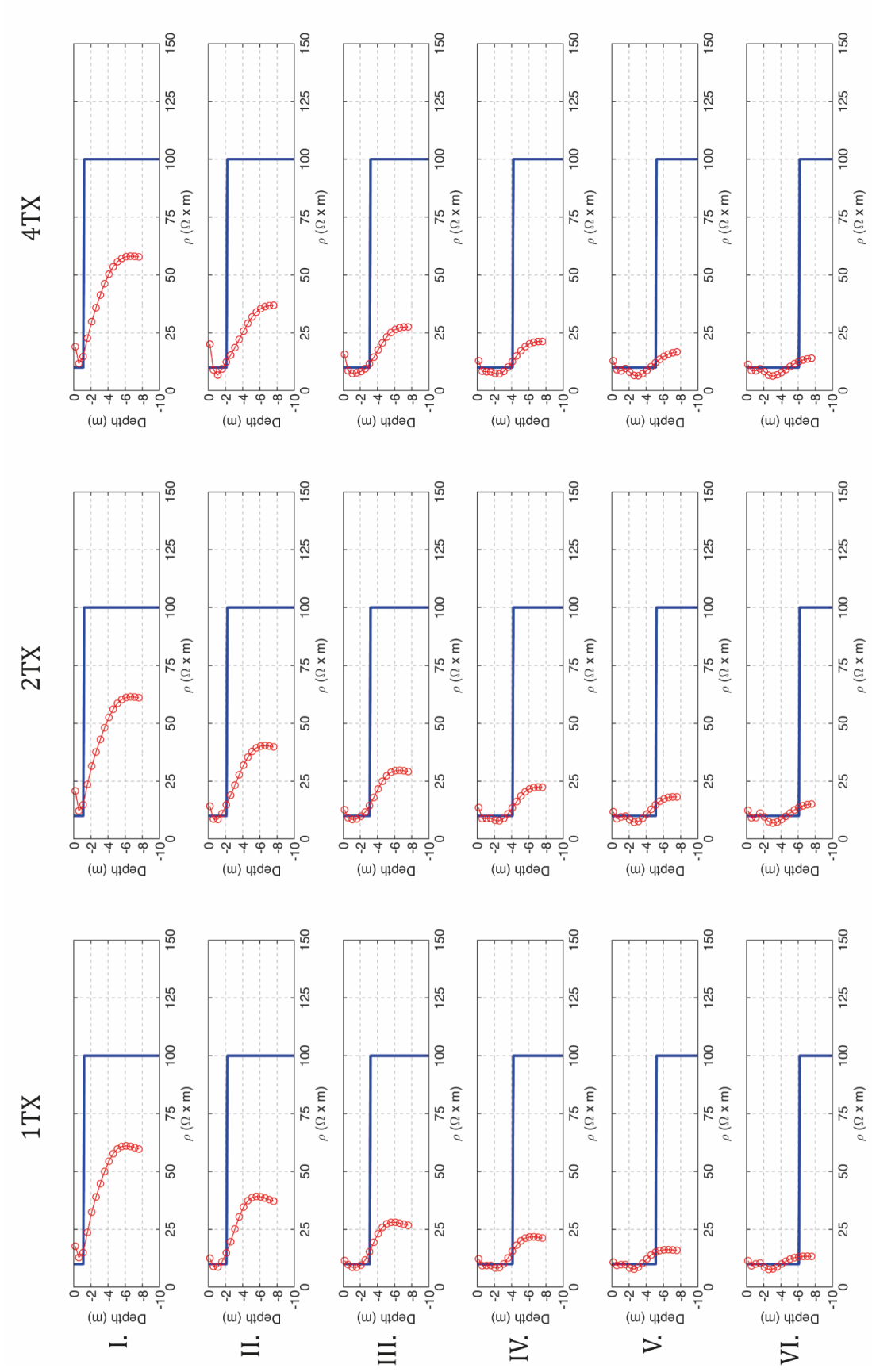

Figure 30: two-strata like model. Resistivity profile averaged from the inverted section (marked red line) superimposed to the reference model (blue line).

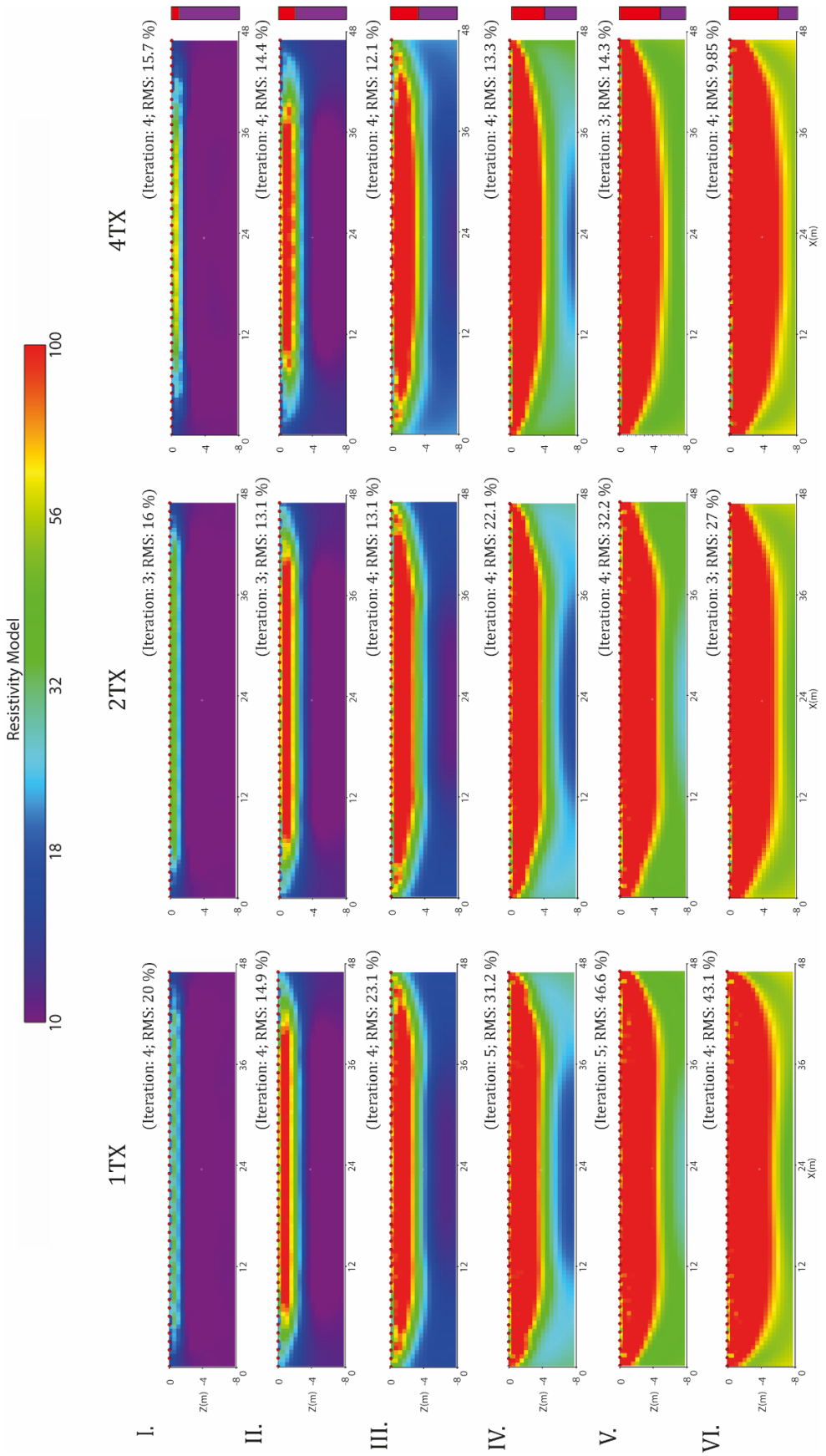

Figure 31: two-strata like model: resistive (100 Ω·m, red) anomaly in conductive (10 Ω·m, purple) background for depth cases I-VI. Inversion results: 1TX: MS single transmitter; 2TX: MS double-transmitter; 4TX: MS quadruple-transmitter.

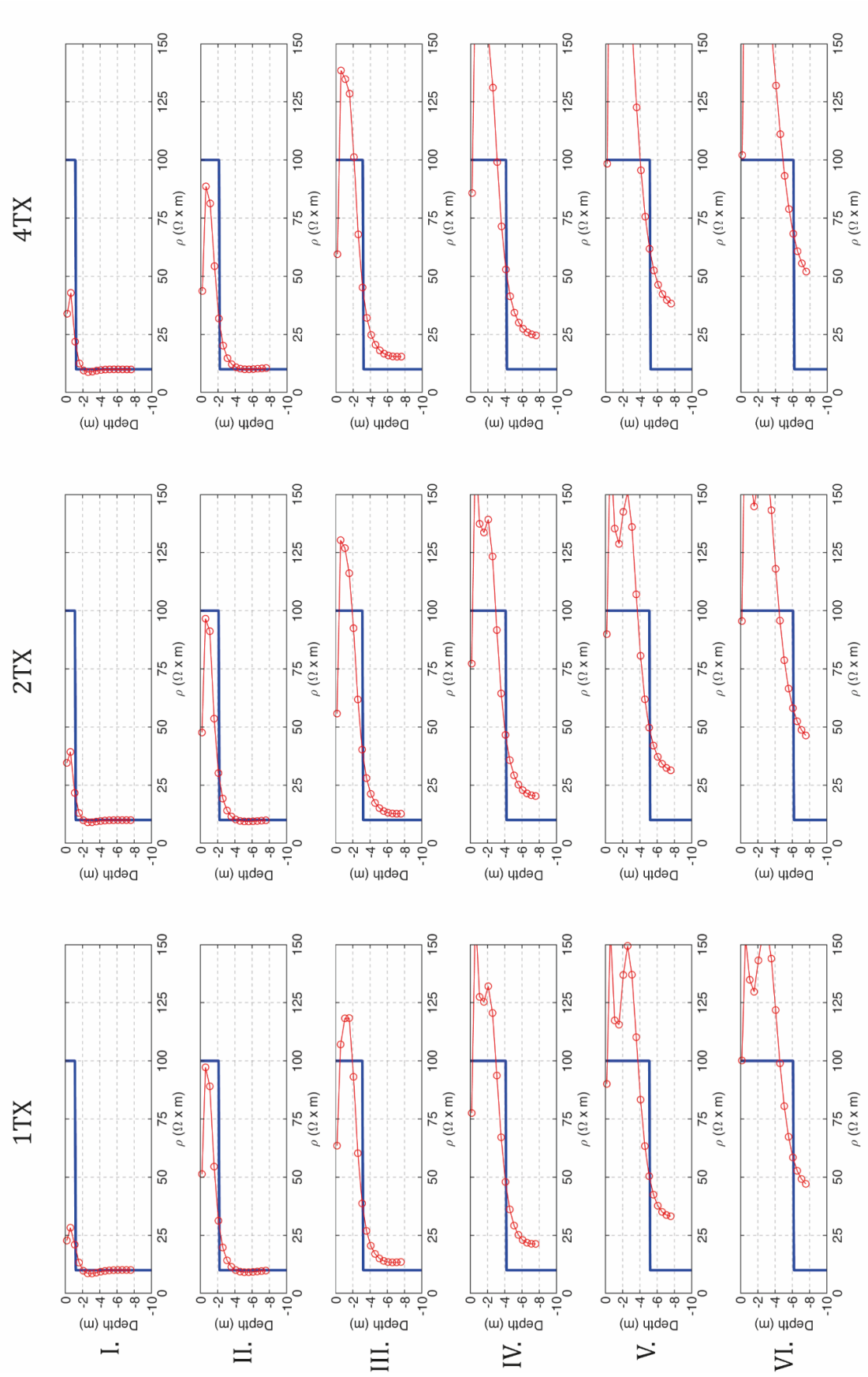

Figure 32: two-strata like model. Resistivity profile averaged from the inverted section (marked red line) superimposed to the reference model (blue line).

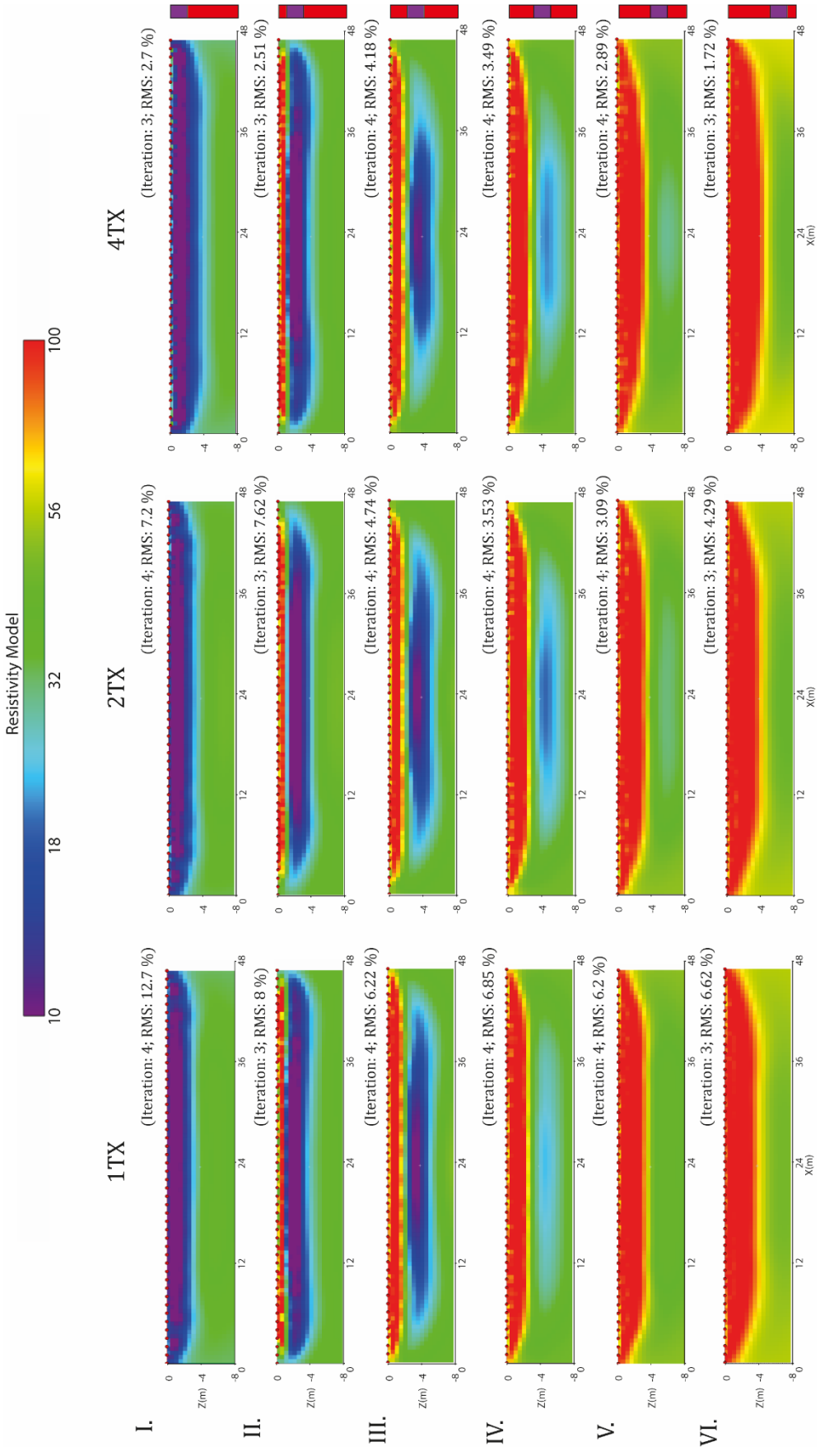

Figure 33: three-strata like model: conductive (10 Ω·m, purple) anomaly in resistive (100 Ω·m, red) background for depth cases I-VI. Inversion results: 1TX: MS single transmitter; 2TX: MS double-transmitter; 4TX: MS quadruple-transmitter.

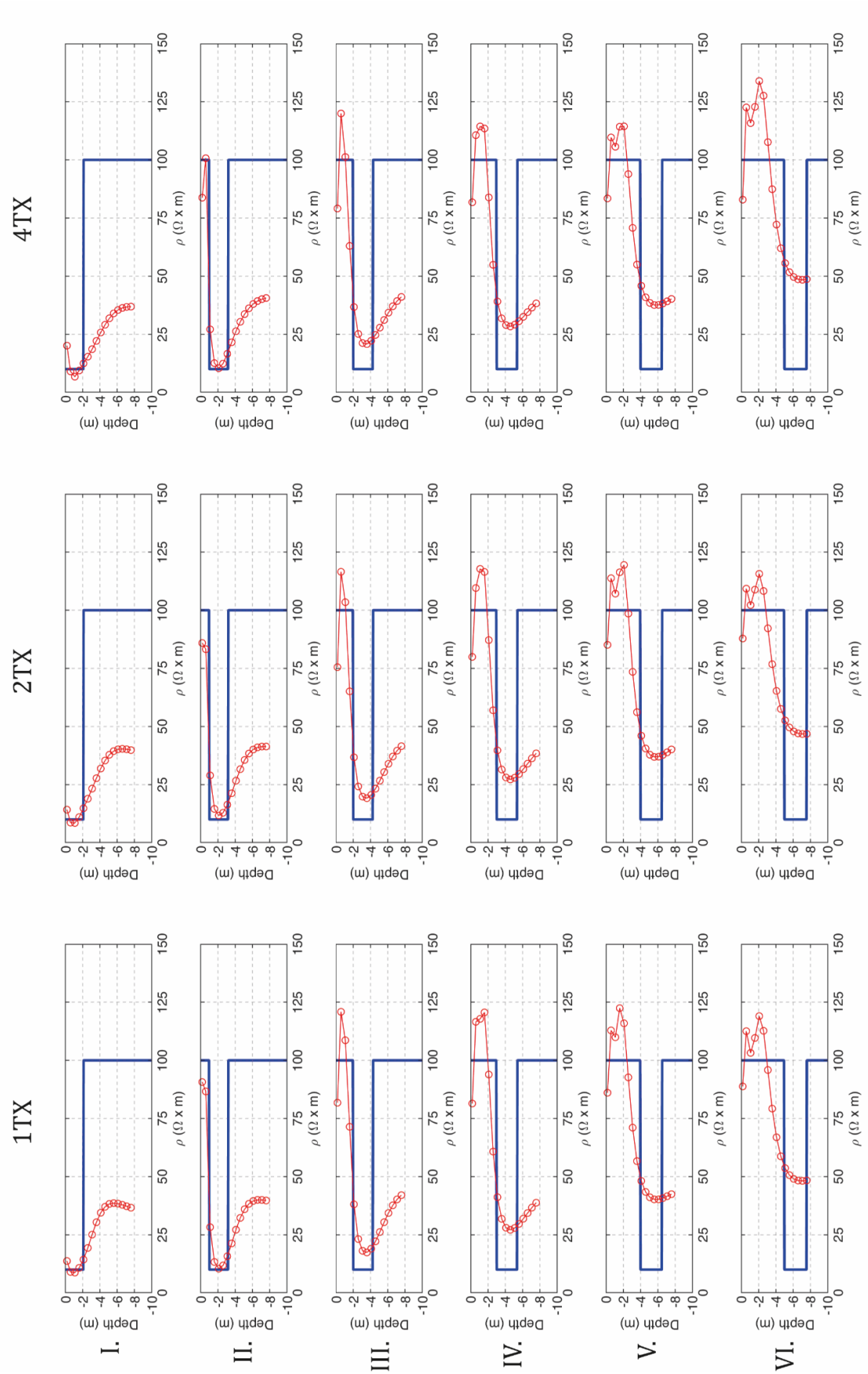

Figure 34: three-strata like model. Resistivity profile averaged from the inverted section (marked red line) superimposed to the reference model (blue line).

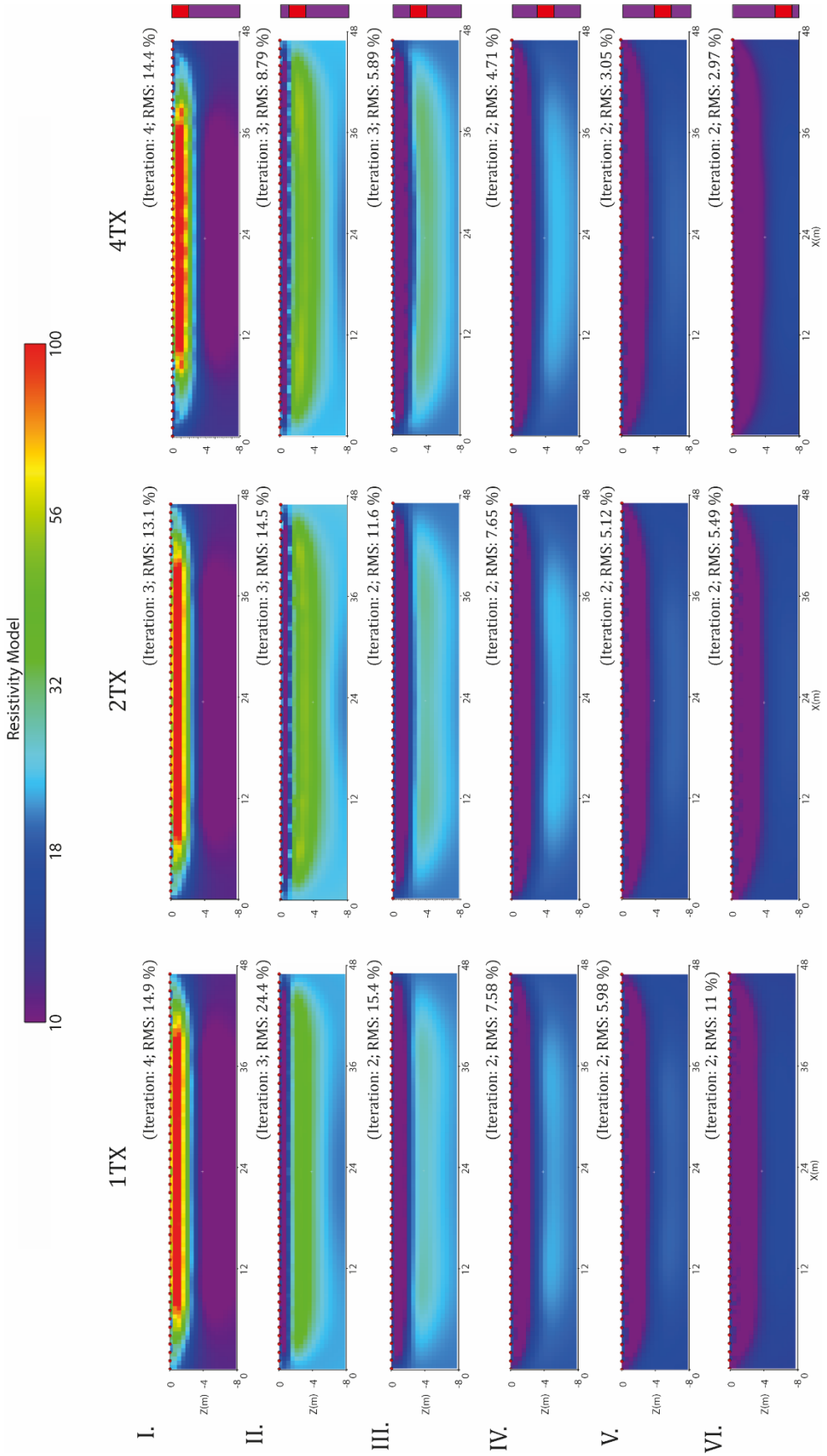

Figure 35: three-strata like model: resistive (100 Ω·m, red) anomaly in conductive (10 Ω·m, purple) background for depth cases I-VI. Inversion results: 1TX: MS single transmitter; 2TX: MS double-transmitter; 4TX: MS quadruple-transmitter.

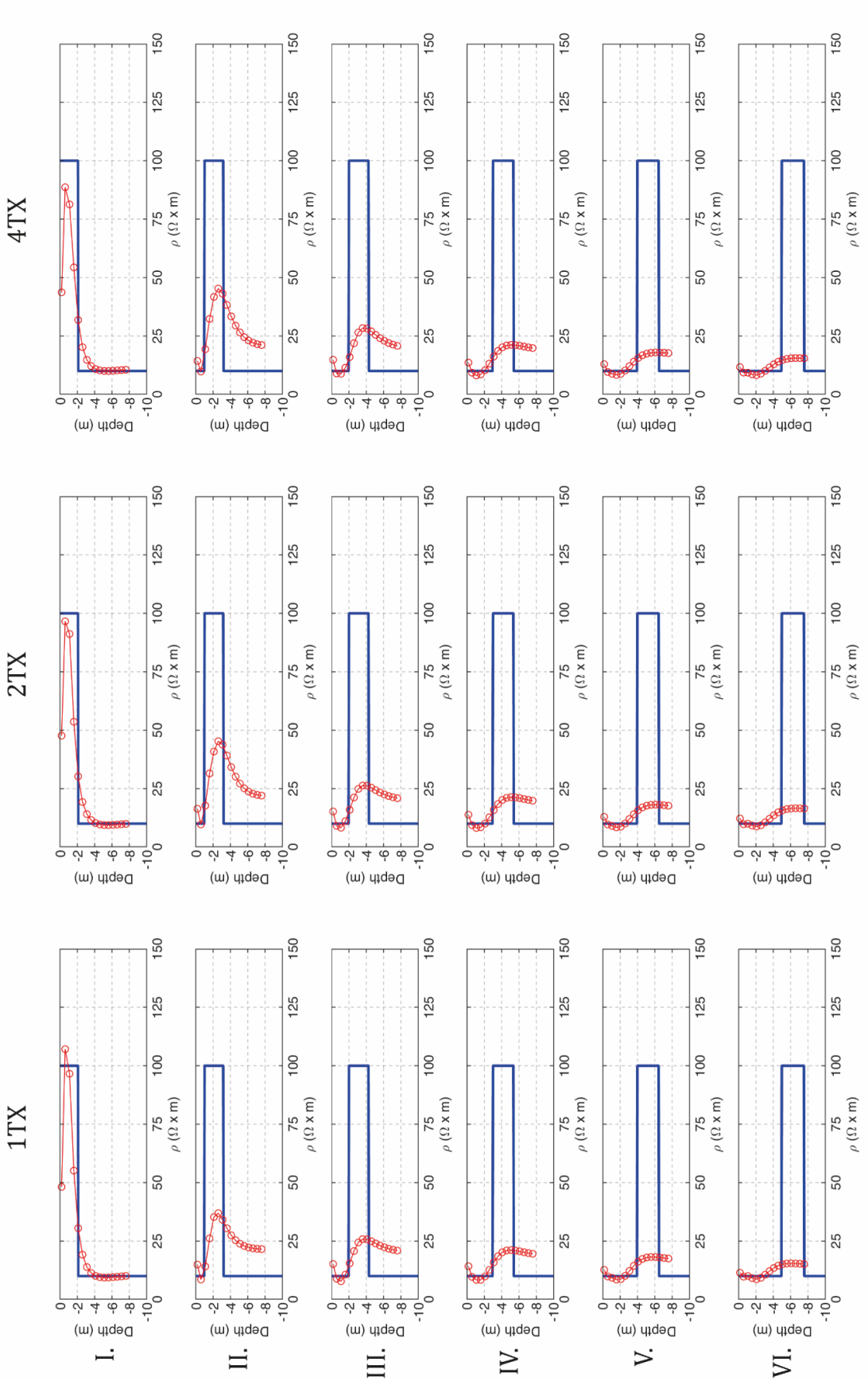

Figure 36: three-strata like model. Resistivity profile averaged from the inverted section (marked red line) superimposed to the reference model (blue line).

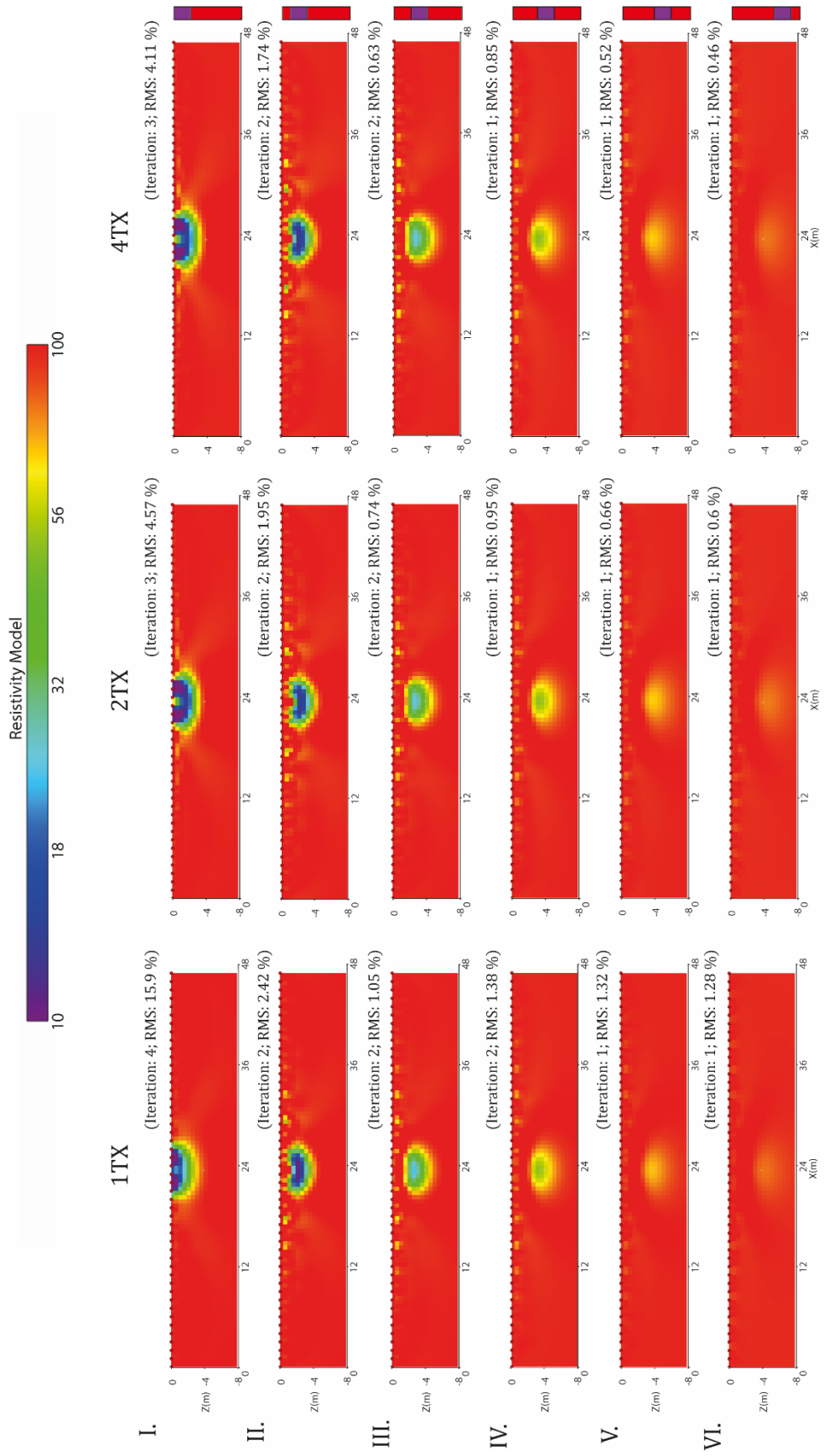

Figure 37: prism like model: conductive (10 Ω·m, purple) anomaly in resistive (100 Ω·m, red) background for depth cases I-VI. Inversion results: 1TX: MS single transmitter; 2TX: MS double-transmitter; 4TX: MS quadruple-transmitter.

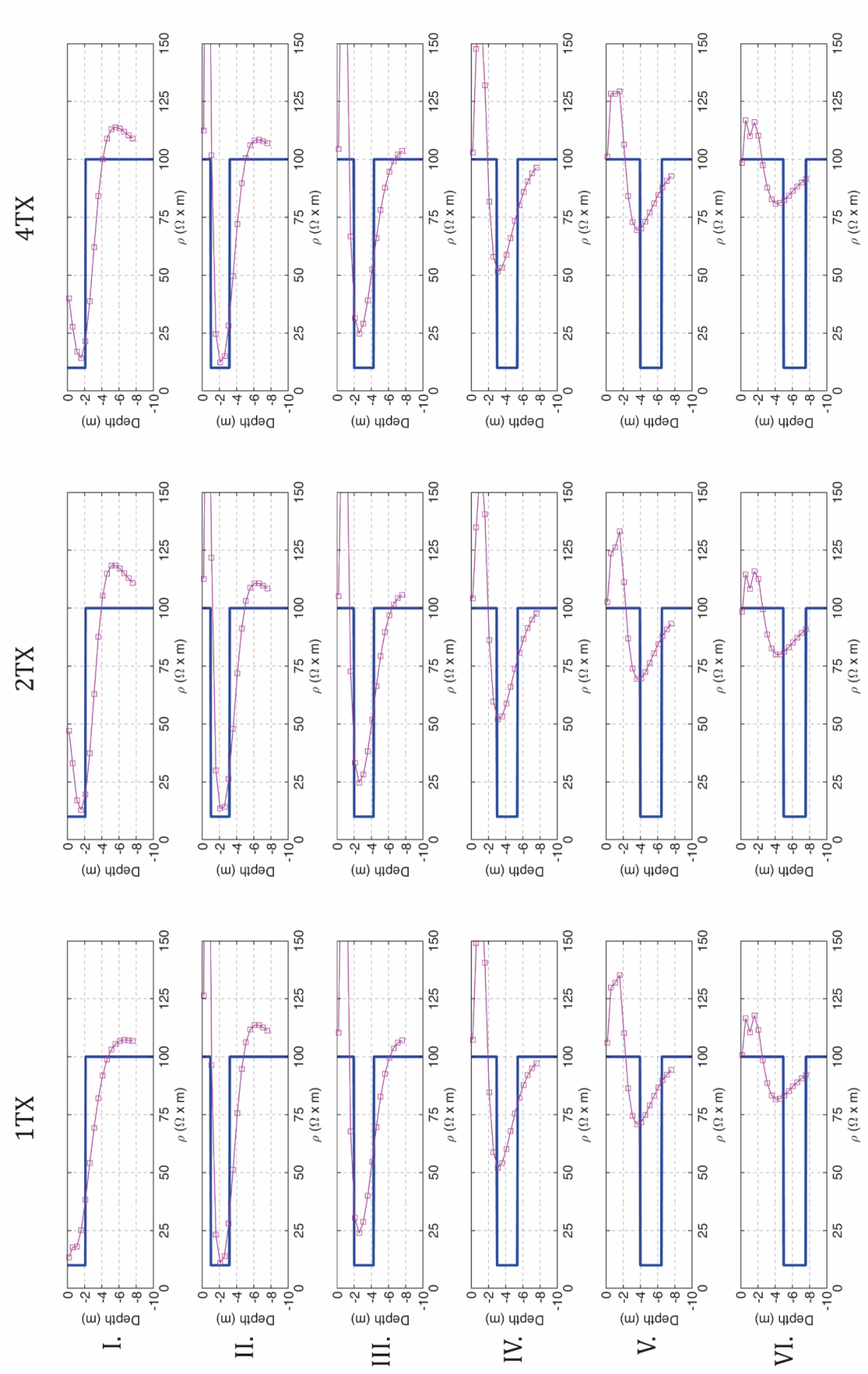

Figure 38: prism like model. Half-line resistivity profile (marked purple line) superimposed to the reference model (blue line).

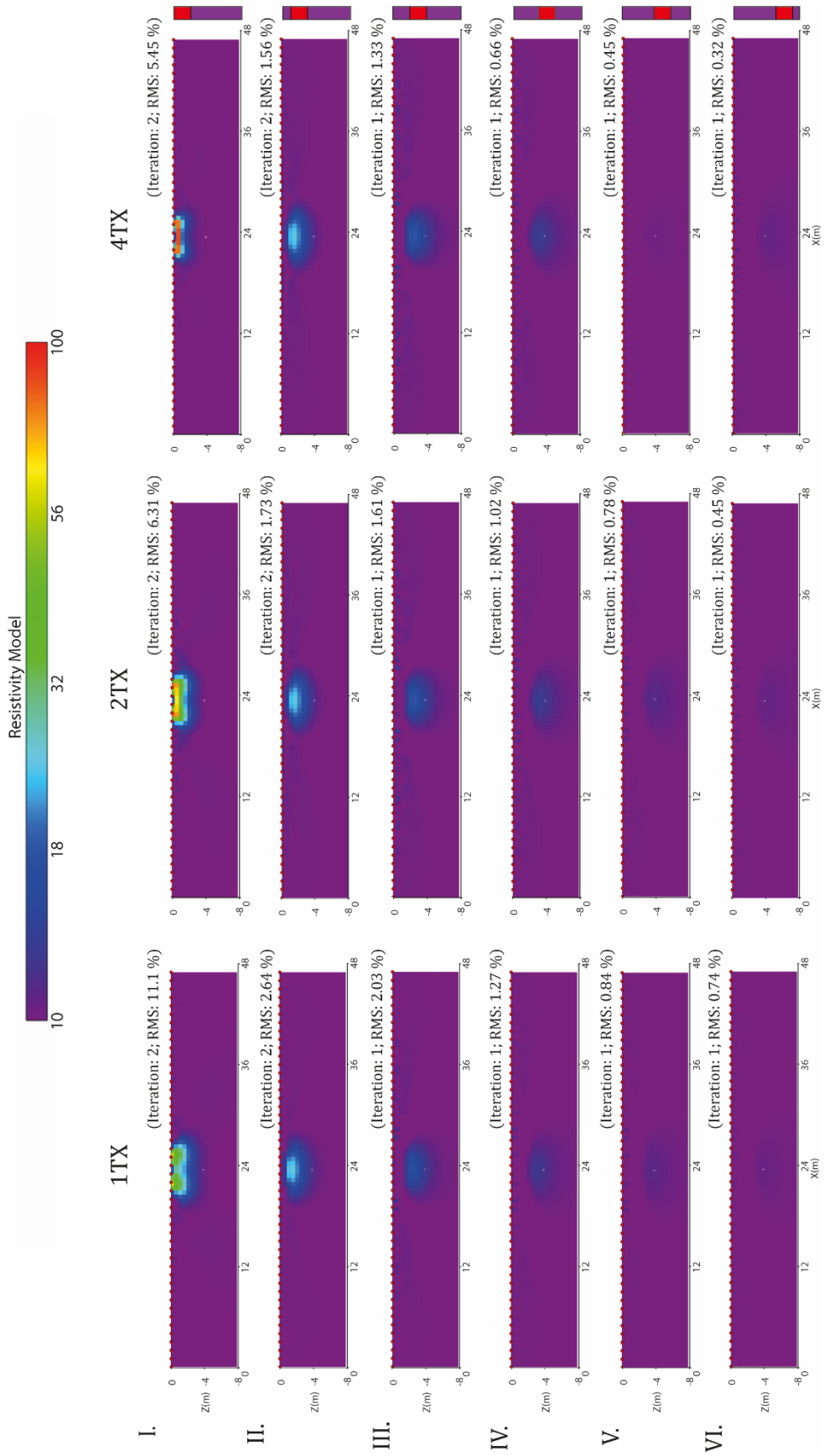

Figure 39: prism like model: resistive (100 Ω·m, red) anomaly in conductive (10 Ω·m, purple) background for depth cases I-VI. Inversion results: 1TX: MS single transmitter; 2TX: MS double-transmitter; 4TX: MS quadruple-transmitter.

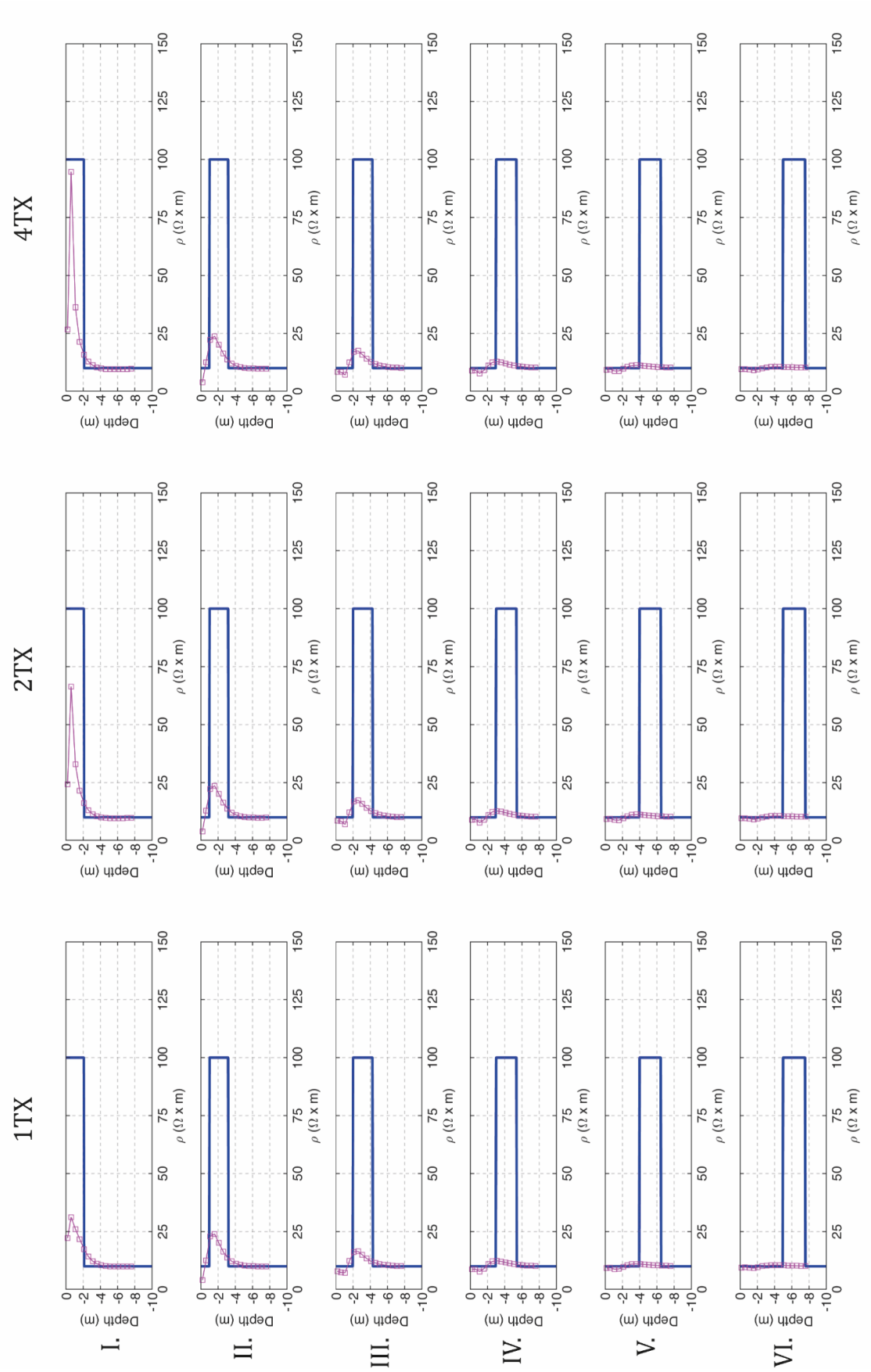

Figure 40: prism like model. Half-line resistivity profile (marked purple line) superimposed to the reference model (blue line).

In the "prism like" models the use of multiple transmitters results in a better fit of the resistivity of the target anomaly for the shallow cases (I-III) . At larger depth (cases V-VI) the resolving power is low for all the tested MS-DD arrays.

The following conclusions could be then drawn for MS-DD arrays:

1) The 2TX mode seems to be a good trade-off between number of measured data-points and resolution capability;

2) The 4TX mode shows some potential for improving the resolution at larger depths but its performance seems to be limited by the reduced number of data-points. The lack of data-points results in a poorly constrained inversion affecting the finale resistivity image.

5.5.3 FINAL REMARKS

The most intriguing aspect of these simulations was the direct comparison between the traditional and MS datasets. In this sense, a one-to-one correspondence could be found between the DD and the MS-DD array performances.

MS-DD, in the "two-strata like" model, seems to be more effective in reproducing the lateral continuity of the interface in case of conductive target anomaly. Numerical artifacts, occurring in the middle of the DD array image, are not visible in the MS inversion. DD delivers a more focused imaged of the interface and a better fit of the background resistivity. The misfit on the target resistivity is higher for the MS-DD array at larger depths (cases V-VI).

In case of a resistive target anomaly the MS-DD array seems to be also more effective in the resolution of near-surface cases (I-III). In MS-DD inversion the target interface looses continuity on the sides but this issue is strictly dependent on the data-point distribution. At larger depth (cases IV-VI) the central portion of the interface is still clearly imaged but the misfit on the background resistivity gets higher.

Similar considerations could be done for "the three-strata-like" model with a target conductive anomaly. The Here, the anomaly looks compressed in the mid-depth case for the MS-DD respect to the trad one. Nevertheless, in this case the anomaly is completely lost in the overestimated background, very similar to what happens for the trad-DD.

In case of a resistive target anomaly the inverted sections from MS-DD and DD are almost identical in the near-surface cases (I-III). The horizontal continuity of the interfaces reduces progressively as the number of transmitters increases (in particular for depth case I). Inversions, in cases IV-VI, deliver poor resistivity images for both MS-DD and DD arrays. The effectiveness of multiple transmitters seems to be limited for this model scenario.

Results for the "prism like" model obtained with both the MS-DD and the DD arrays are comparable. In the MS-DD, in the shallower cases, the target anomaly is very noisy with evident side lobes. In this case also the reason is probably related to the distribution of the data-points in the MS-DD sequences.

Substantially, except for very few cases, results obtained with a traditional or an MS array are quite similar and comparable in the simulated scenarios. Additional modeling is mandatory for multiple transmissions to evaluate where simultaneous injections yield to destructive interference of the resulting electrical field.

In other words, a possibility, for improving the MS-DD response, could result from a different arrangement of transmitting and receiving dipoles. Line geometry should be reconsidered for exploiting MS potentials. For the present study, this solution was not taken into account. Another possibility, is the aggregation of single- and multiple-transmitter datasets prior to carry out data inversion. This could be a major breakthrough as coverage and depth of penetration are both improved. This was not considered in the simulations to avoid further complexities in separating cause and effects while analyzing the inverted data.

A third and very promising possibility is the adaptation of the of the inversion parameters to the peculiarities of the MS data. The default parameters have been used for this firs group of simulations. These parameters are more or less the standard for traditional resistivity-meters with their limitations in sampling accuracy, electronic noise, self-potential suppression, etc.

The MS system was designed specifically for DERT surveying with a particular attention on the detection of low-amplitude signals. High quality circuitry along with sophisticated quality control algorithms, are an additional key component of the system itself .

An improved knowledge on how the MS measures and stores the data is then crucial to tune the inversion parameters and to maximize the imaging capability of such a system.

5.6. NOISE LEVEL IN MS DATA

The MS system is designed in such a manner that dipole-dipole measurements with extreme values of the “n” factor can be collected in most of the surveys. Depending on the number of deployed units the “n” factor could be as high as several tens. The maximum “n” factor resulting by the MS geometry used in numerical simulations was equal to 45 (TX in 1.1-1.2 and RX in 16.2-16.3). Many authors (i.e. ***Loke, 2020***) recommend the use of a threshold “n” factor of 5 for dipole-dipole measurements. According to these authors the injected current, does not perturb the potential when the “n” factor is larger than the recommended threshold. The proposed threshold is not an absolute value but it is electronic- and site-dependent. In low-noise conditions the “n” factor could be raised.

A strict data quality control is implemented in the MS firmware and each data-point is stored with its own standard deviation (STDEV) on the measured potential expressed in Volts.

Careful analysis of resistivity measurements collected during a series of experimental field surveys showed marginal values of STDEV also in case of very high “n” factor. The threshold “n” factor for MS-DD arrays needs then to be properly assessed in order to carry out realistic simulations.

A specific field experiment was then designed to first guess the maximum “n” factor value for MS-DD arrays. The experiment was undertaken during a large-scale DERT survey in the Vajont valley (North-Eastern Italy) right on the top of the large 1963 landslide (***Bocchia et al., 2021***). The landslide filled the axial part of the old Vajont river valley. The morphology is more or less undulated with two major ridges forming as many counterscarps. The major lobe is cut by a narrow valley, whose slope is now reversed, known as the Massalezza ditch (**Fig. 41**).

The DERT survey (**Fig. 41**) was designed and realized right in this part of the old valley, using the MS system: the profile was laid down along an almost EW alignment, for a final overall length of almost 2.1 Km. A total of 8 MS transceivers, with a 25 m electrode spacing, were deployed in the field. The 8 units were then gathered in two blocks of 4 units each. The two blocks were progressively moved along the survey line and the entire profile was covered with 7 acquisition blocks (from b1 to

b7). 8 data loggers (DLs, namely VP523, VP524, VP422, VP193, VP140, VP234, VP258 and VP141) were added to the system in order to better comprehend data quality changes over varying TX-RX distances, especially in the case of multiple current dipoles. Run 4, between blocks 1-5, was selected for the experiment. Few transceivers were located on the bedrock westward to the western margin of the landslide (block 1) and the other MS units were located on the landslide body (block 5). In particular, the transmitters were located in b5. The DLs were put in b1, with an increasing distance from the injection block. The use of DLs was crucial in order to track differential potential variations continuously over time, and so infer MS system potentialities of distinguishing artificial signals respect to spontaneous potentials. The three different transmitter cases already presented were utilized, i.e. the single-transmitter mode (1TX), the double-transmitter mode (2TX) and the quadruple-transmitter mode (4TX).

A first important observation (regardless to the DLs) was about the measured voltage increase with the addition of TX dipoles, considering measurements occurred at the same distance of the TX-RX dipoles. This observation was possible by plotting the measured potentials in the three different runs (1TX, 2TX and 4TX) respect to the geometrical factor of each quadrupole (**Fig. 42**). In particular, the 1TX measurements showed a 107 mV average voltage, increased first at 119 mV in the 2TX case and to 176 mV in the 4TX one. Except for the general higher dispersion rate with the increment of the number of transmitting dipoles, this first numerical analysis gives very robust information on the effectiveness of multiple-transmission to increase the signal intensity.

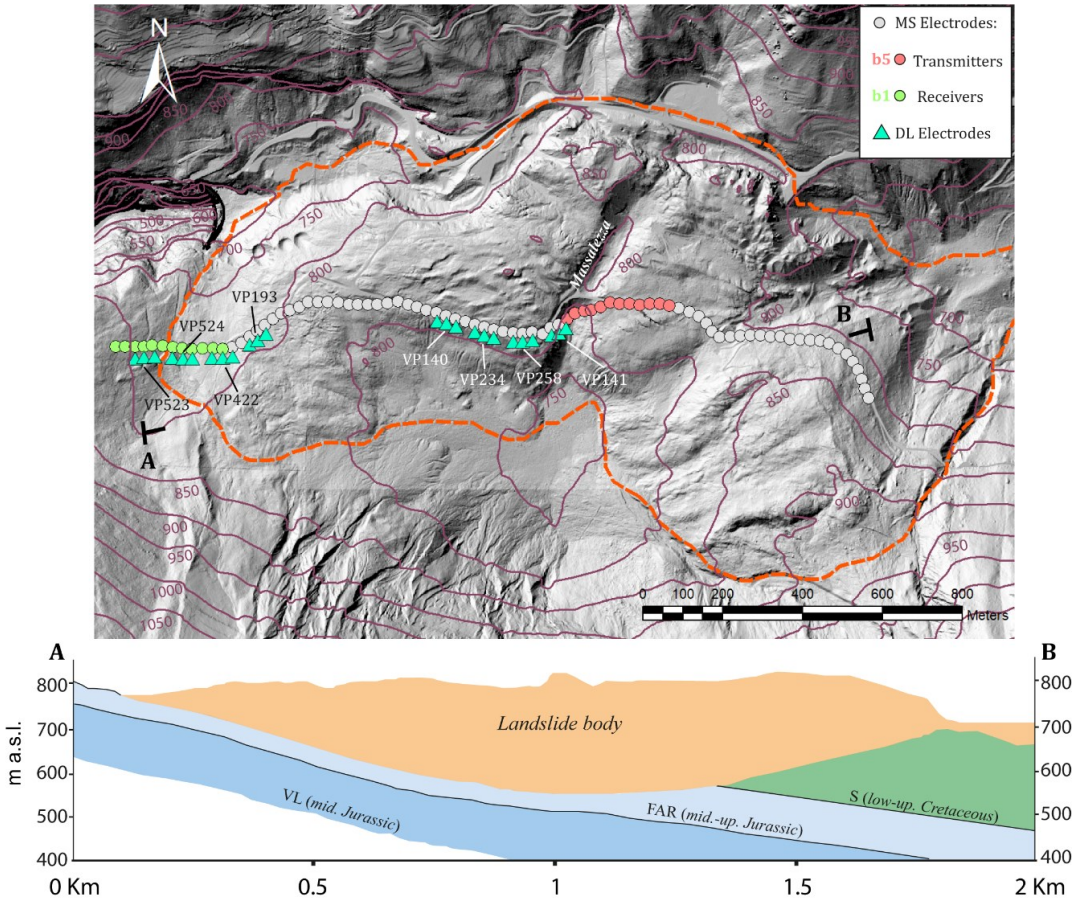

Figure 41: upper: MS data acquisition deployment; electrode positions are indicated with circles. Red and green circles indicate transmitters and receivers respectively (during run 4 of the experiment); lower: schematic geological cross section below the survey line (modified from Broili, 1967). VL: Vajont Limestone (ρ=15-18 KΩ·m); FAR: Fonzaso and Ammonitico Rosso Fms (ρ=0.5-1.1 KΩ·m); S: Soccher Fm (ρ=2.5-4.5 KΩ·m). Simplified from ***Bocchia et al., 2021****.*

The time series recorded by the DLs (**Fig. 43**) show how the 6-cycle squared waveform is clearly recognizable in the 4 inner units (VP141, VP234, VP140 and VP193) for the 1TX case. The artificial potential is 0.12-0.15 mV for the closest unit while it lowers down to to 0.05 mV for the farthest one. The artificial potential is too low (<0.05 mV) and noisy in the outer units (VP422, VP524 and VP523). In the 2TX case, the artificial potential is clearly visible also in the outer unit (i.e. VP422 in Figure 43). The values in the 2TX case are now comprised between 0.3 mV and 0.05 mV.

Lastly, in the quadruple-transmitter case (4TX), the totality of the DLs records the artificial potential, even though some curves are biased (Figure 43c). The measured potentials range from a maximum of 2.20 mV to a minimum of 0.75-0.80 mV.

In the analyzed data set, in single-transmitter mode (**Fig.44a**), the ratio between the average of the potentials measured at n=1 is equal to 55 times the average of the potentials measured at n = 6, in good agreement with Loke (2020) indications. Anyhow, it is worthwhile to notice how the measured potentials show a nice and sharp decreasing trend without the typical dispersion occurring in noisy data sets. The signal strength lowers below 1 mV starting from n=10 and just for a minimum number of data points. The curve describing the average voltage per each distance factor remains almost always above the 1 mV value. The recorded signals at n> 10 (i.e. with ratio higher than 300 times compared to measurements collected at n=1) appear to be still valid as it will be showed later in this section. The signal strength in multiple-transmitter mode increases significantly (**Fig. 44b**).

The ratio 2TX/1TX, for n=10 is equal to 2 while the ratio 4TX/1TX has a value larger than 10. These indications are just partly quantitative as there is not a consolidated way to calculate the distance factor N when using multiple transmitters. For the purpose of comparing the potentials, the distance factor for multiple transmitters was calculated averaging the maximum and minimum values.

In multiple-transmitter mode, the particular transmitting-receiving geometry experimented during the survey resulted particularly effective in stacking the electrical fields generated by the single transmitting dipole resulting in a better increase of the signal strength. The gathering of the available transceivers in two blocks comprised of four units each (in a sort of "super-transmitter" mode) significantly improved the signal intensity compared to previous MS surveys conducted with the fairly consolidated roll-along scheme. The modeled potentials, although slightly higher compared to the real potentials measured by the MS during the survey, somewhat follow a theoretical behavior (***La Brecque et al., 2013b***). The signal strength increases of 2.2 times doubling the transmitters from 1TX to 2TX in the farthermost units (dipole distance > 800 m) while in the inner units (dipole distance < 300 m) the expected signal strength, in 2TX mode, is more than 3 times the signal expected in 1TX mode (**Fig.44c**). The signal strength, further doubling the transmitters from 2TX to 4TX, increases of 5.5 times in the farthermost units (dipole distance > 800 m) while in the inner units (dipole distance < 300 m) the expected signal strength, in 4TX mode, is more than 10 times the signal expected in 1TX mode (**Fig. 44c**). The amplitude ratios of the real signals from single- to multiple-transmitters show comparable trends with the modeled signals. The signal strength increases about 2.4 times doubling the transmitters from 1TX to 2TX in the farthermost units (dipole distance > 800 m) while in the inner units (dipole distance < 300 m) the measured signal strength, in 2TX mode, is around 3 times the signal measured in 1TX mode (**Fig.44d**). The signal ratio, further doubling the transmitters from 2TX to 4TX, increases up to 10 times in the farthermost units (dipole distance > 800 m) while it grows up quickly, similarly to modeled data, in the inner units. The apparent scattering of the ratios visible in the distance interval comprised between 800 and 1200 m is probably related to geological reasons. The landslide edge is located right at the fifth dipole midpoint. In this point there is a sudden jump between the outcropping bedrock and the landslide body and, moreover, this contact is probably occurring along a vertical fault. The electrical field is, then, distorted both by topographical gradients

and by sudden lateral and vertical changes in subsurface resistivity. DOI and maximum sensitivity are just marginally affected by the use of multiple transmitters. The reduction in the DOI, that in the worst case reaches the value of 10% (switching from single-transmitter to four-transmitter mode), could be easily compensated moving forward the transmitting block and collecting just 2TX and 4TX data.

Analyzing numerically and visually these curves and the results obtained by plotting potential signals against the TX-RX distance (for both the two channel of each transceiver) (**Fig. 45**), an important generalization can be concluded: a potential of 0.02 mV can be identified as a primary threshold for data quality. Potential values lower respect to this have never been recognized as artificial signal. Even though this aspect is, for sure, somehow influenced by the geology of the site, it could be also generalized. This threshold could be used as a limit for filtering the MS data before carrying out the inversion. In this experiment the analysis was conducted entirely in TD but it is possible that the threshold could be further lowered filtering out the short-period noise in Frequency Domain (FD). The value of 0.02 mV is much lower as compared to the value of 0.1 mV that among field geophysicists could be considered as a realistic lower limit in various scenarios of electrical noise.

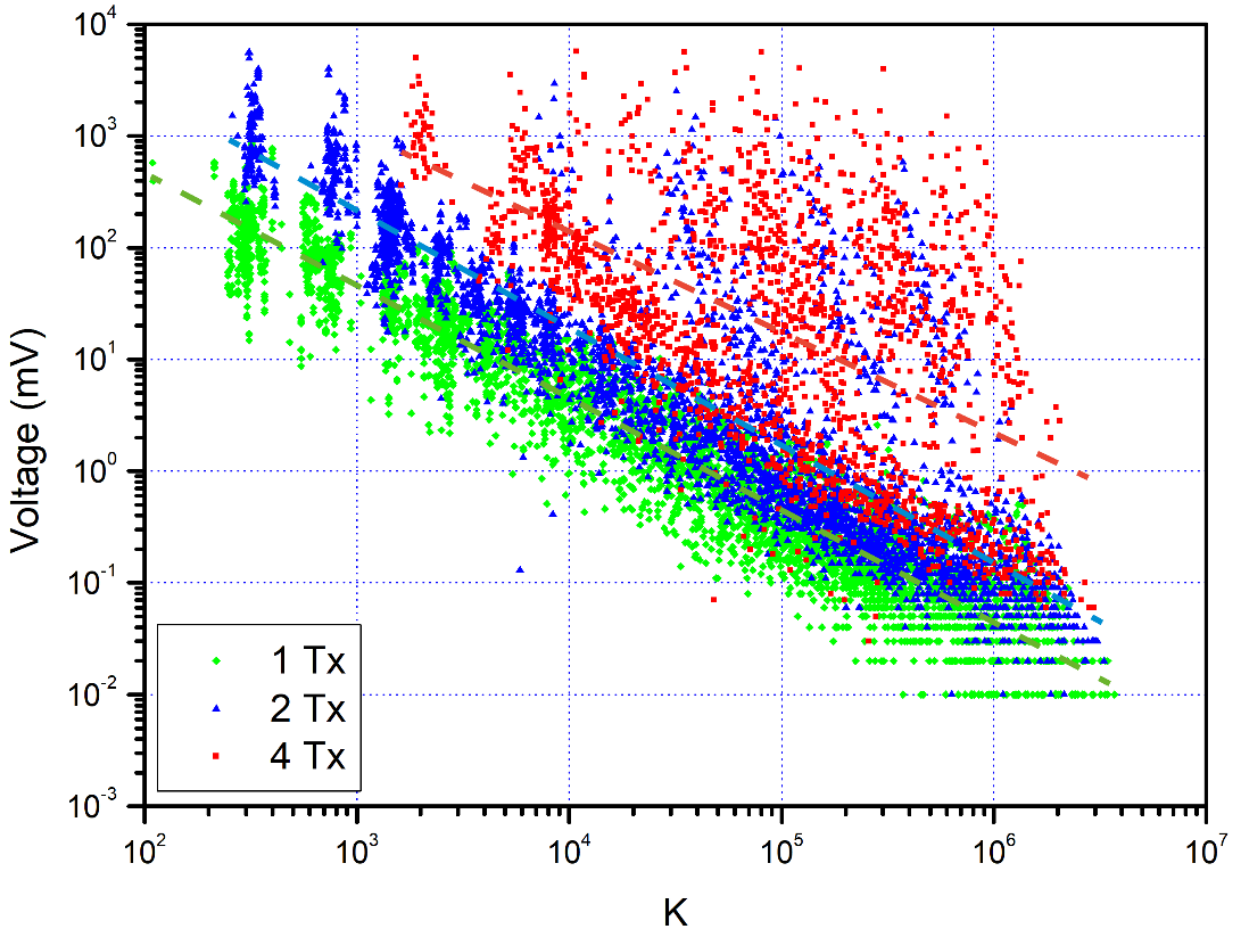

*Figure 42: Measured voltage (V) plotted versus geometric factor (K) in single- and multiple-transmitter modes (**Bocchia et al., 2021**).*

This information is crucial for a realistic forward modeling, resulting in a survey design taking full advantage of the MS potentials. Further implications are related to the tuning of inversion parameters.

In this sense, the modification regards the constant component of noise: by default (as already mentioned) this is set to 0.0001 Ω but, considering the one-order magnitude reduction of the lowest

measurable signal, this threshold can be quietly shut down to 0.00001 Ω. The new inversion parameters that will be used for MS simulations from this point of the work are summarized in the following table (**Tab. 6**).

Table 6: Inversion parameters to be used for inverting MS data.

Roughness (Ω)			Noise (Ω)	
Initial Roughness Factor		10	Percentage error term (%)	1
Multiplier for changing roughness factor		10	Data Constant error term (V/I)	0.00001
Constant Value for parameters weights	x	1		
	y	1		
	z	0.1		

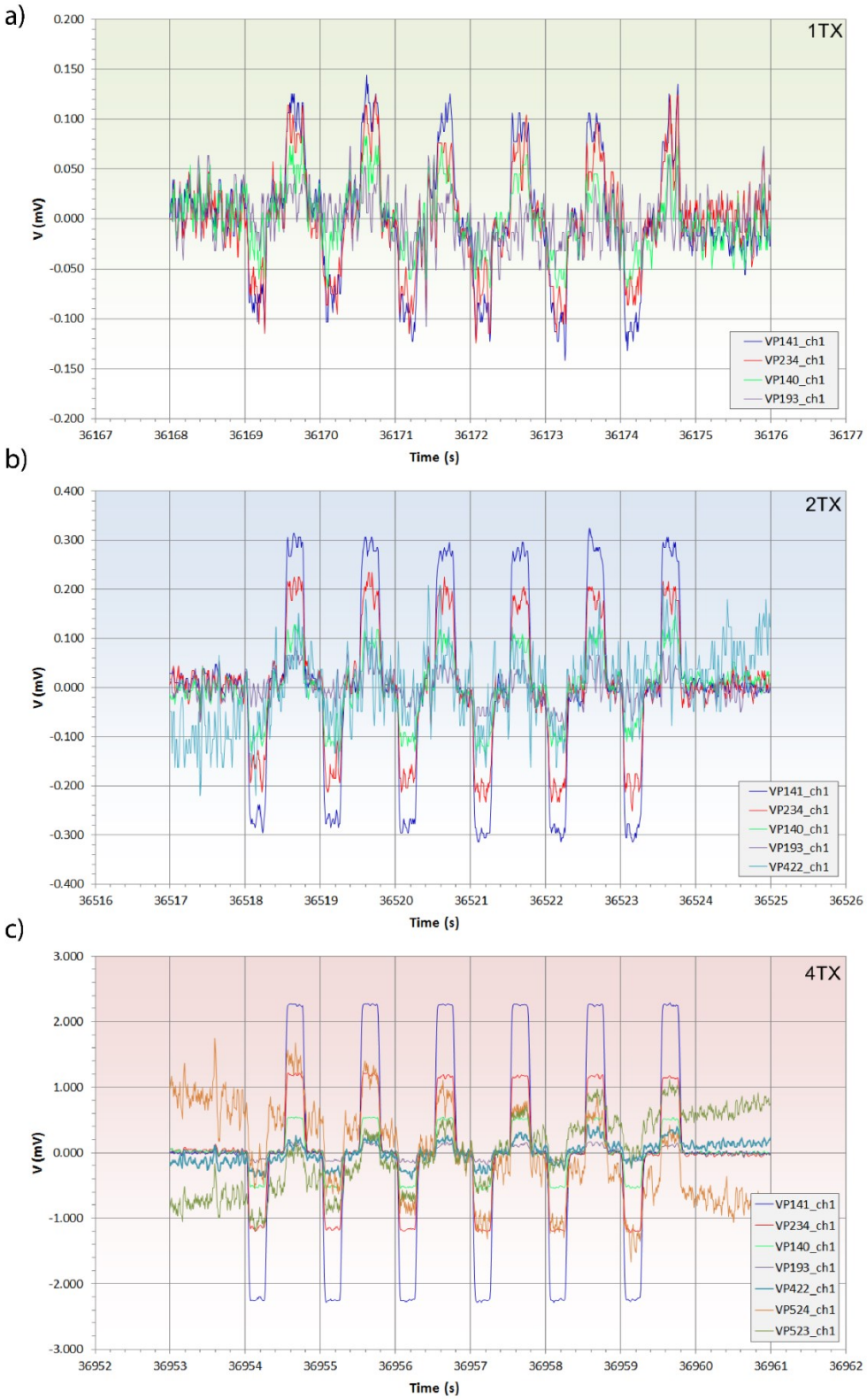

Figure 43: 6-peak wavelet recorded with the DLs in single- and multiple-transmitter mode at various distances; a) 1TX, single-transmitter: units VP141, VP234, VP140 and VP193; b) 2TX multiple-transmitter): units VP141, VP234, VP140, VP193 and VP244; c) 4TX multiple-transmitter: all the deployed units but VP254 that was malfunctioning; see text for details. From ***Bocchia et al., 2021****.*

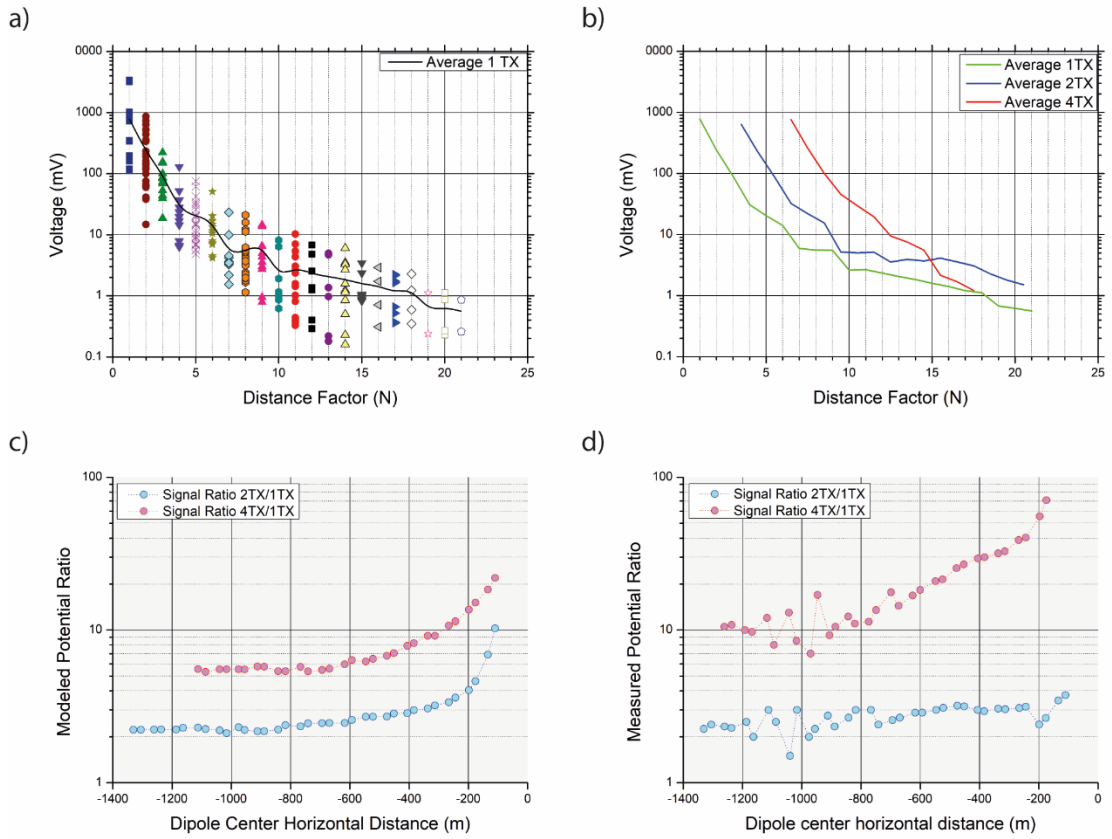

Figure 44: a) Potentials recorded in single-transmitter (1TX) mode plotted versus distance factor N. b) Curves describing the average of the potentials in 1TX, 2TX, and 4TX mode plotted versus distance factor N. c) – d) Potential ratio at increasing distance from the transmitter: c) signal ratio of the modeled potentials switching from single-transmitter (1TX) to multiple-transmitter mode (two transmitters: 2TX) and from single-transmitter (1TX) to multiple-transmitter mode (four transmitters: 4TX). d) Same as above but with measured potentials. Transceivers are located westwards of transmitting block b5 (from ***Bocchia et al., 2021****).*

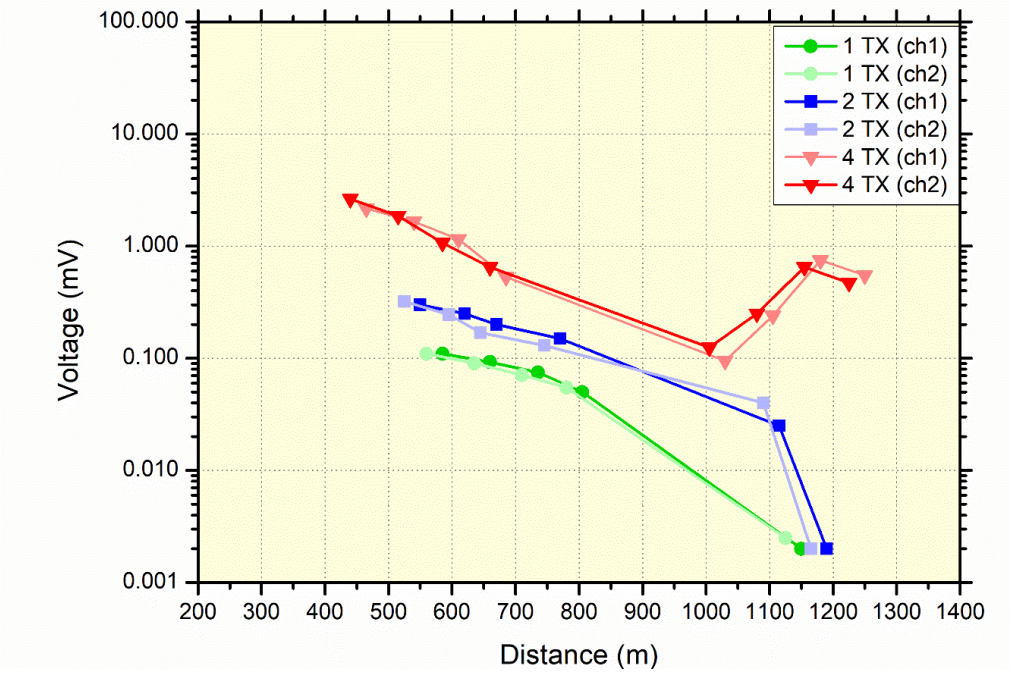

Figure 45: Plot of the voltages measured at the DLs versus transmitting-receiving distance for run R4 (blocks b2-b5); solid and light colors indicate channel #1 and channel #2 of each DL (from ***Bocchia et al., 2021****).*

6. NEAR-SURFACE TARGETS: MODELLING AND APPLICATIONS

Near surface targets are quite easy to model because of the large availability of a variety of data and also because most of the production surveys investigate the uppermost geological layers. River embankments have been selected as an example of near surface targets for two major reasons: the strategic importance of these artificial structures to prevent floods; the well know geophysical problems of properly "illuminating" targets located below a ridge or a mound.

6.1 LEVEES: DEFINITION

Levees (or dikes) are linear artificial structures used to protect people, building and infrastructures from floods. The transverse section of a levee (**Fig. 46a**) is essentially an earthen berm separating the river bed from the surrounding land (***Fauchard and Mèriaux, 2007***). Since their final goal is retaining a water volume, their main features must be at least two: 1) the mechanical resistance and 2) the watertightness (***Dezert et al., 2019***). These properties are determined by their mass and morphology but, more importantly, from their composition. The presence of heterogeneities is the main issue concerning levees. In some cases, their presence can lead to important breaching of the levee body. Four main mechanisms of rupture exist (***Fauchard and Mèriaux, 2007***) (**Fig. 46b-c-d-e**), namely a) the *overtopping*, i.e. the erosion of the surface of the dike, on the crest or on the external (land) side of the levee; b) the *external erosion*, i.e. the material removal caused by waves and/or currents; c) *internal erosion (or piping)*, i.e. the creation of tunnels through the structure caused an hydraulic gradient between the levee body and its foundation; and finally d) the *sliding of the slope*, i.e. the entire creep or slide of the dike caused by water saturation.

A valid methodology for mapping levee anomalies was proposed by some French authors, based on the combination of geophysics and geotechnical techniques (***Lino et al., 2000***; ***Mèriaux et al. 2004***). Further improvements and the introduction of new tools (***Fauchard and Mèriaux, 2007***), resulted in un updated procedure of diagnosis, based on a three-phase process (***Fauchard and Mèriaux, 2007; Royet, 2013***) involving:

1) research of indicators (preliminary study);

2) geophysical imaging of critical segments (e.g. ERT, EMI, GPR, Seismic, etc);

3) geotechnical testing (e.g. field and laboratory tests) and direct observations.

In particular, phase 2) (**Fig.47**) is composed by further 2 steps (***Royet, 2013***):

i) at first, a rapid and cost-effective survey is done, in order to get a global overview about the presence of levee heterogeneities. The state-of-art method for this phase could be EMI, Airborne EM or GPR;

ii) secondly, a detailed but time and cost-consuming survey is performed on anomalous spots. A technique with high resolving power (i.e. ERT) is generally preferred (local zoning).

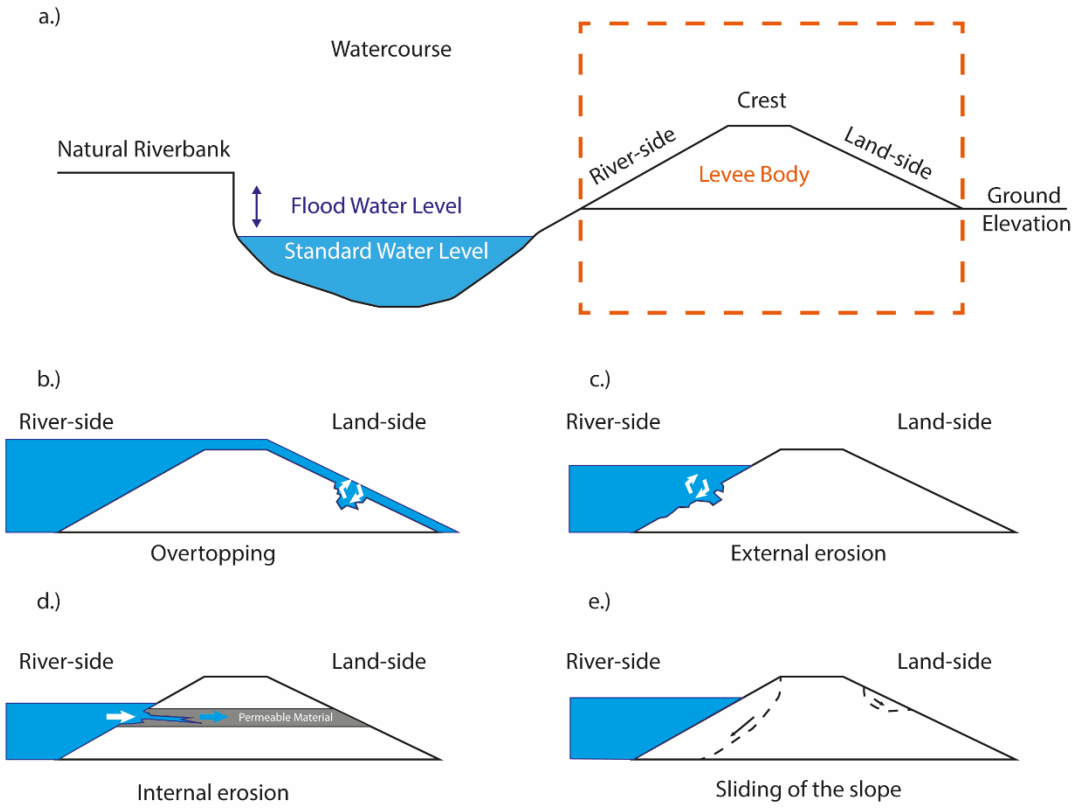

*Figure 46: a) Typical section of river levee and rupture mechanisms: b) overtopping; c) external erosion; d) internal erosion; e) collapse of internal/external slope (modified from **Fauchard and Mèriaux, 2007**).*

6.2 RESISTIVITY IMAGING OF LEVEES

The ERT method is probably the best selection choice for levee imaging (e.g. ***Sjodahl et al., 2008; Inazaki et al., 2011; Weller et al., 2014; Chambers et al., 2014; Jodry et al., 2017; Francese et al., 2018; Hojat et al., 2020***). In general the survey is carried out laying down the electrodes along simple profiles parallel or traverse with respect the levee axis. This deployment enables a quick and effective electrode deployment. Several authors (e.g. ***Bievre et al., 2018***) indicate how collecting data in 2D could lead to the generation of inversion artifacts in case the 3D morphology is not properly modeled. Other authors (e.g. ***Jodry et al., 2017***) suggested the use of 3D acquisition geometry. A full 3D imaging approach is time consuming and not prone to a quick response (***Jodry et al., 2017***). Some authors have proposed further options like the survey optimization for the levee context (***Palma Lopes et al., 2012***) or designing a compromise between full 2D and full 3D acquisition schemes (***Jodry et al., 2017***). Other authors have already proposed a real monitoring and alert system ERT-base to mitigate the flood risks in some critical areas (***Arosio et al., 2017***).

The adaptation of the MS system to these problems could result in the optimization of both the cost-effectiveness and the resolution capability.

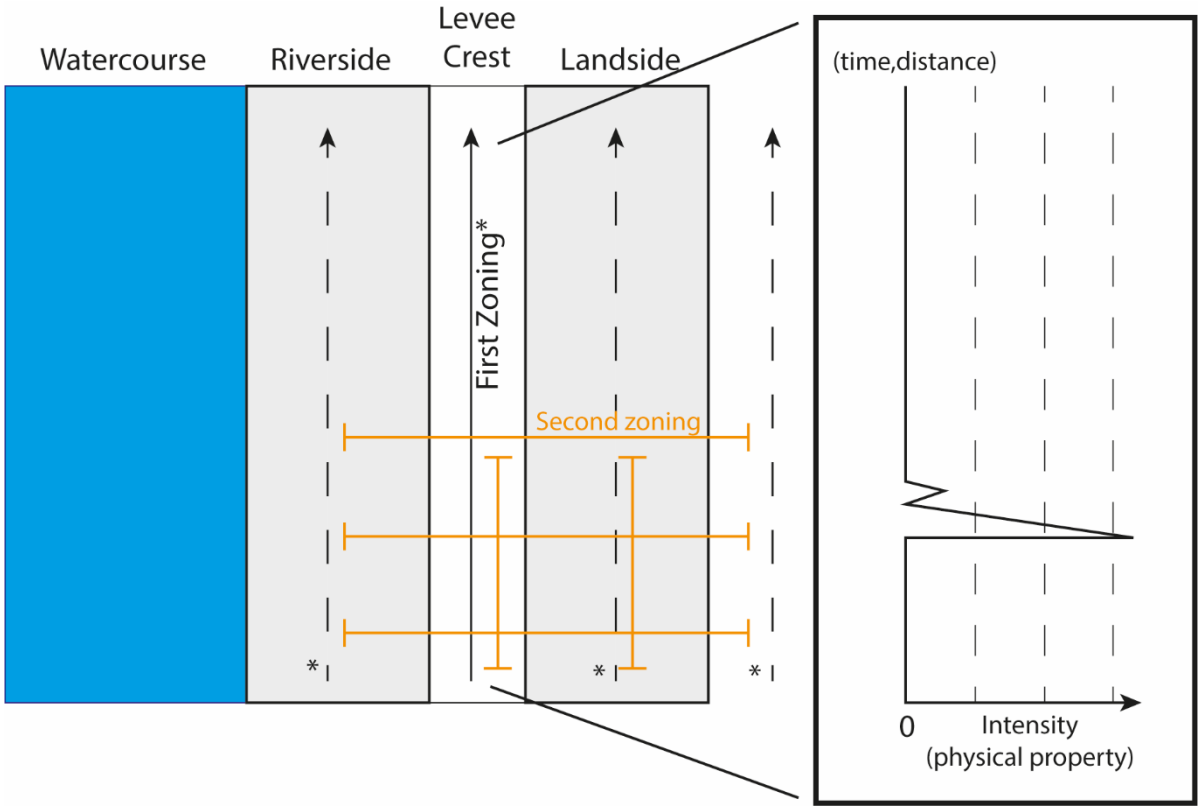

Figure 47: schematic procedure for geophysical diagnosis of earthen levees. A first and faster zoning is applied to locate heterogeneities within the levee and a second and more accurate zoning is applied on the anomalous spots to better define the physical parameters of a specific section.

6.3 GENERAL PROCEDURE

The calculation of the apparent resistivity in case of 3D morphology introduces an additional degree of freedom as the electrodes could be organized in almost infinite combinations.

6.3.1 SURFACE MODELLING

A levee is represented by a typical "hump-shape" structure raising up from an alluvial plain. There is no design standard depending on the geographical location and on the expected flood flow. The trapezoidal geometry is widespread with a typical height/base ratio. Lateral banquettes could be also present.

A simple geometry was assumed for modeling purposes (**Fig.48**). The modeled levee is comprised of a crest and two slopes facing the country and the river respectively. The general rule of B/H = 3/1 (**Sharp, 2013**) was used. Assuming a base B of 21 m the resulting height H is equal to 7 m.

The levee spans over an area of 200 m (longitudinal) by 100 m (transversal) in order to accommodate the background area of the forward modeling mesh. The levee surface was generated using four major breaklines (crest and toe) plus a series of regularly spaced xyz points (**Fig. 48a**). Elevation for both the riverside and the countryside was set to 0.0 m.

An excavated riverbed below elevation 0.0 was not considered.

The final levee model resulted comprised of about 1300 xyz points. This data-point density was found to be a good compromise between the resolution of the topographic model and a very large mesh that could slow down the calculations.

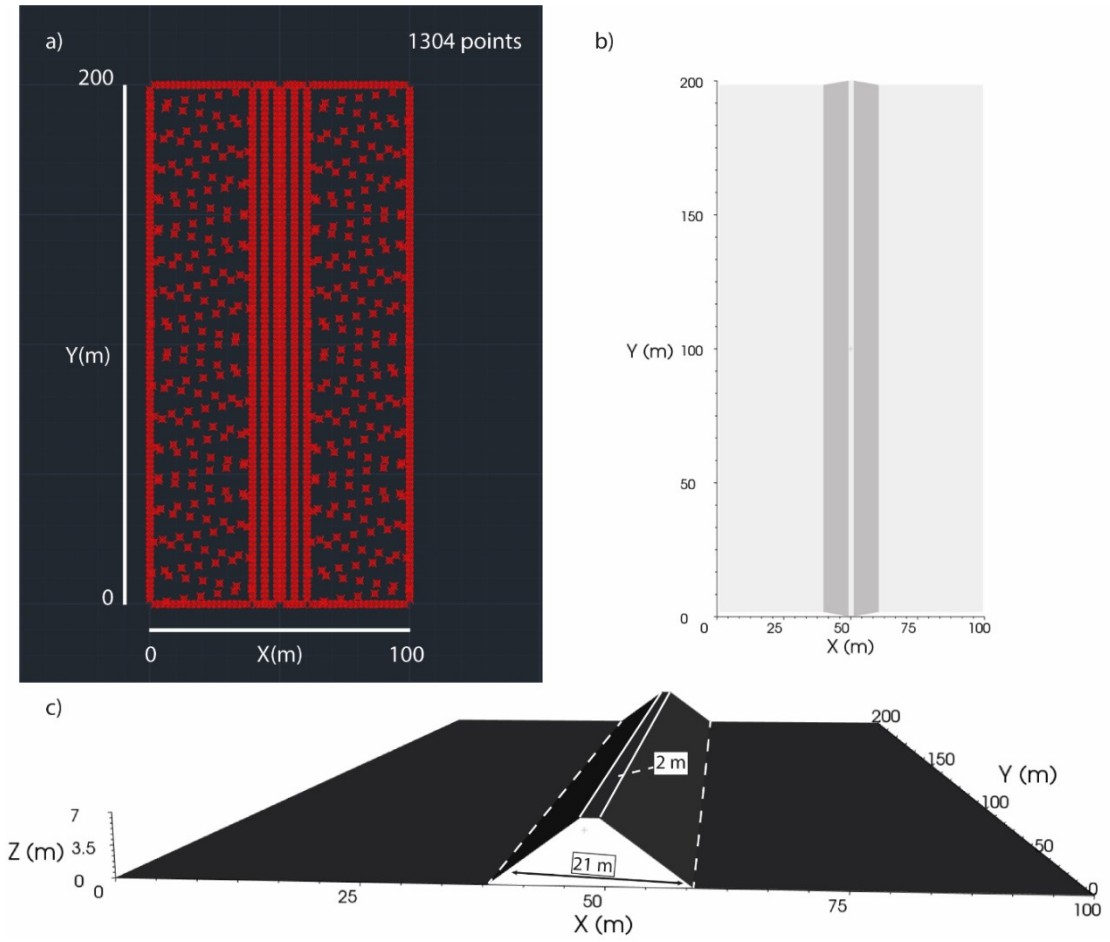

Figure 48: Model of the levee. a) scattered xyz data-points b) plain view; c) 3D view.

6.3.2 ELECTRODE ARRAYS AND LAYOUTS

Three different layouts (**Tab. 7**), comprised of 48 electrodes each, were considered for the numerical simulations:

- transverse profile (2D);

- double profile (3D);

- grid (3D).

The transverse profile was laid down perpendicular to the levee axis, shifted towards the countryside (**Fig. 49a**). The electrode spacing was set to 1.0 m.

The double profile is comprised of two parallel lines with 24 electrodes each. The lines were orientated parallel to the levee axis with no shifting in the +/- Y direction (**Fig.49b**). The first line

was laid down approximately on the levee crest while the second line was located nearby the levee toe. The electrode spacing was set to 2.0 m to match the DOI of the transverse profile. This deployment was chosen because in practical geophysics it is very common for 3D levee imaging (e.g. **Jodry et al., 2017**).

The grid is comprised of 8 lines with 6 electrodes each (corresponding to 2 MS inline units)(**Fig. 49c**). Electrodes were equally spaced of 4.0 m inline and crossline. Complicated 3D acquisition geometry, although described in literature (i.e. ***Chambers et al., 2014***) and sometimes crucial for resolving specific subsurface feature, are not common because of the logistics and of the time required to collect the data. Additional problems could be due to severe coupling effects in case of multiple cables laid down close together. The grid layout was modeled just with the MS-DD array. This specific geometry was designed in order to maximize the potentialities of the multi-transmitting technology.

The other line parameters are reported in **table 7**.

The three layouts, each one with its own electrode spacing, resulted in default meshes with different aperture. The mesh was set to 0.5 m (in xyz) to make resolution comparable. All the mesh parameters are visible in **table 8**.

The DOI for the modeled layouts is 6.4 m for the DD array and 10.0 m (1TX), 9.7 m (2TX) and 8.8 (4TX) m for the MS-DD arrays.

The DD and MS-DD sequences for the transverse profile layout were the same used for base models (see Chapter 4). Also the DD sequence for the double profile layout was recreated using values of "a" and "n" already used for the base models (see Chapter 4). Cross-cable transmissions were added to the sequence resulting in a total of 1084 measurements distributed below and in between the two lines (**Fig. 50**).

The MS-DD sequence for the double profile layout (**Fig. 51**) used all the possible combinations of single and multiple transmitters (1TX, 2TX and 4TX) similarly to the sequence used for base models but for the cross-cable transmissions. Nevertheless, new combinations of transmitters were possible: particularly, the 1.2 TX and the 2.2 TX were tested. These two new configurations introduced the novel concept of multiple simultaneous cross-cable transmitters (not possible with traditional systems). The 1.2TX means a 2 TX configuration, with one transmitter on line 1 and a second transmitter on line 2. The 2.2 TX means a 4TX configuration, with two transmitters on line 1 and two other transmitters on line 2. The number of measurements for these new arrays is 560 data-points for the 1.2TX array and 420 data-points for the 2.2TX. In order to keep naming consistent the convention since this point forward is:

1.1TX = 1TX;

2.1TX = 2TX;

4.1.TX = 4TX.

The grid layout (**Fig. 52**) was designed for testing just the MS-DD array. This layout was not really suitable for a traditional DD array as it mixes inline and equatorial dipoles; its DOI is very low limiting the "n" factor to the value of 5. This layout was designed to take full advantage of the MS, as it enables maximum flexibility in selecting TXs: for this study, six different combinations were tested, but many more were actually possible. The three original deployments were not fully

realizable: the 4.1TX, for example, was no longer possible, because four in-line boxes were necessary. At the same time, a 1.4TX acquisition sequence was achievable, since the high combinations number. The selected arrays were: 1.1TX, 1.2TX, 1.4TX, 1.8TX, 2.1TX, and 2.2 TX, using the same logic of the double profile layout.

Table 7: summary of the acquisition parameters for the three layouts.

Geometry	Array Type	Number of lines	Electrodes per line	Electrode spacings	Line Spacings	N inline transmitters	N offline transmitters	Number of measurements	DOI
Traverse profile (2D)	DD	1	48	1 m	-	1	-	945	-6.4 m
	MS DD					1, 2, 4	-	600 (1TX), 1050 (2TX), 780 (4TX)	-10 m (1TX), -9.7 m(2TX), -7.5 m (4TX)
Double profile (3D)	DD	2	24	2 m	~10 m	1	-	1084	-7.2 m
	MS DD					1, 2, 4	2	600 (1.1TX), 560 (1.2TX), 980 (2.1TX), 420 (2.2TX), 600 (4.1TX)	-9.2 m (1.1TX), -9.4 m (1.2TX), -8.1 m (2.1TX), -8.3 m (2.2 TX), -5.82 m (4.1TX)
Grid (3D)	MS DD	8	6	4 m	4 m	1, 2	8	600 (1.1TX), 980 (1.2TX), 600 (1.4TX), 80 (1.8 TX), 560 (2.1TX), 420 (2.2TX)	-15.2 m (1.1TX), -13.3 m (1.2TX), -10.2 m (1.4TX), -2.1 m (1.8TX), -10.3 m (2.1TX), -9.71 m (2.2TX)

Arrays 1.4TX and 1.8TX are of particularly interest because the signal intensity is expected to grow. Unfortunately there is inverse proportionality between the number of transmitters and the number of resulting data-points. The number of data-points for the 1.8TX array is just 80. Counter wise the 1TX mode and 1.2/2.2TX modes result in a higher DOI with "dense" datasets. The reassuming features of the previous arrays are reported in **table 7**.

6.3.3 REFERENCE MODELS

The three-strata-like model, with a thin resistor in a conductive background, was selected for the numerical simulation. This case represents the typical levee hazard when water seeps throughout the pervious layer during floods.

This resistive target anomaly was modeled with a thickness of 2.0 m (along the Z axis), with a quasi-infinite length in the +/-X direction and finally with a length of 20 m in the +/-Y direction.

The objective of this group of simulations was to gain insight on the capability of the different arrays to properly image the resistive body. The countryside was assigned the reference elevation of 0 m.

Three target depths have been modeled (**Fig.53**):

I - top anomaly: from 4 m to 6 m above countryside;

II – body anomaly: from 1 m to 3 m above countryside;

III - sub-base anomaly: from - 2 m to countryside level.

These depth ranges were not selected randomly, but they represent specific hazard scenarios: top failure; body failure; seepage underneath the levee base.

Table 8: mesh parameters for the three layouts. BR: background region; FR: foreground region.

	X	Y	Z	TOTAL
Traverse				
Min (m)	42	99	0	-
Max (m)	86.7	101	-7.5	-
Size (m)	0.5	0.5	0.5	-
BR pads	1 2 4 8 16 24 32 40 48 56 64	1 2 4 8 16 24 32 40 48 56 64	1 2 4 8 16 24 32 40 48 56 64	-
FR cells	113	27	27	82377
Double profile				
Min (m)	48.2	78	-6	-
Max (m)	58	124	2.8	-
Size (m)	0.5	0.5	0.5	-
BR pads	1 2 4 8 16 24 32 40 48 56 64	1 2 4 8 16 24 32 40 48 56 64	1 2 4 8 16 24 32 40 48 56 64	-
FR cells	55	115	28	148350
Grid				
Min (m)	43	86	-5.7	-
Max (m)	63	114	1.9	-
Size (m)	0.5	0.5	0.5	-
BR pads	1 2 4 8 16 24 32 40 48 56 64	1 2 4 8 16 24 32 40 48 56 64	1 2 4 8 16 24 32 40 48 56 64	-
FR cells	63	79	27	134379

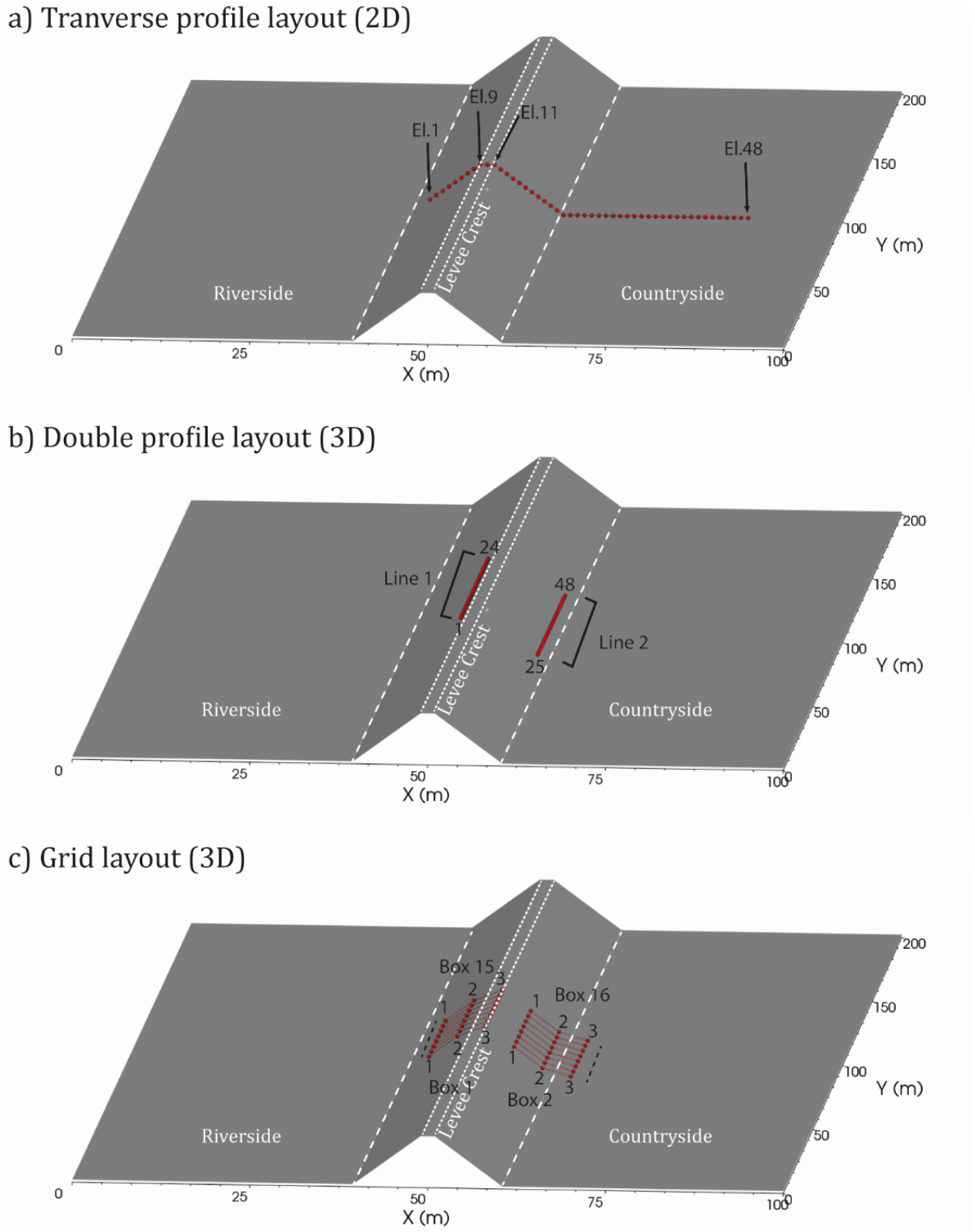

Figure 49: Electrode layouts.

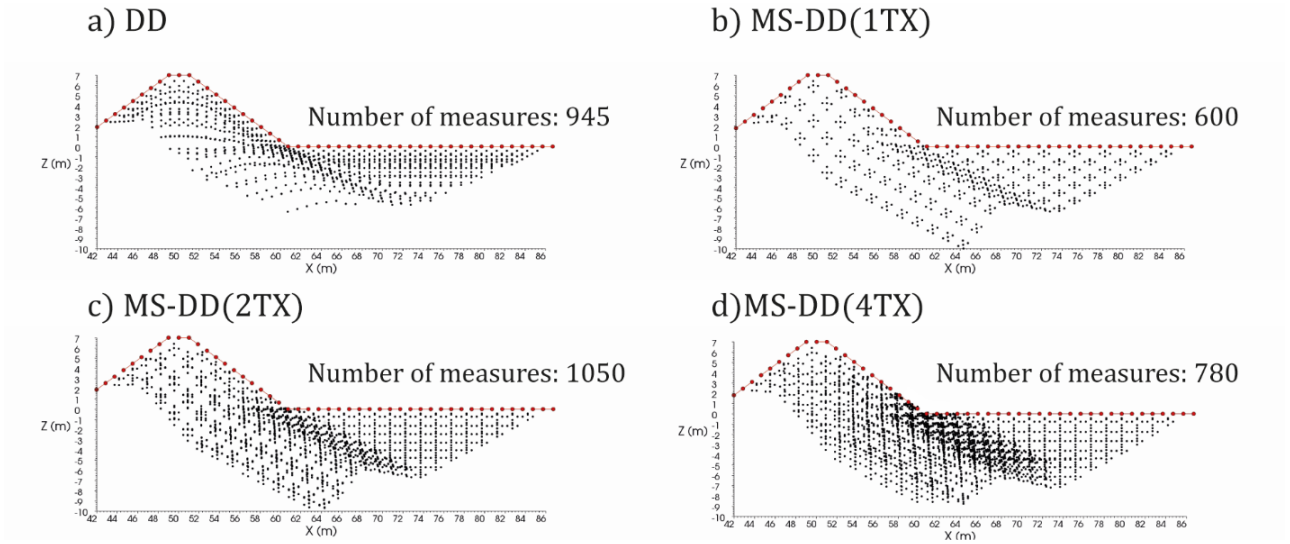

Figure 50: pseudo-plots of resistivity measurements for the transverse profile layout. a) DD, b) MS-DD (1TX), c) MS-DD (2TX), d) MS-DD (4TX). It is worthwhile to notice the irregularity of the data-point distribution.

6.4 NUMERICAL SIMULATIONS RESULTS

Simulation results are described ordered by layout.

6.4.1 TRAVERSE PROFILE (2D)

The top resistive anomaly (case I) is more or less resolved by the totality of the tested arrays (**Fig. 54, a1-b1-c1-d1**). The average misfit of the inversion process is about 7.5 %.

The DD array, in the target depth, images a 30 Ω·m layer below the levee crest while on the sides this layer has two nuclei with a resistivity of approximately 100 Ω·m. The layer appears slightly curved because of topography and it is just thicker than reality.

The MS-DD 1TX and 4TX arrays image a similar resistivity distribution in the target depth. The mean value is about 40 Ω·m with side lobes exhibiting a resistivity of approximately 100 Ω·m.

The MS-DD 2TX array poorly resolves both the target depth and its resistivity. The mean value is about 15-20 Ω·m with side lobes exhibiting a resistivity of approximately 40-50 Ω·m.

The body resistive anomaly (case II) is resolved differently by the tested arrays (**Fig. 54, a2-b2-c2-d2**).

The DD array, in the target depth, images a slightly curved layer, influenced by topography, with a central resistivity of 35-40 Ω·m. Resistivity grows laterally on symmetric side lobes beyond 100 Ω·m.

The response of the various MS-DD arrays is pretty similar. The resistive layer is properly imaged in the target depth with values increasing from the center to the sides. The layer geometry is better defined compared to the DD array with respect to both thickness and lateral continuity. The 2TX response is the most effective with a resistivity ranging from 25-30 Ω·m in the layer center to values of approximately 100 Ω·m on the sides. The layer thickness is overestimated.

The sub-base resistive anomaly (case III) shows a very similar reconstruction in the tested arrays (**Fig. 54, a3-b3-c3-d3**). The resistive layer is only resolved in the outer portion of the levee.

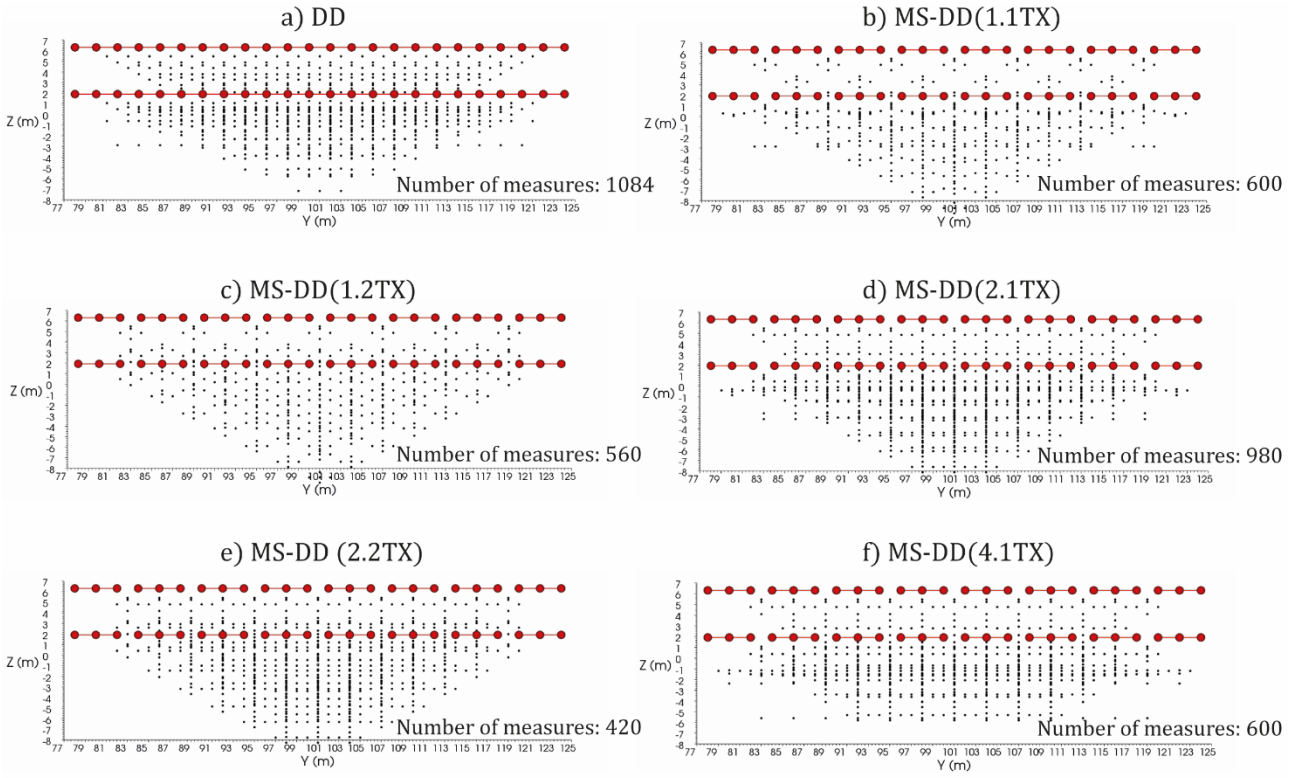

Figure 51: pseudo-plots of resistivity measurements for the double profile layout. a) DD, b) MS-DD (1.1TX), c) MS-DD (1.2TX), d) MS-DD (2.1TX), e) MS-DD (2.2TX), f) MS-DD (4.1TX).

The DD array, at the target depth, images laterally continuous resistive body. This body is characterized by an overall resistivity (90-100 Ω·m) fitting the reference model.

The MS-DD, at the same depth, images smaller lenticular body exhibiting a lower mean resistivity (~60 Ω·m) badly fitting the reference model.

These peculiar responses have been already discussed in chapter 6. The tested arrays perform poorly while attempting to image resistive targets located in depth right below the levee crest. Conversely the fit on the background resistivity is relatively good.

6.4.2 DOUBLE PROFILE (3D)

The top resistive anomaly (I) is well resolved by all the tested arrays (**Fig. 55, a1-b1-c1-d1-e1-f1**) while the misfit on both the target and the background resistivity is array-dependent.

The anomaly is reconstructed similarly for the 1.1TX and the 4.1TX, with high resistivity nuclei (~100 Ω·m) nearby the dike crest. In these two arrays, and for the 2.1TX, the anomaly shows also a more persistent lateral continuity respect to the other three cases, with a higher background resistivity than reference one (30-40 Ω·m). This first group of arrays also shows a similar reconstruction for the remnant portion of the levee, with a background value (15-20 Ω·m) slightly higher compared to the reference model.

On the other hand, for the DD, the 1.2TX and the 2.2TX, the anomaly shows a lower inverted resistivity (40-60 Ω·m), and the transition to the background value (10 Ω·m) is sharply imaged. The anomaly clearly defined also along the +/- Y direction by the DD and by the MS-DD 1.1TX arrays. Increasing the inline transmitter results in blurring (particularly evident in the 4.1TX array) the base of the target anomaly. Increasing the cross-line transmitters results in a better definition of the target anomaly thickness.

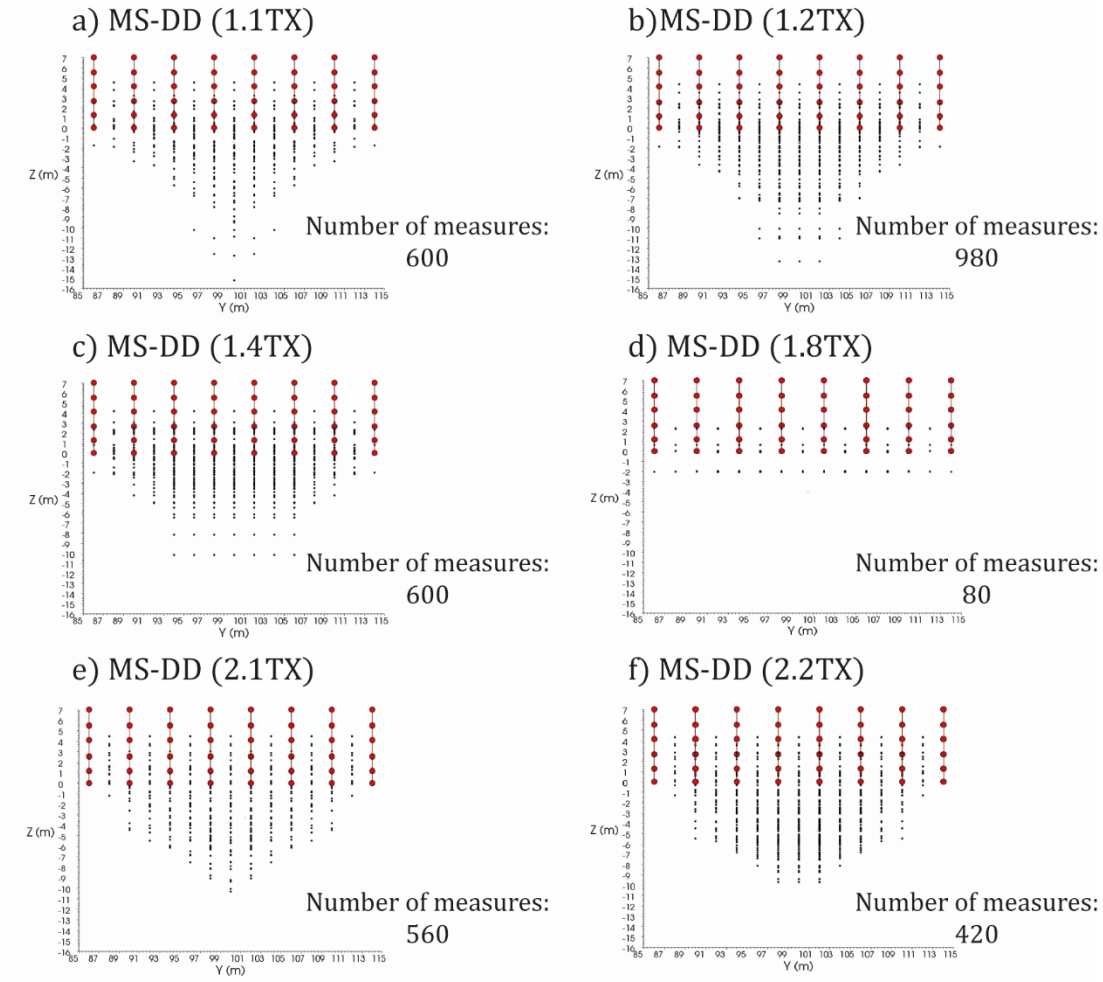

Figure 52: pseudo-plots of resistivity measurements for the grid layout. a) DD, b), MS-DD (1.2TX), MS-DD (1.4TX), MS-DD (1.8TX), MS-DD (2.1TX), MS-DD (2.2TX).

The body resistive anomaly (II) is probably the most variable in terms of inversion results (**Fig. 55, a2-b2-c2-d2-e2-f2**). The 1.2TX and the 2.1TX arrays result in an almost total loss of resolving power below the central portion of the levee.

The DD array is effective in imaging the thickness (slightly overestimated in the middle) and the lateral extension of the target anomaly. The misfit on the target resistivity is lower than 50% while there is a perfect fit to the background resistivity.

The 1.1TX, 2.1TX and 4.1TX arrays show similar responses. The target anomaly is imaged although not fully resolved. In the 4.1TX array the target layer thickness is overestimated. In the +/-Y direction the target anomaly is better resolved by the DD array although the thickness is overestimated. The misfit on the target anomaly is 55-60% for the 1.1TX and 1.2TX arrays while it is higher than 65% for the 4.1TX array. In the 1.2TX image the there is an almost perfect resistivity fit (>95%) in the vicinity of the base electrodes. The misfit on the background resistivity, below the target anomaly, is pretty high (85-90%). The target anomaly is just barely detected in the 1.2TX and 2.2TX arrays.

The sub-base resistive anomaly (case III) is similarly imaged by the different arrays even though with different degrees of resolution (**Fig. 55, a3-b3-c3-d3-e3-f3**).

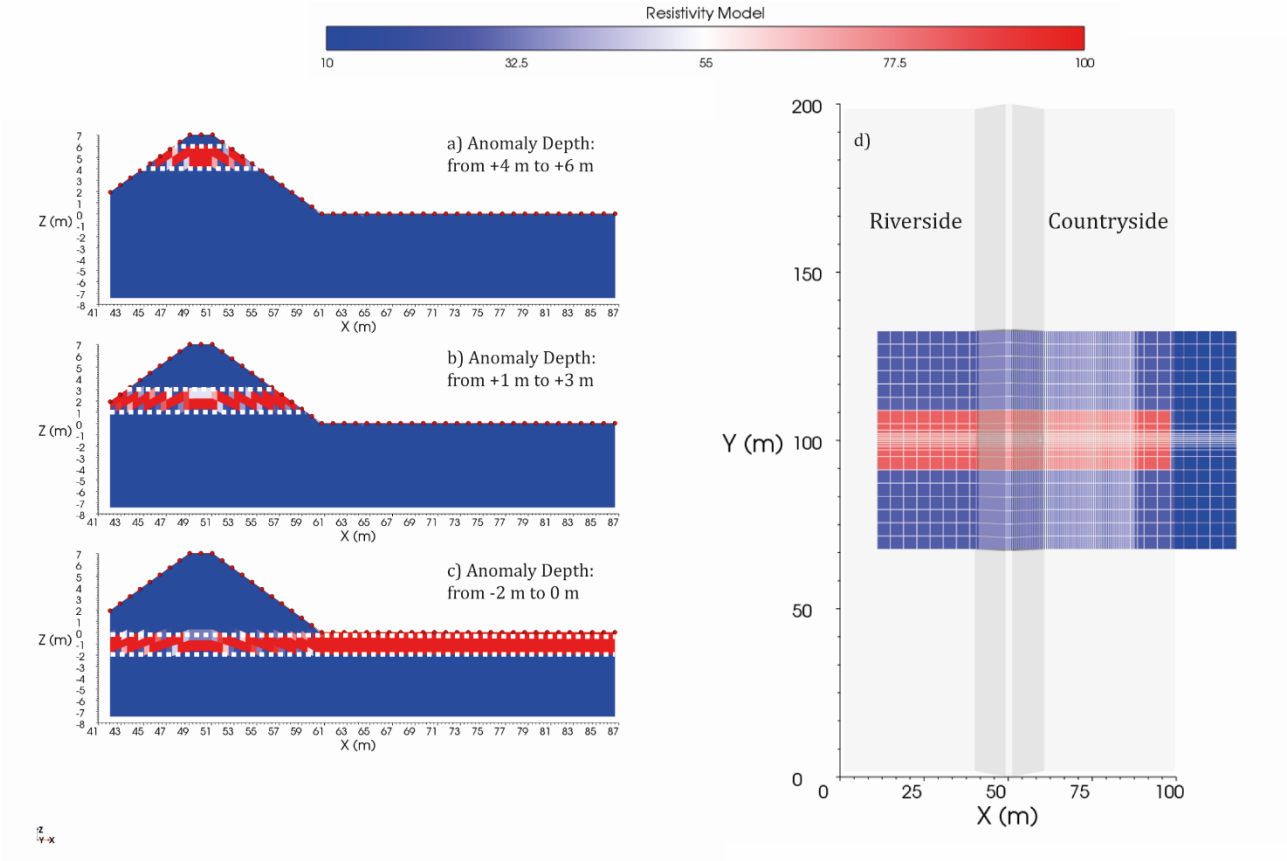

Figure 53: reference resistivity models used for the numerical simulations: a) top anomaly, b) body anomaly, c) sub-base anomaly, View of the anomaly in the XY plane.

The DD array poorly images the target layer in the inner zone of the levee. In the same zone the misfit on the target resistivity is pretty high (>65%). The response of the 1.1TX and 2.1TX is somewhat similar but with a better reconstruction of the continuity of the target anomaly in the inner zone of the levee. The misfit on the target resistivity for the 1.1TX and 1.2TX arrays is approximately 65-70%.

Results from the 4.1TX are still similar but for an improved recovering of the background resistivity.

Inversions from 1.2TX and 2.2TX arrays are particularly effective as for the horizontal and vertical imaging of the target anomaly. Although the geometry of the anomaly is clearly defined the misfit is very high and larger than 80%.

The target anomaly along the +/- Y is resolved by the totality of the tested arrays even though the performance of the 2.1TX and the 4.1TX arrays is affected by numerical noise. Results from arrays 1.2TX and 2.2TX are very good as for the reconstruction of the target anomaly geometry but the misfit on the target resistivity is particularly high. The 4.1TX array response is also affected by numerical noise.

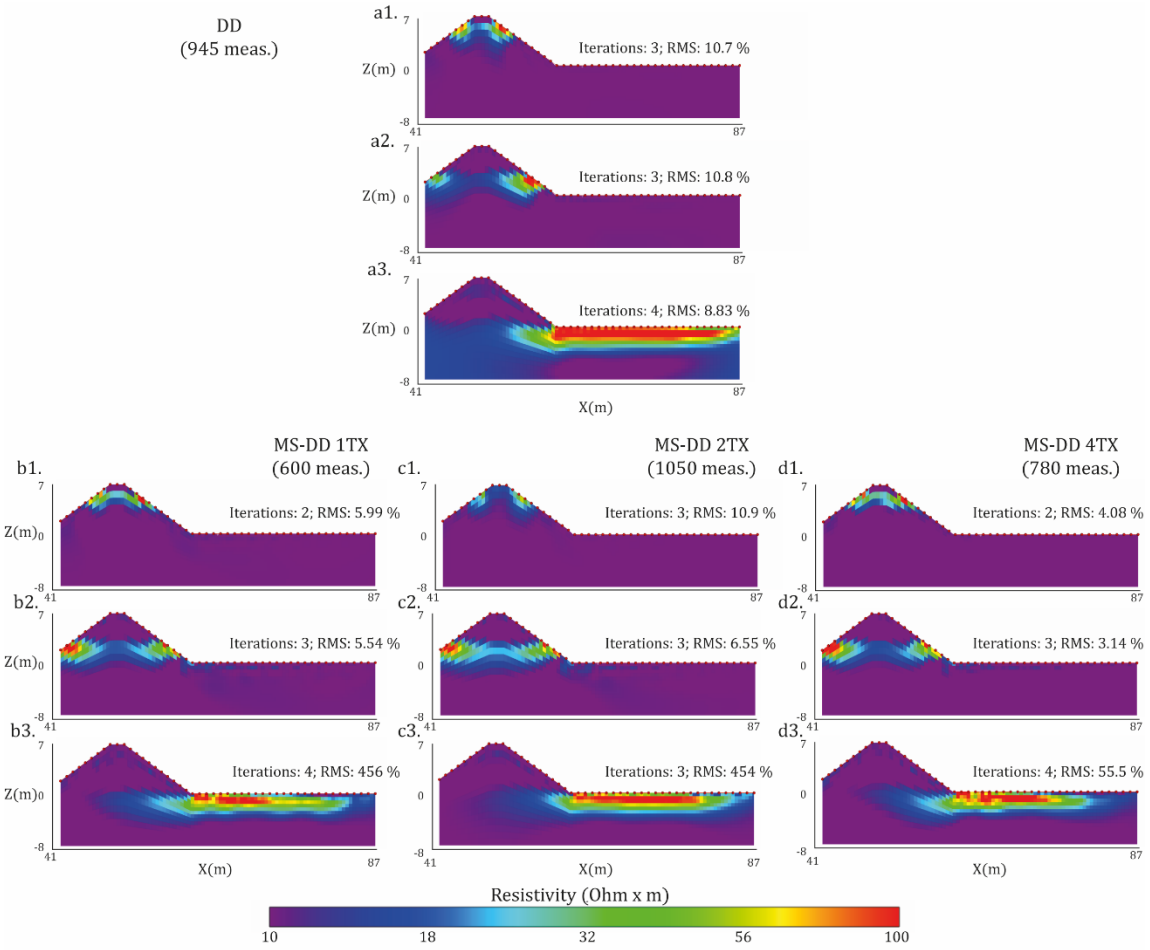

Figure 54: inversion results for the transverse profile. a) DD array: a1 top anomaly; a2 body anomaly; a3 sub-base anomaly. b) MS-DD (1TX) array: b1 top anomaly; b2 body anomaly; b3 sub-base anomaly. c) MS-DD (2TX) array: c1 top anomaly; c2 body anomaly; c3 sub-base anomaly. d) MS-DD (4TX) array: d1 top anomaly; d2 body anomaly; d3 sub-base anomaly.

6.4.3 GRID (3D)

In the top resistive anomaly (case I) is clearly detected by almost all the tested arrays excluding 1.8TX (**Fig. 56, a1-b2-c2-d2-e2-f2**).

The response of 1.1TX and of 1.4TX arrays is similar. The two arrays imaged a curved anomaly whose thickness matches the target anomaly. The misfit is about 60% for the 1.1TX array while it is higher than 70% for the 1.4TX array. The 1.2TX, 2.1TX and 2.2TX arrays returned an improved image with a misfit on the target anomaly of 50-55%.

Numerical artifacts are also visible in the 1.2TX inversion although less evident. The 1.8TX inversion is definitely poor and the target anomaly is just barely imaged. The target anomaly along the +/- Y is imaged by the totality of the tested arrays even but the 1.8TX array.

The body resistive anomaly (case II) has been better imaged using inline transmitters (**Fig. 56, a2-b2-c2-d2-e2-f2**).

Arrays 1.1TX, 1.2TX and 1.4TX effectively outline the target anomaly with a maximum misfit on the target resistivity of about 50% (a little bit higher for the 1.4TX array). A partial distortion of the target anomaly that appears curved is probably due to the harsh topography.

Array 1.8TX is still capable of detecting the target anomaly but it is not resolved and the misfit on the target resistivity is larger than 75%. The fit is higher and the target resistivity is almost matched at the countryside toe of the levee.

Arrays 2.1TX and 2.2TX miss the target anomaly and they fit (>95%) just the background resistivity. Target anomaly is just partly imaged on the outer flank of the levee although with a misfit larger than 80%..

In the sub-base resistive anomaly (case III), arrays 1.1TX, 1.2TX, 2.1TX and 2.2TX return the better images (**Fig. 56, a3-b3-c3-d3-e3-f3**). Array 1.1TX sharply outlines the lateral continuity of the target anomaly with an improved fit (about 50%) nearby the levee toe (hence nearby the electrodes). Array 1.2TX performs similarly even though the target anomaly looses continuity right below the levee crest.

Crossline transmitters arrays 2.1TX and 2.2TX are very effective in outlining the target anomaly in this deep scenario. The misfit on the target resistivity is about 65-70 %. The target anomaly along the +/- Y is imaged by most of the arrays but it appears shorter than reality. The target anomaly is barely visible in the 1.4TX response while it is totally missed by the 1.8TX response.

6.5 CASE STUDY: BRENTA RIVER

6.5.1 GENERAL SETTINGS

DD and MS-DD arrays were tested on the Brenta river embankments, nearby Venice. The site was selected because of the abundance of information about surface geology and stratigraphy of the levees. The levee similarity with respect to numerical simulations was also considered.

The investigated segment is historically critical and water filtration underneath the levee occurs during severe floods. This area of the Venetian plain is comprised of silty sands and silts (***Bondesan et al., 2011***) with the presence of several sandy paleochannels. Water seeping at study site is to be correlated with the presence of a major palaeochannel.

The paleochannel geometry was reconstructed by aid of borehole stratigraphy and geophysical surveying (**Fig. 58**).

The levee, according to borehole data (S1, S2 and S3; **Fig. 59**), is comprised of silt and clay with a variable fraction of sandy silt. A thick coarse sand layer is located in the depth interval -8 m / -11 m below the levee crest. This sand layer thickens moving from S1 to S3 (**Fig.59**).

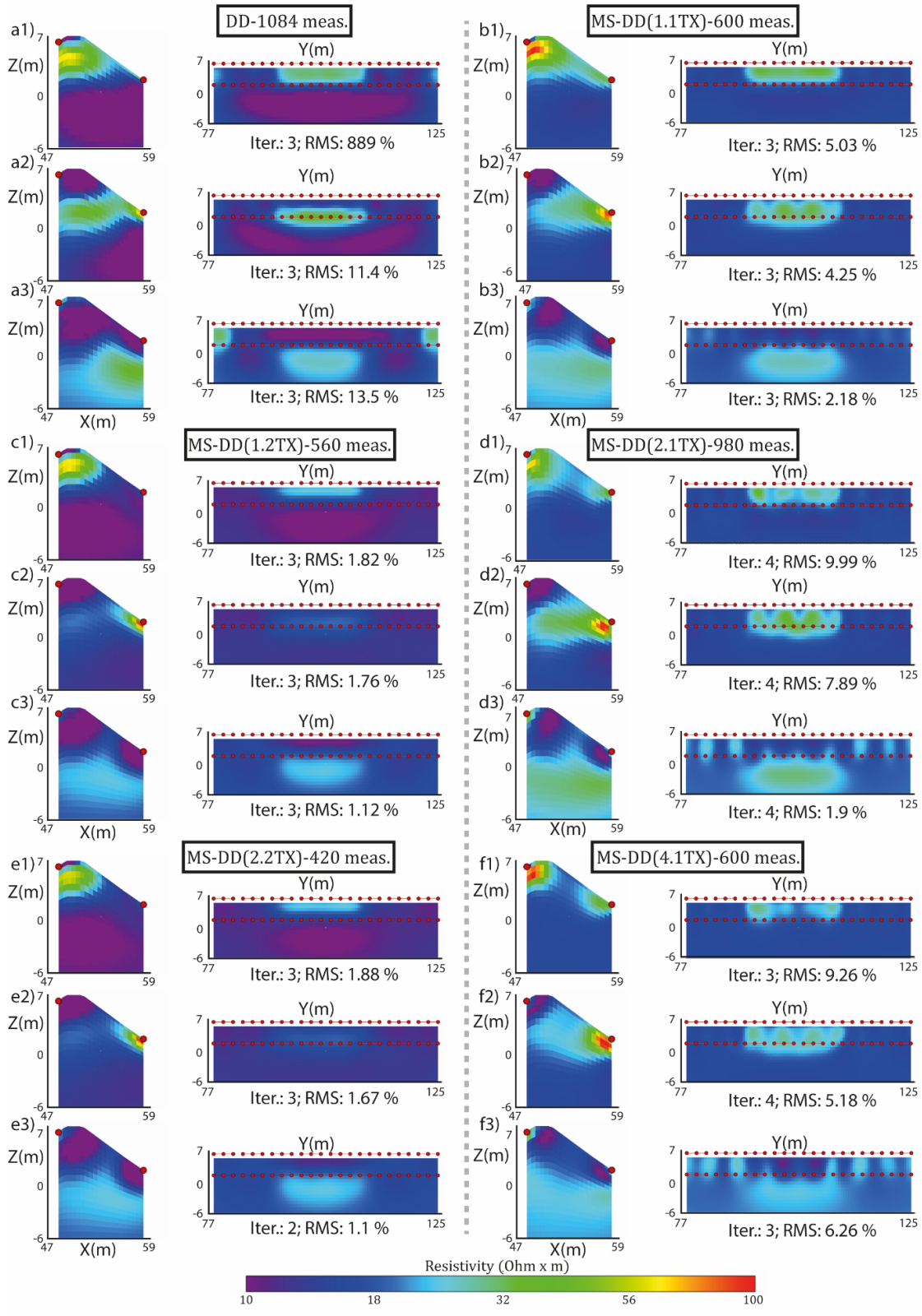

Figure 55: : inversion results for the transverse double profile. a) DD array: a1 top anomaly; a2 body anomaly; a3 sub-base anomaly. b) MS-DD (1.1TX) array: b1 top anomaly; b2 body anomaly; b3 sub-base anomaly. c) MS-DD (1.2TX) array: c1 top anomaly; c2 body anomaly; c3 sub-base anomaly. d) MS-DD (2.1TX) array: d1 top anomaly; d2 body anomaly; d3 sub-base anomaly; e) MS-DD (2.2TX) array: e1 top anomaly; e2 body anomaly; e3 sub-base anomaly. f) MS-DD (4.1TX) array: f1 top anomaly; f2 body anomaly; f3 sub-base anomaly. The X-Z section at Y=101 m; the Y-Z section at X=53m.

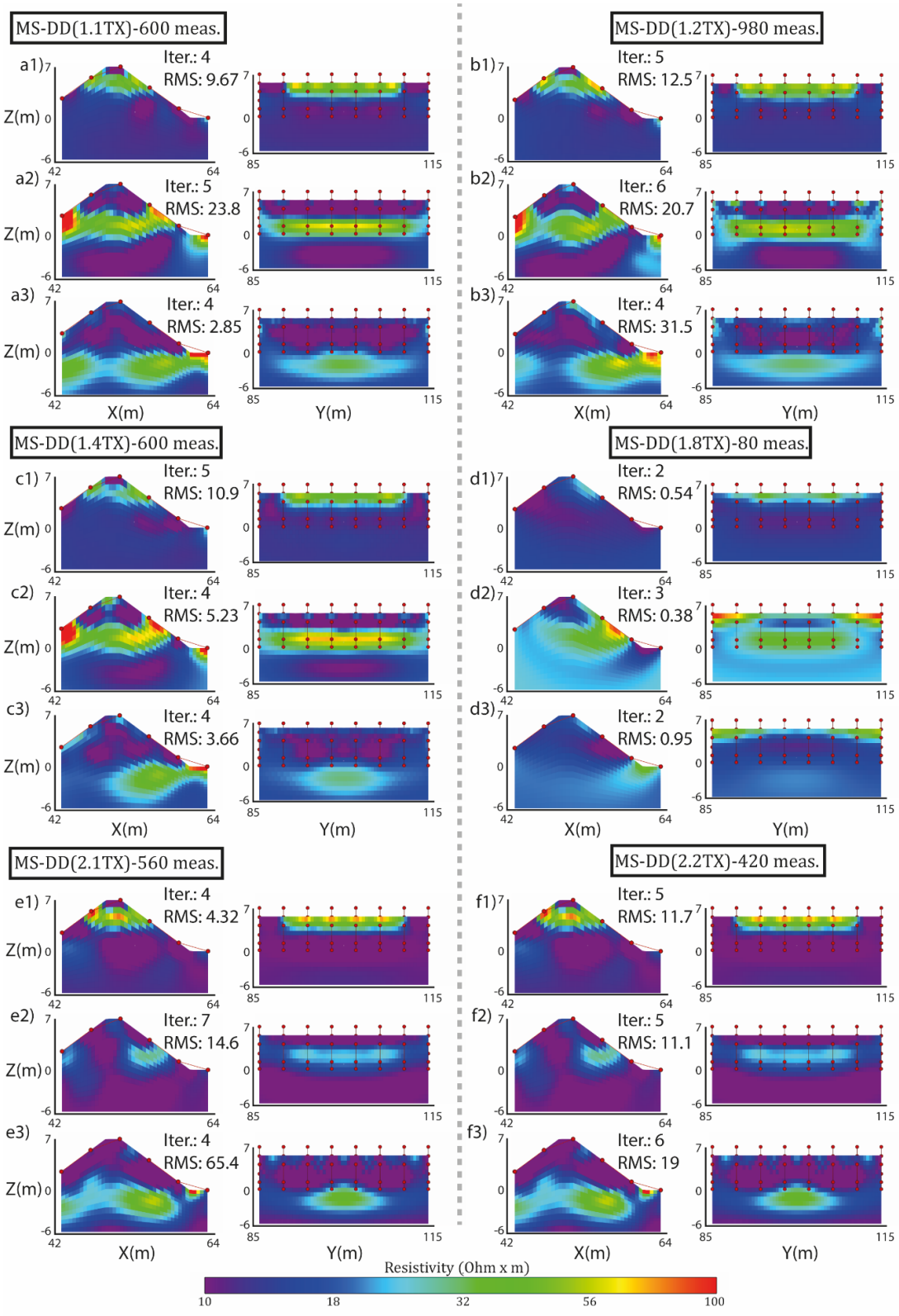

Figure 56: inversion results for the grid. a) MS-DD(1.1TX) array: 1 top anomaly; 2 body anomaly; 3 sub-base anomaly. b) MS-DD (1.2TX) array: 1 top anomaly; 2 body anomaly; 3 sub-base anomaly. c) MS-DD (1.4TX) array: 1 top anomaly; 2 body anomaly; 3 sub-base anomaly. d) MS-DD (1.8TX) array: 1 top anomaly; 2 body anomaly; 3 sub-base anomaly; e) MS-DD (2.1TX) array: 1 top anomaly; 2 body anomaly; 3 sub-base anomaly. f) MS-DD (2.2TX) array: 1 top anomaly; 2 body anomaly; 3 sub-base anomaly. The X-Z section is at Y=100 m; the Y-Z section is at X=53m.

The sand layer geometry was better defined at first via EMI surveying and after by aid of 2D ERT imaging (**Fig. 60**). EMI was utilized for quick mapping of the anomaly while ERT was crucial to resolve anomaly geometry and properties.

Results from EMI and ERT surveying lead to the identification of resistive body (80-100 Ω·m) located few m below the levee base (**Fig. 60B**). The resistor is approximately one hundred m long and few meters thick. According to borehole stratigraphy (**Fig. 59**) the resistor was interpreted as a coarse sand body (an old paleochannel).

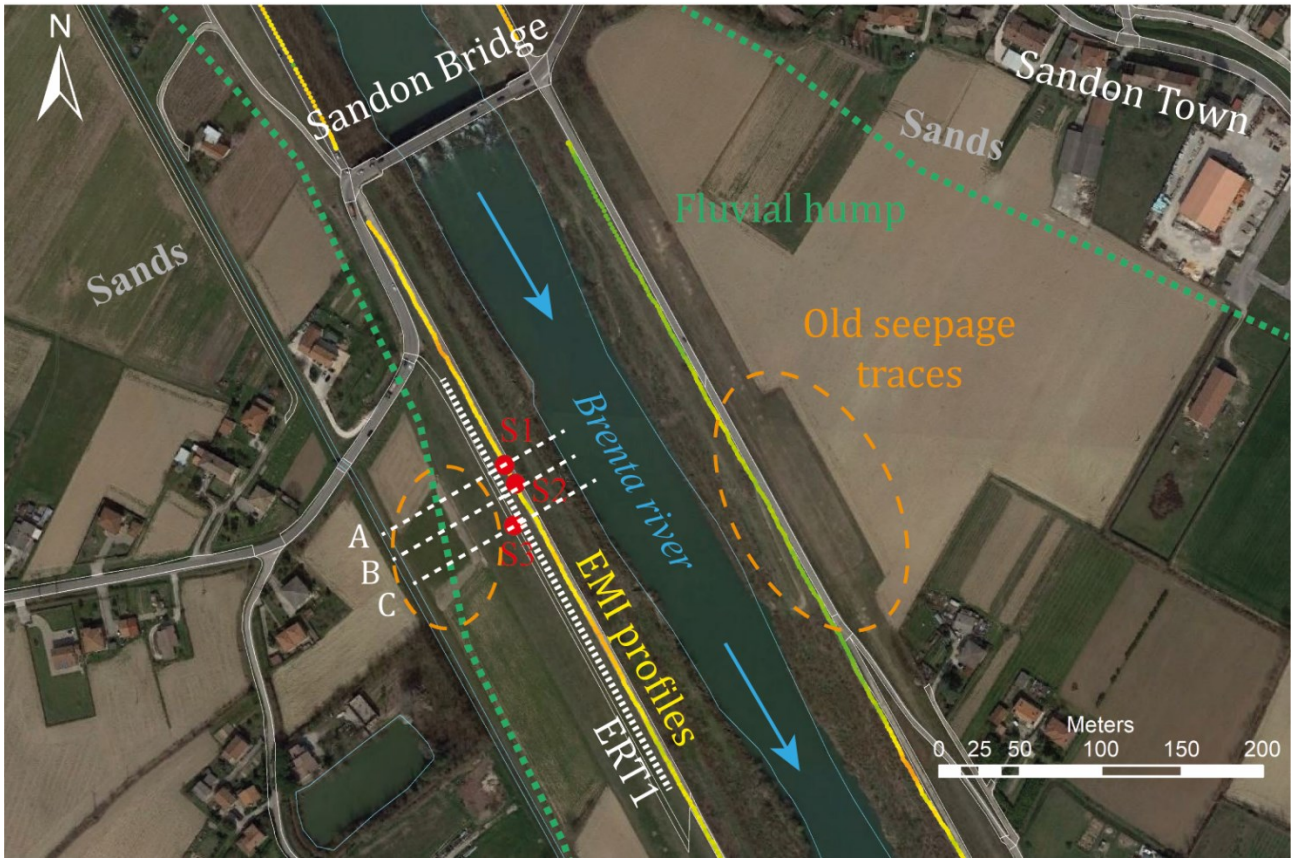

Figure 58: Satellite image of the study area. Red dots: borehole; orange: areas of sand boils; yellow: EMI profile; white: ERT profile; A, B and C indicate the cross section reported in Fig. 59 (modified from Google Earth, 2021).

This geology scenario is very similar to case III (anomaly below the levee base) of the simulations. It was then considered as an excellent study case to test the response of the DD and MS-DD arrays.

The thickness of the sand body inferred by resistivity imaging ranges from 7 m to 8 m. The boreholes are unfortunately shallower providing no constraints on the bottom interface of the sand layer.

Since the DOI of the tested arrays is also low compared to the bottom depth case, the survey target was redefined as the upper interface.

6.5.2 SURVEY DESIGN

Two of the tested layouts were selected to collect the data: the double-line (3D) and the grid (3D) geometry.

Array selection was guided by simulation results. DD and MS 1.1TX, MS 2.1TX and MS 4.1TX were used for the double-line layout while MS 1.1TX, MS 1.2TX, MS 1.4TX and MS 2.2TX were selected for the grid layout.

The DD array was only used in the double-profile layout as the grid layout was specifically designed for the MS system.

Field deployment is visible in Fig. 61. In the double-line layout, electrodes from 1 to 24 were laid down on the inner levee crest while electrodes from 25 to 48 were laid down along the levee toe (**Fig. 61A**). In the grid layout the MS triplets (one triplet per unit) were laid down transversely to the levee along 8 lines. Each line was comprised of two triplets (**Fig. 61B**).

The grid geometry was set up almost identical to the simulations. Electrodes were just slightly shifted to avoid traffic interferences (**Fig. 61B**). The 16 MS units were deployed alternating even and odd boxes. Odd boxes (i.e. 1, 3, 5, etc) where deployed along the inner flank while even boxes (i.e. 2, 4, 6, etc) where deployed on the outer flank (see Figure 61B for details).

A summary of the data acquisition parameters is reported in **Table 10**.

6.5.3 DATA ACQUISITION AND MESH PARAMETERS

Transmission parameters (current intensity and period of injection) for the DD array were set to match the MS default parameters. The desired current intensity was set to 1A with a 0.25 s period of injection.

Survey was carried out in dry conditions and coupling of the electrodes was not straightforward for the high contact resistances. Injected currents ranged from 60 mA to 800 mA. Few data-points were removed prior to carry out the inversion.

The mesh geometry was a replica of the mesh used for numerical simulations. Initialization values for the meshes were slightly different.

Mesh parameters are summarized in **Table 11**.

6.5.4 RESULTS

The results are commented for the two different layouts. The rainbow color scale ranges in the 50-200 Ω·m interval**.**

6.5.4.1 DOUBLE-PROFILE LAYOUT (3D)

The results for all the arrays (DD, MS-DD_1.1TX, MS-DD_2.1TX and MS-DD_4.1TX) are presented as XY resistivity planes (**Fig. 62)**. These depth planes have been extracted at specific Z values: 11 m (levee crest); 7 m (top of the uppermost banquette); 0 m (top strata of the sand body).

Results from DD array show a nice and sharp image of the upper portion of the levee (Z=11m) with a resistivity values higher than >100 Ω·m. In the mid portion of the levee (top of the banquette at Z=7m) resistivity lowers to average values of approximately 30-50 Ω·m. A tiny resistive portion (100-

130 Ω·m) is visible right below the inner line of electrodes. Resistivity, below the levee base (Z=0m) suddenly drops to ~60 Ω·m. The target resistive body is then missed by this array.

Results from the MS-DD (1.1TX) array are promising. The upper depth slices (Z=11m and Z=7m) are similar to the DD array response. A tiny resistive stripe is still visible at Z=7m and below the inner electrode line. Terrain resistivity is even higher (>200-250 Ω·m) compared to the DD array images. A resistive body (of 70-80 Ω·m), laterally continuous for about 15 m, is clearly imaged at Z=0m below the levee base. The target resistive body is then outlined by the MS-DD (1.1TX) array.

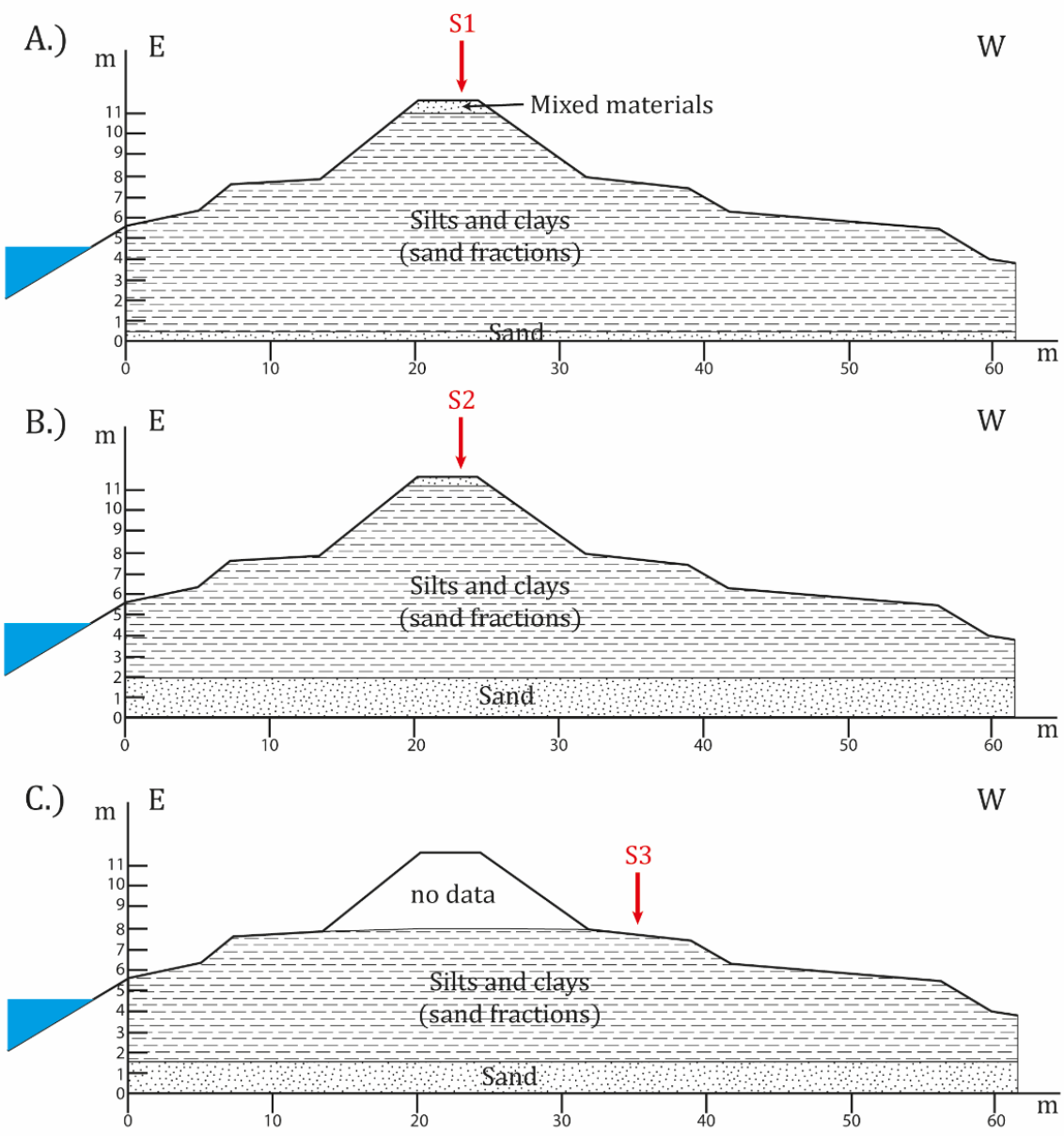

Figure 59: Cross-sections at borehole locations (see Figure 58). Water, during major floods, seeps throughout the pervious sandy paleochannel located below the levee.

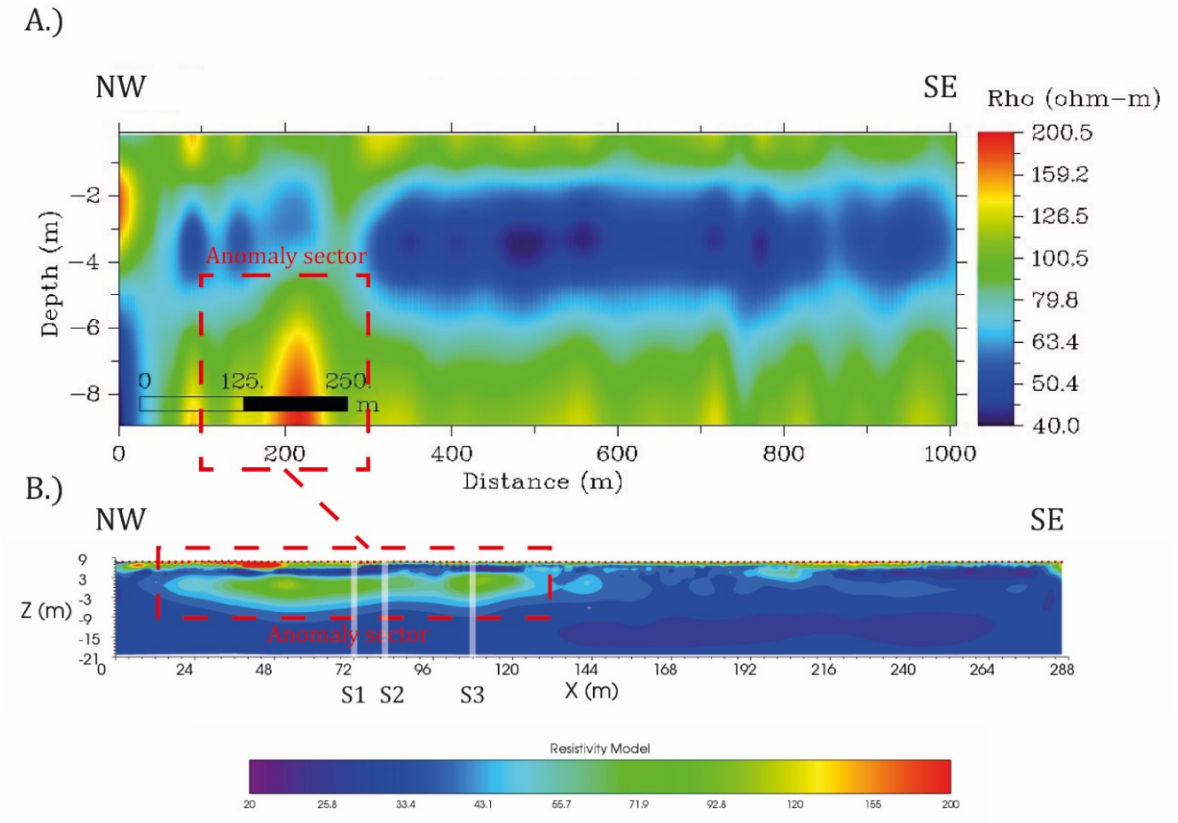

Figure 60: Results of geophysical investigations. A) EMI inversion. B) resistivity inversion. A resistive body is clearly imaged by both the surveys.

Table 10: Summary of the data acquisition parameters for the different layout and arrays.

Geometry	Array Type	Number of lines	Electrodes per line	Electrode spacings	Line Spacings	N inline transmitters	N offline transmitters	Number of measurements	Maximum DOI
Double profile (3D)	DD	2	24	2 m	~13 m	1	-	1084	-7.2 m
	MS DD					1, 2, 4	2	600 (1.1TX), 980 (2.1TX), 600 (4.1TX)	-9.2 m (1.1TX), -8.1 m (2.1TX), -5.82 m (4.1TX)
Grid (3D)	MS DD	8	6	4 m	4 m	1, 2	8	600 (1.1TX), 980 (1.2TX), 600 (1.4TX), 420 (2.2TX)	-15.2 m (1.1TX), -13.3 m (1.2TX), -10.2 m (1.4TX), -9.71 m (2.2TX)

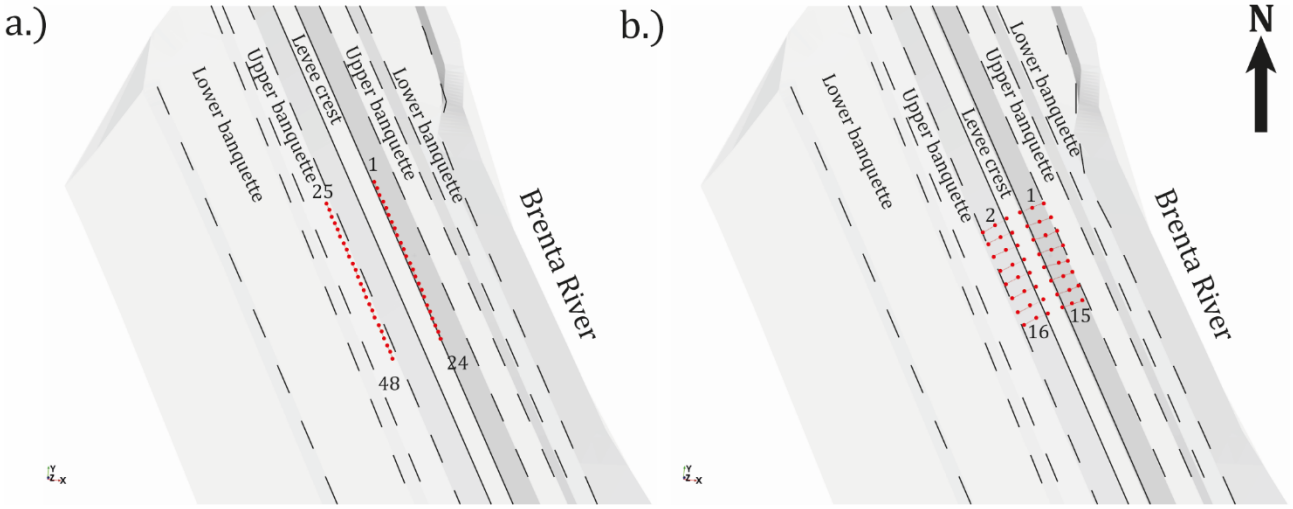

Figure 61: electrode deployment a) double profile layout; b) grid layout.

Results from the MS-DD (2.1TX) array are more or less similar to the previous case. The target resistive body is also outlined by this array. Resistivity is lower (55-60 Ω·m) compared to the MS-DD (1.1TX) response and its lateral extension is also reduced.

Results from the MS-4.1TX array are comparable to the other array responses at Z=11m and at Z=7m. At Z=0 some resistive spots (100 Ω·m) are clearly visible but they lack lateral continuity. The target resistive body is just partly outlined by this array.

7.5.4.2 GRID LAYOUT (3D)

The results for all the arrays (MS-DD_1.1TX, MS-DD_1.2TX, MS-DD_1.4TX and MS-DD_2.2TX) are presented as XY resistivity planes (**Fig. 63)**. These depth planes have been extracted at specific Z values: 11 m (levee crest); 7 m (top of the uppermost banquette); 1 m (top strata of the sand body). Resistivity in planes extracted at Z=11m and at Z=7m shows an inhomogeneous distribution.

Results from the MS-DD (1.1TX) array show a scattered resistivity distribution in XY planes at Z=11m and at Z=7m. Several resistive spots (250-300 Ω·m) are visible in these upper planes. A resistive body (> 200 Ω·m) is clearly imaged at Z=1m below the levee base. The resistive body crosses the plane diagonally. The target resistive body is detected and probably resolved by this array.

Results from the MS-DD (1.2TX) are similar to the previous case for XY planes at Z=11m and at Z=7m. A moderately and discontinuous resistive body (100-120 Ω·m) is imaged at Z=1m below the levee base. The resistive body crosses the plane diagonally similarly to the MS-DD (1.1TX array). The target resistive body is detected by this array.

Results from the MS-DD (1.4TX) are similar to the previous cases for XY planes at Z=11m and at Z=7m. A moderately and discontinuous resistive body (120-200 Ω·m) is imaged at Z=1m below the levee base. The resistive body crosses the plane diagonally but with different orientation with respect to the previous two arrays. The target resistive body seems to be detected by this array.

Results from the MS-DD (2.2TX) show an overall reduction of the resistivity values. Some highly resistive spots (> 100-150 Ω·m) are still visible in XY planes at Z=11m and at Z=7m. The response in depth (Z=1m) is pretty much conductive. There are no evident resistors below the levee base. The target resistive body seems to be missed by this array.

Table 11: Summary of mesh parameters for the two arrays (BR: background region; FR: foreground region).

	X	Y	Z	TOTAL
Double profile DD				
Min (m)	545.7	798	-1.8	-
Max (m)	560.2	844	11.6	-
El. Size (m)	0.5	0.5	0.5	-
BR pads	1 2 4 8 16 24 32 40 48 56 64	1 2 4 8 16 24 32 40 48 56 64	1 2 4 8 16 24 32 40 48 56 64	-
FR cells	52	115	34	203320
Double profile MS-DD				
Min (m)	545.7	798	-1.8	-
Max (m)	560.2	844	11.6	-
El. Size (m)	0.5	0.5	0.5	-
BR pads	1 2 4 8 16 24 32 40 48 56 64	1 2 4 8 16 24 32 40 48 56 64	1 2 4 8 16 24 32 40 48 56 64	-
FR cells	52	115	34	148350
Grid MS-DD				
Min (m)	43	86	-5.7	-
Max (m)	63	114	1.9	-
El. Size (m)	0.5	0.5	0.5	-
BR pads	1 2 4 8 16 24 32 40 48 56 64	1 2 4 8 16 24 32 40 48 56 64	1 2 4 8 16 24 32 40 48 56 64	-
FR cells	63	79	27	134379

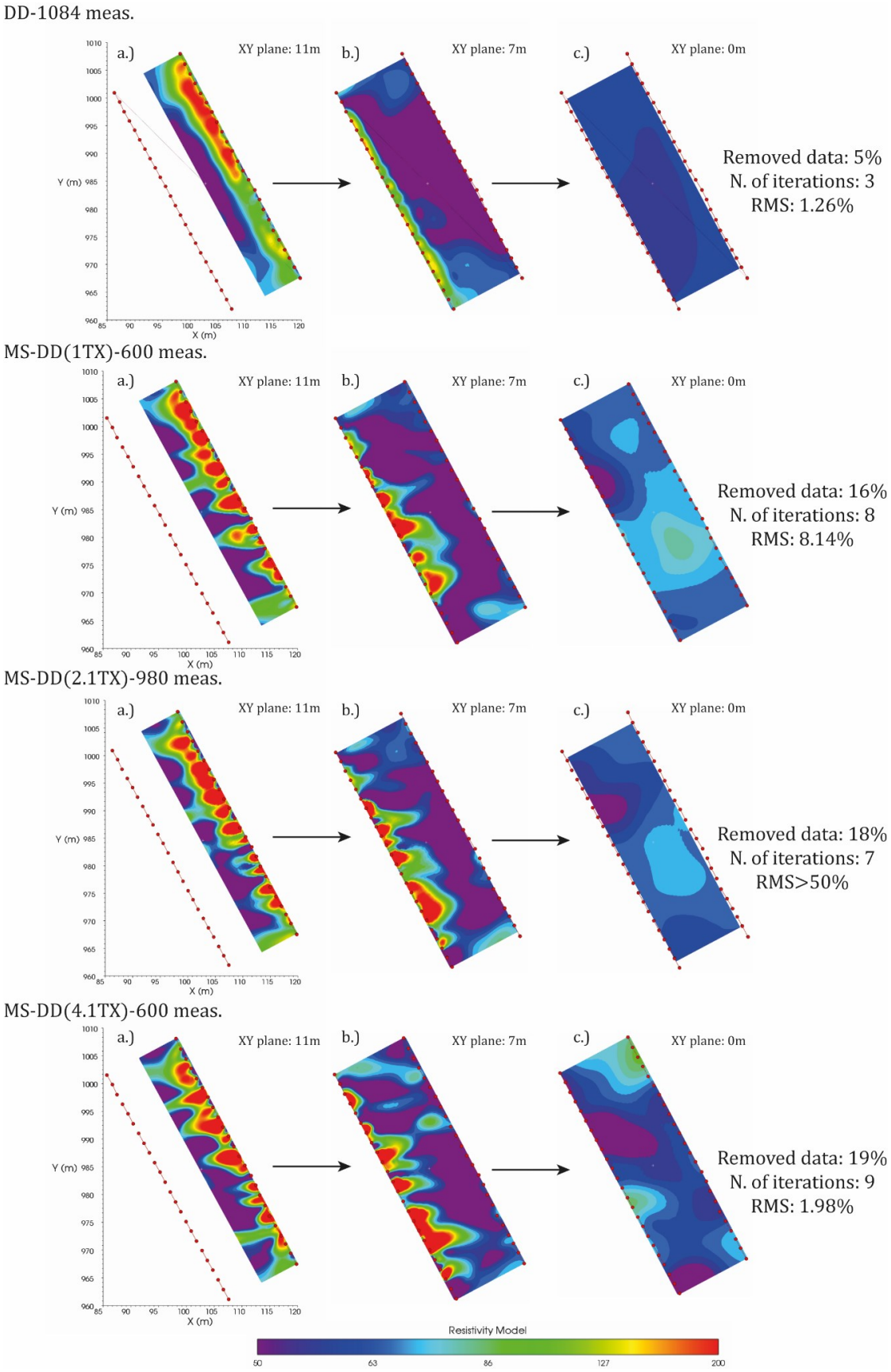

Figure 62: inversion results for the double-line layout. The chosen depth for the XY sections were 11 m (a), 7 m (b) and 0 m (c) above sea level.

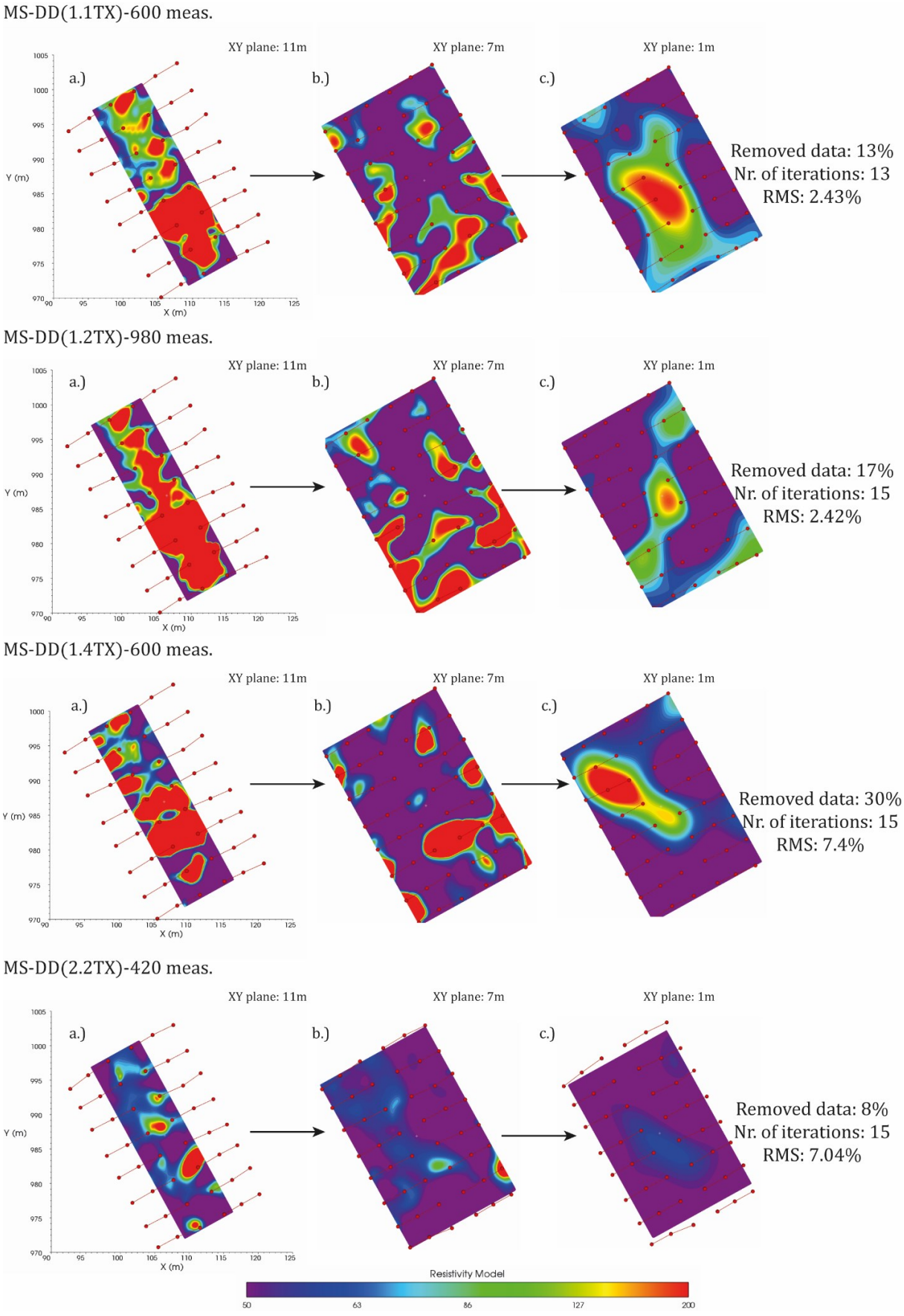

Figure 63: inversion results for the grid layout. The chosen depth for the XY sections were 11 m (a), 7 m (b) and 1 m (c) above sea level.

6.6 DISCUSSION

The objective of numerical simulations and field tests was to get some insight on the performance of the MS system in attempting to solve a typical geophysical problem.

For what concerns the synthetic models, the results brought by the different electrode layouts show a varying effectiveness in resolving the resistive target anomaly.

The reconstruction capability, in transverse layout, is similar for traditional and MS arrays. The performance is good in case of target anomaly located in the top and middle portion of the levee, while it is rather bad for a target anomaly located at larger depth.

The use of multiple inline transmitters (up to four) introduces just marginal imaging improvements in case of anomaly located below the levee base. This occurrence could be explained looking at two key aspects:

- electrodes were located in a strongly conductive layer and this inevitably limits the propagation of the electrical field;
- the layout of the electrodes along a hump-shaped topography causes the sensitivity to be poor in the deep strata below the center of the levee. The sensitivity function is inversely proportional to height and width of the levee.

Increasing the electrode spacing is a possible strategy to overcome this problem. This approach results in reduced data density and could be resolved adding extra-measurements.

A typical MS survey, on a river embankment, could be intended as the combination of several sequences, each one with a different number of transmitters. This approach although feasible in numerical modeling should be carefully evaluated in real study cases. The geometry of the levee strictly controls the way the electrodes could be deployed thus limiting the survey flexibility.

This is not a limitation for traditional arrays as the use of remote poles could easily improve survey coverage. Anyway, I personally advise against the use of the MS system in this sense, also because of lack of information derived from a simple 2D approach respect a 3D one. These are also the reasons that led to the discard of the transverse electrode layout as a tool of investigation in a real study case.

The double-line layout is rather common as survey geometry for levee imaging. It is a good trade-off between production and 3D reconstruction capability compared to transverse profiling.

The elevation difference between the two lines distorts the array sensitivity. A symmetric deploying would result in homogeneous sensitivity map but some drawbacks have to be properly taken into account: the target is outside resolution capability of the array in case of electrodes too close to the levee crest; the levee body remains undetermined in case of electrodes too close to the levee toes. The selected layout is then a reasonable compromise.

The MS-DD arrays proved to be particularly effective in resolving the target anomaly located below the levee base. Arrays MS-DD (1.1TX), MS-DD (2.1TX) and MS-DD (4.1TX) resulted particularly effective. These arrays used inline single- and multiple-transmitter. The DD array is effective in case of shallower target anomaly although its resolution is more or less matched by the MS-DD arrays. The DD array, because of its DOI, detected the target anomaly located below the levee base but it was unable to resolve it.

In other words, the anomaly is visible, but its lateral continuity, below the central portion of the levee (the survey target), could not be outlined. The use of one or more cross-line transmitters is probably inadequate to image target located below the levee base. Numerical simulation results already pointed out the issue. The limit is probably the reduced DOI value and the limited number of data-points to be used for inversion.

The grid layout is not common for real applications as it could be very time-consuming while deploying units and electrodes.

All the tested arrays with inline transmitters, but the MS-DD (1.8TX), were successful in imaging the target anomaly. The poor performance of the MS-DD (1.8TX) probably depends on the reduced number of data-points used for inversion. The use of cross-line transmitters does not really improve the resistivity image below the levee base and inversion results are not satisfying.

The limited number of MS units used for the test did not allow testing of more than eight simultaneous transmitters.

Surprisingly, the 1.1TX seems the best compromise for this kind of acquisition, probably combining at the best the number of measurements and the depth of investigation. The first three adopted arrays are linear in the reconstruction of the designed model, with the proper definition of the presence of the anomaly at the selected depth but, more importantly, with a higher degree of difficulty in the reconstruction with the progressive deepening of the anomaly itself. Said that, a background of 10-15 Ω·m and an anomaly/background ratio of 3:1 is respected for all the reconstructed models. The 1.2TX and the 2.2TX, on the other hand, show a very strange behavior at depth case II: in this case, in fact, the anomaly results as truncated in two small bodies on the two sides of the levee, with a complete lack of communication below levee body. Surprisingly, the anomaly comes back in the deepest scenario, suggesting probably a higher sensitivity of the arrays to the deeper portions of the medium. This information could be useful to integrate this kind of measurements when greater details concerning the deep subsurface are required.

The passage towards the application on a real study case is evidently coupled with a sensible change in the results gained for the different electrode scheme. In particular, the two-parallel lines and the grid geometries were supposed to be particularly promising in this kind of scenario respect to the traverse geometry, with a net prevalence of the second one. Conversely, the MS results look characterized by a sort of "fragmentation effect" in the reconstruction of the upper portions of the levee, especially when we look at the results in proximity of the electrodes position. This fragmentation becomes very evident comparing the results of the MS and the SP for the two-parallel lines geometry, with the inverted resistivity in the SP results looking much more smooth and continuous respect to the MS ones. At this moment, it is not fully understood if this effect is purely derived from the real physical features of the medium or, instead, if it is the result of an amplification effect of these physical features operated by the inhomogeneous distribution of apparent resistivities in the MS datasets. The MS system seems, in this case, to suffer also of a sort of "polarization effect", in the sense that the high resistive small kernels are very high in module compared to their respective in the traditional dataset. It is probable that the also the interdistance between the two measuring lines and, anyway, the textural and lithological features of the dike are first role aspects in the comprehension of this phenomena. Anyway, the resistivity distribution looks consistent to the one reconstructed by the SP system, and so also this superficial datasets can be validated. Said that, the quality of the reconstruction seems to be very high in the deepest tested scenario, and especially

comparing the results to the traditional DD ones. In all the MS arrays, in fact, the artificial electrical field evidently enters in the sand body present from approximately 10-11 m.a.s.l. (looking at S1, S2 and S3 results), and clearly demarked by the higher resistivity bodies (compared to the background value) visible at XY=11m. The real DOI of the traditional DD is evidently insufficient also for this electrode deployment, or maybe the resolution of the array at this depth is not enough to precisely reconstruct the presence of the anomaly. Of course, this last fact can be crucial in the successive step of identifying and dimensioning the proper defense structure to install on site. This fact denotes a first important preference towards the MS system in this kind of study cases, even though it is evident that the MS datasets are also subjected by a higher percentage of noise, also in the four simultaneous transmitters case.

The same general features emerge also looking at the MS grid results, even though this time the absence of a control traditional dataset give us fewer elements in order to validate the final inverted sections. Also for this electrode disposition, for example, a better and smoother in-depth reconstruction emerges respect to the most superficial cases, where the levee seems to be constituted by very heterogeneous materials. This heterogeneity does not seem to have a logic structure for the height of 7 m, while for the most superficial case the axial anomaly visible in all the sections (even though with different shapes) can be quietly attributed also to the highly compacted material present below the transitable crest portion of the levee. The deepest results show a high variability in the reconstruction of the sand body: a first one is definitively defined below the central portion of the section for arrays 1.1TX, 1.2TX and 1.4TX, but with very different dimensions and lateral continuity. The largest one is identified by 1.1TX and seems to prosecute decisively towards the southern border of the section, and more moderately to the north. A similar reconstruction is visible for the 1.2TX, even though this time the central sand body looks subdivided in three more limited bodies. In 1.4TX the sand body seems to migrate towards the NW portion of the section, and its lateral continuity seems much more weak. Only in 2.2TX, no traces of sand body are visible. Of course, also in this case the DOI and the apparent resistivity distributions of the arrays play a key role in the final reconstruction of the model. The 2.2TX is not able to overcome the height of 10 m with a sufficient number of data, and that is the reason of its general inappropriateness respect to the problem studied. Almost the same considerations can be done for the 1.4TX. It appears, in this sense, that an optimal compromise between data density and DOI is again reached by the single or the double transmitter cases. So, almost the grid geometry seems in this sense a good solution in order to study this kind of structure, but an appropriate number of measurements is required at the target depth in order to get a satisfying reconstruction. In other words, the increase in the number of transmitters does not compensate the loss in data number.

The MS arrays tested in this study represent valuable tools for levee imaging applications. Electrode and line spacing could be better designed to match the survey target. In addition the reduced acquisition time is a great aid in speeding up field operations.

also could be compared required to collect traditional DD me some considerations could be done f Additiona tool for future studies, maybe rearranging the electrode and the interline spacings respect to the known or expected target of the survey. A final extra addition in this sense can be outlined also by the times needed to acquire an MS dataset respect a standard DD one (or also other arrays).

Table 12 reports a summary of data acquisition time for the tested arrays.

Table 12: time of acquisition per-each employed array.

Array type	Time of acquisition
Standard dipole-dipole	13 min. and 28 sec.
MS 1.1TX	6 min. and 42 sec.
MS 2.1TX	5 min. and 54 sec.
MS 4.1TX	4 min. and 14 sec.
MS 2.2 X	3 min. and 15 sec.

7. DEEP TARGETS: MODELING AND APPLICATIONS

Deep targets are generally difficult to model because of limited available constraints. Deep-seated gravitational slope deformations are frequent both in the Alps and in the Apennine and very often the sliding surface is hardly imaged with geophysical methods.

7.1 PROBLEM STATEMENT

Resistivity imaging of a deep dipping surface is a challenging scenario. The dipping surface is a sort of hybrid case between the horizontal and the vertical interface.

Very few papers deal with ERT potentials and limitations in resolving this geological feature. ***Dahlin et al. (2004)*** modeled a dipping succession of resistive (300 Ω·m) and conductive (100 Ω·m) layers buried below a till deposit. The layers were tilted of 60 degrees towards the beginning of the survey line; their thickness was variable from one end of the line to the other. In general the electrical image was effective in reconstructing the resistive strata while the conductive strata were poorly resolved.

Putiska et al. (2012) modeled a dipping surface (with angles of 60, 90 and 120 degrees) using four distinct arrays. The surface separates a resistive from a conductive medium, with half of the electrodes on the first domain and the other half on the second one. The resistive domain was subdivided in shallow thin strata of 1000 Ω·m and a deeper sector of 500 Ω·m; counterwise, the conductive domain was subdivided in a 150 Ω·m surficial and a 60 Ω·m sectors. The authors concluded that dipole-dipole and pole-dipole arrays perform better compared to other traditional arrays (i.e. Wenner or Schlumberger). The selection of the inversion algorithm was also crucial, and particularly the re-weighting of the roughness coefficient. In this sense, the L1-norm based inversion, with diagonal roughness filter, generates excellent results.

The accurate resolution of a deep dipping surface could be representative of a variety of challenging geologic scenarios. A frequent case could be represented by a resistive bedrock buried by conductive deposits (the typical landslide). Other examples can be the identification of the lateral termination of a salt-wedge in an area subjected to marine water seepage, or stratigraphic/tectonic abrupt lateral transitions.

7.2 SURVEY DESIGN

The model is pretty simple. An inclined surface separates resistive domain from a conductive domain. The surface intersects topography right in the middle of the electrode array (Fig.63). Simulations were carried out for three angles: 15 degrees, 30 degrees and 90 degrees (vertical surface).

Geologically speaking these models could be assimilated to faults and thrusts, to deep-seated landslides or also to abrupt contacts in a tilted sedimentary succession. The two electrical domains were supposed to extend indefinitely.

Model #1 is a vertical contact while model #2 and model #3 are inclined interfaces of 30 degrees and 15 degrees respectively (**Figures 63-64**).

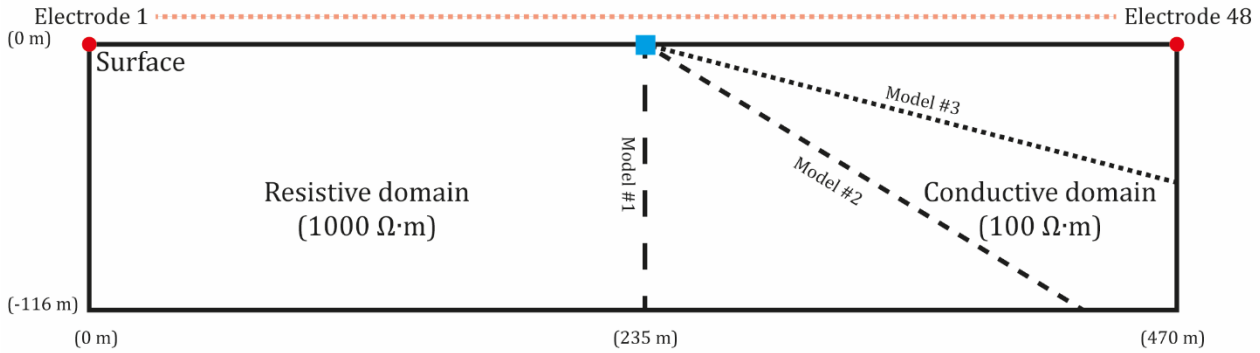

Figure 63: Reference models used in numerical simulations.

The inclined interfaces are the real simulation targets while the vertical interface is a sort of benchmark to test the response of the various arrays. Resistivity in the two domains was set to 1000 Ωm and to 100 Ω·m respectively.

The tetrahedral mesh initialization for model #2 and model #3 was not straightforward because the inclined surface was to be modeled as a sort of "staircase".

The layout was comprised of 48 electrodes spaced of 10.0 m resulting in a total length of 470 m.

The tested arrays are the same already discussed for the other numerical simulations: DD, MS-DD (1.1TX), MS-DD (2.1TX) and MS-DD (4.1TX).

The resulting DOI was: 90 m for the DD array; 115 m for the MS-DD 1.1TX and for the MS-DD 2.1TX arrays; 100 m for the MS-DD 4.1TX array.

The cell size was set to 5 m in the three directions X, Y and Z. Other mesh parameters are summarized in **Table 13**.

Table 13: Mesh parameters.

	X	Y	Z	TOTAL
Min.(m)	0	-2.5	-116	
Max.(m)	470	7.5	0	
El. Size(m)	5	5	5	
BR pads	1 2 4 8 16 24 32 40 48 56 64	1 2 4 8 16 24 32 40 48 56 64	1 2 4 8 16 24 32 40 48 56 64	
FR cells	117	25	35	81900

7.3 NUMERICAL SIMULATION RESULTS

7.3.1 MODEL #1 (vertical contact)

The DD array resolves both the vertical contact and the resistivity values in the uppermost 20-25 m of the model (**Fig.64-a1**). The inversion misfit is 14.7%. The resistive domain is poorly resolved although its reconstruction appears to be more effective compared to the conductive domain. Resistivity drops at depths larger than 90 m with a misfit of about 25% while in the conductive domain the resistivity value is properly fit (misfit of 15-20%) down to a depth of about 60 m below the surface.

Resistivity at further depth in the conductive domain grows to 150-180 Ω·m resulting in a misfit larger than 50%.

The MS arrays fails in imaging the near surface resistivity in the resistive domain. In general resistivity distribution is more or less similar to the DD response (**Fig.64-bcd1**). The average inversion misfit for the tested arrays is 9.8%. Resistivity in the uppermost 15-20 m appears to be fragmented in both the conductive and the resistive domain. These high resistive/conductive spots are probably related to the presence of minima in the sensitivity function. The misfit on these spots is as large as 1000% in the resistive domain and as 400% in the conductive domain. The misfit at large depth in the resistive domain is approximately 50-60% similarly to the DD response .

Increasing the number of transmitters results, in the resistive domain, in extending the resistive response at larger depths. Model fit in the resistive domain increases about 12% switching from 1TX to 2TX and it further increases of 13% switching from 2TX to 4TX. Model fit in the conductive domain increases about 20% switching from 1TX to 2TX and it further increases of 14% switching from 2TX to 4TX. Increasing the number of transmitters results also in increasing the resistivity fragmentation in the near surface layers in both the resistive and the conductive domain.

7.3.2 MODEL #2 (30-degree inclined surface)

The DD array response is pretty chaotic (**Fig.64-a2**) as it shows conductive spots in the resistive domain and vice versa. The inversion misfit is low and it is about 6.5%. The conductive domain appears to be more homogeneous while in the resistive domain the misfit in the uppermost 30-35 m is larger than 1000%. A nucleus of high resistivity is visible in resistive domain in the 60-90 m depth range and it partially extends down to the DOI value for this array. In the conductive domain the misfit is lower than 10% in the uppermost 30-35 m of depth and it jumps up to 100% at 60 m of depth. The areas of poor convergence to the reference model are partly due to numerical artifacts but they are probably mostly related to minima of the sensitivity function.

The MS response is more or less similar for the three arrays (**Fig.64-bcd2**). The average inversion misfit for the tested arrays is 4.5%. Resistivity distribution is rather different in comparison to the DD response. The resistivity in the uppermost 20-25 m appears fragmented in both the conductive and the resistive domain similarly to model #1. These high resistive/conductive spots are probably related to the presence of minima in the sensitivity function. The average misfit is around 50% in the resistive domain while it is as high as 100% or even more in the conductive domain. The conductive wedge is poorly imaged and just in the vicinity of the mid electrodes.

7.3.3 MODEL #3 (15-degree inclined surface)

The DD array response is rather homogeneous (**Fig.64-a3**). The inversion misfit is low and it is about 3.4%. A small conductive stripe is visible right in the middle of the resistive domain and it is probably related to the presence of a depth interval of low sensitivity. These low sensitivity stripes could be also due to overlapping ensembles of data-points with different “a’ factors. The fit on the resistive domain is good (90-95%) in the uppermost 90 m of depth. The conductive domain is properly imaged with a fit larger than 90%. The inclined interface is clearly outlined down to its maximum depth.

The MS response for the three arrays is comparable (**Fig.64-bcd3**). The average inversion misfit for the tested arrays is 4.8%. Similarly to model #2, resistivity distribution is rather different in comparison to the DD response. Resistivity in uppermost 20-25 m appears still fragmented but less

than model #2. The reasons for this fragmentation have already been discussed. The average misfit in the resistive domain is 40-50% while it is much higher in the conductive domain. The small conductive wedge is poorly imaged and just in the vicinity of the mid surface electrodes.

7.4 PRELIMINARY DISCUSSION

Inversion results poorly fit the reference models. This is particularly evident for the MS array but the DD array response is also poor especially for model #2 (30-degree inclined interface).

Model #1 (vertical interface)

The vertical interface is reasonably resolved in the DD response especially for what concerns the shallow lateral transition from the resistive to the conductive domain. The resistivity image at large depths is below expectations. The interface is no more resolved below the depth of 70-75 m although the subsurface partition in two domains is preserved.

MS-DD inversions appear to be very noisy in the near surface layers. The images worsen switching from single to multiple transmitters with a progressive thickening of the noisy layer in the 2.1TX and 4.1TX arrays. The subsurface partition in two domains is preserved in the 1.1TX and 2.1TX responses while it is somewhat blur in the 4.1TX array. The MS-DD, as compared to the DD, seems to improve the imaging at large depths (4.1TX array response). The four-transmitter dataset returns a shrinkage of the image of the resistive domain although it better defines the model bottom. Numerical artifacts in the shallow portion affect the conductive domain. In the same domain the fit to the model resistivity improves below 35-40 m of depth.

Model #2 (30-degree inclined interface)

The DD response is really poor in the near surface layers as the resistivity image appears to be scattered. The resistivity image is fragmented also at intermediate depths with a lateral alternation of highly resistive and conductive lobes. The conductive domain is better imaged although underestimated in thickness.

MS-DD inversions are very noisy in the near surface layers. The dipping interface is imaged in the upper portion of the section down to a depth of 40-50 m. The imaged segment of the interface is sharper in the MS-DD response with respect to DD array results. Resistivity values in the resistive and conductive domains poorly converge to the reference model values.

Model #3 (15-degree inclined interface)

The interface is resolved in the DD response. The transition from the resistive to the conductive domain is outlined down to its maximum depth. The lateral termination of the dipping interface is not resolved but this depends on the lower data-points coverage below the outermost electrodes. The fit to the conductive domain is very good and it ranges in the 90-95% interval. The fit is high also in the resistive domain but for a conductive stripe located 15-20 m below the surface. The resistor in the first half of the section is fit down to a depth of about 70m. The misfit at larger depths is around 70%.

MS-DD response is somewhat similar to inversions obtained for model #2. The response is noisy in the near surface layers. The dipping interface is imaged in the upper portion of the section down to a depth of 25-30 m. The imaged segment of the interface is sharper in the MS-DD response. Resistivity values in the resistive and conductive domains do not converge to the reference model values. The

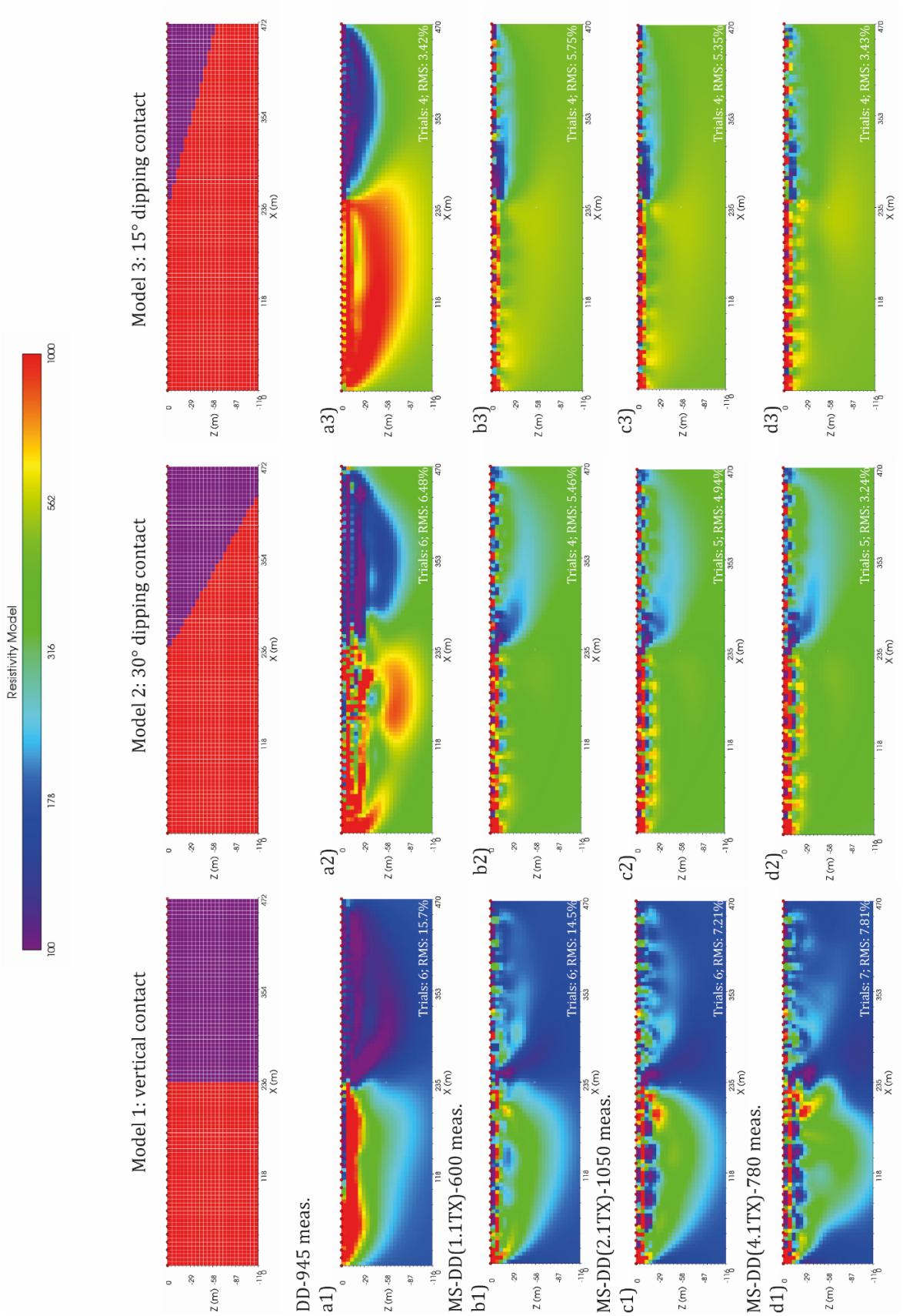

Figure 64: Inverted resistivity models for DD and MS-DD arrays using default parameters: vertical interface (1); 30-degree inclined surface (2); 15-degree inclined surface (3). a) DD array response. b) MS-DD (1.1TX) array response. c) MS-DD (2.1TX) array response. d) MS-DD (1.4TX).

misfit in the deep layers reduces progressively switching from a single to multiple transmitters. The misfit at the bottom of the section is about 25-30% in the 4.1TX array.

In general, the inverted models are not satisfying in terms of reconstruction accuracy. The low accuracy is particularly evident for the MS-DD arrays but the DD array also performs quite poorly. The numerical artifacts visible in model #2, in both MS-DD and DD responses suggest that the noise percentage has been increased for computing purposes to speed up convergence during inversion.

Inversion procedure tries to optimize the trade-off between accuracy and computing time required to complete the process. In other words, when the difference between the modeled and the measured resistivity remains high after several iterations, the algorithm introduces some noise in specific cells to speed up the convergence and complete the inversion. This inverse problem-solving approach could result in the degradation of the resistivity value in the near surface cells. This part of the process is controlled by a parameter called NPCG. NPCG is the maximum number of internal iterations (N) used by the preconditioned conjugate gradients (PCG) method to solve a linear system. In the current case NPCG controls the exactness of the linear equations system solution (for each external iteration). A high number of NPCG results on a high control on the accuracy of the numerical solution. A value of N=15, at the time the solver was implemented, was found to be a good compromise between accuracy and computing time.

This limitation is particularly true for the near surface portion of the inverted models where the cells are constrained by the majority of the measurements. The lowering of the resolution at larger depths (less measurements) generally results in much smoother models affected by with minor numerical artifacts. Initial resistivity values in the very bottom cells are often just marginally altered during the inversion process. Performance and capabilities of modern computers overcome this limitation allowing for the search of a more accurate solution in the near surface cells.

An additional run, with updated parameters, resulted in a new set of inversions (**Fig. 65**). NPCG was raised to a value of 100 and also the model roughness was recalculated for each each external iteration.

The new inverted models appear to be much smoother with a minimal fragmentation of resistivity values in the near surface layers. The similarity between MS-DD and DD response was improved along with the degree of convergence to the reference model. The DD array is probably the most effective but also the MS-DD array introduces some novelties in the inverted models.

MS-DD response for model #1 is really effective in outlining the vertical interface that, in depth, appears to be resolved much better than in the DD response. In the 1.4TX mode the resistive response is shifted down to the bottom of the inverted model with a better convergence with respect to the DD array nearby the vertical interface.

MS-DD response for model #2 is particularly sharp with very few numerical artifacts and its response is more or less comparable to the DD array. The misfit on the resistive domain is lower than 15% down to the maximum depth. The inclined interface is resolved down to

MS-DD response for model #3 is not as sharp as for the previous model but the low-dipping interface is resolved down to its maximum depth. The resistivity image is noisier than the DD response but the fit to reference model is still good and with very few numerical artifacts in the near surface layers.

The inclined interface model is a challenging target for both the MS-DD and the traditional DD arrays. The varying resistivity in both the X and the Z directions limit the effectiveness of the inversion

process. These simple simulations were particularly useful to obtain an initial insight of the resolution capability of the tested systems in specific array configurations. A second achievement is the better control of the inversion parameter in these subsurface model settings. At a first glance the traditional DD arrays delivers a better resolving power on the sudden lateral changes of resistivity in the near surface layers. This is particularly evident in the run with the updated inversion parameters. The MS-DD array, as expected, provides a better fit on the reference model in the deep layers and this is really clear in the vertical interface model (model #1).

The use of multiple transmitters could be a major breakthrough to gain a better control on the resistivity distribution in depth. The latter is pretty coherent with the concept design of the MS system itself.

It is worthwhile to mention that DD measurements, in a real case, are expected to be noisier compared to these simulations. MS-DD data as already mentioned and as demonstrated in the previous chapter, are not as noisy. Three major factors probably controls this improved accuracy in reconstructing the electrical signals: the reduced coupling effects (the are no cable-connection between units); the sophisticated control on the self-potentials during data acquisition; the high-quality system circuitry.

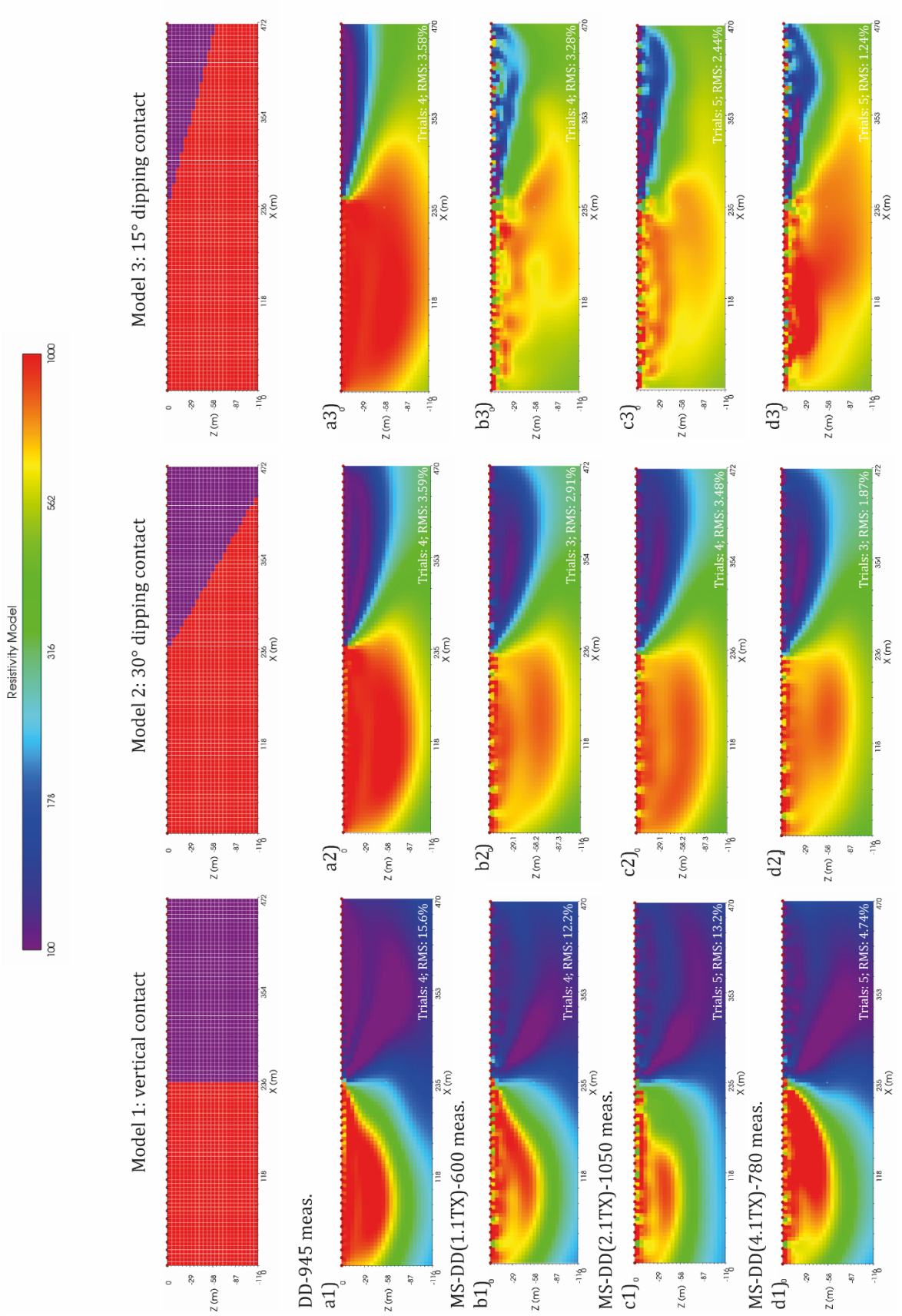

Fig 65: inverted resistivity models for DD and MS-DD arrays using updated parameters: vertical interface (1); 30-degree inclined surface (2); 15-degree inclined surface (3). a) DD array response. b) MS-DD (1.1TX) array response. c) MS-DD (2.1TX) array response. d) MS-DD (1.4TX).

7.5 THE VAJONT STUDY CASE

Traditional arrays and MS-DD were tested on the large 1963 Vajont rockslide targeting the western portion of the sliding surface located below the glided succession. The surface, inclined at an angle of 20-25 degrees, was selected because there are some geological constraints about its depth and geometry. This interface, according to ***Broili et al., (1967)***, separate the calcareous bedrock comprised of the hard and resistive rocks of the Vajont Limestone Fm. from relatively conductive and moderately soft rocks of the glided succession.

Two different ERT systems were deployed on the landslide mass with the purpose of comparing results and actuate acquisition strategies to image the subsurface as deeper and as most accurate as possible.

7.5.1 DATA ACQUISTION

A 48-electrode traditional PD/W-α array (STD) and a 8-unit (24-electrode) MS-DD array (MS) were used to collect the resistivity data.

STD system

A profile of approximately 1.3 Km (**Fig. 66**), with 20 m electrode spacing, was covered combining a base and a roll-along sequence. The overlap of the roll-along sequence was 50% (corresponding to a group of 24 electrodes). Forward and backward remote poles were located at a distance of ~260 m from both line ends. The collected sequences were a PD and a W-α for a total of 1335 plus 360 data-points.

MS-DD system

A profile of approximately 1.4 Km (**Fig. 66**), with 25 m electrode spacing, was covered with a block-based layout..Units were gathered in two blocks of 4 units each (b1, b2, b3, etc. in Table 14). Each block could operate both as transmitter (TX) or receiver (RX intra- and extra-block).

The outer block (i.e. electrodes 13-24), after the first run with all the units/electrodes deployed sequentially, was then moved forward of four stations (position b3) and data acquisition was repeated (Table 14). The block was then further moved forward of other four stations (position b4). Acquisition continued until all the possible block positions were occupied.

The collected sequence was an ensemble of 1TX (280 data-points), 2TX (210 data-points) and 4TX mode (100 data-points) for each run.

DOI is approximately 210 m for the STD while it is as high as 350 m for the MS-DD. Nominally the MS-DD, using a block-based layout, penetrates 1.7 times deeper than the STD. The STD deployment is just 6.4% shorter than the MS-DD but the latter DOI is 41% higher.

The roll-along strategy, used for the deployment of the STD line, is very accurate in mapping lateral resistivity variations even though less efficient in detecting deep resistivity changes.

Table 14: the block-based layout used to collect MS data. The "TX/RX blocks" column indicates the transmitting and the receiving blocks at each run. b1, b2, … ,b5 are block station positions along the survey line.

Run	TX/RX blocks	b1				b2				b3				b4				b5			
1	b1-b2	1	2	3	4	5	6	7	8												
2	b1-b3	1	2	3	4					9	10	11	12								
3	b1-b4	1	2	3	4									13	14	15	16				
4	b1-b5	1	2	3	4													17	18	19	20
5	b2-b3					5	6	7	8	9	10	11	12								
6	b2-b4					5	6	7	8					13	14	15	16				
7	b2-b5					5	6	7	8									17	18	19	20
8	b3-b4									9	10	11	12	13	14	15	16				
9	b3-b5									9	10	11	12					17	18	19	20
10	b4-b5													13	14	15	16	17	18	19	20

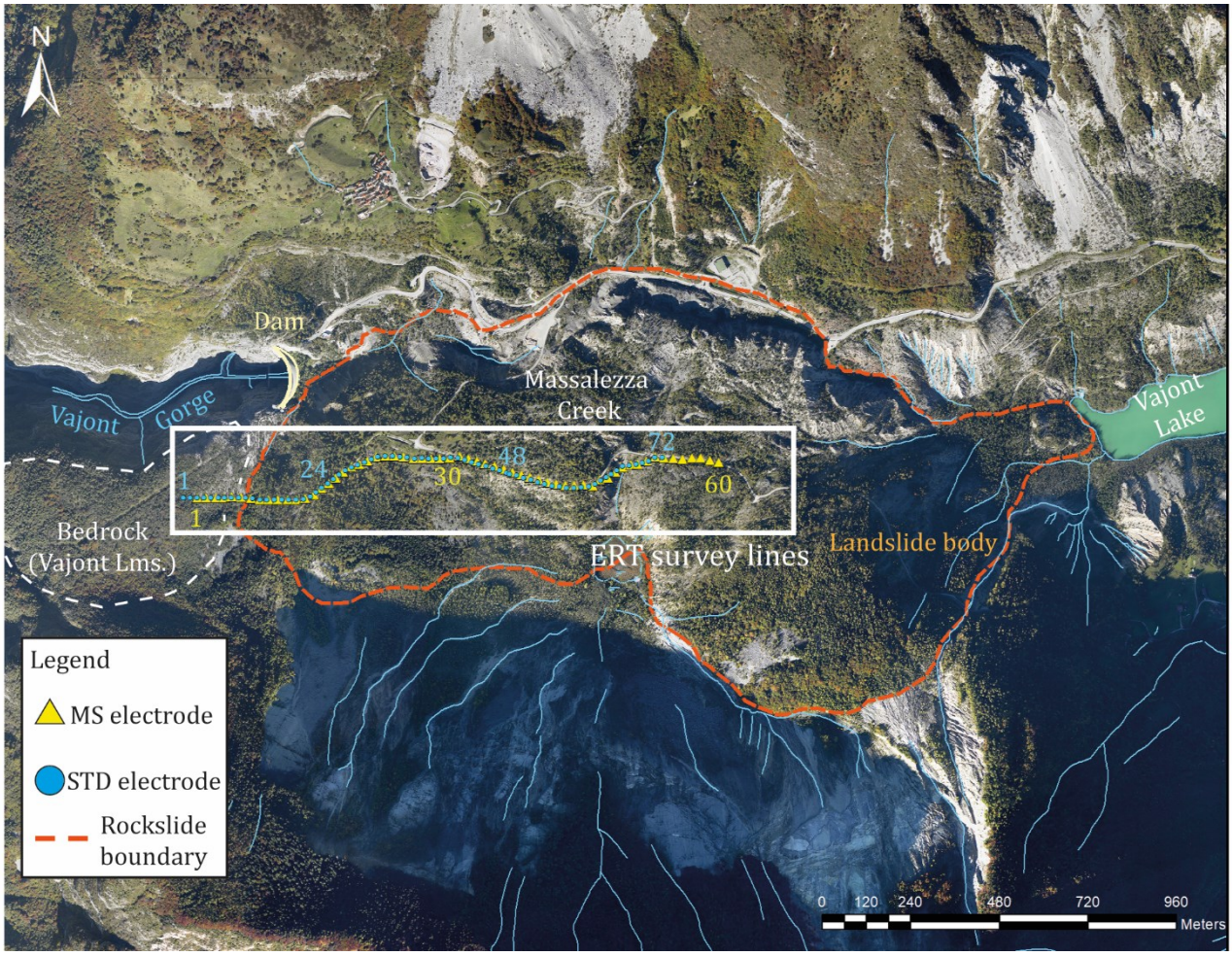

Figure 66: Traditional system and MS-DD deployments on the Vajont rockslide. Electrode location is indicated with yellow (traditional system) and blue (MS-DD) triangles.

7.5.2 DATA ANALYSIS AND PROCESSING

STD system

Voltages (V) range from -1450 mV to 15000 mV with an average value of 420 mV and a standard deviation (σ) of 1000 mV.

Current intensities (I) vary between 35 mA and 695 mA, with an average value of 290 mA and standard deviation of 140 mA.

Geometrical factors (K) range from -32000 m to 60000 m, with an average of almost 2050 m and a standard deviation of 6900 m.

MS-DD system

Reciprocal measurements were removed from the various MS-DD datasets. Outliers, negative values and noisy data caused by poor electrode coupling were also removed.

Voltages (V) were distributed on a -5270-2498 mV, with an average value of almost -81 mV, and a standard deviation of 492 mV.

The current intensity was in the range of 45-414 mA, with an average value of almost 200 mA, and a standard deviation of 82 mA.

The geometrical factors (K) ranged mainly in a -74000-74000 m interval.

The resulting apparent resistivity was in the range of the 63-20000 Ω·m, with an average of 2263 Ω·m and a σ=2260 Ω·m.

The apparent resistivity distribution in the STD and MS-DD pseudo-sections is more or less similar (**Fig. 68**). Few differences are related to the sequence used to collect the data. High apparent resistivity data (>3500 Ω·m) were mainly measured in the western portion of the survey line (outcropping limestone) and on the opposite end below the Massalezza creek. The central and shallow portion of the pseudo-resistivity section is dominated by relatively conductive values (500-2000 Ω·m). The boundary between the resistive and the relatively conductive domain is dipping eastwards 30-40 degrees. The boundary is particularly evident in the MS-DD dataset and at the bottom of the section there several data-points with apparent resistivity larger then 8000 Ω·m indicating that the electrical field generated by the outermost dipoles penetrated the underlying basement.

7.5.2.1 Inversion parameters

Subsurface was discretized using equal cell size for the STD and MS-DD datasets. The element geometry was 10 m along the X, Y and Z axes. This approach was meaningful because electrode spacing was comparable for the two different acquisitions.

The number of cells for the two meshes is slightly different because of the larger DOI in the MS-DD dataset and also because the MS-DD line is approximately 100 m longer than the STD line.

Mesh parameters are summarized in **Tabb. 15-16**.

Both meshes were initialized with a resistivity value of 3000 Ω·m computed averaging the values of previous electrical surveys (***Bohm et al., 2014***). NPCG was set to 100 while noise constant error term was set to 0.00001 Ω.

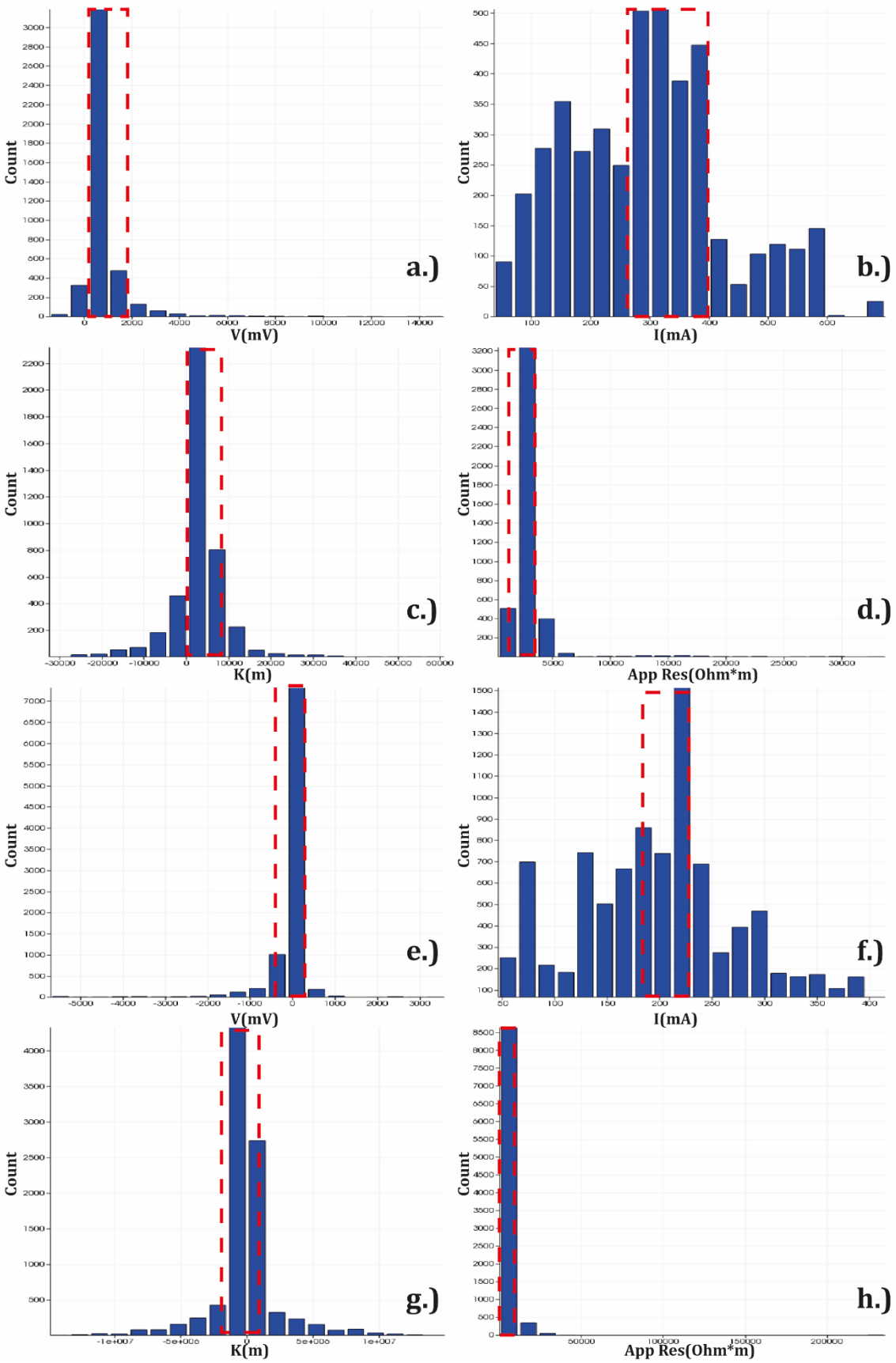

Figure 67: Statistics for the collected data: a, b, c and d for STD; e, f, g and h for MS-DD.

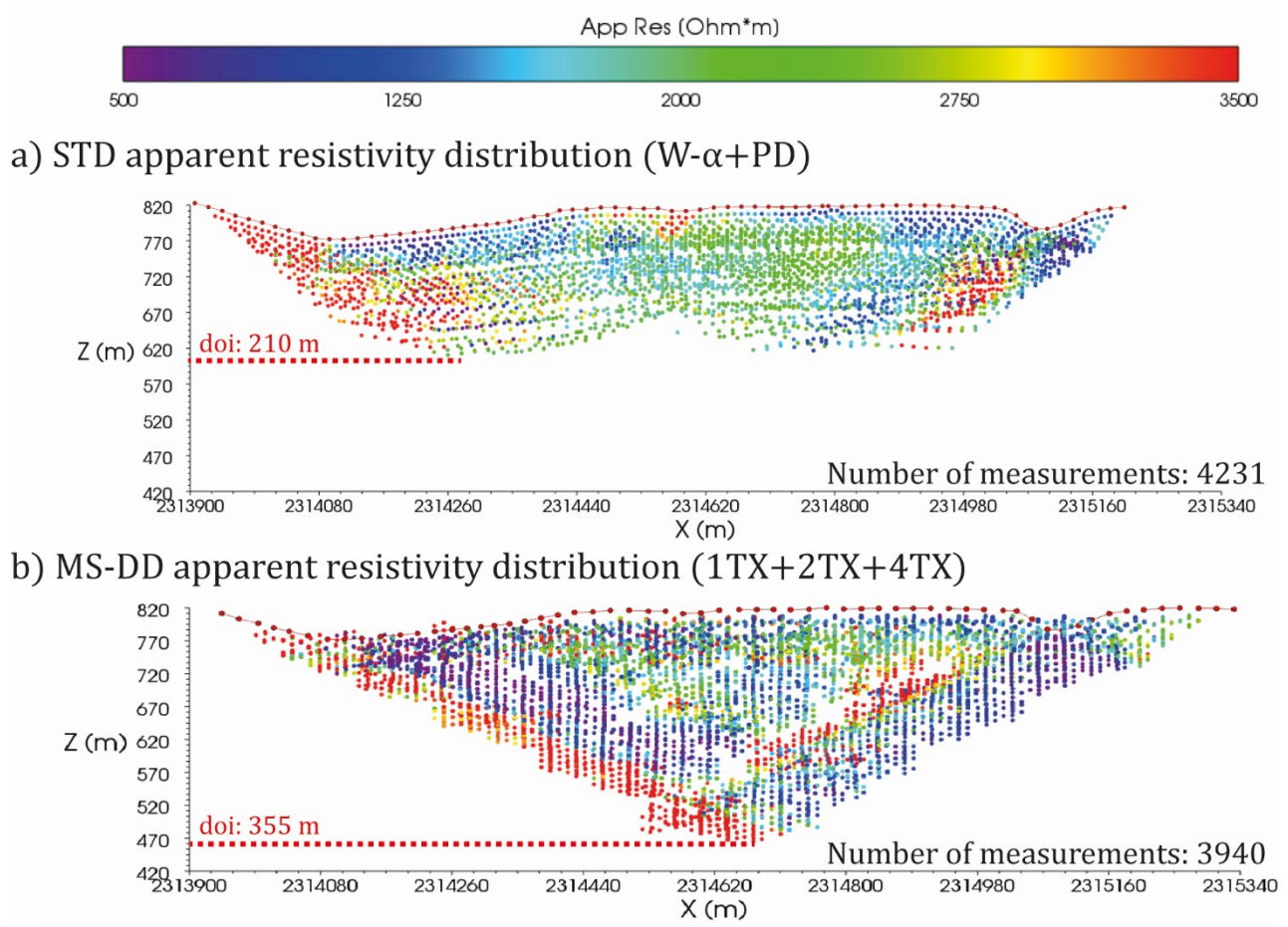

Figure 68: Apparent resistivity distributions for the STD (a) and MS-DD (b) datasets. The dotted-red line marks the DOI.

Table 15: mesh parameters for the STD dataset.

	X	Y	Z	TOTAL
Min.(m)	2579057	4998755	555	
Max.(m)	2580358	4998866	822	
El. Size(m)	10	10	10	
BR pads	1 2 4 8 16 24 32 40 48 56 64	1 2 4 8 16 24 32 40 48 56 64	1 2 4 8 16 24 32 40 48 56 64	
FR cells	153	34	34	176868

Table 16: mesh parameters for the MS-DD dataset.

	X	Y	Z	TOTAL
Min.(m)	2579095	4998756	540 m	
Max.(m)	2580485	4998866	820 m	
El. Size(m)	10 m	10 m	10 m	
BR pads	1 2 4 8 16 24 32 40 48 56 64	1 2 4 8 16 24 32 40 48 56 64	1 2 4 8 16 24 32 40 48 56 64	
FR cells	162	34	35	192780

7.5.3 RESULTS

Resistivity, in the inverted sections (**Fig. 69**), range from 1000 Ω·m to values larger than 4000 Ω·m.

The resistivity distribution in the STD inversion show three main sectors (**Fig. 69a**). The first (Sector 1) is a resistive shoulder (HRD) dominated by high resistivity values (>3000-3500 Ω·m) near the surface and in depth. At X ≈ 200 m resistivity in the shallow layers drops to about 1200 Ω·m (conductive body CB1). HRD is truncated, about 40 m below the surface, by a vertical boundary at X ≈ 300 m (electrode 17).

The second (Sector 2) spans from X≈320 m to X≈1110 m. An east-verging composite body, comprised of three layers, is visible this sector. A near surface conductive body is comprised of two nuclei (CB4 and CB5). An intermediate dipping resistive body (DRB) occupies the central and eastern portion of this sector. A deep and thick conductive body (CB2, CB3) spans over almost the entire sector.

A third and last sector (Sector 3) begins beyond X≈1110 m (electrode 60) and it extends towards the end of the line. Resistivity in this sector is pretty low. A near surface syncline is located just below the Massalezza ditch (CB6). A moderately resistive body (RB2) is located at intermediate depth while a second conductor (CB7) occupies the lower and deeper portion of the sector.

The MS inverted section seems a less diversified in terms of resistivity distribution (**Fig. 69b**).

The resistivity distribution in the MS-DD is more homogeneous compared to STD inversion. The resistivity image could be further divided in two sectors (**Fig. 69b**).

The first (Sector 1) is the same resistive shoulder (HRD) visible in the STD section with similar background values. Sector 1 is almost identical in the two inverted sections with the sole difference of a the presence of a barely inclined boundary (at electrode 17) between Sector 1 and Sector 2. Shallow CB1 conductor shows roughly the same geometry as in the STD inversion.

The second (Sector 2) spans from X≈290 m to the end of the section. The composite body visible in the STD inversion appears to be not as defined in MS-DD data although the same three units could be easily recognized. A thin near surface body, with alternate resistivity, spans from X≈720 m to the end section; conductive nucleus CB5 (visible in the STD inversion) is part of this near surface body. A variable-thickness resistive (>4000 Ω·m) body (VTRB) is visible from X≈350 m to almost X≈1350 m; its maximum thickness is about 150 m. A third and moderately conductive body extends from the bottom boundary of VTRB down to the maximum depth; nuclei CB2, CB3 , and CB7 are part of this body and they could be easily correlated, although more resistive, to the STD inversion.

Resistivity increases in the central and deep portion of the MS-DD inversion. This domain of deep and higher resistivity (RDI, 2700-2800 Ω·m) is particularly important because it points out how MS-DD measurements reach the underlying calcareous basement.

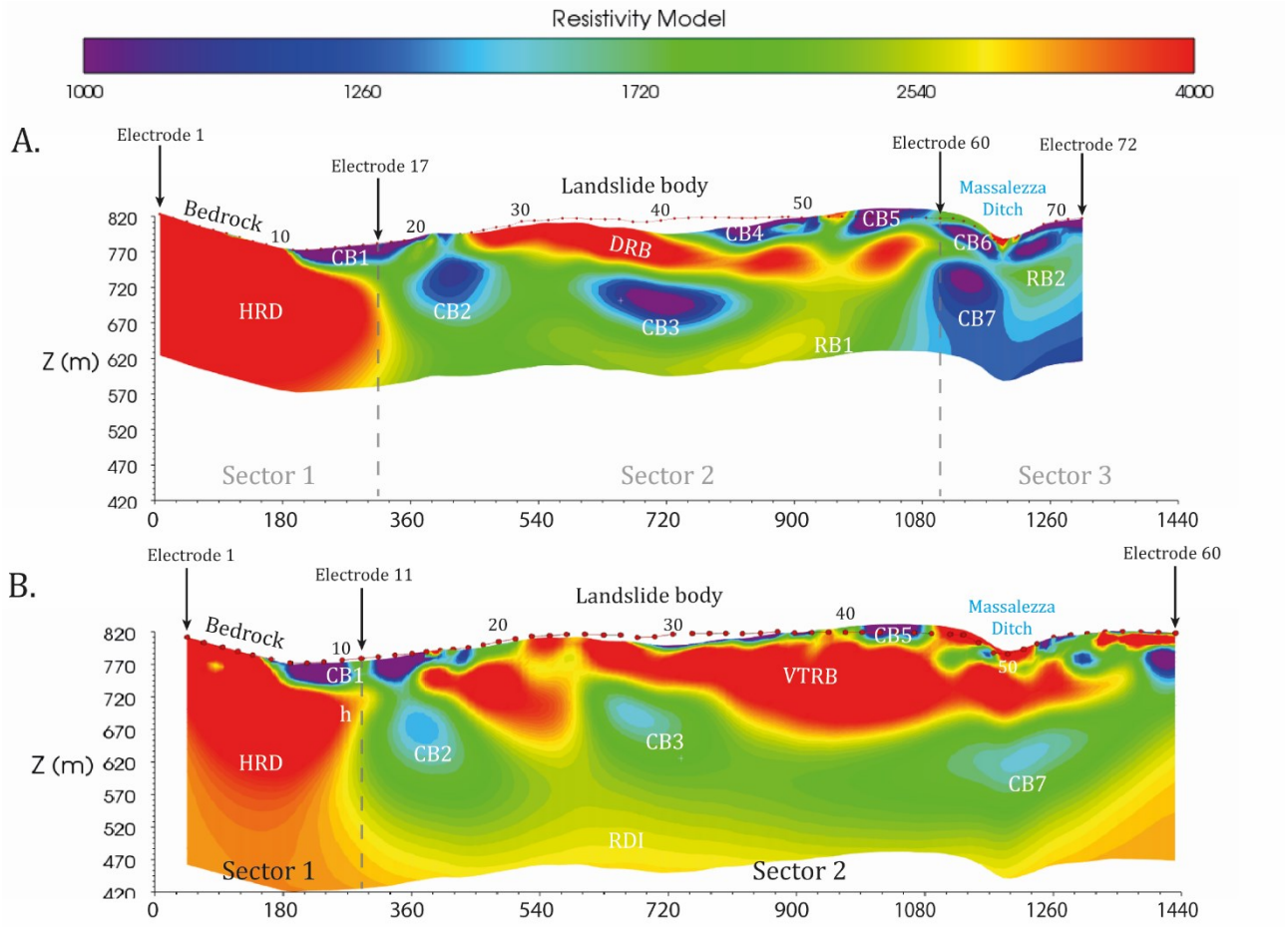

Figure 69: inverted resistivity models for the STD array (A) and for the MS-DD array (B). HRD: high resistivity domain; CB: conductive body; DRB: dipping resistive body; RB: resistive body; VTRB: variable-thickness resistive body; RDI: deep resistivite layer.

7.5.4 DISCUSSION

The two sections show the same resistivity framework (**Fig. 70**), which is also consistent with the expected geological architecture of the subsurface (***Broili et al., 1967***).

HRD is clearly interpretable as the response of the Vajont Limestone formation. This is the stiffer and the thicker unit outcropping in this portion of the valley, and its presence is confirmed also at great depths (550-570 m a.s.l.) by borehole information. In other words, this first sector, present in both the two sections, proves the presence of the Vajont Limestones down to large depth and it also defines its geometrical relationship with to the respect the landslide body. The conductive wedge CB1 could be interpreted as a lateral expansion of the landslide body or as a thin layer of Late Jurassic limestones.

The eastern termination of HDR is depicted as an abrupt boundary. This could be interpreted as a tectonic contact or as due to a loss of resolving power caused by the conductive body comprised of CB2 and CB3. Both the two hypotheses are reasonable. CB2 in the MS-DD inversion probably causes the above boundary to curve.

DRI, in the MS-DD section, is a crucial interpretative element as it indicates the presence of a deep resistor. This key aspect is, probably, the most important feature of the MS-DD section and it proves the higher depth of investigation of the MS-DD with respect to STD.

DRI denotes the penetration of the artificial electrical field within the Vajont Limestone beneath the western-central portion of the line, in optimal conditions of sensitivity. A 50-m thick layer, extended from X≈510 m to X≈900 m, outlines this deep increase in the resistivity values. The penetration of the electrical field in the basement is also confirmed by the apparent resistivity distribution (see par. 7.5.2).

Additional geological insight could be brought by the resistivity image. The intermediate resistive body (DRB and VTRB) could be interpreted as detached and glided flakes of stiff Cretaceous limestones while the deep conductive body (CB2, CB3 and CB7) is probably comprised of detached and glided upper Jurassic and lower Cretaceous limestones. The resistive layer visible in the Massalezza ditch is comprised of Quaternary alluvial and fluvio-glacial deposits (***Francese et al., 2013***). The mirrored dipping conductive layer CB6 is the well-known Massalezza syncline (***Massironi et al., 2013***).

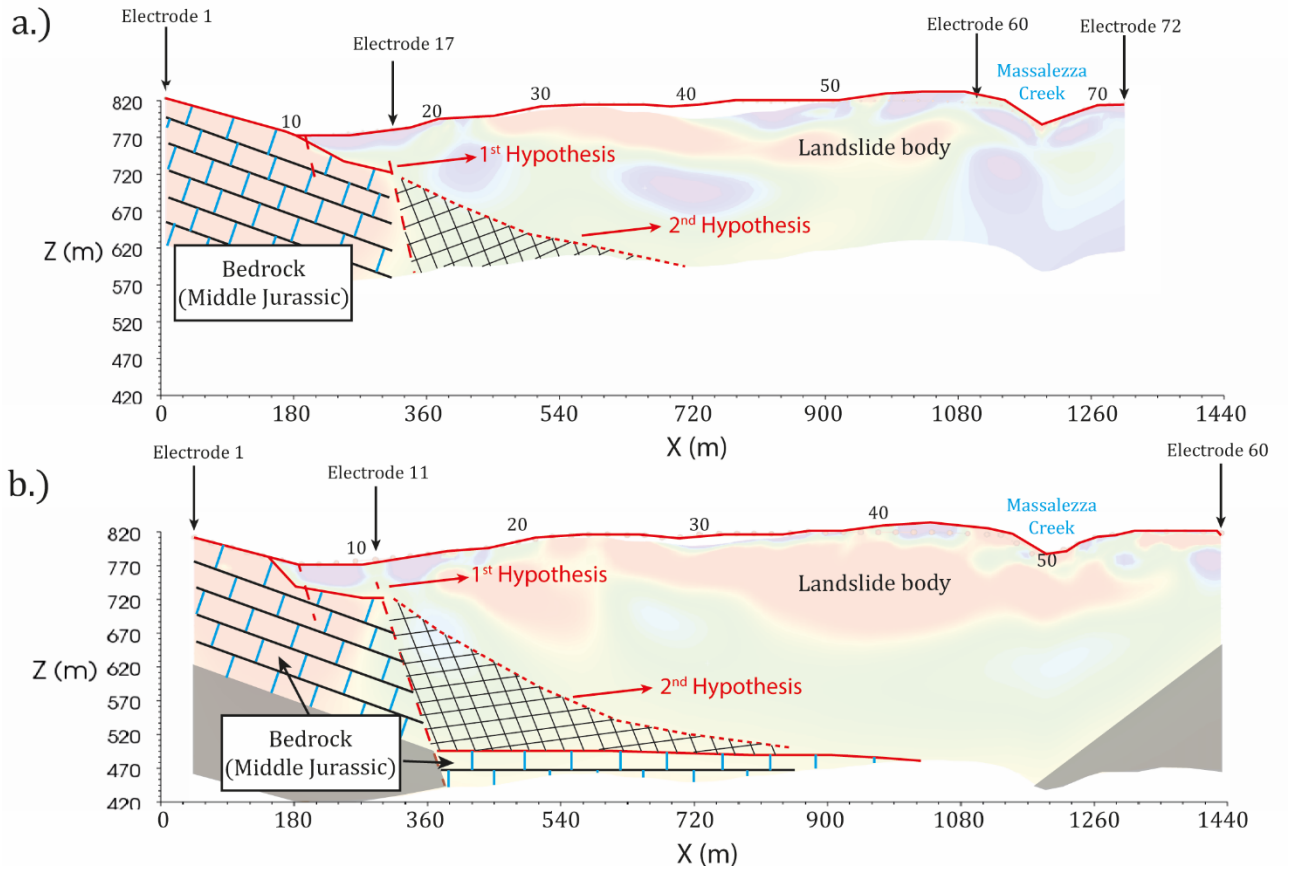

Figure 70: Tentative interpretation of the STD (a) and MS-DD (b) inversion. Different hypotheses for the interpretation of the basement-landslide boundary. 1st hypothesis: tectonic contact; 2nd hypothesis: "ghost" contact.

The description is consistent for the two inverted resistivity sections, even though important differences emerge in the electrical properties of the subsurface. For example, the western termination of the resistive superficial body visible in this central sector looks much more complex in the MS-DD section, as well as the continuity of the small conductive body demarking the passage between sectors 1-2. The presence of this big resistive structure can be the results of a slightly different resolution capability of the MS respect to the SP system, given primarily by its different data density.

Moreover, the presence of deep resistive bodies towards the maximum depth could act as a sort of amplifier, at the bottom of the section, of the superficial resistive body.

The overall images of the two inversions show an almost one to one correspondence. The near surface layers, because of the data-points distribution, are better resolved by the STD array. The DRV / VTRB bodies are pretty similar but for a very high-resistive body centered at X≈510 m. The deep conductive body is also imaged in both the sections although it is about 40% more conductive in the STD inversion.

The MS-DD array, as expected, penetrates deeper compared to the STD array. The block-based design of MS-DD acquisition exploited MS potentials as the outermost dipoles measured very low but still usable signals at values of the "n" factor as high as 22.

8. CONCLUSIONS

The MS is a new-generation resistivity-meter mostly conceived for 3D and DERT surveys. Major innovations of the MS are 1) the capability of injecting current using different simultaneous dipoles, 2) the articulation in wireless autonomous transmitting / receiving units 3) the flexibility during deployment and its portability, 4) the high-quality of the electronic circuitry .

The objective of this research was to carry out a comprehensive testing to gain initial insight on the system itself. Tests were conducted by aid of numerical simulations and application to real study cases. Testing results proved how the MS has promising potentials and it could be a major breakthrough for ERT surveying.

The combination of the simultaneous current injections along with the sophisticated electronic circuitry result in an up-to-date procedure to increase the signal-to-noise-ratio of faraway transmitting and receiving dipoles. The threshold for a reliable signal was estimated with a dedicated experiment. Single and multiple transmissions were recorded with an ensemble of data loggers, laid out in parallel with the MS units, to evaluate the signal decay with distance. The recorded multi-cycle signal amplitude was compared to the signals stored in the MS unit memory. Low-amplitude and barely recognizable signals in the time series of the data loggers resulted were perfectly reconstructed by the MS electronics. The value of 0.02 mV was then established as the proper signal threshold for MS measurements. This value results in an improved accuracy of about 5 times compared to traditional resistivity measurements. This threshold value of 0.02mV was obtained for both single- and multiple-transmitter modes. This signal amplitude results from dipoles having an “n” factor as high as 20. High values of the “n” factor results in larger DOI thus in an increased penetration of the electrical field

A second implication of such a low signal threshold is the possibility of the best selection in setting the noise percentage for data inversion.

Another important aspect is related to the high degree of freedom in laying down multiple simultaneous transmitters and receivers, especially when the survey is comprised of several lines. A series of MS arrays with varying number of simultaneous transmitters (1, 2, 4 and 8) were tested on a levee-like shallow scenario simulating different orientation (parallel, transverse, etc), different number of electrode lines as well as inline and cross-line transmitters. The double-transmitter was particularly effective in resolving the target anomaly geometry and in fitting its resistivity value. Three-dimensional acquisition geometry resulted in a further improvement of the double-transmitter effectiveness. In this scenario the double-transmitter represents the trade-off between signal intensity (directly proportional to the number of transmitters) and the number of data-points. The single-transmitter mode also resulted in sharp images but with poorly focused depth targets. The use of this mode should be then evaluated on a case-by-case basis. The quadruple-transmitter mode generates low-resolution resistivity images mostly because of the reduced number of data-points.

The application to a real levee case proved to be consistent with the simulation results. A target sand layer located below the levee base was clearly outlined by the single- and double-transmitter arrays while it was just barely detected by a traditional dipole-dipole array. The target resistivity was moderately fit by the MS arrays.

The third important aspect, although party investigated in this study, is the MS system capability of better imaging deep targets, taking full advantage of multiple transmitters. Results from numerical simulations indicated that the double-transmitter array is again the trade-off between resolution and depth of penetration. The quadruple-transmitter array, in case of vertical interface, further focuses subsurface geometry and improves the fit on the target resistivity. In case of vertical interface the dipole-dipole array performs poorly at large depths.

The application to a real case (i.e. the mapping of a deep failure surface of a giant landslide in the Alps) proved to be more or less consistent with the simulation results. Based on simulation results the survey strategy was modified implementing a block-based layout in order to increase the depth of penetration. This approach is not suitable for traditional systems. The sliding surface was imaged at a depth of more than 250 m below the surface.

Several others advantages should be mentioned for the MS. For example, the time required to collect the data with a typical 48-electrode array is less than half compared to a traditional resistivity-meter. A traditional system has a limited number of receiving channels while in the MS, due to GPS synchronization, all, but the transmitting units, record the potential signals simultaneously. Reciprocal measurements, natively collected by the MS, are an additional benefit as they provide a strict control on data quality. This procedure, although feasible in traditional systems, in never implemented because it is significantly time-consuming.

There also some drawbacks for the MS. The major limitations are probably intrinsic in the concept design. Data has to be collected in dipole-dipole configuration. In single-transmitter mode the data-point distribution is clustered. This is caused by the impossibility of enabling cross-unit transmitters and/or receivers. The aperture of the transmitting/receiving dipoles is also limited by the concept design of the MS as the maximum aperture is realized using the first and the third electrodes of each unit. These limits could be easily overcome with a free distribution of the electrodes (i.e. using large transmission dipoles) connected to each unit but it is probably beyond the purpose of this new system.

Other problems can be related to battery transport and endurance, especially when suveys need to be carried out on rough terrains; moreover, also some communication problems may arise through radio signals, for example when big TX-RX distances are necessary or when vegetation is present.

An addition problem, that is more of a logistic problem, is the weight of each single unit as it incorporates the transmission battery.

Future developments of the MS should be supported by a detailed analysis of the sensitivity function over specifically designed targets, to enhance field procedures minimizing the gaps in the data-points distribution and maximizing the resolution of both geometry and resistivity value at large depths.

Field experiments in different subsurface scenarios are also required to validate simulation results and understand how to get the most novel concept and challenging electrical resistivity tomography system.

CREDITS

There are many persons that have made possible the accomplishment of this work and without them this simply would not have happened.

First of all, a big mention is for my supervisor, Prof. Roberto Francese, for giving me the possibility to spend these three prolific (even though strange and unlucky) years at the University of Parma, for the precious advices and the uncountable expertises you tried to transfer to me. Your guide in this small part of the world of geophysics has been crucial for me.

A second huge remark is for Doct. Federico Fischanger and his infinite patience and professionalism in teaching me the various aspects related to resistivity modeling and inversion. I hope I have learned only even a small part of your know-how.

A third huge thank goes to Doct. Massimo Giorgi for the possibility you gave me to join to several surveys and learn from your experience. You made possible this work by giving me access to the MS, especially for the field surveys. Your cookery refinement was appreciated too.

I wish to thank particularly also my only colleague-geophysicist in Parma, Doct. Oziel Souza de Araujo, or simply Ozi. You gave me a lot of advices and technical opinions, theoretical and practical, and you helped me to grow since your arrival almost three years ago. You are an example for me, and I hope to develop many more skills as you suggested me.

There are countless other persons who helped me to grow in those years, even though just by-passage in terms of time: of these, I remember Doct. Giancarlo Ceresoli (Progea Consulting s.r.l.) and the staff of Geostudi Astier s.r.l.; Doct. Stefano Picotti and Doct. Michela Dal Cin of the "Istituto Nazionale di Oceanografia e Geofisica Sperimentale (OGS)"; Prof. Matteo Lupi and its young and talented team of researchers at the University of Geneva (Switzerland); or again Prof. Aldino Bondesan (Università di Padova, Adastra Engineering) and Doct. Giovanni Rigatto (Adastra Engineering).

I wish also to thank all my Bachelor and Master degree professors of the Earth Sciences course at the University of Parma, where I spent the last 8 (short) years of my life. When I enrolled at the first year of bachelor I was just a young and inexperienced guy who was fascinated by the exploration of the unknown. You gave me the possibility to go deeper in this passion, and you opened my mind to new exciting disciplines. This has no price, and cannot be rewarded.

Finally, I wish to thank all the persons who love me, or with which I spent good times in these last three years, from my family and Adele to my friends and PhD mates. This work is dedicated to them, and especially to my grandma, “Nonna Ione”, who passed away more than a year ago. This work is dedicated to me, also, and to the path I have been into in those last times.

BIBLIOGRAPHY

Alpin, L. M. (1950). The theory of dipole sounding, in: "Dipole methods for measuring earth conductivity", Consultant Bureau, New York, 1966, I-I.

Anderson L.A. and Keller G.V. (1966). Experimental deep resistivity probes in the Central and Eastern United States. Geophysics, Vol. XXXI, NO. 6, pp. 1105-1122, 20 figs.

Archie G.E. (1942). The Electrical Resistivity Log as an Aid in Determining Some Reservoir Characteristics. Petroleum Transactions of AIME, vol. 146, 1942, pp. 54–62.

Arosio, D., Munda, S., Tresoldi, G., Papini, M., Longoni, L. and Zanzi, L. (2017) A customized resistivity system for monitoring saturation and seepage in earthen levees: installation and validation. Open Geosciences 9, 457–467. https://doi.org/10.1515/geo-2017-0035.

Bievre, G., Oxarango, L., G¨ unther, T., Goutaland, D. and Massardi,M. (2018) Improvement of 2DERT measurements conducted along a small earth-filled dyke using 3D topographic data and 3D computation of geometric factors. *Journal of Applied Geophysics*, 153, 100–112.

Binley, A., & Slater, L. (2020). Resistivity and Induced Polarization: Theory and Applications to the Near-Surface Earth. Cambridge: Cambridge University Press. doi:10.1017/9781108685955.

Bocchia F., Francese R.G., Giorgi M., Fischanger F. and Picotti S. (2021). The impact of multiple transmitters on signal strenght in Deep Electrical Resistivity Tomography data: an experiment in the Vajont valley (North-Eastern Italy). Bulletin of Geophysics and Oceanography. Vol. DOI: 10.4430/bgta0359.

Boehm G., Francese R. and Giorgi M. (2014). 3D geophysical model of the Vajont rockslide from Seismic and Geoelectric surveys. 20th European meeting of Environmental and Engineering Geophysics. Athens, Greece, 14-18 September 2014.

Bondesan A., Meneghel M. (2011). Carta geomorfologica della provincia di Venezia. Tavola 9, scala 1:100.000.

Candansayar M.E. (2008). Two-dimensional individual and joint inversion of three- and four-electrode array DC resistivity data. *Journal of Geophysics and Engineering* **5**, 290–300, doi:10.1088/1742-2132/5/3/005.

Carey A.M., Paige G.B., Carr B.J., Dogan M. (2017). Forward modeling to investigate inversion artifacts resulting from time-lapse electrical resistivity tomography during rainfall simulations. Journal of Applied Geophysics 145 (2017) 39–49.

Carrara E., Rapolla A., Roberti R. (1992). Le indagini geofisiche per lo studio del sottosuolo: metodi geoelettrici e sismici. Liguori editore.

Chambers J.E., Wilkinson P.B., Penn S., Meldrum P.I., Kuras O., Loke M.H., Gunn D.A. (2013). River terrace sand and gravel deposit reserve estimation using three-dimensional electrical resistivity tomography for bedrock surface detection. Journal of Applied Geophysics 93 (2013) 25–32.

Chambers J.E., Gunn D.A., Wilkinson P.B., Meldrum P.I., Haslam E., Holyoake S., Kirkham M., Kuras O., Merritt A. and Wragg J. (2014). 4D electrical resistivity tomography monitoring of soil moisture dynamics in an operational railway embankment. Near Surface Geophysics, 2014, 12, 61-72. doi:10.3997/1873-0604.2013002.

Constable, S. C., Parker, R. L., and Constable, C. G. (1987). Occam's inversion: A practical algorithm for generating smooth models from electromagnetic sounding data: Geophysics, 52, 289-300.

Dahlin T. and Zhou B. (2004). A numerical comparison of 2D resistivity imaging with 10 electrode arrays *Geophys. Prospect.* **52** 379–98.

Dahlin, T., Zhou, B. (2006). Multiple gradient array measurements for multi-channel 2D resistivity imaging. Near Surface Geophysics 4 (2), 113–123.

deGroot-Hedlin, C., Constable, S. (1990). Occam's inversion to generate smooth, twodimensional models from magnetotelluric data. Geophysics 55 (12), 1613–1624.

Dezert T., Fargier Y., Palma Lopes S., Côte P. (2019). Geophysical and geotechnical methods for fluvial levee investigation: A review. Engineering Geology, Volume 260, 2019, https://doi.org/10.1016/j.enggeo.2019.105206.

Eaton, P., B. Anderson, S. Queen, I. Mackenzie, and D. Wynn (2010). NEWDAS: The Newmont Distributed IP Data Acquisition System: 80th Annual International Meeting, SEG, Expanded Abstracts, **29**, no. 1, 1768–1772. http://dx.doi.org/10.1190/1.3513184.

Edwards L.S. (1977). A modified pseudosection for resistivity and induced-polarization. Geophysics, 42, 1020-1036.

Fauchard, C., Mériaux, P. (2007). Geophysical and Geotechnical Methods for Diagnosing Flood Protection Dikes: Guide for Implementation and Interpretation. Quae.

Fox R.C., Hohmann G.W., Killpacks T.J. and Rijo L. (1980). Topographic effects in resistivity and induced-polarization surveys. Geophysics. Vol. 45, No.1 (January 1980); p: 75-93, 19 Figs.

Francese R., Giorgi M., Boehm G., Bistacchi A., Bondesan A., Massironi M. and Genevois R. (2013). 3D geophysical imaging of the Vajont landslide and of its surroundings. Italian Journal of Engineering Geology and Environment. International conference Vajont 1963-2013. Thoughts and analyses after 50 years since the catastrophic landslide. Padua, Italy-8-10 October 2013.

Francese R., Morelli G., Monteiro Santos F., Bondesan A., Giorgi M. and Tessarollo A. (2018). An integrated geophysical approach to scan river enbankments. Fast times, Vol. 23, 3.

Ghosh, D.P. (1971). The application of linear filter theory to the direct interpretation of geoelectrical resistivity sounding measurements. Geophysical Prospecting 19 (2), 192–217.

Griffiths, D.H., Turnbull J. (1985). A multi-electrode array for resistivity surveying. First Break 3 (7), 16-20.

Guzzi R. (2012). Introduzione ai metodi inversi. Con applicazioni alla geofisica e al telerilevamento. Springer-Verlag.

Hadamard J.(1923) Lectures on Cauchy's problem in linear partial differential equations, Dover Phoenix editions, Dover Publications, New York.

Hallof P. G. (1957). On the interpretation of resistivity and induced polarization results: Ph.D. thesis, MIT, Cambridge.

Herrera G., Mateos R. M., García-Davalillo J. C., Grandjean G., Poyiadji E., Maftei R., Filipciuc T.C., Jemec Auflič M., Jež J., Podolszki L., Trigila A., Iadanza C., Raetzo H., Kociu A., Przyłucka M., Kułak M., Sheehy M., Pellicer X. M., McKeown C., Ryan G., Kopačková V., Frei M., Kuhn D., Hermanns R. L., Koulermou N., Smith C. A., Engdahl M., Buxó P., Gonzalez M., Dashwood C., Reeves H., Cigna F., Liščák P., Pauditš P., Mikulėnas V., Demir V., Raha M., Quental L., Sandić C., and Jensen O. A. (2018). Landslide databases in the Geological Surveys of Europe, Landslides, 15, 450: 359-379.

Hojat A., Arosio D., Ivanov V.I., Loke M.H., Longoni L., Papini M., Tresoldi G. and Zanzi L. (2020). Quantifying seasonal 3D effects for a permanent electrical resistivity tomography monitoring system along the embankment of an irrigation canal. Near Surface Geophysics, 2020, 18, 427–443. doi: 10.1002/nsg.12110.

Inazaki, T., Sakamoto, T. (2005). Geotechnical characterization of levee by integrated geophysical surveying. In: Proceedings of the International Symposium on Dam Safety and Detection of Hidden Troubles of Dams and Dikes.

Inman, J.R. (1975). Resistivity inversion with ridge regression. Geophysics 40 (5), 798–817.

Jodry, C., Palma Lopes, S., Fargier, Y., Côte, P., Sanchez, M. (2017). A cost-effective 3D Electrical resistivity imaging approach applied to Dike investigation. Near Surf. Geophys. 15, 27–41. https://doi.org/10.3997/1873-0604.2016036.

Lino M., Meriaux P., Royet P. (2000): *Méthodologie de diagnostic des digues appliquée aux levées de la Loire moyenne*, Cemagref Editions, ISBN 2-85362-524-9, 224 p.

Keller, G. V., and Frischknecht, F. C. (1966). Electrical methods in geophysical propecting: Pergamon Press.

Keller G.V., Furgerson R., Lee C.Y., Harthill N. and Jacobson J.J. (1975). The dipole mapping method. Geophysics, Vol. 40, NO. 3, pp. 451-472, 23 figs.

Kingman, J. E. E., J. G. Donohue, and T. J. Ritchie (2007). Distributed acquisition in electrical geophysical systems, in B. Milkereit, ed., Proceedings of Exploration07: Fifth Decennial International Conference on Mineral Exploration, 425–432, http://library.seg.org/doi/ref/10.1190/segam2014-0619.1

Koefoed, O. (1979). Geosounding Principles 1: Resistivity Sounding Measurements. Elsevier Science Publishing Company, Amsterdam.

Kunetz G. (1966). Principle of Direct Current Resistivity Prospecting. Geopublication Associates. Series 1-No.1.

Kuras O., Wilkinson P.B., Meldrum P.I., Oxby L.S., Uhlemann S., Chambers J.E., Binley A., Graham J., Smith N.T., Atherton N. (2016). Geoelectrical monitoring of simulated subsurface leakage to support high-hazard nuclear decommissioning at the Sellafield Site, UK. Science of the Total Environment 566–567 (2016) 350–359.

LaBrecque, D.L., Miletto, M., Daily, W., Ramirez, A. & Owen, E. (1996). The effects of noise on Occam's inversion of resistivity tomography data, Geophysics, **61,** 538–548.

LaBrecque D., Casale D., Brigham R. and Flinchum B. (2013a): A multi-source approach for electrical resistivity tomography. In: Symposium on the application of Geophysics to Engineering and Environmental Problems 2013, Environmental & Engineering Geophysical Society, p. 795, doi: 10.4133/sageep2013-230.1.

LaBrecque D.J., Morelli G., Fischanger F., Lamoureux P. and Brigham R. (2013b): Field trials of the multi-source approach for resistivity and induced polarization data acquisition. In: Abstracts, AGU Fall Meeting, American Geophysical Union, San Francisco, CA, USA, NS34A-03.

La Compagnie Generale de Gèophysique (1963). Abaques de sondages electrique. Geophys. Prosp., 3, Suppl. 3.

Lee H., Jung H., Cho S., Lee Y.S. (2015): Design for fast 3D electrical resistivity survey for deep exploration using a moving multi-source and distributed acquisition. SEG, Annual meeting, pp. 942-946.

Legault, J. M., D. Carriere, and L. Petrie (2008). Synthetic model testing and distributed acquisition DC resistivity results over an unconformity uranium target from the Athabasca Basin, northern Saskatchewan: The Leading Edge, **27**, 46–51. http://dx.doi.org/10.1190/1.2831679.

Li, Y., Oldenburg, D.W. (1992). Approximate inverse mappings in DC resistivity problems. Geophysical Journal International 109 (2), 343–362.

Loke, M.H. and Barker, R.D. (1995). Least-squares deconvolution of apparent resistivity pseudosections. Geophysics, 60, 1682-1690.

Loke M.H., Chambers J.E., Rucker D.F., Kuras O., Wilkinson P.B. (2013). Recent developments in the direct-current geoelectrical imaging method. Journal of Applied Geophysics 95, 135–156.

Maillet, R., and Doll, H. G. (1932) Theoreme relatif aux millieux electriquement anisotropes et ses applications a la prospection electrique en courant continu: Erganzungshefte fur Angewante Geophysik, v. 3, p 109-124.

Martorana R., Fiandaca G., Casas A.P. and Cosentino P.L. (2009). Comparative tests on different multi-electrode arrays using models in near-surface geophysics. *Journal of Geophysics and Engineering* **6**, 1–20.

Massironi, M., Superchi L., Zampieri D., Bistacchi A., Ravagnan R., Bergamo A., Ghirotti M..& Genevois R. (2013) - Geological Structures of the Vajont landslide. Italian Journal of Engineering Geology and Environment. International conference Vajont 1963-2013. Thoughts and analyses after 50 years since the catastrophic landslide. Padua, Italy-8-10 October 2013.

Mériaux P., Royet P. et Folton C. (2004). Surveillance, entretien et diagnostic des digues de protection contre les inondations. Guide pratique à l'usage des gestionnaires, Paris, Cemagref Éditions.

Monteiro Santos F.A., Andrade Afonso A.R. and Mendes Victor L.A. (1997). Study of the Chaves geothermal field using 3D resistivity modeling. Journal of Applied Geophysics, 37, 85-102.

Mooney H.M., Wetzel W.W. (1956). The potentials about a point electrode and apparent resistivity curves for a two-, three-, and four-layer earth. University of Minnesota Press.

Morelli, G.; LaBrecque, D.J. (1996). Advances in ERT inverse modelling. Eur. J. Environ. Eng. Geophys. Soc., 1, 171–177.

Müller-Huber, E., Schön, J., Börner, F. (2015). The effect of a variable pore radius on formation resistivity factor. J. Appl. Geophys. 116, 173–179.

Mundry E., Homilius J. (1979). Three layer model curves for geoelectrical resistivity measurements – Schlumberger array -. E. Schweizerbart'sche Verlagsbuchhandlung, Hannover.

Orellana E. (1982). Prospeccion geoelectrica en corriente continua. Secunda Edicion. Editorial Paraninfo, Madrid.

Orellana E., Mooney H.M., (1966). Master tables and curves for vertical electrical sounding over layered structures. Interciencia, Madrid.

Palma-Lopes S., Fargier Y., Fauchard C., Jacqueline D., Francois D. and Cote P. (2012). Improving DC-Electrical Resistivity Imaging techniques for water infiltration detection and monitoring in earth hydraulic structures. ICSE 6, Paris.

Papadopoulos N.G., Yi M.G., Kim J.H., Tsourlos P., Tsokas G.N. (2010). Geophysical investigation of tumuli by means of surface 3D Electrical Resistivity Tomography. Journal of Applied Geophysics 70 (2010) 192–205.

Park, S.K., Van, G.P. (1991). Inversion of pole–pole data for 3-D resistivity structures beneath arrays of electrodes. Geophysics 56 (7), 951–960.

Poupon, A., Loy, M.E., Tixier, M.P. (1954). A contribution to electrical log interpretation in shaly sands. Trans. AIME 201, 138–145.

Press, W. H., Flannery, B. P., Teukolsky, S. A., and Vetterling, W. T. (1986). Numerical recipes, Cambridge Univ. Press, Chap. 9.

Pridmore D.F., Hohmann G.W., Ward S.H., and Sill W.R. (1981), "An investigation of finite-element modeling for electrical and electromagnetic data in three dimensions," GEOPHYSICS 46: 1009-1024.

Putiska R., Dostàl I., Kusnirak D. (2012). Determination of dipping contacts using electrical resistivity tomography. Contributions to geophysics and geodesy, Vol.42/2, 161-180.

Rizzo E. and Giampaolo V. (2019). New deep electrical resistivity tomography in the High Agri Valley basin (Basilicata, Southern Italy). Geomatics, Natural Hazards and Risk, Vol. 10, NO.1, 197-218. https://doi.org/10.1080/19475705.2018.1520150.

Rosenfeld, A., and Kak, A. C. (1981), Digital Picture Processing (2nd ed.), New York: Academic Press.

Roy, A. and Apparao, A. (1971). Depth of investigation in direct current methods. Geophysics, 36, 943-959.

Royet P., Palma Lopes S., Fauchard C., Mériaux P., Auriau L. (2013). Rapid and Cost-Effective Dike Condition Assessment Methods: Geophysics and Remote Sensing. FloodProBE Project.

Rucker, C., Gunther, T. & Spitzer, K. (2006). Three–dimensional modelling and inversion of dc resistivity data incorporating topography I: modelling, Geophys. J. Int., **166,** 495–505.

Rucker, D.F., Noonan, G.E. (2013). Using marine resistivity to map geotechnical properties: A case study in support of dredging the Panama Canal. Near Surface Geophysics. http://dx.doi.org/10.3997/1873-0604.2012017.

Scales J.A., Smith M.L., Treitel S. (2001). Introductory geophysical inverse theory. Samizdat Press.

Schmidt-Hattenberger C., Bergmann P., Labitzke T., Wagner F., Rippe D. (2016). Permanent crosshole electrical resistivity tomography (ERT) as an established method for thelong-term CO2 monitoring at the Ketzin pilot site. International Journal of Greenhouse Gas Control 52 (2016) 432–448.

Schön J.H. (2015). Physical Properties of Rocks—Fundamentals and Principles of Petrophysics. Elsevier. ISBN: 978-0-08-100404-3.

Sharp, M., Wallis, M., Deniaud, F., Hersch-Burdick, R., Tourment, R., Matheu, E., Seda-Sanabria, Y., Wersching, S., Veylon, G., Durand, E., et al. (2013). The International Levee Handbook. CIRIA, London.

Sjödahl, P., Dahlin, T., Johansson, S., Loke, M.H. (2008). Resistivity monitoring for leakage and internal erosion detection at Hällby embankment dam. J. Appl. Geophys. 65 (3-4), 155–164.

Spangenberg, E. (2001). Modeling of the influence of gas hydrate content on the electrical properties of porous sediments. J. Geophys. Res. 106 (B4), 6535_6548.

Spitzer, K. (1995). A 3D finite difference algorithm for DC resistivity modelling using conjugate gradient methods, Geophys. J. Int., 123, 903-914.

State Public Works Service (1969). Standard graphs for resistivity prospecting. E.A.E.G., Netherlands.

Stefanesco, S. S. (1932). Etudes theorique sur la prospection Electrique du sous-sol. 2• se. [Theoretical studies on electrical prospecting of the substrata, part 2]: Inst. geol. Romanieri, v. 14, pt. 2, p. 1-128. Resistivity, Electromagnetic theory.

Storz H, Storz W. and Jacobs S. (2000). Electrical Resistivity Tomography to investigate geological structures of the earth's upper crust. Geophysical Prospecting, 48, 455-471.

Stummer, P., Maurer, H.R., Horstmeyer, H., Green, A.G. (2002). Optimization of DC resistivity data acquisition: real-time experimental design and a new multi-electrode system. IEEE Transactions on Geoscience and Remote Sensing 40 (12), 2727–2736.

Supper, R., Ottowitz, D., Jochum, B., et al. (2014). Geoelectrical monitoring: an innovative method to supplement landslide surveillance and early warning. Near Surf. Geophys. 12, 133–150. http://dx.doi.org/10.3997/1873-0604.2013060.

Szalai, S., Kopp´an, A., Szokoli, K. & Szarka, L., (2013). Geoelectric imaging properties of traditional arrays and of the optimized Stummer configuration, *Near Surf. Geophys.,* **11,** 51–62.

Szalai, S. & Szarka, L., (2008). On the classification of surface geoelectric arrays, *Geophys. Prospect.,* **56,** 159–175.

Tamburiello G., Balasco M., Rizzo E., Harabaglia P., Lapenna V. and Siniscalchi A. (2008). Deep electrical resistivity tomography and geothermal analysis of Bradano foredeep deposits in Venosa area (Southern Italy): preliminary results. Annals of Geophysics, VOL. 51, N. 1, February.

Tarantola A. (2005). Inverse Problem Theory and Methods for Model Parameter. Society of industrial and applied mathematics.

Telford, W., Geldart, L., & Sheriff, R. (1990). Applied Geophysics (2nd ed.). Cambridge: Cambridge University Press. doi:10.1017/CBO9781139167932.

Tejero-Andrade A., Argote-Espino D.L., Cifuentes-Nava G., Hernàndez-Quintero E., Chàvez R.E., García-Serrano A. (2018). 'Illuminating' the interior of Kukulkan's Pyramid, Chichèn Itzà, Mexico, by means of a non-conventional ERT geophysical survey. Journal of Archaeological Science 901e11.

Tikhonov, A. N., and Arsinen, V. Y. (1977). Solutions of ill-posed problems: V. H. Winston and Sons.

Trigilia A. and Iadanza C. (2008). Landslides in Italy. Special report 2008. Italian National Institute for Environmental Protection and Research.

Trigilia A., Iadanza C., Bussettini M., Lastoria B. (2018). Dissesto idrogeologico in Italia: pericolosità ed indicatori di rischio. Edizione 2018. ISPRA, Rapporti 287/2018. ISBN 978-88-448-0901-0.

Van Hoorde M., Hermans T., Dumont G., Nguyen F. (2017). 3D electrical resistivity tomography of karstified formations using cross-line measurements. Engineering Geology 220 (2017) 123–132.

Van Nostrand R.G., Cook K.L. (1966). Interpretation of resistivity data. Geological survey professional paper 499.

Viero A., Galgaro A., Morelli G., Breda A. and Francese R.G. (2015). Investigations on the structural setting of a landslide-prone slope by means of three-dimensional electrical resistivity tomography. Nat Hazards **78,** 1369–1385 (2015). https://doi.org/10.1007/s11069-015-1777-8.

Ward S.H. (1990). Resistivity and Induced Polarization Methods.

Waxman, M.H., Smits, L.J. (1968). Electrical conductivities in oil bearing shaly sands. SPE J. 8 (2), 107–122.

Weller A., Lewis R., Cahn T., Moller M. and Scholz B. (2014). Geotechnical and Geophysical Long-term Monitoring at a Levee of Red River in Vietnam. Journal of environmental and engineering geophysics. September 2014. Volume 19, Issue 3, pp- 183-192.

Whiteley R.J. (1973). Electrode arrays in resistivity and IP prospecting: A review. *Bulletin of the Australian Society of Exploration. Geophysicists.* **4**, 1–29.

Wilkinson P.B., Uhlemann S., Chambers J.E., Meldrum P.I. and Loke M.H. (2015). Development and testing of displacement inversion to track electrode movements on 3-D electrical resistivity tomography monitoring grids. Geophys. J. Int. (2015) 200, 1566–1581. doi: 10.1093/gji/ggu483.